HIGHLY TURBULENT TAYLOR-COUETTE FLOW

DENNIS P.M. VAN GILS

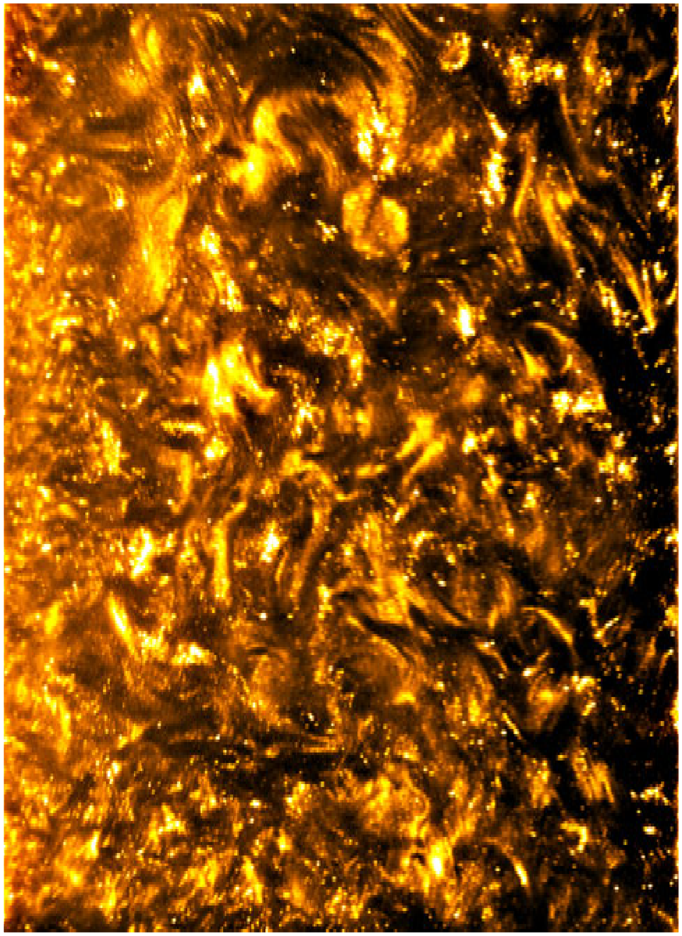

HIGHLY TURBULENT
TAYLOR-COUETTE FLOW

Dennis Paulus Maria van Gils

The work in this thesis was primarily carried out at the Physics of Fluids group of the Faculty of Science and Technology of the University of Twente. It is supported by the Dutch Technology Foundation STW, which is part of the Netherlands Organisation for Scientific Research (NWO) and partly funded by the Ministry of Economic Affairs, Agriculture and Innovation (project number 07781).

Committee members:

Chairman	
Prof. dr. Leen van Wijngaarden	University of Twente
Promotor	
Prof. dr. Detlef Lohse	University of Twente
Assistant promotor	
Dr. Chao Sun	University of Twente
Members	
Prof. dr. ir. Theo H. van der Meer	University of Twente
Prof. dr. Roberto Verzicco	University of Twente & Rome
Prof. dr. ir. Tom J.C. van Terwisga	Delft University of Technology / MARIN
Prof. dr. ir. Jerry Westerweel	Delft University of Technology

Nederlandse titel:
Hoog Turbulente Taylor-Couette Stroming

Cover:
High-speed imaging snapshot showing fully developed turbulent structures inside the T^{3}C gap, seeded with reflective flakes and illuminated by a laser sheet. On the left is the inner cylinder wall, on the right the outer cylinder wall.

Publisher:
Dennis P.M. van Gils, Physics of Fluids, University of Twente,
P.O. Box 217, 7500 AE Enschede, The Netherlands
http://pof.tnw.utwente.nl d.p.m.vangils@alumnus.utwente.nl

Ph.D. Thesis, University of Twente. Printed by Gildeprint Drukkerijen, Enschede.
ISBN: 978-90-365-3272-3 DOI: 10.3990/1.9789036532723

HIGHLY TURBULENT TAYLOR-COUETTE FLOW

PROEFSCHRIFT

ter verkrijging van
de graad van doctor aan de Universiteit Twente,
op gezag van de rector magnificus,
prof. dr. H. Brinksma,
volgens besluit van het College voor Promoties
in het openbaar te verdedigen
op vrijdag 16 december 2011 om 16.45 uur

door

Dennis Paulus Maria van Gils

geboren op 2 mei 1981
te Roosendaal en Nispen

This dissertation has been approved by:

Promotor: Prof. dr. Detlef Lohse
Assistant promotor: Dr. Chao Sun

Turbulent flows persist to remain enigmatic
to mankind – in its details and *main features – still*
after more than 400 years of scientific research.
Does this then imply that to pursue a complete
understanding of turbulence is an exercise in
futility? Perhaps so, hopefully not, more definitely
it is no reason to stop researching. Let this thesis
be a new part of this ongoing puzzle.

Contents

1

Introduction

1.1 Renewed interest

Taylor-Couette (TC) flow, i.e. fluid confined between two concentric and independently rotating cylinders, is one of the classical geometries to study turbulence, see Fig. 1.1a-left for a schematic drawing. The strong point of such a geometry is the closed flow, enabling a well defined energy-balance between the large-scale power input into the flow provided by the cylinder walls' angular velocity, and the small-scale energy dissipation rate manifesting itself as a torque on the cylinder walls. Given the correct experimental conditions it allows for statistically stationary states to be achieved, and such flows are relatively straightforward to investigate experimentally.

A widely acknowledged publication by Taylor in 1923 [1] introduced a solid basis for TC flow at low to moderate turbulence, combining experiments with theory. Others have followed in this turbulent regime, studying primarily the onset and transitions of turbulence, see [2–4] to list a few. In this, mostly experimental, thesis we will focus on the strong turbulent regime, far beyond the initial transitions into turbulence. Prior experimental work was done by Wendt [5] and Taylor [6] around the 1930's, and – after a period of little interest – by Smith & Townsend [7], Townsend [8], Tong *et al.* [9], Lathrop *et al.* [10, 11], Lathrop [12], Lewis [13], Lewis & Swinney [14] and van den Berg *et al.* [15] around the 1980's to 2000's, all at moderately to highly turbulent TC flow. Remarkably, only the experiments by Wendt [5] featured two independently rotating cylinders in the high turbulent regime, enabling an extra dimension to be studied in the phase space, whereas the rest had a fixed outer cylinder, see Fig. 3.1 for an overview.

Recently several new turbulent TC facilities with independently rotating cylinders have been constructed, see e.g. Ravelet *et al.* [16] and Borrero-Echeverry *et al.* [17], both operating at fairly high turbulence up to Reynolds numbers of 10^5. A tremendous amount of work can still be done in this regime to aid the understanding of turbulent TC flow, or turbulence in general. However, we wish to surpass the turbulence levels that have been studied before. To enter the domain of unexplored high TC turbulence our Physics of Fluids group has constructed a new TC facility, called "Twente turbulent Taylor-Couette" (T^3C) facility, which we present in chapter 2. It features two independently rotating cylinders of ~ 1 m in height, is able to reach rotation rates of 20 Hz for the inner cylinder and ±10 Hz for the outer cylinder resulting in a liquid power dissipation of > 10 kW, with torque sensors embedded inside the inner cylinder measuring the drag on the wall, precise temperature and rotation control, and it provides bubble injection, amongst other things.

We kindly acknowledge our colleagues of the University of Maryland (UMD) who recently also entered the highly turbulent TC regime with independently rotating cylinders by updating their TC facility [18]. Most of the experimental data presented in this thesis is obtained from the T^3C, with the exception of chapter 6 whose data originate from the old UMD TC setup with a stationary outer cylinder, and chapter 5 in which we combine experimental results of the UMD TC and the T^3C facility.

1.2 Taylor-Couette flow and the analogy to Rayleigh-Bénard convection

A common way to express the dimensionless driving control parameters of TC flow is given by the inner and outer Reynolds numbers,

$$Re_i = \frac{\omega_i r_i (r_o - r_i)}{\nu}, \tag{1.1}$$

$$Re_o = \frac{\omega_o r_o (r_o - r_i)}{\nu}, \tag{1.2}$$

where r is the cylinder radius, ω is the angular velocity and ν is the kinematic viscosity of the fluid. The subscripts $_i$ and $_o$ denote the inner and outer cylinder, respectively, see Fig. 1.1a-left for the geometry. Additional dimensionless control parameters are the geometric radius ratio $\eta = r_i/r_o$ and aspect ratio $\Gamma = L/d$, where L is the height and $d = r_o - r_i$ is the width of the TC gap. As is depicted in Fig. 1.1a-right, the system responds to sufficiently strong driving by the organization of convective winds (blue arrows) transporting angular velocity from the inner wall to the outer wall (solid green line) under influence of the driving centrifugal force field F_{cent} (red arrow). This transport of angular velocity is coupled to the torque τ, which is necessary to keep the inner cylinder rotating at constant angular velocity.

A visualization is provided on the turbulent transport inside the TC gap. The back cover of this thesis shows high-speed imaging snapshots of the transient flow inside the TC gap at the startup of inner cylinder rotation. Turbulent plumes grow on the inner cylinder (left) and are advected outwards towards the outer cylinder (right), filling the complete gap with turbulence over time. Visualization is achieved by seeding the flow with reflective flakes (Kalliroscope corp., Massachusetts, USA) illuminated by a laser sheet. The front cover shows the same visualization, but this time for fully developed turbulence, which is the topic throughout this thesis.

There exists another fundamental type of flow which shares great similarities to TC flow in its emergent turbulent behavior. It occurs inside a Rayleigh-Bénard (RB) convection cell [19, 20] of diameter D and height L in which fluid is heated from below at an excess temperature Δ with respect to the cooler top plate of temperature T_0, see Fig. 1.1b-left. The dimensionless driving control parameter* is given by the Rayleigh number $Ra = \beta g \Delta L^3 / \kappa\nu$, where β is the thermal expansion coefficient, g is the gravitational acceleration and κ is the thermal diffusivity. An additional dimensionless control parameter is based on the fluid properties expressed by the Prandtl number $Pr = \nu/\kappa$. Analogously to TC flow, this system responds to sufficiently strong driving by the organization of convective winds (blue arrows) transporting heat from the bottom plate to the top plate (solid green line) under influence of the driving gravitational force field F_g inducing buoyancy (red arrow), see Fig. 1.1b-right. This transport of heat is coupled to the power input P, which is necessary to maintain a constant temperature difference between the top and bottom plate.

Building on the work of Bradshaw [21] and Dubrulle & Hersant [22] the analogy between both systems is exploited by Eckhardt, Grossmann & Lohse [23], who derived out of the Navier-Stokes equations exact relations for the transport quantities and the energy dissipation rates and predicts scaling laws between the driving control parameters and the dimensionless transport quantities. For RB flow the conserved quantity that is transported is the flux J of the heat field θ, given by $J = \langle u_z \theta \rangle_{A,t} - \kappa \partial_z \langle \theta \rangle_{A,t}$, where the first term is the convective contribution with u_z as the vertical fluid velocity and the second term is the diffusive contribution, with $\langle \ldots \rangle_{A,t}$ characterizing averaging over time and a circular surface with constant height from the bottom plate. Likewise, for TC flow, the conserved quantity of transport is the flux J^ω of the angular velocity field ω, given by $J^\omega = r^3 \left(\langle u_r \omega \rangle_{A,t} - \nu \partial_r \langle \omega \rangle_{A,t} \right)$, where the first term is the convective contribution with u_r as the radial fluid velocity and the second term is the diffusive (viscous) contribution, with $\langle \ldots \rangle_{A,t}$ characterizing averaging over time and a cylindrical surface with constant r from the axis.

The transport of both systems (RB, TC) can now be nondimensionalized by comparing the turbulent flux to the flux in the 'base' state, i.e. (fully conductive $J_{conductive}$, fully laminar J^ω_{lam}), expressed by the Nusselt number (Nu, Nu_ω). In the case of TC

---

*Under the assumption of the Oberbeck-Boussinesq approximation.

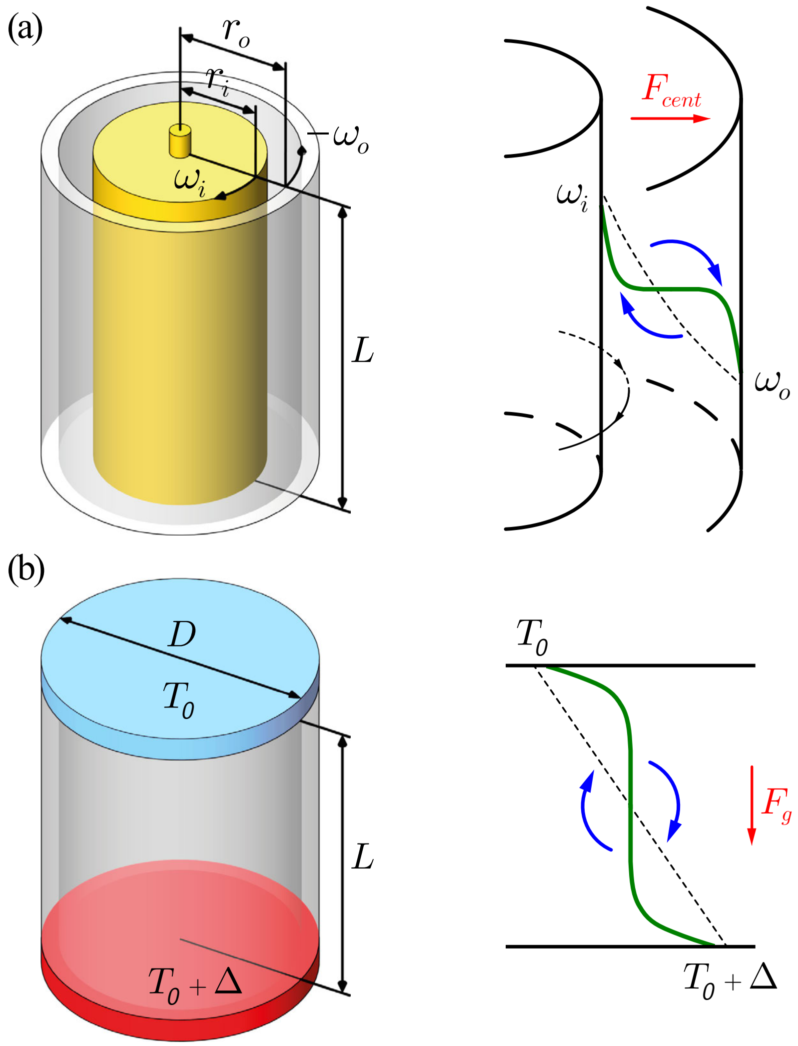

Figure 1.1: Cartoons of two fundamental flows sharing great similarity in their emergent turbulent characteristics. (a) left: Taylor-Couette (TC) geometry. Fluid confined between two concentric cylinders of height L, inner cylinder radius r_i and outer cylinder radius r_o, rotating at angular velocities ω_i and ω_o, respectively. (b) left: Rayleigh-Bénard (RB) geometry. Fluid confined in a cylindrical vessel of height L and diameter D, heated from below at an excess temperature Δ compared to the cooler top plate of temperature T_0. (a) and (b) right: cartoons of the flow after turbulence has developed, leading to convective winds (blue arrows) that modify the profile of the transported quantity (solid green line) – angular velocity (TC) and heat (RB) under influence of the driving force field, centrifugal F_{cent} and gravitational F_g, respectively. The dashed line indicates the profile when the system would be fully laminar (TC) or fully conductive (RB).

Table 1.1: Analogous relations between RB and TC flow, leading to similar effective scaling laws as derived by Eckhardt, Grossmann & Lohse (EGL) [23]. The energy dissipation rate equations (1.9) and (1.10) are listed for completeness but are not mentioned in this chapter.

Rayleigh-Bénard	**Taylor-Couette**
Conserved: heat flux $J = \langle u_z \theta \rangle_{A,t} - \kappa \partial_z \langle \theta \rangle_{A,t}$ (1.3)	Conserved: angular velocity flux $J^{\omega} = r^3 \left(\langle u_r \omega \rangle_{A,t} - \nu \partial_r \langle \omega \rangle_{A,t} \right)$ (1.4)
Dimensionless transport: $Nu = \frac{J}{J_{conductive}}$ (1.5)	Dimensionless transport: $Nu_{\omega} = \frac{J^{\omega}}{J^{\omega}_{lam}} \quad \left(= \frac{\tau}{2\pi L \rho J^{\omega}_{lam}} \right)$ (1.6)
Driven by: $Ra = \frac{\beta g \Delta L^3}{\kappa \nu}$ (1.7)	Driven by: $Ta = \frac{1}{4} \frac{\sigma (r_o - r_i)^2 (r_i + r_o)^2 (\omega_i - \omega_o)^2}{\nu^2}$ (1.8)
Exact relation: $\tilde{\varepsilon}_u = (Nu - 1)\, Ra Pr^{-2}$ (1.9)	Exact relation: $\tilde{\varepsilon}'_u = \tilde{\varepsilon}_u - \tilde{\varepsilon}_{u,lam}$ $= (Nu_{\omega} - 1)\, Ta \sigma^{-2}$ (1.10)
Prandtl number: $Pr = \nu / \kappa$ (1.11)	Pseudo 'Prandtl' number: $\sigma = \left(1 + \frac{r_i}{r_o}\right)^4 / \left(4 \frac{r_i}{r_o}\right)^2$ (1.12)
Scaling: $Nu \propto Ra^{\gamma}$ (1.13)	Scaling: $Nu_{\omega} \propto Ta^{\gamma}$ (1.14)

flow the flux J^{ω}_{lam} can be derived analytically out of the laminar ω profile, and as $Nu_{\omega} J^{\omega}_{lam}$ is directly linked to the torque τ one has access to J^{ω} out of experiments by measuring the torque. By choosing proper dimensionless driving control parameters one can now work out a scaling law between the dimensionless transport quantity and the dimensionless driving control parameters, based on the analogy between the RB and TC system. Whereas for RB flow the effective scaling law $Nu \propto Ra^{\gamma}$ holds, Eckhardt, Grossmann & Lohse [23] derived an analogues scaling law for TC flow as $Nu_{\omega} \propto Ta^{\gamma}$ by choosing the Taylor number definition,

$$Ta = \frac{1}{4} \frac{\sigma (r_o - r_i)^2 (r_i + r_o)^2 (\omega_i - \omega_o)^2}{\nu^2}$$

as driving control parameter in which σ plays the role of a pseudo 'Prandtl' number. Table 1.1 gives an overview of the mentioned relations.

1.3 Guide through Part I — Experimental setup

The Twente turbulent Taylor-Couette facility

In chapter 2 we introduce the new TC facility of our Physics of Fluids group, called "Twente turbulent Taylor-Couette" – T^{3}C for short. In section 2.1.3 we present the features of the T^{3}C facility, in section 2.2 we discuss in detail the global and local sensors it is equipped with and the system control and measurement accuracy, and in section 2.3 we finish with a few examples of initial results.

1.4 Guide through Part II — Single-phase TC flow

Torque scaling in turbulent Taylor-Couette flow with co- and counter-rotating cylinders

In chapter 3 we go into the proposed effective scaling $Nu_\omega \propto Ta^\gamma$ [23] by performing global torque experiments on the T^{3}C facility with radius ratio $\eta = 0.716$. The parameters we investigate are the nondimensional angular velocity transport Nu_ω obtained from the measured torque as function of Ta and a newly introduced parameter $a \equiv -\omega_o/\omega_i$, i.e. the ratio between the angular velocity of the outer to the inner cylinder wall indicating counter-rotation for $a > 0$ and co-rotation for $a < 0$. The ranges we cover are $a = [-0.4,\ 2]$ with Ta up to $\sim 10^{13}$, equivalent to Reynolds numbers $(Re_i, Re_o) \sim (2\times 10^6, \pm 1.4\times 10^6)$. The questions we ask are:

- Does a universal scaling law between Nu_ω and Ta exist, i.e. is γ constant in $Nu_\omega = \text{prefactor}(a) \times Ta^\gamma$ over the investigated range?
- If so, what is the amplitude of the prefactor as function of a?
- And at what a does maximum transport of angular velocity occur?

We put this research also in light of the observed 'ultimate' regime in RB where $Nu \propto Ra^{0.38}$ is found as indication that the interior of the RB cell is completely filled with turbulent flow [24, 25]. Furthermore, we feature an overview of past experiments in turbulent TC flow presented in (Re_i, Re_o) parameter space, see Fig. 3.1.

Optimal Taylor-Couette turbulence

In chapter 4 we focus on global and *local* properties of the flow in the T^{3}C facility with radius ratio $\eta = 0.716$. We pick up the torque scaling discussed in chapter 3 by providing further and more precise data on the maximum in the conserved turbulent angular velocity flux $Nu_\omega(Ta, a) = f(a)\cdot Ta^\gamma$ as a function of a. The value of a at which we find maximum transport is denoted by a_{opt}. The questions we address in section 4.3 are:

- Can we give an interpretation of the maximum in $f(a)$?

- How does this maximum depend on the radius ratio η?

If we exploit TC-RB analogy we can predict [26] the angular velocity transport which should scale like $Nu_\omega \sim Ta^{1/2} \times$ log-corrections, leading to an effective scaling law $Nu_\omega \propto Ta^{0.38}$ in the present parameter regime. The log-corrections that need to be applied on the $Ta^{1/2}$ scaling associated with fully turbulent boundary layers, depend on the convective wind Reynolds number Re_w. Hence in section 4.3 we also ask:

- Does the prediction $Nu_\omega \sim Ta^{1/2} \times$ log-corrections match the observations?

Next we employ laser Doppler anemometry (LDA) measurements inside the TC gap and we scan the liquid angular velocity $\omega(r)$ radially along the gap for the various investigated a. Note that the radial derivative on the $\omega(r)$ profile tells us directly the viscous contribution to the total angular velocity flux J^ω, i.e. the second term of Eq. (1.4) reading $-r^3\nu\partial_r\langle\omega\rangle_{A,t}$. In section 4.4 we go into the velocity profiles of the flow in the bulk and ask:

- What is the connection between the transport Nu_ω and the mean $\langle\omega(r)\rangle_t$ profiles?
- What are the relative contributions of the convective and viscous parts of the angular velocity flux J^ω per individual case of a?
- What is the radial position of zero angular velocity, i.e. $\langle\omega(r)\rangle_t = 0$ or the so called ‘neutral line’, in the counter-rotation cases $a > 0$?

It is known that inner cylinder rotation has a destabilizing effect on the flow and outer cylinder rotation has a stabilizing but shear enhancing effect [6]. Therefore we can expect rich flow behavior at the radial border to which these effects reach and meet, presumably around the neutral line. The LDA measurements allow us to go into the probability density functions of the ω profiles per radial position r and per a. In section 4.5 we ask:

- How does the turbulent flow organization change for different a?

Eckhardt, Grossmann & Lohse [23] predicted the ratio of the outer to the inner boundary layer thickness in turbulent TC flow. We extrapolate the $\omega(r)$ profiles in the bulk towards the cylinder walls and find the intersections with the viscous boundary layer profiles – obtained from assuming a viscosity dominated J^ω transport – to approximate the boundary layers. In section 4.6 we ask:

- Does the prediction by Eckhardt, Grossmann & Lohse [23] on the boundary layer ratio fall in line with our approximations?

Additionally, in section 4.2 we address the height dependence of the azimuthal flow profile and finite size effects to strengthen the claim that the torque sensing middle section of the inner cylinder is able to measure ‘clean’ torque, i.e. not influenced by end-effects induced by the top and bottom plates, at least for the case of pure inner cylinder rotation $a = 0$.

Angular momentum transport and turbulence in laboratory models of Keplerian flows

In chapter 5 we take a look at the angular momentum $r^2\omega$ transport for Keplerian-like flow profiles obtained from global torque measurements on the T^3C and UMD TC facilities with nearly equal radius ratios of $\eta \approx 0.7$. The application of this research can be found in astrophysical flows such as accretion disks, i.e. often circumstellar disks formed by diffuse material in orbital motion around a central body – typically a star or a black hole – following a Keplerian profile. For matter to fall inwards it must, besides losing gravitational energy, also reduce its angular momentum. As angular momentum is a conserved quantity, there must be a transport mechanism that transfers momentum radially outwards. It is highly debated whether this redistribution of angular momentum can be attributed to hydrodynamics in the form of turbulent viscous dissipation. The angular momentum distribution has a direct influence on the rate of accretion $\dot{M}$ as is elaborated in section 5.2.5. The questions we ask are:

- Do quasi-Keplerian TC flows exhibit turbulent viscous dissipation?
- What is the amplitude of the non-dimensional momentum transport inside the TC apparatuses, in specific for quasi-Keplerian profiles?
- Does the accretion rate $\dot{M}$ deduced from the TC experiments match the observed accretion rates as found in astrophysical disks?
- Can TC flow correctly simulate the astrophysical disk flows, taking into account finite-size effects?

1.5 Guide through Part III — Bubbly TC flow

The motivation behind this part can be found in the naval research, where the goal is to achieve skin friction reduction on ships hulls by injecting bubbles into the boundary layer flow, with summum bonum the reduction of fuel consumption and minimization of the ecological footprint. Given the complex nature and rich interactions between air bubbles and water in these highly turbulent two-phase flows, it is not surprising that a practical and efficient application is not commonly achieved yet. A solid understanding behind the driving mechanism(s) of bubbly drag reduction needs to be provided on a fundamental level first.

TC flow is an ideal flow environment to study drag reduction (DR) under influence of bubble injection, because statistically stationary states are straightforward to achieve and because the liquid energy dissipation rate is directly linked to the torque on the inner wall. In addition, the global gas volume fraction can easily be controlled and measured due to the confined flow geometry, see section 7.2.3.

Bubbly turbulent drag reduction is a boundary layer effect

In previous experiments by van den Berg *et al.* [27], performed on the old UMD TC facility which was outfitted with bubble injectors for that occasion, it is shown that bubble deformability seems to play a crucial role in the observed DR of up to 20% when injecting large bubbles of 1 mm in diameter into turbulent TC flow of $Re \sim 10^6$ up to global gas volume concentrations of 5%. These findings match the direct numerical simulations by Lu, Fernandez & Tryggvason [28] who performed front-tracking on large deformable bubbles in the near wall regions of turbulent flows, leading to the physical interpretation that deformable bubbles tend to align themselves between the boundary layer and the bulk of the flow preventing the transfer of momentum and hence resulting in DR.

The cylinder walls in the experimental work of van den Berg *et al.* [27] were perfectly smooth. As rough walls are more realistic than smooth walls in practical applications, we study in chapter 6 the influence of step-like wall roughness on bubbly DR on the same TC setup. Using this kind of step-like wall roughness, van den Berg *et al.* [15] proved that the interior of the TC gap is completely dominated by bulk turbulence and that hence, the smooth turbulent boundary layers are completely destroyed. In this light we ask:

- Does the injection of large bubbles still lead to DR when the TC walls are step-like roughened hence preventing a smooth turbulent boundary layer to develop?

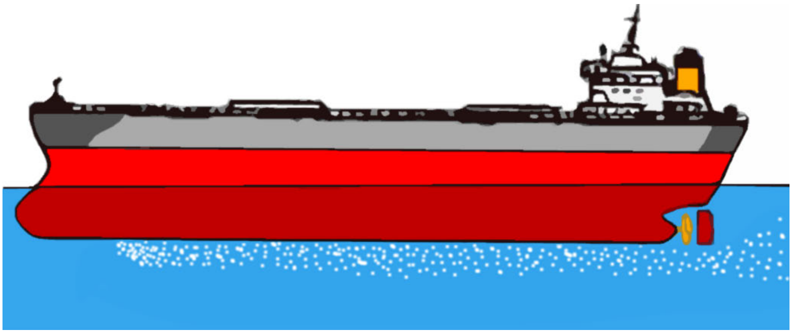

Figure 1.2: Impression of skin friction reduction by bubble injection applied on ships.

Bubble deformability is crucial for strong drag reduction in turbulent Taylor-Couette flow

In chapter 7 we continue the research of van den Berg *et al.* [27] on the T^{3}C facility by studying the DR on turbulent TC flow under influence of bubble injection with diameters ~ 1 mm up to global gas volume fractions of $\alpha_{global} = 4\%$. We extend the previously explored Reynolds space to $Re = 2 \times 10^6$ and we investigate the globally measured torque as well as local flow quantities, such as the liquid azimuthal velocity and the local bubble distribution inside the TC gap. In section 7.4 we focus first on the global torque measurements and we ask:

- Do we observe the same DR behavior as found by van den Berg *et al.* [27]?
- Does the trend of increasing DR with increasing Re continue in our experiments?

Based on the global torque results we chose two separate cases to study the flow locally: One case at $Re = 5.1 \times 10^5$ and $\alpha_{global} = 3\%$ falling in the ‘moderate’ DR regime — based on an estimation indicating that the bubbles are nearly spherical in this regime, expressed by the non-dimensional Weber number $We \sim 1$ — and one case at $Re = 1.0 \times 10^6$ and $\alpha_{global} = 3\%$ in the ‘strong’ DR regime — based on an estimation indicating that the bubbles are deformable in this regime, i.e. $We > 1$. The questions we address in section 7.5 are:

- How do the bubbles in the two two-phase flow cases change the liquid azimuthal flow profile with respect to the single-phase case?
- What is the local gas concentration profile across the TC gap for the two cases?

Out of the local liquid velocity and the local bubble concentration statistics we can calculate a local Weber number and a local ‘centripetal Froude number’ Fr_{cent}, the latter resembling the ability of the turbulent velocity fluctuations to draw bubbles into the bulk of the flow against the centripetal force pushing the bubbles towards the inner wall. Additionally, we can ask:

- Does the amplitude of the gas concentration profiles match the Fr_{cent} profiles?
- And ultimately: Do the measured local Weber number profiles match the assumption that bubble deformability is the dominant mechanism behind strong DR in turbulent TC flow?

We finish in section 7.6 with a discussion on the practical application of our findings and we try to project the results onto other wall bounded flows, such as channel flows and plate flows.

— PART I —

Experimental setup

2

The Twente turbulent Taylor-Couette facility *

A new turbulent Taylor-Couette system consisting of two independently rotating cylinders has been constructed. The gap between the cylinders has a height of 0.927 m, an inner radius of 0.200 m and a variable outer radius (from 0.279 to 0.220 m). The maximum angular rotation rates of the inner and outer cylinder are 20 Hz and 10 Hz, respectively, resulting in Reynolds numbers up to 3.4×10^6 *with water as working fluid. With this Taylor-Couette system, the parameter space* (Re_i, Re_o, η) *extends to* (2.0×10^6, $\pm 1.4 \times 10^6$, $0.716 - 0.909$)*. The system is equipped with bubble injectors, temperature control, skin-friction drag sensors, and several local sensors for studying turbulent single-phase and two-phase flows. Inner-cylinder load cells detect skin-friction drag via torque measurements. The clear acrylic outer cylinder allows the dynamics of the liquid flow and the dispersed phase (bubbles, particles, fibers etc.) inside the gap to be investigated with specialized local sensors and nonintrusive optical imaging techniques. The system allows study of both Taylor-Couette flow in a high-Reynolds-number regime, and the mechanisms behind skin-friction drag alterations due to bubble injection, polymer injection, and surface hydrophobicity and roughness.*

---

*Based on: D.P.M. van Gils, G.-W. Bruggert, D.P. Lathrop, C. Sun, and D. Lohse, *The Twente turbulent Taylor-Couette (T^3C) facility: Strongly turbulent (multiphase) flow between two independently rotating cylinders*, Rev. Sci. Instrum. **82**, 025105 (2011).

2.1 Introduction

2.1.1 Taylor-Couette Flow

Taylor-Couette (TC) flow is one of the paradigmatical systems in hydrodynamics. It consists of a fluid confined in the gap between two concentric rotating cylinders. TC flow has long been known to have a similarity [21–23] to Rayleigh-Bénard (RB) flow, which is driven by a temperature difference between a bottom and a top plate in the gravitational field of the earth [19, 20]. Both of these paradigmatical hydrodynamic systems in fluid dynamics have been widely used for studying the primary instability, pattern formation, and transitions between laminar flow and turbulence [29]. Both TC and RB flows are closed systems, i.e., there are well-defined global energy balances between input and dissipation. The amount of power injected into the flow is directly linked to the global fluxes, i.e. angular velocity transport from the inner to the outer cylinder for the TC case, and heat transport from the hot bottom to the cold top plate for RB case. To obtain these fluxes, one only has to measure the corresponding global quantity, namely the torque required to keep the inner cylinder rotating at constant angular velocity for the TC case, and the heat flux through the plates required to keep them at constant temperature for the RB case. In both cases the total energy dissipation rate follows from the global energy balances [23]. From an experimental point of view, both systems can be built with high precision, thanks to the simple geometry and the high symmetry.

For RB flow, pattern formation and flow instabilities have been studied intensively over the last century in low-Rayleigh (Ra) numbers, see e.g. review [30]. With increasing Rayleigh numbers, RB flow undergoes various transitions and finally becomes turbulent. In the past twenty years, the investigation on RB flow has been extended to the high-Rayleigh-number regime, which is well beyond onset of turbulence. To vary the controlled parameters experimentally, RB apparatuses with different aspect ratios and sizes have been built in many research groups in the past twenty years [24, 31–38]. Direct numerical simulation (DNS) of three-dimensional RB flow allows for quantitative comparison with experimental data up to $\mathrm{Ra} = 10^{11}$ [39], which is well beyond the onset of turbulence [31]. The dependence of global and local properties on control parameters, such as Rayleigh number, Prandtl number, and aspect ratio, has been well-explored. The RB system has shown surprisingly rich phenomena in turbulent states (see, e.g., the review articles in Refs. [19] and [20]), and it is still receiving tremendous attention (see Ref. [40]).

With respect to flow instabilities, flow transitions, and pattern formation, TC flow is equally well-explored as RB flow. Indeed, TC flow also displays a surprisingly large variety of flow states just beyond the onset of instabilities [2–4]. The control parameters for TC flow are the inner cylinder Reynolds number Re_i, the outer cylinder Reynolds number Re_o, and the radius ratio of the inner to outer cylinders

$\eta = r_i/r_o$. Similar to RB flow, TC flow undergoes a series of transitions from circular Couette flow to chaos and turbulence with increasing Reynolds number [41]. The flow-state dependence on the rotation frequencies of the inner and outer cylinder in TC flow at low Reynolds numbers has been theoretically, numerically and experimentally well-studied in the last century [1, 42–46]. This is in marked contrast to the turbulent case, for which only very few studies exist, which we will now discuss.

Direct numerical simulation of TC flow is still limited to Reynolds numbers up to 10^4, which is still far from fully-developed turbulence [47, 48]. Experimentally, few TC systems are able to operate at high Reynolds numbers ($\mathrm{Re}_i > 10^4$), which is well beyond the onset of chaos. Smith and Townsend [7, 8] performed velocity-fluctuation measurements with a hot-film probe in turbulent TC flow at $\mathrm{Re}_i \sim 10^4$, when only the inner cylinder was rotating. Systematic local velocity measurements on double rotating systems at high Reynolds numbers can only be found in Ref. [5] from 1933. However, the measurements [5] were performed with pitot tubes, which are an intrusive experimental technique for closed systems. Recently, Ravelet *et al.* [16] built a Taylor-Couette system with independently rotating cylinders, capable of Reynolds numbers up to 10^5, and they performed flow structure measurements in the counter-rotation region using particle image velocimetry.

The most recent turbulent TC apparatus for high Reynolds numbers ($\mathrm{Re}_i \sim 10^6$) was constructed in Texas by Lathrop, Fineberg and Swinney in 1992 [11, 12]. This turbulent TC setup had a stationary outer cylinder and was able to reach a Reynolds number of $\mathrm{Re} = 1.2 \times 10^6$. Later, the system was moved to Lathrop's group in Maryland. This setup will be referred to as the Texas-Maryland TC, or T-M TC in short. The apparatus was successfully used to study the global torque, local shear stress, and liquid velocity fluctuations in turbulent states [10–15].

The control parameter Re_i was extended to $\mathrm{Re}_i \sim 10^6$ by the T-M TC; however, the roles of the parameters Re_o and η in the turbulent regime still have not been studied. Flow features inside the TC gap are highly sensitive to the relative rotation of the cylinders. The transition path from laminar flow to turbulence also strongly depends on the rotation of both the inner and the outer cylinders. A system with a rotatable outer cylinder clearly can offer much more information to better understand turbulent TC flow, and this is the aim of our setup. On the theoretical side, Eckhardt, Grossmann, and Lohse [23] extend the unifying theory for scaling in thermal convection [49–52] from RB to TC flow, based on the analogy between RB and TC flows. The gap ratio is one of the control parameters in TC flow, and it corresponds to the Prandtl number in Rayleigh-Bénard flow [23]. They define the "geometrical quasi-Prandtl number" as $\{[(1+\eta)/2]/\sqrt{\eta}\}^4$. In TC flow the Prandtl number characterizes the geometry, instead of the material properties of the liquid as in RB flow [23]. From considerations of bounds on solutions to the Navier-Stokes equation, Busse [53] calculated an upper bound of the angular velocity profile in the bulk of the gap for infinite Reynolds number. The prediction suggests a strong radius ratio dependence. It is of great interest to study the role of the ”geometrical quasi-Prandtl number” in TC flow. This can only be done in a TC system with variable gap ratios.

The T-M TC system was designed 20 years ago and unavoidably exhibits the limitations of its time. To extend the parameter space from only (Re_i, 0, fixed η) to (Re_i, Re_o, variable η), we built a new turbulent TC system with independently rotating cylinders and variable radius ratio.

2.1.2 Bubbly drag reduction

Another motivation for building a new TC system is the increasing interest in two-phase flows, both from a fundamental and an applied point of view. For example, it has been suggested that injecting bubbles under a ship's hull will lower the skin-friction drag and thus reduce the fuel consumption; for a recent review on the subject we refer to Ref. [54]. In laboratory experiments skin-friction drag reductions (DR) by bubble injection up to 20% and beyond have been reported [55, 56]. However, when supplying an actual-scale ship with bubble generators, the drag reduction drops down to a few percent [57], not taking into account the power needed to generate the air bubbles. A solid understanding of the drag reduction mechanisms occurring in bubbly flows is still missing.

The conventional systems for studying bubbly DR are channel flows [58], flat plates [59, 60], and cavitation flows [54]. In these setups it is usually very difficult to control the power input into the flow, and to keep this energy contained inside the flow. In 2005, the T-M TC was outfitted with bubble injectors in order to examine bubbly DR and the effect of surface roughness [27, 61]. The strong point of a Taylor-Couette system, with respect to DR, is its well defined energy balance. It has been proved that the turbulent TC system is an ideal system for studying turbulent DR by means of bubble injection [27, 61, 62].

The previous bubbly DR measurements in TC flow were based only on the global torque, which is not sufficient to understand the mechanism of bubbly DR. Various fundamental issues are still unknown. How do bubbles modify the liquid flow? How do bubbles move inside the gap? How do bubbles orient and cluster? What is the effect of the bubble size? These issues cannot be addressed based on the present TC system. Ref. [27] found that significant DR only appears at Reynolds numbers larger than 5×10^5 for bubbles with a radius ~ 1 mm. The maximum Reynolds number of the T-M TC is around 10^6, which is just above that Reynolds number. A system capable of larger Reynolds numbers is therefore favored for study of this hitherto-unexplored parameter regime. The influence of coherent structures on bubbly DR can be systematically probed with a TC system when it has independently rotating cylinders.

2.1.3 Twente turbulent Taylor-Couette

Using the design of the T-M TC system as a starting point, we now present a new TC system with independently rotating cylinders, and equipped with bubble injectors, dubbed "Twente turbulent Taylor-Couette" (T^3C). We list the main features of the T^3C facility (the material parameters are given for water at 21°C as the working fluid):

- The inner and outer cylinder rotate independently. The maximum rotation frequencies for the inner and outer cylinder are f_i = 20 Hz and f_o = 10 Hz, respectively.
- The aspect ratio and radius ratio are variable.
- The maximum Reynolds number for the counter-rotating case at the radius ratio of $\eta = 0.716$ is 3.4×10^6. The Reynolds number for double rotating cylinders is defined as Re = $(\omega_i r_i - \omega_o r_o)(r_o - r_i)/\nu$, where $\omega_i = 2\pi f_i$ and $\omega_o = 2\pi f_o$ are the angular velocities of the inner and outer cylinder, and ν is the kinematic viscosity of water at the operation temperature.
- The maximum Reynolds numbers at the radius ratio of $\eta = 0.716$ are $\mathrm{Re}_i =$

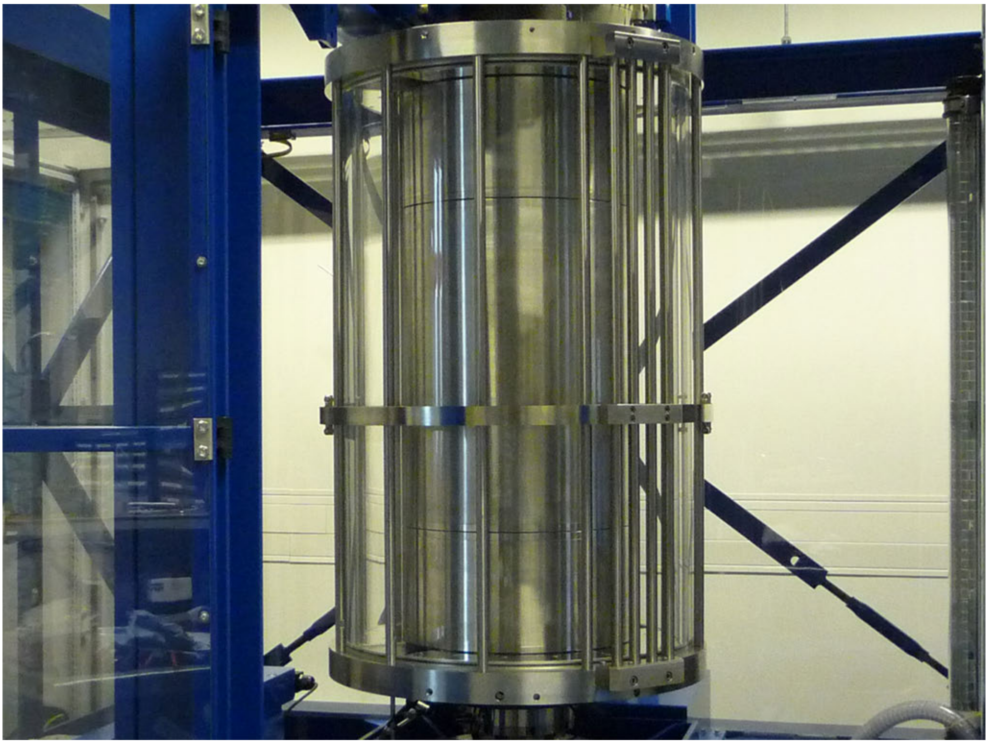

Figure 2.1: A photograph of the T^3C system. The height of the cylinder is about 1 m.

$\omega_i r_i(r_o - r_i)/\nu = 2.0 \times 10^6$ for inner cylinder rotation and $\mathrm{Re}_o = \omega_o r_o(r_o - r_i)/\nu = 1.4 \times 10^6$ for outer cylinder rotation.

- Bubble injectors are incorporated for injecting bubbles in a range of diameters (100 μm to 5 mm), depending on the shear strength inside the flow.
- The outer cylinder and parts of the end plates are optically transparent, allowing for optical measurement techniques like laser Doppler anemometry (LDA), particle image velocimetry (PIV) and particle tracking velocimetry (PTV).
- Temperature stability and rotation rate are precisely controlled.
- Local sensors (local shear stress, temperature, phase-sensitive constant temperature anemometry (CTA), etc.) are built in or are mountable.

2.2 System description

Figure 2.1 is a photograph of the T^{3}C mounted in the frame. The details of the system will be described in Secs. 2.2.1–2.2.9.

2.2.1 Geometry and materials

As shown in Fig. 2.2, the system contains two independently rotating cylinders of radii r_i and r_o. The working liquid is confined in the gap between the two cylinders of width $d = r_o - r_i$. The height of the gap confined by the top and bottom plate is L. By design, one set of radius ratios ($\eta = r_o/r_i$) and aspect ratios $\Gamma = L/(r_o - r_i)$ of the T^{3}C nearly match those of the T-M TC in order to allow for a comparison of the results. To increase the system capacity for high Reynolds numbers, the present T^{3}C system has twice the volume compared to that of the T-M TC. The maximum Reynolds number of the T^{3}C system is 3.4 × 10^6 when the two cylinders at a radius ratio of $\eta = 0.716$ are counter-rotating with water at 21 ^oC as the working fluid. Table 2.1 lists the geometric parameters.

As shown in Fig. 2.2, the inner cylinder (IC) consists of three separate sections $\mathrm{IC}_{\mathrm{bot}}$, $\mathrm{IC}_{\mathrm{mid}}$ and $\mathrm{IC}_{\mathrm{top}}$, each able to sense the torque by means of load cell deformation embedded inside the arms connecting the IC sections to the IC drive shaft. End effects induced by the bottom and top of the TC tank are significantly reduced when focusing only on the $\mathrm{IC}_{\mathrm{mid}}$ section. The gap between neighbouring sections is 2 mm. The material of the IC sections is stainless steel (grade 316) with a machined cylindricity (radial deviations) of better than 0.02 mm.

The outer cylinder (OC) is cast from clear acrylic, providing full optical access to the flow between the cylinders. The OC is machined to within tolerances by Blanson Ltd. (Leicester, UK) and the final machining was performed by Hemabo (Hengelo, Netherlands), which consisted of drilling holes in the OC for sensors, and removing the stresses in the acrylic by temperature treatment. The thickness of the OC is 25.4

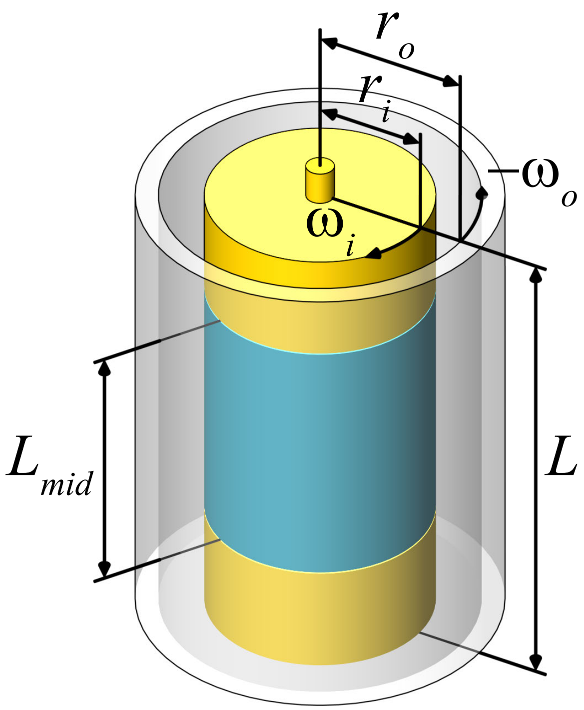

Figure 2.2: Schematic Taylor-Couette setup consisting of two independently rotating coaxial cylinders with angular rotation rates ω_i and ω_o. The gap between the cylinders is filled with a fluid.

Table 2.1: Geometric parameters of both TC setups, with inner radius r_i, outer radius r_o, gap width d, radius ratio η, aspect ratio Γ and gap volume V_{gap}. The outer radius of the T^{3}C gap can be varied resulting in different aspect and radius ratios. The value of 0.220 in the brackets refers to the case of a sleeve around the inner cylinder.

	T-M TC	T^{3}C			
L (m)	0.695	0.927			
L_{mid} (m)	0.406	0.536			
r_i (m)	0.160	0.2000	(0.220)		
r_o (m)	0.221	0.2794	0.260	0.240	0.220
$d = r_o - r_i$ (m)	0.061	0.0794	0.060	0.040	0.020
$\eta = r_i/r_o$	0.725	0.716	0.769	0.833	0.909
$\Gamma = L/d$	11.43	11.68	15.45	23.18	46.35
V_{gap} (m^3)	0.051	0.111	0.080	0.051	0.024

mm. The bottom and top of the TC tank are connected by the OC and rotate as one piece, embedding the IC completely with the IC drive axle protruding through the top and bottom plates by means of mechanical seals.

The frame itself, as shown in blue in Fig. 2.1, is supported by adjustable air springs underneath each of its four support feet; they lift the frame fully off the ground. In combination with an inclination sensor, the frame can automatically level itself to ensure vertical alignment of the IC and OC with respect to the gravity.

2.2.2 Varying gap width and IC surface properties

Additional clear acrylic cylinders are available for this new T^3C system, and can be fitted between the original OC and IC. These ”filler” cylinders will rotate together with the original OC and provide a way to decrease the outer radius of the gap. The nominal gap width of 0.079 m can thus be varied to gap widths of 0.060, 0.040 and 0.020 m, resulting in the aspect and radius ratios as shown in Table 2.1.

Instead of a smooth stainless steel IC surface, other IC surfaces with alternative chemical and/or surface structure properties can be employed, preferably in a perfectly reversible way. Thus we employed a set of cylindrical stainless steel sleeves, installed around the existing IC sections, leaving the original surface unaltered. These sleeves each clamp onto the IC sections by means of a pair of polyoxymethylene clamping rings between the sleeve and the IC. The inner radius of the gap is hence increased by 0.020 m. For good comparison at least two sets of sleeves need to be available; one set with a bare smooth stainless steel surface to determine the effect of a changing gap width, and one set with the altered surface properties. The sleeves themselves can be easily transported for surface-altering treatment.

2.2.3 Wiring and system control

A sketch of the control system is shown in Fig. 2.3. All sensors embedded inside the IC are wired through the hollow IC drive axle, and exit to a custom-made slip ring from Fabricast (El Monte, USA) on top, with the exception of the shear stress CTA (Constant Temperature Anemometry) sensors described in Sec. 2.2.9. The slip ring consists of silver-coated electrical contact channels with 4 silver-graphite brushes per channel. The 4 brushes per channel ensure an uninterrupted signal transfer during rotation, and increase the signal-to-noise ratio. The most important signals being transferred are the signal-conditioned temperature signals and the signal conditioned load cell signals of IC_{top}, IC_{mid} and IC_{bot}, in addition to grounding and voltage feed lines. These conditioned output signals are current-driven instead of voltage-driven, leading to a superior noise suppression. From the slip ring, each electrical signal runs through a single shielded twisted-pair cable, again reducing the noise pick-up with respect to unshielded straight cables, and is acquired by data acquisition modules

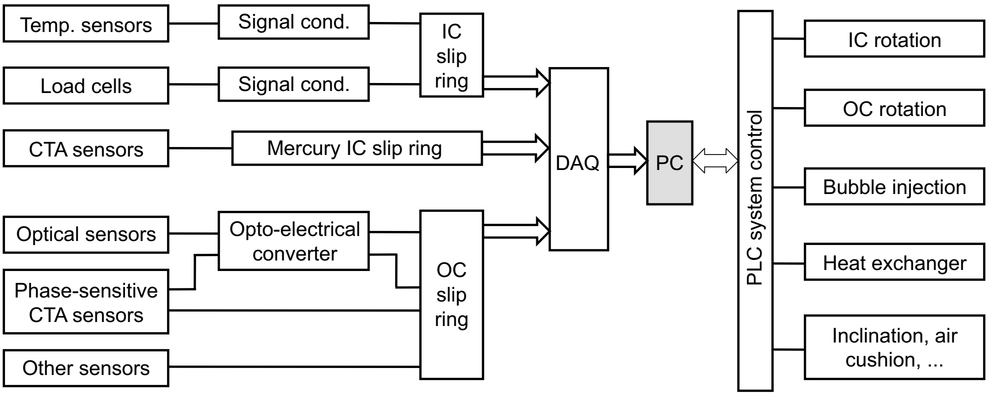

Figure 2.3: A sketch of the signal and control system of the T^3C system. The abbreviations in the sketch: OC (outer cylinder), IC (inner cylinder), DAQ (data acquisition), PLC (programmable logic controllers), and PC (personal computer).

from Beckhoff (Verl, Germany) operating at a maximum sampling rate of 1 kHz at 16-bit resolution.

The shear stress CTA signals are fed to a liquid mercury-type slip ring from Mercotac (Carlsbad, USA). The liquid mercury inside the slip ring is used as a signal carrier and eliminates the electrical contact noise inherent to brush-type slip rings. This feature is important as additional (fluctuating) resistance between the CTA probe and the CTA controller can drastically reduce the accuracy of the measurement.

The sensors embedded in the OC are also wired through the OC drive axle and exit to a custom-made slip ring from Moog (Böblingen, Germany). Those sensors include optional CTA probes and optical fiber sensors for two-phase flow.

The T^3C system is controlled with a combination of programmable logic controllers (PLC) from Beckhoff which interact with peripheral electronics, and with a PC running a graphical user interface built in National Instruments LABVIEW that communicates with the PLCs. The controlled quantities include rotation of the cylinders, bubble injection rate, temperature, and inclination angle of the system.

2.2.4 Rotation rate control

The initial maximum rotation rates of the IC and OC are 20 Hz and 10 Hz, respectively. As long as the vibration velocities occurring in the main ball bearings of the T^3C fall below the safe threshold value of 2.8 mm/s rms, there is room to increase these maximum rotation rates in case the total torque on the drive shaft is still below the maximum torque of 200 Nm. The measured vibration velocity in the T^3C system was found to be much less than that threshold, even when the system was running at these initial maximum rotation rates. The system is capable of operating at even

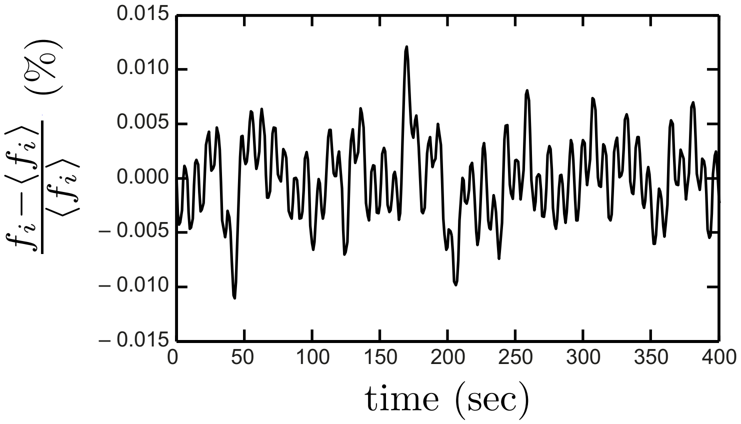

Figure 2.4: The measured instantaneous rotation rate fluctuations normalized by the time-averaged rotation rate. Here the inner cylinder was preset to rotate at 5 Hz.

higher rotation rates.

Both cylinders are driven by separate but identical ac motors, using a timing belt with toothed pulleys in the gear ratio 2:1 for the IC and 9:4 for the OC. Each motor, type 5RN160L04 from Rotor (Eibergen, Netherlands), is a four pole 15 kW squirrel-cage induction motor, powered by a high-frequency inverter, Leroy Somer Unidrive SP22T, operating in closed-loop vector mode. A shaft encoder mounted directly onto the ac motor shaft provides the feedback to the inverter. Electronically upstream of each inverter is a three-phase line filter and an electromagnetic compatibility filter from Schaffner (Luterbach, Switzerland), types FN3400 and FS6008-62-07, respectively. Downstream, i.e. between the inverter and the ac motor, are two additional filters from Schaffner, FN5020-55-34 and FN5030-55-34, which modify the usual pulse-width-modulated driving signal into a sine-wave. Important features of this filter technique are foremost the reduction of electromagnetic interference in the lab and the reduction of audible motor noise usually occurring in frequency-controlled motors.

The rotation rate of each cylinder is independently measured by magnetic angular encoders, ERM200, from Heidenhain (Schaumburg, USA), mounted onto the direct drive shafts of the IC and the OC. The magnetic line count used on the IC is 1200, resulting in an angular resolution of 0.3°, and 2048 lines, resulting in an angular resolution of 0.18° on the OC. The given angle resolutions do not take into account the signal interpolation performed by the Heidenhain signal controller, improving the resolution by a factor of 50 at maximum. Fig. 2.4 shows one measured time series of the rotation frequency when the system was rotating at $\langle f_i \rangle = 5$ Hz. The figure shows the measured instantaneous rotation rate f_i fluctuation as a function of time. It is clearly shown that the rotation is stable within 0.01% of its averaged value $\langle f_i \rangle$.

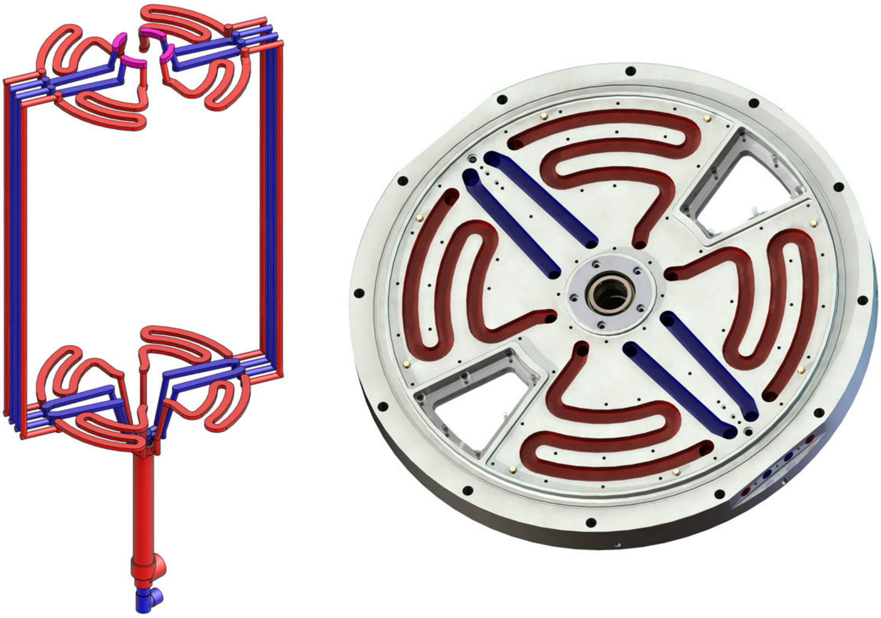

Figure 2.5: *Left*: Schematic sketch of the coolant flow through the T^3C. Coolant enters at the bottom rotary union (blue) and flows straight up to the top plate by piping on the outside of the TC tank. Then the coolant enters the curling channels in the top plate (red) and is fed downwards again to run through the curling channels of the bottom plate before it exits at the second rotary union. *Right*: Bottom plate with the copper cover removed.

2.2.5 Temperature control

The amount of power dissipated by degassed water at 21 °C, in the case of a stationary OC and the IC rotating at 20 Hz with smooth unaltered walls, is measured to be 10.0 kW. Without cooling this would heat the 0.111 m^3 of water at a rate of ≈ 1.3 K/min. As the viscosity of water lowers by 2.4% per K, it is important to keep the temperature stable (to within at least 0.1 K) to exclude viscosity fluctuations and thus errors. While the temperature-viscosity relation of water is well-tabulated and will be corrected for during measurements, other fluids like glycerin solutions might not share this feature. In the case of glycerin, a 1 K temperature increase can lower the viscosity by $\approx 7\%$.

To ensure a constant fluid temperature inside the TC tank, a 20 kW Neslab HX-750 chiller (Thermo Fisher Scientific Inc., Waltham, USA) with an air-cooled compressor and a listed temperature stability of 0.1 K is connected to the T^3C. Two rotary unions, located at the bottom of the OC drive axle, are embedded inside each other and allow the coolant liquid to be passed from the stationary lab to the rotating OC, as shown in Fig. 2.5. Both the stainless steel bottom and top plate of the OC contain internal cooling channels which are covered by a 5 mm-thick nickel-coated copper plate, which in turn is in direct contact with the TC's inner volume.

The temperature inside the TC tank is monitored by three PT100 temperature sensors, each set up in a 4-leads configuration with pre-calibrated signal conditioners IPAQ-H^{plus} from Inor (Malmö, Sweden) with an absolute temperature accuracy of 0.1 K. The relative accuracy is better than 0.01 K. Each sensor is embedded at mid-height inside the wall of the hollow $\mathrm{IC}_{\mathrm{top}}$, $\mathrm{IC}_{\mathrm{mid}}$, and $\mathrm{IC}_{\mathrm{bot}}$ sections, respectively (shown in Fig. 2.8). Thus one can check for a possible axial temperature gradient across the IC. The sensors do not protrude through the wall so as to keep the outer surface smooth, leaving 1 mm of stainless steel IC wall between the sensors and the fluid. Except for the direct contact area with the wall, the PT100s are otherwise thermally isolated. Inside each IC section, the signal conditioner is mounted and its electrical wiring is fed through the hollow drive axle, ending in an electrical slip ring. The average over all three temperature sensors is used as feedback for the Neslab chiller. An example of temperature time tracers is plotted in Fig. 2.6, which shows that the temperature stability is better than 0.1 K. This data was acquired with the IC rotating at 20 Hz, a stationary OC and water as the working fluid, resulting in a measured power dissipation by the water of 10.0 kW. To check the effects of this small temperature difference on the TC flow, we calculate the Rayleigh number based on the temperature difference of $\Delta = 0.1$ K over the distance (L_{RB} = 0.366 m) of the middle and top sensor positions: the result is $\mathrm{Ra} = \beta g L_{RB}^3 \Delta / \kappa \nu = 5.9 \times 10^6$ (β is the thermal expansion coefficient, κ the thermal diffusivity and ν the kinematic viscosity). The corresponding Reynolds number is estimated to be around $\mathrm{Re}_{RB} \sim 0.25 \times \mathrm{Ra}^{0.49} = 500$ [19], which

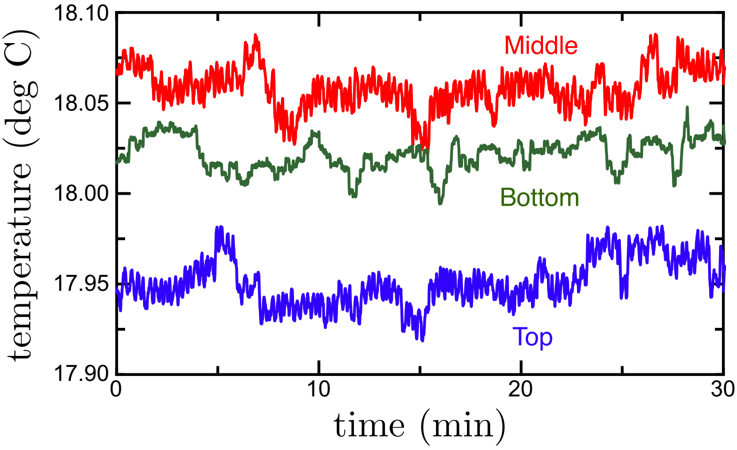

Figure 2.6: Time traces of the measured temperature at three positions. The data were taken with the IC rotating at 20 Hz, a stationary OC and water as the working fluid. The measured power dissipation by the water was 10.0 kW.

is significantly smaller than the system Reynolds number of 2×10^6. The effects of this small temperature gradient can thus be neglected in this high-Reynolds-number turbulent flow.

2.2.6 Torque sensing

Each of the $\mathrm{IC_{bot}}$, $\mathrm{IC_{mid}}$ and $\mathrm{IC_{top}}$ sections are basically hollow drums. Each drum is suspended on the IC's drive axle by two low-friction ball bearings, which are sealed by rubber oil seals pressed onto the outsides of the drums, encompassing the drive axle. A metal arm, consisting of two separate parts, is rigidly clamped onto the drive axle and runs to the inner wall of the IC section. The split in the arm is bridged by a parallelogram load cell (see Fig. 2.7). The load cells can be replaced by cells with different maximum-rated load capacity to increase the sensitivity to the expected torque. At this moment two different load cells, type LSM300 from Futek (Irvine, USA), are in use with a maximum-rated load capacity of 2224 N and 222.4 N, respectively. Each load cell comes with a pre-calibrated Futek FSH01449 signal conditioner operating at 1 kHz, which is also mounted inside the drum. The electrical wiring is fed through the hollow drive axle to a slip ring on top. The hysteresis of each load cell assembly is less than 0.2 Nm, presented here as the torque equivalent. Calibration of the load cells is done by repeated measurements, in which a known series of monotonically increasing or decreasing torques is applied to the IC surface. The IC is not taken out of the frame and is calibrated *in situ*. The torque is applied by strapping a belt around the IC and hanging known masses on the loose end of the belt, after having been redirected by a low-friction pulley to follow the direction of gravity.

Local fluctuations in the wall-shear stress can be measured using the flush-mounted hot-film probes (type 55R46 from Dantec Dynamics) on the surfaces of the inner and outer cylinder, shown in Fig. 2.8.

An important construction detail determines how the torque is transferred to the load cell. Only the azimuthal component is of interest and the radial and axial components, due to possible non-azimuthal imbalances inside the drum or due to the centrifugal force, should be ignored. This is accomplished by utilizing the parallelogram geometry of the load cell, lying in the horizontal plane. It is evident that during a measurement the rotation rate of the IC should be held stable to prevent the rotational inertia of the IC sections from acting as a significant extra load. The mass balance of the system is important in decreasing this effect.

2.2.7 Balancing and vibrations

All three sections of the IC and the entire OC are separately balanced, following a one-plane dynamical balancing procedure with the use of a Smart Balancer 2 from Schenck RoTec (Auburn Hills, USA). The associated accelerometer is placed on the

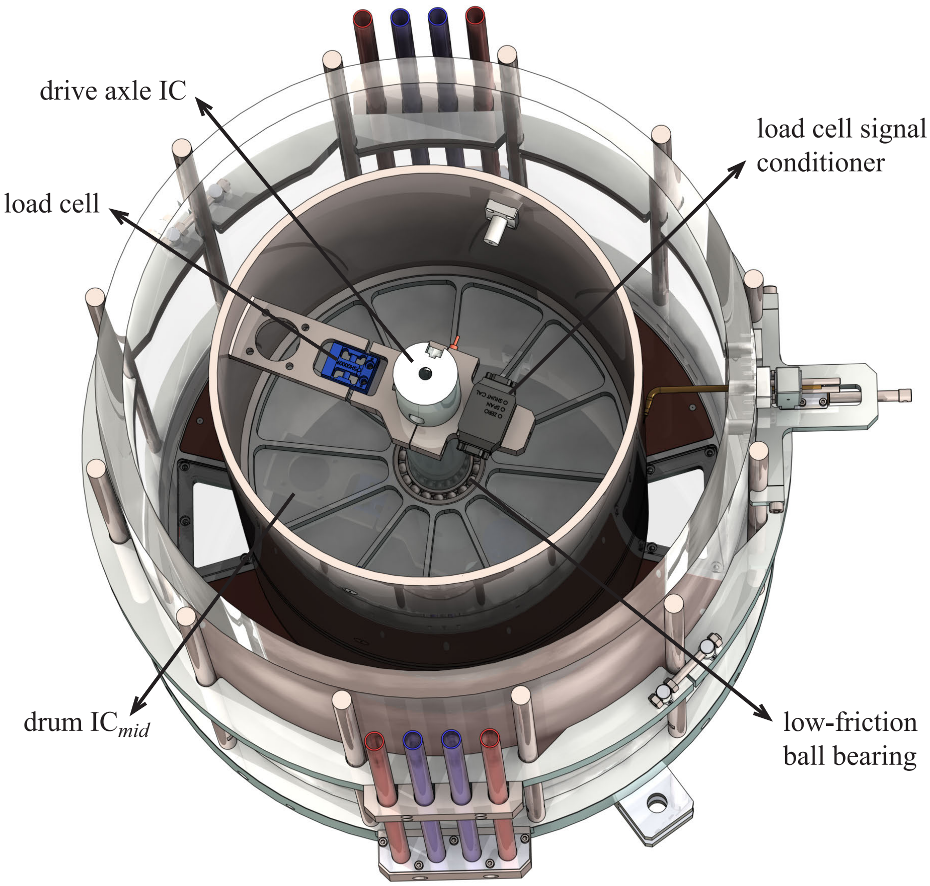

Figure 2.7: Horizontal cut-away showing the load-cell construction inside the IC_{mid} drum. The load cell spans the gap in the arm, connecting the IC drive axle to the IC wall.

main bottom ball bearing. The balancing procedure is reproducible to within 5 grams leading to a net vibration velocity of below 2 mm/s rms at the maximum rotation rates. According to the ISO standard 101816-1 [63] regarding mechanical vibrations, the T^3C system falls into category I, for which a vibration velocity below 2.8 mm/s rms is considered acceptable.

Another feature is the air springs, i.e. pressure regulated rubber balloons, placed between the floor and each of the four support feet of the T^3C frame. They lift the frame fully off the ground and hence absorb vibrations leading to a lower vibration severity in the setup itself and reducing the vibrations passed on to the building.

Two permanently installed velocity transducers from Sensonics (Hertfordshire, UK), type PZDC 56E00110, placed on the top and bottom ball bearings, constantly monitor the vibration severity. An automated safety PLC circuit will stop the IC and

OC rotation when tripped. Thus, dangerous situations or expensive repairs can be avoided, as this acts as a warning of imminent ball bearing failure or loss of balance.

2.2.8 Bubble injection and gas concentration measurement

Eight bubble injectors, equally distributed around the outer perimeter of the TC gap as shown in Fig. 2.8, are built into the bottom plate of the TC tank. Each bubble injector consists of a capillary housed inside a custom-made plug ending flush with the inside wall. They can be changed to capillaries of varying inner diameter: 0.05, 0.12, 0.5 and 0.8 mm. This provides a way to indirectly control the injected bubble radius, estimated to be in the order of 0.5 mm to 5 mm, depending on the shear stress inside the TC. Smaller bubbles of radius less than 0.5 mm, or microbubbles, can be injected by replacing the capillaries inside the plugs with cylinders of porous material.

Two mass flow controllers from Bronkhorst (Ruurlo, Netherlands), series EL-Flow Select, are used in parallel for regulating the gas, i.e. filtered instrument air, with a flow rate at a pressure of 8 bars. One controller with a maximum of 36 l/min takes care of low-gas volume fractions, and the second controller with a maximum of 180 l/min of high-gas volume fractions, presumably up to 10%. The gas enters the gap by a third rotary union located at the very bottom of the OC drive axle, below the coolant water rotary unions. Thus the OC drive axle has three embedded pipes running through its center, which are fed by three rotary unions at the bottom. Each pipe is split into separate channels again inside of the OC drive assembly to be routed where needed.

Vertical channels running through the near-center of the TC tank's top plate con-

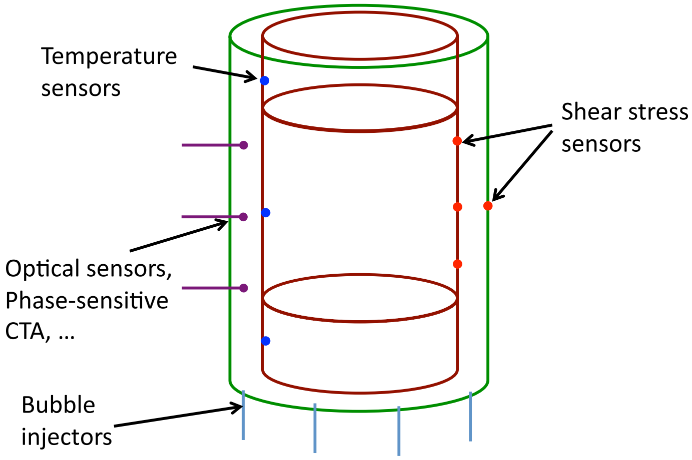

Figure 2.8: A sketch of local sensors and bubble injectors in the system.

nect the tank volume to a higher located vessel in contact with the ambient air. Excess liquid or gas can escape via this route to prevent the build-up of excessive pressure. We refer to it as an expansion vessel. The expansion vessel can also be used to determine the global gas volume fraction inside the TC tank. The vessel is suspended underneath a balancer which continuously registers the vessel's mass. Starting at zero percent gas volume fraction to tare the vessel's mass, one can calculate the global gas volume fraction by transforming the liquid's mass that is subsequently pushed into the vessel by the injected gas, into its equivalent volume. In the case of a rotating OC the stationary expansion vessel can not (yet) be connected and excess liquid is collected in a stationary collecting ring encompassing the rotating top plate.

The original concept for measurement of the global gas volume fraction would not have had the restriction of a stationary OC. It makes use of a differential pressure transducer attached to the OC that measures the pressure difference between the top and bottom of the TC tank. Comparing this difference to the expected single-phase hydrostatic pressure difference, one could calculate the gas volume fraction. This method depends on the dynamic pressure being equal at the top and bottom. It fails however, due to unequal dynamic pressure induced by secondary flows. This is not unexpected as a wide variety of flow structures can exist in turbulent TC flow, like Taylor-vortices.

2.2.9 Optical access and local sensors

Flow structure and velocity fluctuations of TC flow have been studied extensively at low Reynolds numbers, but few experiments have been performed at high Reynolds number ($\mathrm{Re} > 10^5$). Previous velocity measurements were mainly done with intrusive measurement techniques like hot-film probes. Indeed it was found that the wake effects induced by an object inside a closed rotating system can be very strong [64]. Better velocity measurements inside the TC gap use nonintrusive optical techniques such as LDA [13], PIV [16], PTV. The optical properties of the outer cylinder are hence crucial for this purpose.

The outer cylinder of the T^3C is transparent, and four small areas of the top and bottom plates consist of viewing portholes made of acrylic to allow for optical access in the axial direction, as can be seen in Figs. 2.5 and 2.7. The outer cylinder was thermally treated to homogenize the refractive index and to remove stresses inside the acrylic. Thanks to this optical accessibility, all three velocity components inside the gap can be measured optically. For the velocity profile measurements, we use LDA (see Sec. 2.3.2).

Various experimental studies have been done to examine bubbly DR. However, two main issues of bubbly DR in turbulent TC are still not well-studied. How do bubbles modify the turbulent flow? And: How do bubbles distribute and move inside the gap? It is certainly important to measure local liquid and bubble information inside the gap. Various local sensors, shown in Fig. 2.8, can be mounted to the T^{3}C system. Here we highlight two of them: the phase-sensitive CTA and the 4-point optical fiber probe.

Phase-sensitive CTA

Optical techniques (such as LDA and PIV) are only capable of measuring flow velocities in a bubbly flow when the gas volume fraction is very low (typically less than 1%). Hot-film measurements in bubbly flows also impose considerable difficulty due to the fact that liquid and gas information is present in the signal. The challenge is to distinguish and classify the signal corresponding to each phase. The hot-film probe does not provide by itself means for successful identification [65]. To overcome this problem, a device called phase-sensitive CTA has been developed (see Refs. [66–69]). In this technique, an optical fiber is attached close to the hot-film so that when a bubble impinges on the sensor it also interacts with the optical fiber. The principle behind the optical fiber is that light sent into the fiber leaves the fiber tip with low reflectivity when immersed in water, and with high reflectivity when immersed in air. Hence the fiber is able to disentangle the phase information by measuring the reflected light intensity. It has proved to be an useful tool for liquid velocity fluctuation measurements in bubbly flows [68]. Phase-sensitive CTA probes are only mounted through the holes of the outer cylinder when necessary.

4-Point optical probe

Instead of using a single optical fiber to discriminate between phases as described in the previous paragraph, one can construct a probe consisting of four such fibers. The four fiber tips are placed in a special geometry: three fiber tips of equal length are placed parallel in a triangle, and the fourth fiber is placed in the center of gravity and protrudes past the other fiber tips (see Ref. [70] for a schematic of the probe). Knowing this geometry and processing the four time series on the reflected light intensity, it becomes possible to estimate not only the size of the bubble that impinges onto the fiber tips, but also the velocity vector and the aspect ratio. To measure the bubble distribution inside the TC gap and other bubble dynamics, the 4-point optical probe is mounted through the holes of the outer cylinder only when necessary. We refer to Ref. [71] for details on the measurement principle of the 4-point optical probe. Support for this probe is built into the T^{3}C by incorporating opto-electrical converters into the outer cylinder's bottom plate.

2.3 Examples of results

In this section we will demonstrate that the facility works by outlining our initial observations of the torque, velocity profiles and bubbly effects.

2.3.1 Torque versus Reynolds number for single phase flow

We first measure the global torque as a function of the Reynolds number in the present T^{3}C apparatus with a stationary outer cylinder. The torque τ on the middle section of the inner cylinder is measured for Reynolds numbers varying from 3×10^5 to 2×10^6. We use the same normalization as Ref. [23] to define the non-dimensional

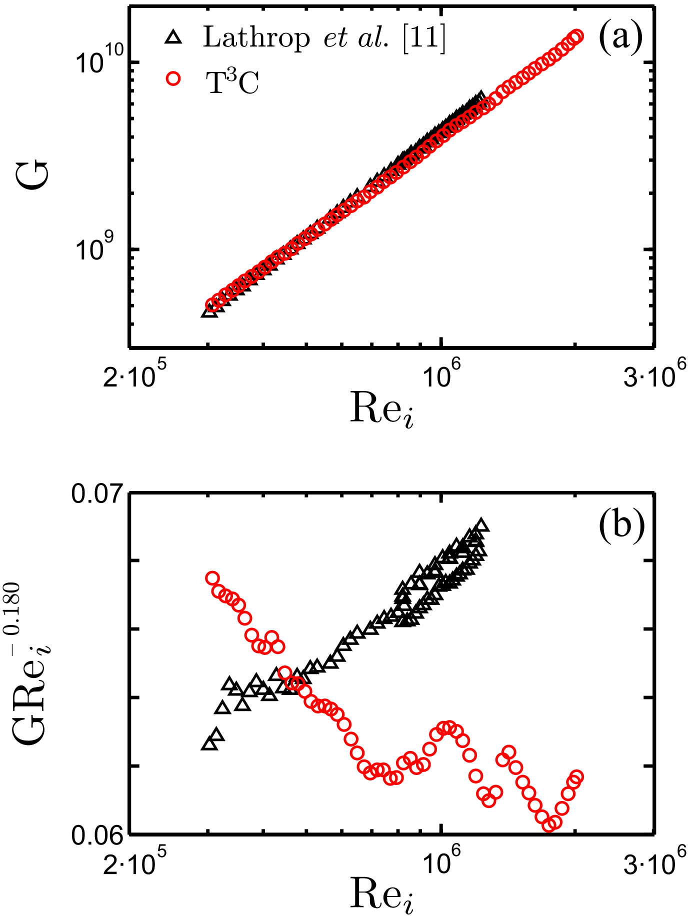

Figure 2.9: (a) The non-dimensional torque and (b) the compensated torque $\mathrm{GRe}_i^{-1.80}$ versus Reynolds number in the high-Reynolds-number regime for the measurements with the T-M TC (open triangles) and T^{3}C (open circles) apparatuses.

torque as $G = \tau/2\pi\rho\nu^2 L_{\text{mid}}$. The present measurements are performed in the T^{3}C with a radius ratio η = 0.716, which is close to the value η = 0.725 of the T-M TC examined by Lathrop *et al.* [11]. Figure 2.9(a) shows G versus Re$_i$ for $\text{Re}_i > 3\times10^5$. The fitting exponent for the data by Lathrop *et al.* [11] is 1.86, and the result of the present measurement gives 1.75.

To better compare these data, we use $G^{-1.80}$ to compensate for the torque $G\text{Re}_i^{-1.80}$, which is shown in Fig. 2.9(b). Overall, the data of Ref. [11] shows a higher exponent than the compensated value of 1.80, and the present measurement is lower. However, both data sets clearly exhibit deviations from a single power law. The present measurement shows an oscillating trend when the Reynolds number is higher than 8×10^5. This is likely induced by transitions between different flow structures, which will be studied systematically in the T^{3}C apparatus with high scrutiny as this trend was not anticipated.

We also examine the torque versus Reynolds number in the co- and counter-rotation regime, which is the topic of chapters 3 and 4 of this thesis.

2.3.2 Velocity profile measured with LDA

Previous velocity measurements were mainly done with intrusive measurement techniques like hot-film probes. A better way for velocity measurements inside the TC gap are nonintrusive optical techniques such as LDA. Due to the curvature, the angle between two LDA beams slightly depends on the radial position along the gap. We have corrected for this via a ray-tracing calculation based on the system parameters [72]. Refraction effects have also been taken into account. To test the reliability of the correction, we perform a velocity profile measurement when the system is in solid-body rotation, i.e. $f = f_i = f_o = 2$ Hz. Open circles in Fig. 2.10 show the azimuthal velocity profile measured with LDA. The exact solid-body velocity profile, r/r_o, is shown with the solid line in the figure. The velocity has been normalized by its value on the inner wall of the outer cylinder. Figure 2.10 clearly indicates that the LDA measurements agree with the solid-body profile (within 0.6%).

When only the outer cylinder rotates, the TC flow with an infinite aspect ratio is linearly stable. The laminar azimuthal Couette velocity profile for infinite aspect ratio (i.e. without end-plate effects) reads [73]:

$$u_{\phi,lam}(r) = Ar + B/r,\ A = \frac{2\pi f_o}{1-\eta^2},\ B = \frac{-2\pi f_o r_i^2}{1-\eta^2}. \tag{2.1}$$

The corresponding laminar profile with the present system parameters, for f_o = 7.2 Hz, is shown with the dashed line in Fig. 2.10. The open squares are the measured azimuthal velocity profile with LDA when the outer cylinder is rotating at f_o = 7.2 Hz. The measurement is carried out with the T^{3}C at a statistically stationary state. The velocity has been normalized by its value on the inner wall of the outer cylinder.

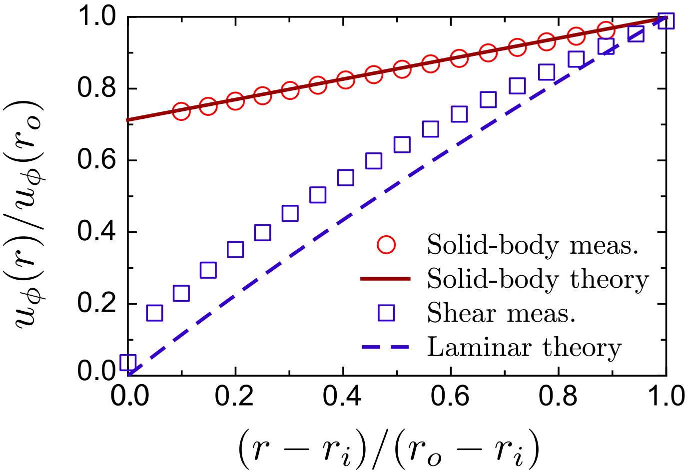

Figure 2.10: Open circles: the azimuthal velocity profile measured with LDA when the system is in solid-body rotation ($f_i = f_o = 2$ Hz). The solid line corresponds to r/r_o of the solid-body flow. Open squares: the azimuthal velocity profile measured with LDA in the T^{3}C system with a stationary inner cylinder ($f_i = 0$, $f_o = 7.2$ Hz). The dashed line corresponds to the laminar profile described in Eqn. (2.1), applicable to a laminar profile between the cylinders, with no top and bottom plate effects.

A clear deviation is found between the measurement results with the laminar profile. The reason for this deviation is due to end-plate effects [72, 74, 75] – the laminar flow profile of type (2.1) only exists when the aspect ratio of TC is infinite. More measurements are upcoming for studying velocity profiles in high-Reynolds-number Taylor-Couette flow. Certainly the end-plate effects will be significantly reduced for the turbulent cases, when the liquid velocity fluctuations dominate the flow. Additional results on velocity profiles in T^{3}C and a detailed discussion will be published elsewhere.

2.3.3 Torque versus gas concentration for bubbly TC flow

The T^{3}C apparatus is designed for studying both single- and two-phase flows. We refer to chapter 7 in which the focus lies on torque measurements and local information on bubbly flows in the present T^{3}C apparatus.

2.4 Summary and outlook

A new turbulent Taylor-Couette apparatus, named T^{3}C, has been developed, consisting of two independently rotating cylinders. The torque measurements for pure inner cylinder rotation agree well with previous results in the overlapped parameter regime. We also performed experiments in the unexplored parameter regime of large Reynolds number and counter-rotation of the cylinders. The data of G versus Re_i for the counter-rotation situation are not simple translations of the pure inner cylinder curve, but depend on the rotation frequency of the outer cylinder in a nontrivial way. The nonintrusive measurement technique LDA is applied to the system for measuring velocity profiles through the transparent outer cylinder of the $\mathrm{T}^3\mathrm{C}$, and it has proved to be an excellent tool for flow velocity measurements inside TC. The torque measurements of bubbly flow in the $\mathrm{T}^3\mathrm{C}$ system showed surprisingly large drag reduction (more than 50%) at high Reynolds numbers, which was not attainable by previous measurements in other TC apparatuses.

The inner cylinder Reynolds number Re_i of older existing turbulent TC facilities can be as high as 10^6. However, another two control parameters, the outer cylinder Reynolds number Re_o and radius ratio η, still have not been explored in the highly turbulent regime ($\mathrm{Re} \gtrsim 10^5$). With this newly-built Taylor-Couette system, the parameter space (Re_i, Re_o, η) has been extended to (2.0×10^6, $\pm 1.4 \times 10^6$, $0.716 - 0.909$), as shown in Fig. 2.11. Various research issues of single-phase turbulent TC flows can be studied with this new $\mathrm{T}^3\mathrm{C}$ facility; for example, turbulent momentum transport in the unexplored parameter space of co- and counter-rotation, the role of the "geometrical quasi-Prandtl number" [23] on turbulent momentum transport, angular momentum/velocity profiles, and the connections with the global torque, and statistics of turbulent fluctuations of different velocity components. These studies will bridge the gap between RB flow and TC flow in the turbulent regime toward a better understanding of closed turbulent systems.

The injection of bubbles offers another degree in the parameter space for studying two-phase TC flows. The study of the bubbly DR can be improved further by combining the global torque and the local measurements of the bubble velocity and

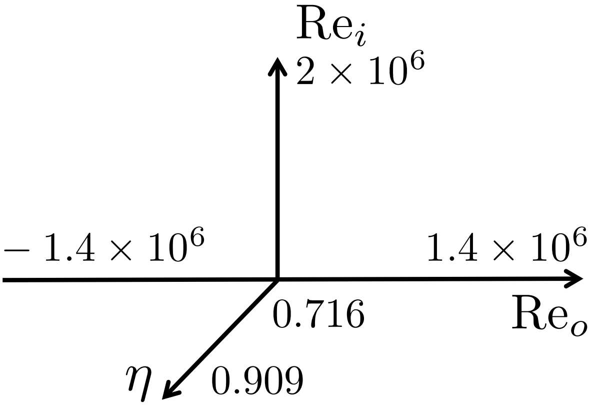

Figure 2.11: Parameter space of the $\mathrm{T}^3\mathrm{C}$.

distribution (see Fig. 2.12). Apart from studying bubbly DR, T^3C is also an ideal system for studying other issues in dispersed multiphase flows; for example, the Lagrangian properties of particles/bubbles in turbulence [68, 76, 77], and liquid velocity fluctuations induced by dispersed bubbles/particles [78, 79]. It was found that even in homogeneous and isotropic turbulence, particles, drops and bubbles are not distributed homogeneously, but cluster [80]. One example of bubble clustering in turbulent TC flow is shown in Fig. 2.12. Given the rich flow structures inside turbulent TC flow, it is of great interest to quantify particles/bubbles clustering with varying turbulent structures, and this will also be done in future research.

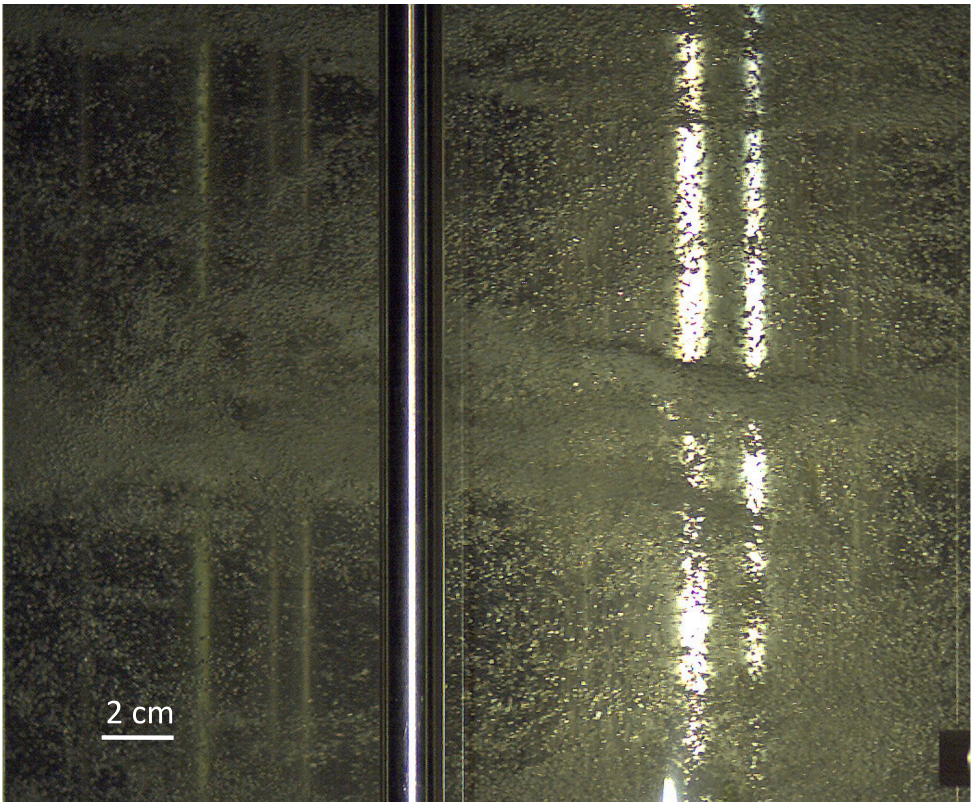

Figure 2.12: A snapshot of the bubble distribution in the T^3C, $\mathrm{Re}_i = 1.0 \times 10^6$. The outer cylinder is stationary. This flow is studied in detail in chapter 7.

— Part II —

Single-phase Taylor-Couette flow

3

Torque scaling in turbulent Taylor-Couette flow with co- and counter-rotating cylinders *

We analyze the global transport properties of turbulent Taylor-Couette flow in the strongly turbulent regime for independently rotating outer and inner cylinders, reaching Reynolds numbers of the inner and outer cylinders of $Re_i = 2 \times 10^6$ *and* $Re_o = \pm 1.4 \times 10^6$*, respectively. For all* Re_i*,* Re_o*, the dimensionless torque* G *scales as a function of the Taylor number* Ta *(which is proportional to the square of the difference between the angular velocities of the inner and outer cylinders) with a universal effective scaling law* $G \propto Ta^{0.88}$*, corresponding to* $Nu_\omega \propto Ta^{0.38}$ *for the Nusselt number characterizing the angular velocity transport between the inner to the outer cylinders. The exponent 0.38 corresponds to the ultimate regime scaling for the analogous Rayleigh-Bénard system. The transport is most efficient for the counter-rotating case along the diagonal in phase space with* $\omega_o \approx -0.4\omega_i$*.*

---

* Based on: D.P.M. van Gils, S.G. Huisman, G.-W. Bruggert, C. Sun, and D. Lohse, *Torque scaling in turbulent Taylor-Couette flow with co- and counterrotating cylinders*, Phys. Rev. Lett. **106**, 024502 (2011).

3.1 Introduction

Global transport properties of turbulent flows are of prime importance for many applications of fluid dynamics, but also for a fundamental understanding, as they reflect the interplay between the boundary layer and the bulk. The two canonical systems used to analyze the transport properties in closed turbulent systems are Rayleigh-Bénard (RB) convection and Taylor-Couette (TC) flow, and they are conceptually closely related [21–23]. In RB flow, heat (in dimensionless form the Nusselt number) is transported from the hot bottom plate to the cold top plate [19, 20], whereas in TC flow angular velocity is transported from the inner to the outer cylinder (for $\omega_i > \omega_o$). In analogy to RB flow, Eckhardt *et al.* [23] identified, from the underlying Navier-Stokes equations,

$$J^{\omega} = r^3 (\langle u_r \omega \rangle_{A,t} - \nu \partial_r \langle \omega \rangle_{A,t}), \tag{3.1}$$

as a relevant conserved transport quantity, representing the flux of angular velocity from the inner to the outer cylinder. Here $u_r (u_\phi)$ is the radial (azimuthal) velocity, $\omega = u_\phi / r$ the angular velocity, and $\langle \ldots \rangle_{A,t}$ characterizes averaging over time and an area with constant r from the axis. J^{ω} is made dimensionless with its value $J^{\omega}_{lam} = 2\nu r_i^2 r_o^2 (\omega_i - \omega_o)/(r_o^2 - r_i^2)$ for the laminar case, giving a “Nusselt number” as a dimensionless transport quantity,

$$\mathrm{Nu}_{\omega} = J^{\omega} / J^{\omega}_{lam}, \tag{3.2}$$

where $r_{i,o}$ and $\omega_{i,o}$ denote the radius and the angular velocity of the inner and outer cylinders, respectively, and ν is the kinematic viscosity of the fluid. Nu_{ω} is closely connected to the torque τ that is necessary to keep the inner cylinder rotating at a constant angular velocity or, in dimensionless form, to

$$G = \frac{\tau}{2\pi L \rho_{fluid} \nu^2} = \mathrm{Nu}_{\omega} \frac{J^{\omega}_{lam}}{\nu^2} = \mathrm{Nu}_{\omega} G_{lam}, \tag{3.3}$$

where L is the height of the cylinder and ρ_{fluid} the density of the fluid. Yet another often used possibility to represent the data is the friction coefficient $c_f = [(1-\eta)^2/\pi] G/\mathrm{Re}_i^2$ [10].

For RB flow, the scaling properties of the Nusselt number in the fully turbulent regime (i.e., for very large Rayleigh numbers, say $\mathrm{Ra} \geq 10^{10}$) have received tremendous attention in the last decade and various heat flux measurements have been performed; again, see the review article [19]. In contrast, TC flow in the fully turbulent regime has received much less attention, with the only exception being the Texas experiment by Swinney, Lathrop, and coworkers [10, 11, 14, 15]. In that experiment a Reynolds number $\mathrm{Re}_i = 10^6$ of the inner cylinder was reached (with the outer cylinder at rest) and an effective power law of $G \propto \mathrm{Re}_i^{\gamma}$ with $\gamma \approx 1.6 - 1.86$ was detected [10, 11] in the turbulent regime, though the scaling properties are not particularly good and, strictly speaking, γ depends on Re_i; i.e., there is no pure scaling. Indeed, in Refs. [23, 81, 82] we have argued that there should be a smooth transition from $\gamma = 3/2$ for the small Reynolds number of a boundary layer dominated flow to $\gamma = 2$ for the larger Reynolds number of a flow dominated by the turbulent bulk. Turbulent TC experiments get even more scarce for TC flow with inner and outer cylinders rotating independently. We are only aware of the Wendt experiments in the 1930s [5], reaching $\mathrm{Re}_i \approx 10^5$ and $\mathrm{Re}_o \approx \pm 10^5$ and the recent ones by Ravelet *et al.* [16], reaching $\mathrm{Re}_i \approx 5\times 10^4$ and $\mathrm{Re}_o = \pm 2\times 10^4$. The hitherto explored phase diagram of TC flow with independently rotating cylinders is shown in Fig. 3.1. An alternative representation of the phase diagram is given by Dubrulle *et al.* [75], who introduce a shear Reynolds number and a rotation number as an alternative representation of the phase space (see below).

In the phase diagram [Fig. 3.1] we have also added the Re_i, Re_o numbers that we explored with our newly constructed Twente turbulent TC facility (T^{3}C), which we have described in great detail in section 2.2. One of the goals we want to achieve with this new facility is to explore the (Re_i, Re_o, $\eta = r_i/r_o$) parameter space, thus entering *terra incognita*, and measure the torque [i.e., transport of the angular velocity (Nu_ω in dimensionless form) or, again expressed differently, the overall drag] and the internal Reynolds number of the flow.

3.2 Experimental method

In this chapter we will focus on the required torque for fully developed turbulent flow (Re_i, $\mathrm{Re}_o > 10^5$), where $\eta = 0.716$ with independently rotating inner and outer cylinders, which hitherto has not been explored. The examined parameter space in this chapter is shown in the space of (Re_i, Re_o) in Fig. 2.2 (a), (Ta, a) in Fig. 2.2 (b), and (Ta, R_Ω) in Fig. 2.2 (c), to be explained below. We will not address the question whether pure scaling laws exist: First, the explored Reynolds number range is too short to answer this question, and second, the earlier work [10, 11, 14, 23, 81, 82] gives overwhelming experimental and theoretical evidence that there are no pure scaling laws, even up to Reynolds numbers of 10^6. So all scaling exponents in this chapter have to be read as effective scaling laws.

3.3 Results

Our results for the counter-rotating case for the dimensionless torque G as function of Re_i for fixed Re_o are shown in Fig. 3.3. One immediately sees that counter-rotation enhances the torque (and thus the overall drag), but that for general $\mathrm{Re}_o \neq 0$ the

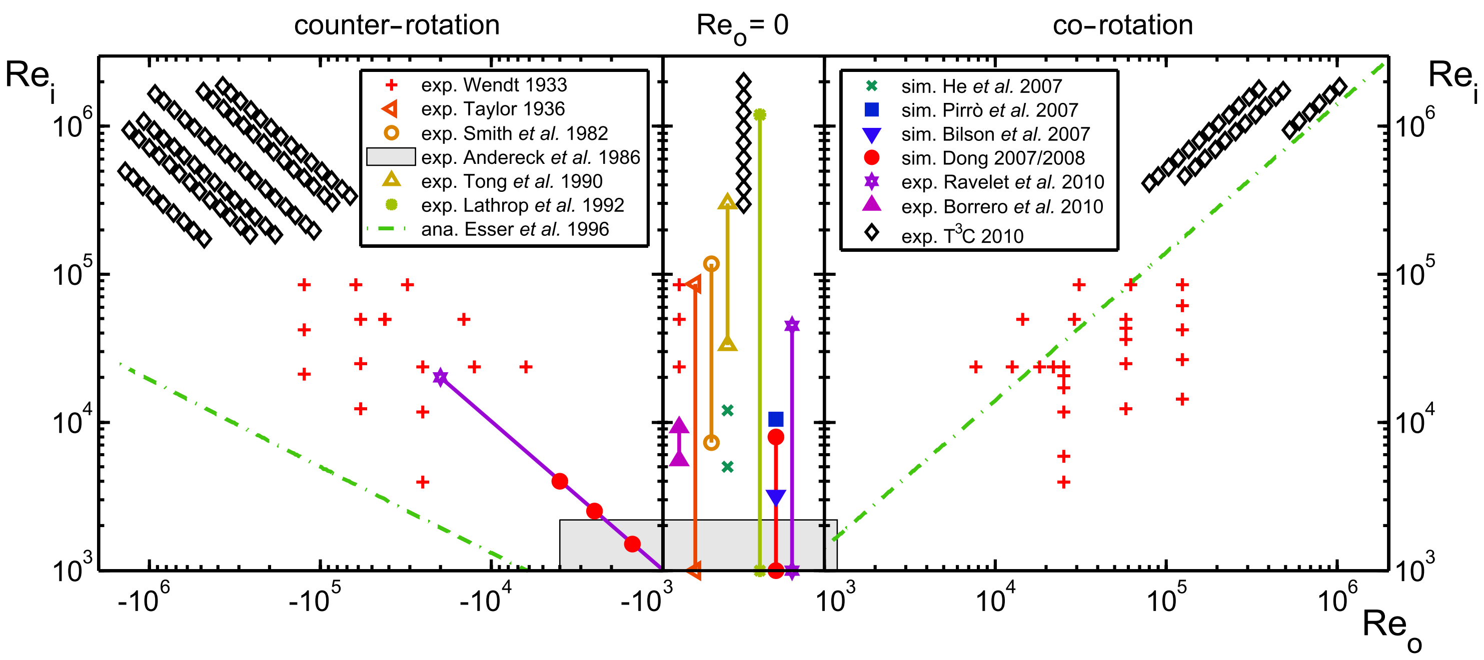

Figure 3.1: Explored phase space (Re$_o$, Re$_i$) of TC flow with independently rotating inner and outer cylinders. To the right of the horizontal axis the cylinders are co-rotating, to the left of it they are counter-rotating, and a log-log representation has been chosen. Experimental data by Wendt [5] (pluses), Taylor [6] (left triangles), Smith and Townsend [7] (open circles), Andereck *et al.* [3] (grey box), Tong *et al.* [9] (upward triangles), Lathrop *et al.* [10] (stars), Ravelet *et al.* [16] (hexagrams), Borrero-Echeverry *et al.* [17] (upward solid triangles), and simulations by Pirro and Quadrio [83] (solid squares), Bilson and Bremhorst [84] (downward solid triangles), and Dong [47, 48] (solid circles). The dashed lines are Esser and Grossmann's [46] estimate for the onset of turbulence with $\eta = 0.71$. The many data points in the small Reynolds number regime of pattern formation and spatial temporal chaos (see e.g. [3, 29, 42]) have not been included in this phase diagram. Our data points for this publication are the black diamonds. Our data points for this publication are the black diamonds.

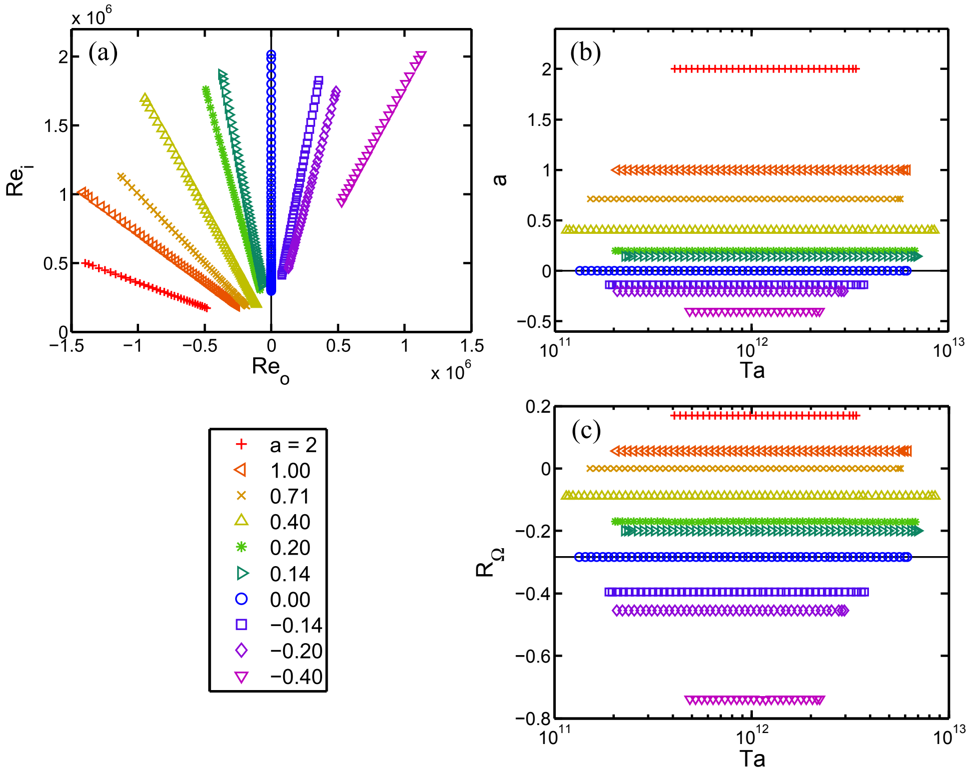

Figure 3.2: (a) Our data points in the (Re_o, Re_i) phase diagram on a linear scale. (b) Our data points in the phase space (Ta, a); note that Ta also depends on a. (c) Our data points in the phase space (Ta, R_Ω) [see Eq. (3.7)].

effective power law $G \propto \mathrm{Re}_i^{1.76}$, that holds in the case of inner cylinder rotating only, gets lost; in fact, there is even no effective power law at all.

How can we represent the data to better reveal the transport properties of the system? The analysis of Eckhardt *et al.* [23] and the analogy of the TC system to the RB system suggest to better plot Nu_ω as a function of the Taylor number

$$\mathrm{Ta} = \frac{1}{4}\sigma d^2 (r_i + r_o)^2 (\omega_i - \omega_o)^2 \nu^{-2}, \tag{3.4}$$

where $\sigma = \{[(1+\eta)/2]/\sqrt{\eta}\}^4$, i.e., along the diagonals

$$\omega_o = -a\omega_i \tag{3.5}$$

in the parameter space[†], Fig. 3.2 (a). Indeed, Eckhardt *et al.* [23] derived, from the

---

[†] We define Eq. (3.5) with a minus sign, as our focus is on the counter-rotating case.

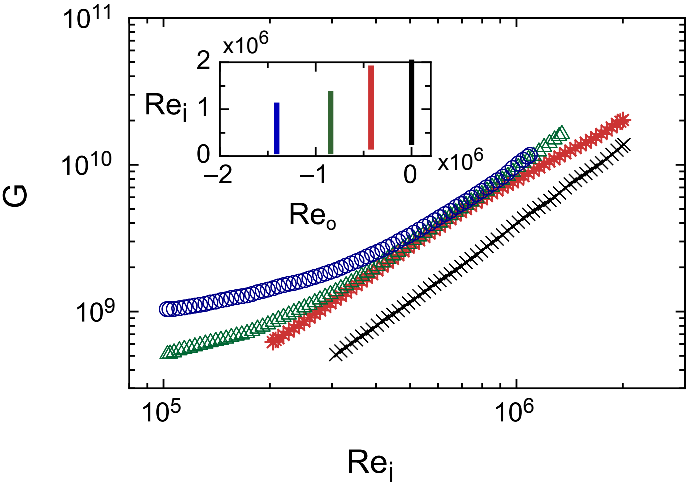

Figure 3.3: The dimensionless torque $G(\mathrm{Re}_i)$ for counter-rotating TC flow for four different fixed values of $\mathrm{Re}_o = -1.4 \times 10^6$, -0.8×10^6, -0.4×10^6, and 0 (top to bottom data sets); see inset for the probed area of the parameter space.

underlying Navier-Stokes equation, the exact relation

$$\varepsilon_w = \varepsilon - \varepsilon_{lam} = \nu^3 d^{-4} \sigma^{-2} \mathrm{Ta}(\mathrm{Nu}_\omega - 1) \tag{3.6}$$

for the excess kinetic energy dissipation rate ε_w [i.e., the total kinetic energy dissipation rate ε minus the kinetic energy dissipation rate in the laminar case $\varepsilon_{lam} = 4\nu r_i^2 r_o^2 (r_i + r_o)^{-2} d^{-2} (\omega_i - \omega_o)^2$]. In Eq. (3.6) σ can be interpreted as a (geometric) Prandtl number, and Ta and Nu_ω are the exact TC analogs to the Rayleigh and Nusselt numbers in RB flow. Along the diagonal, Eq. (3.5), in parameter space, one has $\mathrm{Ta} = \frac{1}{4}\sigma d^2 (r_i + r_o)^2 (1+a)^2 \omega_i^2 \nu^{-2}$, and the well-studied [19] effective scaling law $\mathrm{Nu} \propto \mathrm{Ra}^{\tilde{\gamma}}$ for RB flow (with $\tilde{\gamma} \approx 0.31$ [19, 34]) would now correspond to an effective scaling law $\mathrm{Nu}_\omega \propto \mathrm{Ta}^\gamma$ for TC flow.

Nu_ω vs Ta is shown in Fig. 3.4 (a) for various a, i.e., along various straight lines through the origin of the parameter space, Fig. 3.2 (a). A *universal*, i.e. a-indepedent, effective scaling $\mathrm{Nu}_\omega \propto \mathrm{Ta}^\gamma$ with $\gamma \approx 0.38$ is clearly revealed. This corresponds to a scaling of $G \propto \mathrm{Re}_i^{1.76}$ for the dimensionless torque along the straight lines, Eq. (3.5), in the parameter space, Fig. 3.2, to $c_f \propto \mathrm{Re}_i^{-0.24}$ for the drag coefficient, and to $G \propto \mathrm{Ta}^{0.88}$. The compensated plots $\mathrm{Nu}_\omega/\mathrm{Ta}^{0.38}$ in Fig. 3.4 (b) demonstrate the quality of the effective scaling and, in addition, show the a dependence of the prefactor of the scaling law.

The a dependence of the prefactor $\mathrm{Nu}_\omega/\mathrm{Ta}^{0.38}$ is plotted in Fig. 3.5. It shows a pronounced maximum around $a = 0.4$, i.e., for the moderately counter-rotating case, signaling the most efficient angular velocity transport from the inner to the outer

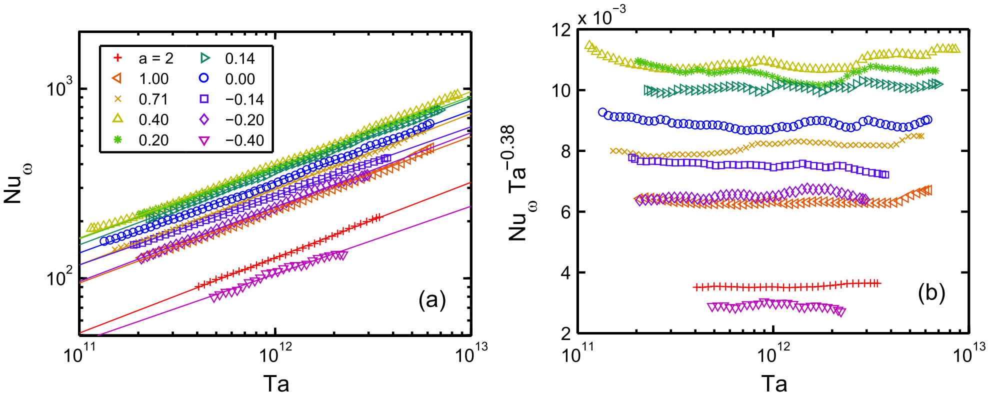

Figure 3.4: (a) Nu_ω vs Ta for various a; see Fig. 3.2(a) for the location of the data in parameter space. A universal effective scaling $\mathrm{Nu}_\omega \propto \mathrm{Ta}^{0.38}$ is revealed. The compensated plots $\mathrm{Nu}_\omega/\mathrm{Ta}^{0.38}$ in (b) show the quality of the effective scaling and the a-dependent prefactor of the scaling law.

cylinder at that value. We mention that it is obvious that this curve has a maximum, as in both limiting cases $a \to \pm\infty$ (rotating of the outer cylinder only) the flow is laminar and $\mathrm{Nu}_\omega = 1$, but it is interesting to note that the maximum does not occur for the most pronounced counter-rotating case $\omega_o = -\omega_i$ (or $a = 1$). Compared to the case of pure inner cylinder rotation ($a = 0$), at $a = 0.4$ the angular velocity transport from the inner to the outer cylinder is enhanced by more than 20%.

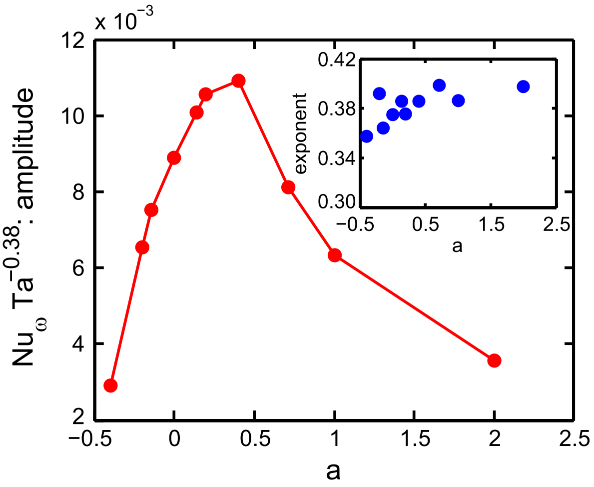

Figure 3.5: Prefactor of the effective scaling law $\mathrm{Nu}_\omega \propto \mathrm{Ta}^{0.38}$ (shown in Fig. 3.4) as a function of $a = -\omega_o/\omega_i$. The inset shows the effective exponents γ which results from an individual fit of the scaling law $\mathrm{Nu}_\omega \propto \mathrm{Ta}^{\gamma}$.

The parameter $a = -\omega_o/\omega_i$ is connected to the so-called rotation number

$$\mathrm{R}_\Omega = (1-\eta)(\mathrm{Re}_i + \mathrm{Re}_o)/(\eta \mathrm{Re}_o - \mathrm{Re}_i) \tag{3.7}$$

introduced by Dubrulle *et al.* [75] and used by Ravelet *et al.* [16], namely, $\mathrm{R}_\Omega = (1-\eta)\eta^{-1}(a-\eta)(a+1)^{-1}$. We also plot our data points in the phase space of (Ta, R_Ω), as shown in Fig. 3.2 (c). The optimal value $a \approx 0.4$ we found for the transport properties of the system corresponds to $\mathrm{R}_\Omega \approx -0.09$. In this chapter we prefer a as compared to R_Ω, as the sign of a immediately signals whether the system is co-rotating or counter-rotating.

3.4 Conclusion

In conclusion, we have explored the *terra incognita* of fully developed turbulent TC flow with independently rotating inner and outer cylinders, beyond Reynolds numbers of 10^6, finding a universal scaling law $G \propto \mathrm{Ta}^{0.88}$, corresponding to $\mathrm{Nu}_\omega \propto \mathrm{Ta}^{0.38}$, for all (fixed) $a = -\omega_o/\omega_i$, with optimal transport quantities at $a \approx 0.4$. It is remarkable that the effective scaling exponent 0.38 exactly resembles the analogous effective scaling exponent in $\mathrm{Nu} \propto \mathrm{Ra}^{0.38}$ in RB convection in the ultimate regime of thermal convection [24, 25], reflecting the analogy between TC and RB flow also in the strongly turbulent regime.

The next steps will be to further extend the parameter space, Fig. 3.1, towards further radius ratios η to see whether the observed universality carries on towards an even larger parameter range, and to also measure the Taylor-Reynolds number and the wind Reynolds numbers of the internal flow, which are closely connected to Nu_ω and for which theoretical predictions exist [23]. With such measurements and characterizations of the flow structures, we will also be able to check whether these are reflected in the overall transport properties.

4

Optimal Taylor-Couette turbulence [*]

Strongly turbulent Taylor-Couette flow with independently rotating inner and outer cylinder with a radius ratio of $\eta = 0.716$ *is experimentally studied. From global torque measurements we analyze the dimensionless angular velocity flux* $Nu_\omega(Ta, a)$ *as a function of the Taylor number Ta and the angular velocity ratio* $a = -\omega_o/\omega_i$ *in the large Taylor number regime* $10^{11} \lesssim Ta \lesssim 10^{13}$ *and well off the inviscid stability borders (Rayleigh lines) for co-rotation* $a = -\eta^2$ *and* $a = \infty$ *for counter-rotation. We analyze the data with the common power law ansatz for the dimensionless angular velocity transport flux* $Nu_\omega(Ta, a) = f(a) \cdot Ta^\gamma$*, with an amplitude* $f(a)$ *and an exponent* $\gamma(a)$*. The data are consistent with an exponent* $\gamma = 0.39 \pm 0.03$ *for all a, but we discuss a possible a-dependence in the co- and weakly counter-rotating regime. The amplitude of the angular velocity flux* $f(a) \equiv Nu_\omega(Ta, a)/Ta^{0.39}$ *is measured to be maximal at slight counter-rotation, namely at an angular velocity ratio of* $a_{opt} = 0.368 \pm 0.001$*, i.e. along the lines* $\omega_o = -0.368\omega_i$*. This value is theoretically interpreted as the result of a competition between the destabilizing inner cylinder rotation and the stabilizing but shear-enhancing outer cylinder counter-rotation. – With the help of laser Doppler anemometry we provide angular velocity profiles and in particular identify the radial position* r_n *of the neutral line, defined by* $\langle \omega(r_n) \rangle_t = 0$ *for fixed height z. For these large Ta-values the ratio* $a_{opt} = 0.368$ *is distinguished by a zero angular velocity gradient* $\partial\omega/\partial r = 0$ *in the bulk. While for moderate counter-rotation* $-0.368\omega_i \lesssim \omega_o < 0$ *(i.e.* $0 < a \lesssim a_{opt}$*) the neutral line still remains close to*

---

[*] Submitted to J. Fluid Mech. as: D.P.M. van Gils, S.G. Huisman, S. Grossmann, C. Sun, and D. Lohse, *Optimal Taylor-Couette turbulence*.

the outer cylinder and the probability distribution function of the bulk angular velocity is observed to be mono-modal, for stronger counter-rotation $\omega_o \lesssim -0.368\omega_i$ *(i.e.* $a \gtrsim a_{opt}$*) the neutral line is pushed inwards towards the inner cylinder; in this regime the probability distribution function of the bulk angular velocity becomes bi-modal, reflecting intermittent bursts of turbulent structures beyond the neutral line into the outer flow domain, which otherwise is stabilized by the counter-rotating outer cylinder. Finally, a hypothesis is offered allowing a unifying view and consistent interpretation for all these various results.*

4.1 Introduction

Taylor-Couette (TC) flow — the flow between two coaxial, independently rotating cylinders — is next to Rayleigh-Bénard (RB) flow — the flow in a box heated from below and cooled from above — the most prominent "drosophila" to test hydrodynamic concepts for flows in closed containers. For outer cylinder rotation and fixed inner cylinder the flow is linearly stable. In contrast, for inner cylinder rotation and fixed outer cylinder the flow is linearly unstable thanks to the driving centrifugal forces, see e.g. DiPrima & Swinney [2], Smith & Townsend [7], Coles [41], Pfister & Rehberg [42], Mullin *et al.* [43], Pfister *et al.* [44], Buchel *et al.* [45], Esser & Grossmann [46], Mullin *et al.* [85]. The case of two independently rotating cylinders has been well analyzed for low Reynolds numbers, see e.g. Andereck *et al.* [3]. For large Reynolds numbers, where the bulk flow is turbulent, studies have been scarce, see for example the historical work by Wendt [5] or the experiments by Andereck *et al.* [3], Ravelet *et al.* [16], Borrero-Echeverry *et al.* [17], Dubrulle *et al.* [75], Richard [86], van Hout & Katz [87]. Recently, in two independent experiments, van Gils *et al.* [88] and Paoletti & Lathrop [18] supplied precise data for the torque scaling in the turbulent regime of the flow between independently rotating cylinders.

We use cylindrical coordinates r, ϕ and z. Next to the geometric ratio $\eta = r_i/r_o$ between the inner cylinder radius r_i and the outer cylinder radius r_o, and the aspect ratio $\Gamma = L/d$ of the cell height L and the gap width $d = r_o - r_i$, the dimensionless control parameters of the system can either be expressed in terms of the inner and outer cylinder Reynolds numbers $Re_i = r_i\omega_i d/\nu$ and $Re_o = r_o\omega_o d/\nu$, respectively, or, alternatively, in terms of the ratio of the angular velocities

$$a = -\omega_o/\omega_i \tag{4.1}$$

and the Taylor number

$$Ta = \frac{1}{4}\sigma(r_o - r_i)^2(r_i + r_o)^2(\omega_i - \omega_o)^2\nu^{-2}. \tag{4.2}$$

Here according to the theory by Eckhardt, Grossmann & Lohse [23] (from now on called EGL), $\sigma = (((1+\eta)/2)/\sqrt{\eta})^4$ (thus $\sigma = 1.057$ for the current $\eta = 0.716$ of the T^{3}C facility) can be formally interpreted as a "geometrical" Prandtl number and ν is the kinematic viscosity of the fluid. With $r_a = (r_i + r_o)/2$ and $r_g = \sqrt{r_i r_o}$, the arithmetic and the geometric mean radii, the Taylor number can be written as

$$Ta = r_a^6 r_g^{-4} d^2 \nu^{-2} (\omega_i - \omega_o)^2. \tag{4.3}$$

The angular velocity of the inner cylinder ω_i is always defined as positive, whereas the angular velocity of the outer cylinder ω_o can be either positive (co-rotation) or negative (counter-rotation). Positive a thus refers to the counter-rotating case on which our main focus will lie.

The response of the system is the degree of turbulence of the flow between the cylinders — e.g. expressed in a wind Reynolds number of the flow, measuring the amplitude of the r- and z-components of the velocity field — and the torque τ, which is necessary to keep the inner cylinder rotating at constant angular velocity. Following the suggestion of EGL, the torque can be non-dimensionalized in terms of the laminar torque to define the (dimensionless) "Nusselt number"

$$Nu_\omega = \frac{\tau}{2\pi L \rho_{fluid} J^\omega_{lam}}, \tag{4.4}$$

where ρ_{fluid} is the density of the fluid between the cylinders and $J^\omega_{lam} = 2\nu r_i^2 r_o^2 (\omega_i - \omega_o)/(r_o^2 - r_i^2)$ is the conserved angular velocity flux in the laminar case. The reason for the choice (4.4) is that

$$J^\omega = J^\omega_{lam} Nu_\omega = r^3 \left(\langle u_r \omega \rangle_{A,t} - \nu \partial_r \langle \omega \rangle_{A,t} \right) \tag{4.5}$$

is the relevant conserved transport quantity, representing the flux of angular velocity from the inner to the outer cylinder. This definition of J^ω is an immediate consequence of the Navier-Stokes equations. Here u_r (u_ϕ) is the radial (azimuthal) velocity, $\omega = u_\phi / r$ the angular velocity, and $\langle \ldots \rangle_{A,t}$ characterizes averaging over time and a cylindrical surface with constant radius r. With this choice of control and response parameters, EGL could work out a close analogy between turbulent TC and turbulent RB flow, building on Grossmann & Lohse [49] and extending the earlier work of Bradshaw [21] and Dubrulle & Hersant [22]. This was further elaborated by van Gils *et al.* [88].

The main findings of van Gils *et al.* [88], who operated the TC setup, known as the Twente turbulent Taylor-Couette system or T^{3}C, at fixed $\eta = 0.716$ and for $Ta > 10^{11}$ as well as the variable a well off the stability borders $-\eta^2$ and ∞, are as follows: (i) in the (Ta, a) representation, $Nu_\omega(Ta, a)$ within the experimental precision factorizes into $Nu_\omega(Ta, a) = f(a) \cdot F(Ta)$. (ii) $F(Ta) = Ta^{0.38}$ for all analyzed $-0.4 \le a \le 2.0$ in the turbulent regime. (iii) $f(a) = Nu_\omega(Ta, a)/Ta^{0.38}$ has a pronounced maximum around $a_{opt} \approx 0.4$. Also Paoletti & Lathrop [18], at slightly different $\eta = 0.725$ found such a maximum in $f(a)$, namely at $a_{opt} \approx 0.35$. For this

a_{opt} the angular velocity transfer amplitude $f(a_{opt}(\eta))$ for the transport from the inner to the outer cylinder is maximal. — From these findings one has to conclude: Although counter rotation of the outer cylinder should in principle stabilize the flow for all $\omega_o < 0$, the angular velocity transport flux, instead, for not too strong counter-rotation $-0.4\omega_i \lesssim \omega_o < 0$ is still further enhanced. There is still stronger turbulence attributed to the enhanced shear between the counter-rotating cylinders. Only for strong enough counter-rotation $\omega_o < -a_{opt}\omega_i$ (i.e. $a > a_{opt}$) the transport amplitude decreases with further increasing a.

The aims of this paper are (i) to provide further and more precise data on the maximum in the conserved turbulent angular velocity flux $Nu_\omega(Ta,a)/Ta^\gamma = f(a)$ as a function of a and a theoretical interpretation of this maximum, including a speculation on how it depends on η (section 4.3), (ii) to provide laser Doppler anemometry (LDA) measurements of the angular velocity profiles $\langle\omega(r)\rangle_t$ as functions of height, and to show that the maximum in $f(a)$, for these asymptotic Ta and deep in the instability range at $a = a_{opt}$, coincides with a vanishing angular velocity gradient $\partial\omega/\partial r$ in the bulk of the flow, and to identify the location of the neutral line r_n, defined by $\langle\omega(r_n)\rangle_t = 0$ for fixed height z, finding that it remains still close to the outer cylinder r_o for weak counter-rotation, $0 < a < a_{opt}$, but starts moving inwards towards the inner cylinder r_i for $a \gtrsim a_{opt}$ (section 4.4), and (iii) to show that the turbulent flow organization totally changes for $a \gtrsim a_{opt}$, where the stabilizing effect of the strong counter rotation reduces the angular velocity transport (section 4.5). In this strongly counter-rotating regime the probability distribution function of the angular velocity in the bulk becomes bi-modal, reflecting intermittent bursts of turbulent structures beyond the neutral line towards the outer flow region, which otherwise, i.e. in between such bursts, is stabilized by the counter-rotating outer cylinder. In section 4.6 we discuss the BL thicknesses. The paper ends with a summary, further discussions of the neutral line inside the flow, and an outlook. However first — in section 4.2 — we will provide more experimental details and we will in particular discuss the height dependence of the flow profile and finite size effects.

4.2 Experimental setup and discussion of end-effects

The core of our experimental setup — the Taylor-Couette cell — is shown in Fig. 2.2. In particular, the fixed geometric dimensionless numbers are $\eta = 0.716$ and $\Gamma = 11.68$. The details of the setup are given in section 2.2. The working liquid is water at a continuously controlled constant temperature (precision ±0.5K) in the range 19°C - 26°C. The accuracy in a is ±0.001 based on the angular velocity stability of the T^{3}C facility. To reduce edge effects, similarly as in Lathrop *et al.* [10, 11] the torque is measured at the middle part (length ratio $L_{mid}/L = 0.578$) of the inner cylinder only. Lathrop *et al.* [11]'s original motivation for this choice was that the height of the remaining upper and lower parts of the cylinder roughly equals the size of one Taylor-vortex. While the respective first or last Taylor vortex indeed will be affected by the upper and lower plates (which in our T^3C cell are co-rotating with the outer cylinder), the hope is that in the strongly turbulent regime the turbulent bulk is not affected by such edge effects. Note that for the laminar case — e.g. for pure outer cylinder rotation — this clearly is not the case, as has been known since G. I. Taylor, see e.g. the classical experiments by Coles & van Atta [74], the numerical work by Hollerbach & Fournier [89], or the review by Tagg [90]. For such weakly rotating systems, profile distortions from the plates propagate into the fluid and dominate the whole laminar velocity field. The velocity profile will then be very different from the classical height-independent laminar profile (see e.g. Landau & Lifshitz [73]) with periodic boundary conditions in vertical direction,

$$u_{\phi,\mathrm{lam}} = Ar + B/r\ , \qquad A = \frac{\omega_o - \eta^2\omega_i}{1-\eta^2}\ , \qquad B = \frac{(\omega_i - \omega_o)r_i^2}{1-\eta^2}\ . \tag{4.6}$$

To control that edge effects are indeed negligible in the strongly turbulent case under consideration here ($10^{11} < Ta < 10^{13}$ and $-0.40 \leq a \leq 2.0$, so well off the instability borders), we have measured time series of the angular velocity $\omega(r,t) = u_\phi(r,t)/r$ for various heights $0.32 < z/L < 1$ and radial positions $r_i < r < r_o$ with laser Doppler anemometry (LDA). We employ a backscatter LDA configuration set up with a measurement volume of 0.07mm x 0.07mm x 0.3mm. The seeding particles have a mean diameter of 5 μm (PSP-50 Dantec Dynamics). We account for the refraction due to the cylindrical interfaces, details are given by Huisman [72]. Figure 4.1a shows the height dependence of the time-averaged angular velocity at mid-gap, $\tilde{r} = (r-r_i)/(r_o-r_i) = 1/2$, for $a = 0$ and $Ta = 1.5 \times 10^{12}$, corresponding to $Re_i = 1.0 \times 10^6$ and $Re_o = 0$. The dashed-dotted line corresponds to the transition from the middle-part of the inner cylinder, with which we measure the torque, and the upper part. Along the middle-part the time-averaged angular velocity is a z-independent constant within 1%, as is demonstrated in the inset, showing an enlarged relevant section of the ω axis. From the upper edge of the middle-part of the inner cylinder towards the highest position that we can resolve, 0.5 mm below the top plate, the mean angular velocity decays by only 5%. This finite difference might be due to the existence of Ekman layers near the top and bottom plate (Greenspan [91]). Since at $z/L = 1$ we have $\omega(r,t) = 0$, as the upper plate is at rest for $a = 0$ or $\omega_o = 0$, 95% of the edge effects on ω occur in such a thin fluid layer near the top (bottom) plate that we cannot even resolve it with our present LDA measurements.

For the angular velocity fluctuations shown in Fig. 4.1b we observe a 25% decay in the upper 10% of the cylinder, but again in the measurement section of the inner cylinder $0.2 < z/L < 0.8$ there are no indications of any edge effects. The plots of Fig. 4.1 together confirm that edge effects are unlikely to play a visible role for our torque measurements in the middle-part of the cylinder. Even the Taylor-vortex

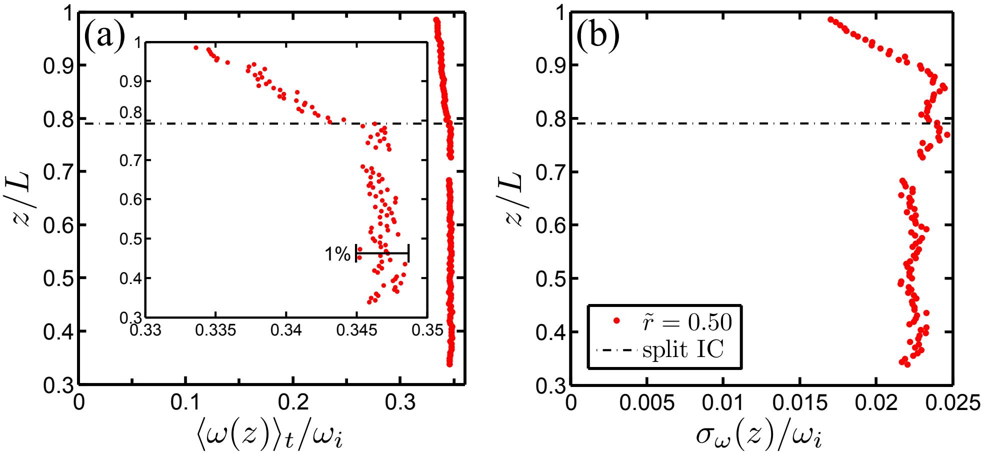

Figure 4.1: Time averaged axial profiles of the azimuthal angular velocity inside the T^{3}C measured with LDA at mid-gap, i.e. $\tilde{r} = (r - r_i)/(r_o - r_i) = 0.5$, for the case $Re_i = 1.0 \times 10^6$ and $Re_o = 0$ (corresponding to $a = 0$ and $Ta = 1.5 \times 10^{12}$). The height z from the bottom plate is normalized against the total height L of the inner volume of the tank. (a): the time-averaged angular velocity $\langle\omega(z, \tilde{r} = 1/2)\rangle_t$ normalized by the angular velocity of the inner cylinder wall ω_i. (b): the standard deviation of the angular velocity $\sigma_\omega(z)$ normalized by the angular velocity of the inner wall. The split between the middle and the top inner cylinder sections is indicated by the dash-dotted line. As can be appreciated in this figure, the end-effects are negligible over the middle section where we measure the global torques as reported in this work. The velocities near the top plate, $z/L = 1$, are not sufficiently resolved to see the boundary layer.

roll-structure, which dominates TC flow at low Reynolds numbers (Andereck *et al.* [3], Dominguez-Lerma *et al.* [4], Tagg [90], Dominguez-Lerma *et al.* [92]), is not visible at all in the time averaged angular velocity profile $\langle\omega(z, \tilde{r} = 1/2, t)\rangle_t$.

To double check that this z-independence not only holds at mid-gap $\tilde{r} = 1/2$ but also for the whole radial ω profiles, we measured time series of $\omega(z, \tilde{r}, t)$ at three different heights $z/L = 0.34$, 0.50, and 0.66. The radial dependence of the mean value and of the fluctuations are shown in Fig. 4.2. The profiles are basically identical for the three heights, with the only exception of some small irregularity in the fluctuations at $z/L = 0.34$ in the small region $0.1 < \tilde{r} < 0.2$, whose origin is unclear to us. Note that in both plots of Fig. 4.2 the radial inner and outer boundary layers are again not resolved; in this paper we will focus on bulk properties and global scaling relations.

Based on the results of this section, we feel confident to claim that (i) edge effects are unimportant for the global torque measurements on the middle-part of the inner cylinder as reported in section 4.3 and that (ii) the local profile and fluctuation measurements done close to mid-height $z/L = 0.44$, which will be shown and analyzed in sections 4.4 and 4.5, are representative for any height in the mid-part of the cylinder.

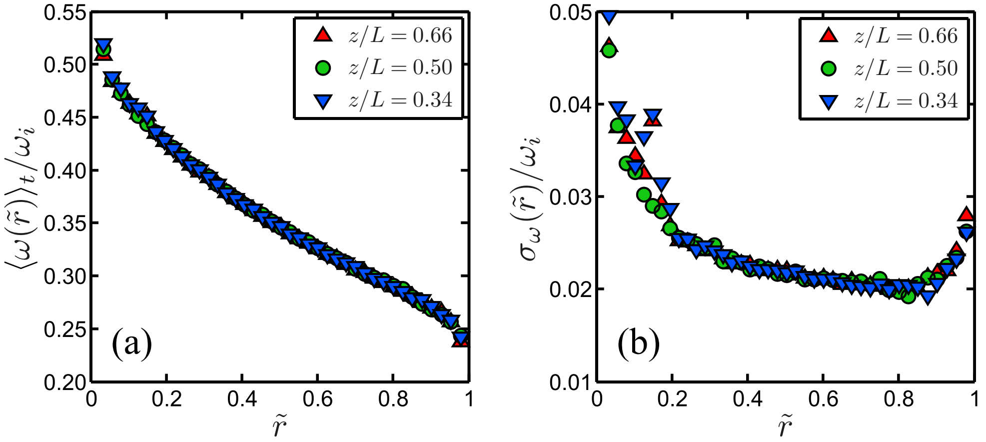

Figure 4.2: Radial profiles of the azimuthal angular velocity as presented in Fig. 4.1, scanned at three different heights $z/L = 0.66$, 0.50 and 0.34, plotted against the dimensionless gap distance $\tilde{r} = (r - r_i)/(r_o - r_i)$, again for $Re_o = 0$ and $Re_i = 1 \times 10^6$. (a): the time-averaged angular velocity $\langle\omega(\tilde{r})\rangle_t$ normalized by the angular velocity of the inner wall ω_i. All profiles fall on top of each other, showing no axial dependence of the flow in the investigated axial range. (b) Standard deviation of the angular velocity $\sigma_\omega(\tilde{r})$ normalized by the angular velocity of the inner wall. The boundary layers at the cylinder walls are not resolved.

4.3 Global torque measurements

In this section we will present our data from the global torque measurements for independently inner and outer cylinder rotation, which complement and improve precision of our earlier measurements in van Gils *et al.* [88]. The data as functions of the respective pairs of control parameters (Ta, a) or (Re_i, Re_o) for which we performed our measurements are given in tabular form in table 4.1 and in graphical form in Figs. 4.3a and 4.4, respectively.

As shown in Fig. 4.5a in a compensated plot we find a universal effective scaling $Nu_\omega(Ta, a) \propto Ta^{0.39}$. If each curve for each a is fitted individually, the resulting Ta-scaling exponents $\gamma(a)$ scatter with a, but only very slightly depend on a, see Figs. 4.5b and 4.5c. For linear fits different below and above a_{opt} (or $\psi = 0$), we obtain $\gamma = 0.3783 + 0.0284a \pm 0.01$, the exponent slightly decreasing towards less counter-rotation, and a constant exponent $\gamma = 0.3941 \pm 0.0055$ for increasing counter-rotation beyond the optimum. One cannot safely exclude a trend in the exponents for $a < a_{opt}$, but the data are also compatible with a constant $\gamma = 0.386$ and a merely statistical scatter of ± 0.03. It is in this approximation that $Nu_\omega(Ta, a)$ factorizes.

Van Gils *et al.* [88] interpreted the effective scaling $Nu_\omega(Ta, a) \sim Ta^{0.39}$ as an indication of the so-called "ultimate regime" – distinguished by both a turbulent bulk and turbulent boundary layers. Such scaling was predicted by Grossmann & Lohse

Table 4.1: The measured global torque data for the individual cases of fixed $a \equiv -\omega_o/\omega_i$ at increasing Ta, as presented in Fig. 4.4, equivalent to straight lines in the (Re_i, Re_o) parameter space, as presented in Fig. 4.3a. We list the minimum and maximum values of the driving parameters — Ta, ω_i, ω_o, Re_i, and Re_o — and we list the minimum and maximum values of the response parameters — dimensionless torque $G(Ta,a)$ and dimensionless angular velocity transport flux $Nu_\omega(Ta,a) = f(a) \cdot F(Ta)$. The variable a can be transformed to the angle ψ, i.e. the angle in (Re_i, Re_o) space between the straight line characterized by a and the one characterized by a_{bis}, describing the angle bisector of the instability range, see Fig. 4.3a and Eq. (4.9). The second to last column lists the effective scaling exponent $\gamma(a)$ obtained from fitting $Nu_\omega(Ta,a)$ to a least-square linear fit in log-log space for each individual case of a, as presented in Fig. 4.5b and c. The pre-factor $f(a)$, as given in the last column, is determined by fixing $\gamma(a)$ at its average encountered value of $\gamma \approx 0.39$ and by averaging the compensated $Nu_\omega Ta^{-0.39}$ over Ta, as presented in Fig. 4.6.

a	ψ deg	Ta min $\times 10^{11}$	Ta max $\times 10^{11}$	ω_i min rad/s	ω_i max rad/s	ω_o min rad/s	ω_o max rad/s	Re_i min $\times 10^5$	Re_i max $\times 10^5$	Re_o min $\times 10^5$	Re_o max $\times 10^5$	G min $\times 10^9$	G max $\times 10^9$	Nu_ω min	Nu_ω max	$\gamma(a)$	$f(a)$ $\times 10^{-3}$
2.000	43.1	4.07	34.0	10.5	30.7	-61.5	-21.1	1.72	4.99	-13.95	-4.82	0.49	3.29	91	212	0.397	2.71
1.000	27.2	2.07	62.3	11.3	61.9	-61.9	-11.3	1.84	10.12	-14.15	-2.58	0.49	10.30	129	492	0.386	4.84
0.714	17.7	1.52	57.1	11.4	69.3	-49.5	-8.1	1.84	11.31	-11.29	-1.84	0.47	12.08	143	603	0.399	6.21
0.650	15.0	1.85	52.3	12.0	62.6	-40.7	-7.8	2.12	11.25	-10.21	-1.92	0.58	11.91	162	621	0.396	6.58
0.600	12.8	1.52	52.2	11.4	65.8	-39.5	-6.9	1.97	11.59	-9.71	-1.65	0.53	12.57	162	656	0.392	6.98
0.550	10.3	1.63	53.7	11.9	67.4	-37.1	-6.5	2.11	12.13	-9.33	-1.63	0.57	13.42	168	691	0.401	7.23
0.500	7.7	1.43	57.5	11.7	73.3	-36.7	-5.9	2.04	12.97	-9.06	-1.43	0.55	15.32	172	762	0.398	7.66
0.450	4.9	1.33	66.5	12.0	83.0	-37.4	-5.4	2.04	14.43	-9.08	-1.28	0.54	18.07	177	836	0.396	7.98
0.400	2.0	1.15	85.4	12.6	93.6	-37.5	-5.0	1.97	16.93	-9.47	-1.10	0.52	22.96	184	937	0.386	8.36
0.368	0.0	2.65	63.2	18.9	89.2	-32.8	-7.0	3.05	14.90	-7.67	-1.57	1.08	18.20	250	864	0.389	8.60
0.350	-1.2	1.16	64.6	12.3	90.1	-31.5	-4.3	2.04	15.28	-7.47	-1.00	0.52	18.67	181	876	0.391	8.61
0.300	-4.5	1.15	65.0	12.4	93.0	-27.9	-3.7	2.11	15.91	-6.67	-0.89	0.52	18.36	185	859	0.383	8.60
0.250	-8.0	1.07	63.4	13.0	97.5	-24.4	-3.2	2.12	16.35	-5.71	-0.74	0.48	17.35	177	822	0.381	8.37
0.200	-11.6	2.03	67.7	19.0	105.8	-21.2	-3.8	3.05	17.59	-4.91	-0.85	0.83	17.57	219	805	0.375	8.07
0.143	-15.9	2.27	69.4	22.1	112.5	-16.1	-3.2	3.38	18.70	-3.73	-0.68	0.83	17.21	208	779	0.386	7.69
0.100	-19.3	4.78	60.0	31.5	112.6	-11.3	-3.2	5.10	18.08	-2.52	-0.71	1.56	14.72	269	717	0.395	7.37
0.000	-27.2	1.34	61.7	18.2	124.0	0.0	0.0	2.97	20.15	0.00	0.00	0.49	13.73	158	660	0.375	6.81
-0.140	-38.3	1.90	37.4	25.5	112.4	3.6	15.7	4.11	18.25	0.80	3.57	0.55	7.07	151	436	0.364	5.76
-0.200	-42.8	2.08	29.6	28.6	107.7	5.7	21.5	4.62	17.44	1.29	4.87	0.49	5.10	128	354	0.392	5.00
-0.400	-56.4	4.87	22.2	58.3	124.3	23.3	49.8	9.44	20.16	5.28	11.27	0.47	1.68	80	135	0.358	2.21

[26] for very strongly driven RB flow. As detailed in Grossmann & Lohse [26] it emerges from a $Nu_\omega(Ta) \sim Ta^{1/2}$ scaling with logarithmic corrections originating from the turbulent boundary layers. Remarkably, the corresponding wind Reynolds number scaling in RB flow does *not* have logarithmic corrections, i.e. $Re_w \sim Ta^{1/2}$. These RB scaling laws for the thermal Nusselt number and the corresponding wind Reynolds number have been confirmed experimentally by Ahlers *et al.* [93] for Nu and by He *et al.* [94] for Re_w. According to the EGL theory this should have its correspondence in TC flow. That leads to the interpretation of $\gamma = 0.39$ as an indication for the ultimate state in the presently considered TC flow. Furthermore, Huisman *et al.* [95] indeed also found from particle image velocimetry (PIV) measurements in the present strongly driven TC system for the scaling of the wind $Re_w \propto Ta^{1/2}$.

We note that in our available Ta regime the effective scaling law $Nu_\omega \sim Ta^{0.39}$ is practically indistinguishable from the prediction of Grossmann & Lohse [26], namely,

$$Nu_\omega \sim Ta^{1/2} \mathscr{L}(Re_w(Ta)), \tag{4.7}$$

with the logarithmic corrections $\mathscr{L}(Re_w(Ta))$ detailed in Eqs. (7) and (9) of Grossmann & Lohse [26]. The result from Eq. (4.7) is shown as a solid line in Fig. 4.5a, showing the compensated plot $Nu_\omega/Ta^{0.39}$: Indeed, only detailed inspection reveals that the theoretical line is not exactly horizontal.

Coming back to our experimental data: The (nearly) horizontal lines in Fig. 4.5a imply that $Nu_\omega(Ta,a)$ within present experimental precision nearly factorizes in $Nu_\omega(Ta,a) = f(a) \cdot Ta^{0.39\pm0.03}$. We now focus on the a-dependence of the angular velocity flux amplitude $f(a) = Nu_\omega(Ta,a)/Ta^{0.39}$, shown in Fig. 4.6a, and the idea of its interpretation. One observes a very pronounced maximum at $a_{opt} = 0.368$, reflecting the optimal angular velocity transport from the inner to the outer cylinder at that angular velocity ratio. Naively, one might have expected that $f(a)$ has its maximum at $a = 0$, i.e. $\omega_o = 0$, no outer cylinder rotation, since outer cylinder rotation stabilizes an increasing part of the flow volume for increasing counter rotation rate. On the other hand, outer cylinder rotation also enhances the total shear of the flow, leading to enhanced turbulence, and thus more angular velocity transport is expected. The a-dependence of $f(a)$ thus reflects the mutual importance of both these effects.

Generally, one expects an increase of the turbulent transport if one goes deeper into the control parameter range (Ta,a) in which the flow is unstable. The optimum positions for the angular velocity transport should consist of all points in parameter space, which are equally distant from both the right branch (1st quadrant, co-rotation) of the instability border and its left branch (2nd quadrant, counter-rotation). In inviscid approximation these two branches are the Rayleigh lines given by the relations $a = -\eta^2$ and $a = \infty$, respectively. The line of equal distance from both is the angle bisector of the instability range. Its relation can easily be calculated to be

$$a_{bis}(\eta) = \frac{\eta}{\tan\left[\frac{\pi}{2} - \frac{1}{2}\arctan\left(\eta^{-1}\right)\right]}. \tag{4.8}$$

For $\eta = 0.716$ this gives $a_{bis} = 0.368$. Noteworthy the measured value $a_{opt} = 0.368 \pm 0.001$ agrees indistinguishably within experimental precision with the bisector line, supporting our interpretation. It also explains why only the lines $a = \text{const}$ scan the parameter space properly. This reflects the straight character of the instability lines — as long as one is not too close to them to see the details of the viscous corrections, i.e. if Ta is large and a is well off the instability borders at $a = -\eta^2$ for co-rotation and $a \to \infty$ for counter-rotation.

Instead of the line a one can introduce the angle ψ between the line of chosen a and the angle bisector of the instability range denoted by a_{bis}; thus $a = a_{bis}$ corresponds to $\psi = 0$.

$$\psi(a) = \frac{\pi - \arctan\left(\eta^{-1}\right)}{2} - \arctan\left(\frac{\eta}{a}\right). \tag{4.9}$$

The transformation (4.9) is shown in Fig. 4.7a and the resulting $f(\psi)$ in Fig. 4.6b. While the function $f(a)$ as a function of a is strongly asymmetric both around its peak at a_{opt} and at its tails, presumably because of the different viscous corrections at $a = -\eta^2$ (decrease $\propto Re_o^{-2}$ towards the Rayleigh line) and at $a = \infty$ (nonvanishing, even increasing correction $\propto Re_o^{3/5}$) (and non-normal-nonlinear (shear) instability, see e.g. Grossmann [96]), the function $f(\psi)$ is by definition symmetric around its (quadratic) maximum at $\psi_{bis} = 0$. Of course, the asymmetry at its tails remains.

We do not yet know whether the optimum of $f(a)$ coincides with the bisector of the Rayleigh-unstable domain for *all* η. Both could coincide incidentally for $\eta = 0.716$, analyzed here. But if this were the case for all η, we can predict the η-dependence of $a_{opt}(\eta)$. This then is given by equation (4.8). This function is plotted in Fig. 4.7. In future experiments we shall test this dependence with our T^{3}C facility. The three extra points we will be able to achieve are marked as white, empty circles. The precision of our facility is good enough to test equation (4.8), but clearly further experiments at much smaller η are also needed.

We note that for smaller Ta one can no longer approximate the instability border by the inviscid Rayleigh lines. The effect of viscosity on the shape of the border lines has to be taken into account. The angle bisector of the instability range in (Re_i, Re_o)-parameter space (Fig. 4.3a) will then deviate from a straight line; we therefore also expect this for a_{opt}. The viscous corrections of the Rayleigh instability criterion were first numerically calculated by Dominguez-Lerma *et al.* [92], then analytically estimated by Esser & Grossmann [46], and finally exactly calculated by Dutcher & Muller [97]. Figures 4.3b and 4.3c show enlargements of the (Re_i, Re_o)-parameter space, together with the Rayleigh-criterion (green) and the Esser & Grossmann [46]

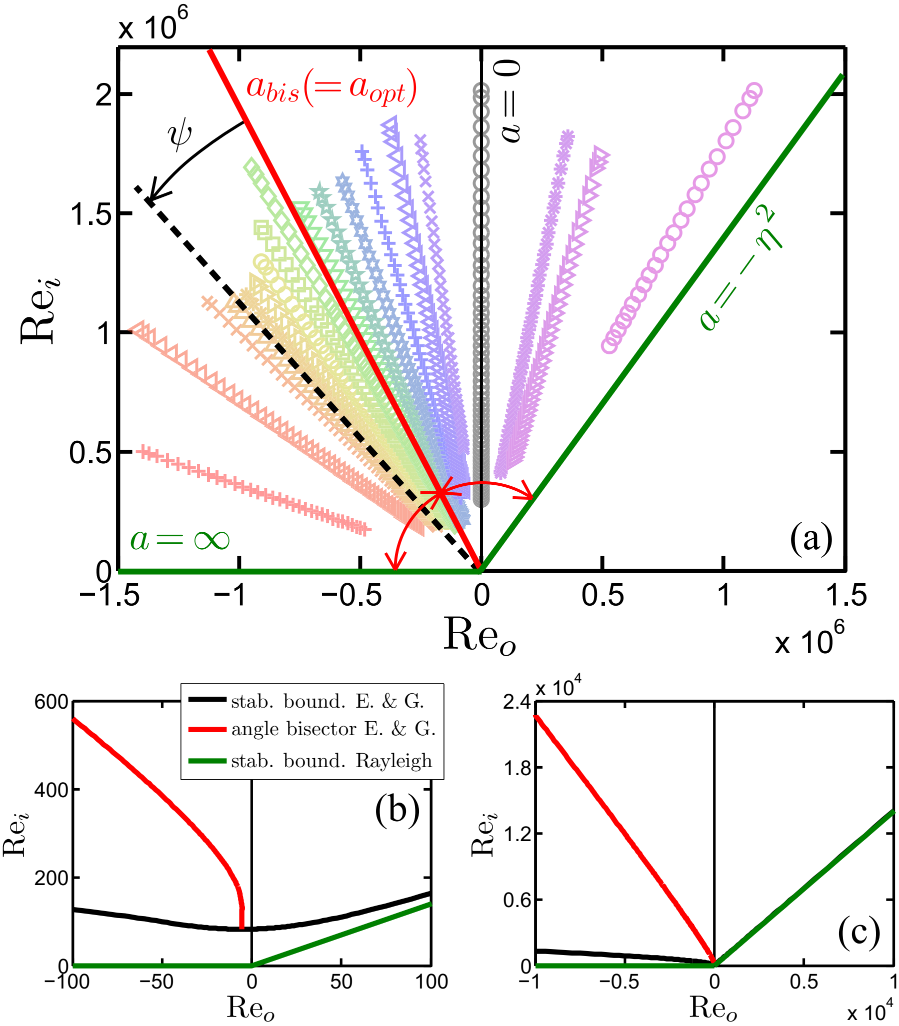

Figure 4.3: (a): Reynolds number phase space showing the explored regime of the T^{3}C as symbols with washed-out colors. The solid green lines are the boundaries between the unstable (upper-left) and stable (lower-right) flow region, shown here for the radius ratio $\eta = 0.716$ as experimentally examined in this work. The green line in the right quadrant is the analytical expression for the stability boundary as found by Esser & Grossmann [46], which recovers to the Rayleigh stability criterion $Re_o/Re_i = \eta$ for $Re_i, Re_o \gg 1$, the viscous corrections decreasing $\propto Re_o^{-2}$. The green line in the left quadrant also follows the stability boundary by Esser and Grossmann ($Re_i \propto Re_o^{3/5}$), but is taken here as $Re_o = 0$. This inviscid approximation is sufficient, if a is not too large, i.e. away from the stability curve. Similar to van Gils *et al.* [88], we define the parameter $a \equiv -\omega_o/\omega_i$ as the (negative) ratio between the angular rotation rates of the outer and inner cylinders. We assume maximum instability and hence optimal turbulence on the bisector of the unstable region, indicated by the solid red line. (b) and (c): enlargements of the Re-space at different scales showing the curvatures of the stability boundaries and the corresponding bisector (red). Above $Re_i, Re_o > 10^5$ the viscous deviation from straight lines becomes negligible.

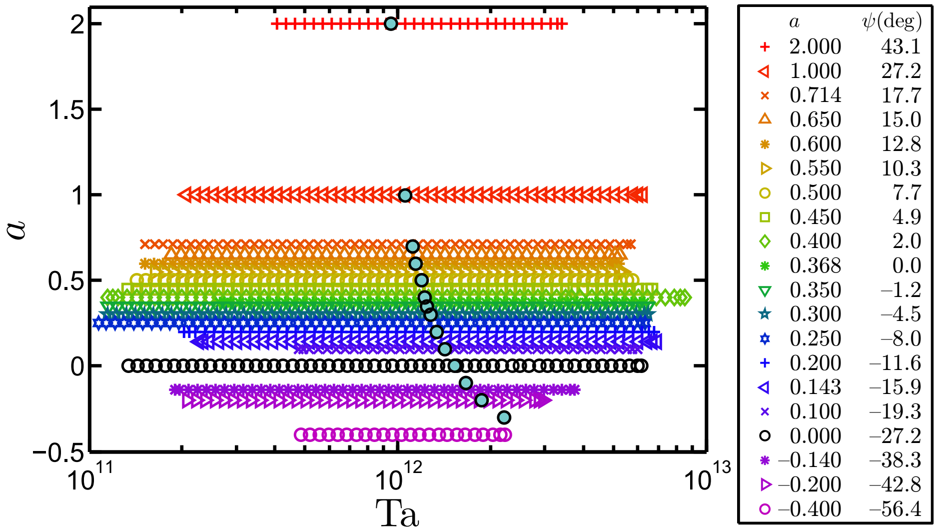

Figure 4.4: The probed (Ta, a) parameter space, equivalent to the (Re_i, Re_o) space shown in Fig. 4.3. Each horizontal data line corresponds to a global torque measurement on the middle section of the inner cylinder at different constant a (and hence ψ). The (blue) filled circles correspond to local measurements on the angular velocity at fixed Ta and a as will be discussed in section 4.4.

Table 4.2: LDA experimental conditions. Each case of a is examined at fixed $Re_i - Re_o = 1.0 \times 10^6$. $a, \psi, Ta, \omega_{i,o}, Re_{i,o}$ as defined before, see also Table 4.1. The minimum and maximum number of detected LDA bursts along the radial scan is given by $\mathrm{N}_{\mathrm{min}}$ and $\mathrm{N}_{\mathrm{max}}$, respectively. Idem for the minimum and maximum average burst rate $F_{s,\mathrm{min}}$ and $F_{s,\mathrm{max}}$.

a	ψ deg	Ta $\times 10^{12}$	ω_i rad/s	ω_o rad/s	Re_i $\times 10^6$	Re_o $\times 10^6$	$\mathrm{N}_{\mathrm{min}}$ $\times 10^3$	$\mathrm{N}_{\mathrm{max}}$ $\times 10^3$	$F_{s,\mathrm{min}}$ 1/s	$F_{s,\mathrm{max}}$ 1/s
2.000	43.1	0.95	16.3	-32.6	0.26	-0.74	35	60	70	2.4k
1.000	27.2	1.06	25.8	-25.8	0.42	-0.58	26	60	52	1.6k
0.700	17.2	1.12	31.2	-21.9	0.51	-0.49	55	80	46	0.7k
0.600	12.8	1.15	33.6	-20.1	0.54	-0.46	67	80	56	0.5k
0.500	7.7	1.20	36.4	-18.2	0.59	-0.41	31	60	63	0.6k
0.400	2.0	1.22	39.5	-15.8	0.64	-0.36	10	25	57	0.7k
0.350	-1.2	1.25	41.4	-14.5	0.67	-0.33	11	25	45	0.5k
0.300	-4.5	1.28	43.6	-13.1	0.70	-0.30	12	25	64	0.8k
0.200	-11.6	1.34	48.3	-9.65	0.78	-0.22	14	25	78	1.0k
0.100	-19.2	1.42	54.2	-5.46	0.88	-0.12	17	25	93	1.3k
0.000	-27.2	1.53	61.8	0.00	1.00	0.00	13	25	72	2.3k
-0.100	-35.2	1.67	71.9	7.21	1.16	0.16	25	25	147	1.7k
-0.200	-42.8	1.87	85.7	17.1	1.39	0.39	22	25	121	1.6k
-0.300	-50.0	2.21	106.0	31.9	1.72	0.72	6	25	32	7.5k

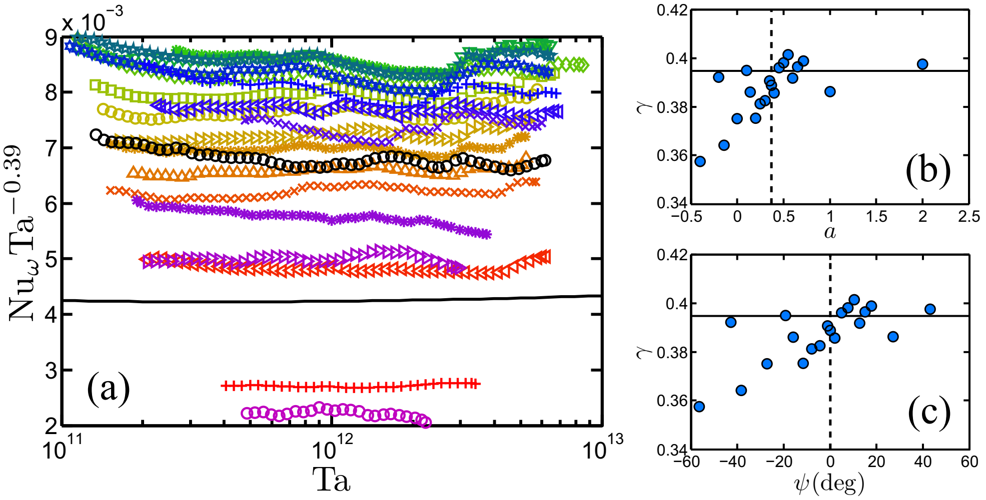

Figure 4.5: (a): $Nu_\omega(Ta,a)$ – compensated by $Ta^{0.39}$ – for various a as a function of a, revealing universal scaling. The colored symbols follow the same coding as given in the legend of Fig. 4.4. The solid line shows the predicted exponent from Eq. (4.7), cf. Grossmann & Lohse [26]. We used $Re_w = 0.0424 \times Ta^{1/2}$ as found by Huisman *et al.* [95] for the case $a = 0$ over the range $4 \times 10^9 < Ta < 6 \times 10^{12}$, and the von Kármán constant $\bar{\kappa} = 0.4$, and $b = 0.9$. – The $Nu_\omega(Ta)$ exponent for each of the individual line series, fitted by a least-square linear fit in log-log space, is plotted versus a in (b) and versus ψ in (c). Assuming a-independence the average scaling exponent is $\gamma = 0.39 \pm 0.03$, which is well consistent with the effective exponent $\gamma = 0.386$ of the first order fit on $\log_{10}(Nu_\omega)$ vs. $\log_{10}(Ta)$ in the shown Ta-regime.

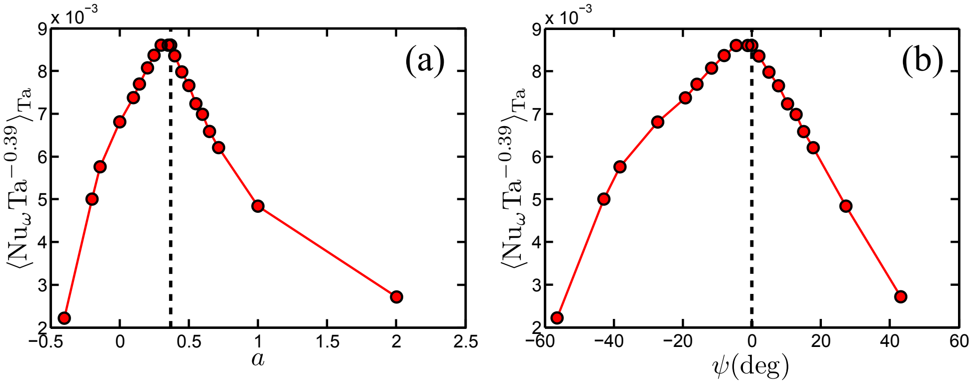

Figure 4.6: Amplitude $f(a)$ of the effective scaling law $Nu_\omega \propto Ta^{0.39}$ (shown in Fig. 4.5) as function of a (a) and as function of ψ (b). The dashed line in both figures corresponds to the suggested case of optimal turbulence as given by Eq. (4.8). (The connecting lines between the data points are guides for the eyes.) The angular velocity transport flux amplitude is systematically larger towards the co-rotating instability borders $a = -\eta^2$ or $\psi \approx -62.8°$.

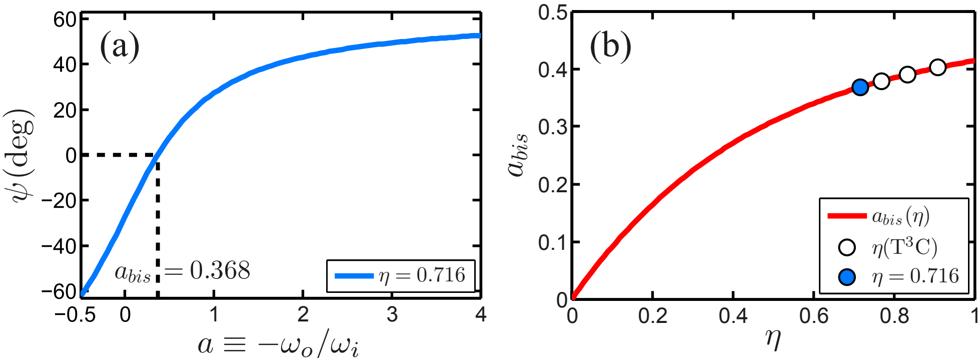

Figure 4.7: (a): The transformation from a to ψ as given by Eq. (4.9), shown here for the radius ratio $\eta = 0.716$ used in the present work. Note that the domain of $a = [-\eta^2, \infty]$ from co- to counter-rotation, spanning the complete unstable flow regime, is transformed to the range $\psi \approx [-62.80^\circ, +62.80^\circ]$ for this specific η. (b): The dependence of a_{bis} on η as given by Eq. (4.8), shown as the red line. Four circles: the radius ratios accessible in the T^{3}C, i.e. $\eta = 0.716; 0.769; 0.833; 0.909$. Blue indicated circle: radius ratio $\eta = 0.716$ of the present work, suggesting optimal turbulence at $a_{bis} = 0.368$.

analytical curve (black) for $\eta = 0.716$. Note that the minimum of that curve is *not* at $Re_o = 0$, but shifted to a slightly negative value $Re_o \approx -5$, where the instability sets in at $Re_i \approx 82$. If we again assume that the optimum position for turbulent transport is distinguished by equal distance to the two branches of the Esser-Grossmann curve, we obtain the red curve in Fig. 4.3b. On the Ta-scale of Figs. 4.3c and 4.3a it is indistinguishable from a straight line through the origin and can hence be described by Eq. (4.8). — As another consequence of the viscous corrections, the factorization of the angular velocity transport flux $Nu_\omega = f(a) \cdot F(Ta)$ will no longer be a valid approximation. For this to hold Ta must be large and a well off the instability lines. This could further be tested by choosing the parameter a sufficiently large, the line approaching or even cutting the stability border for strong counter-rotation. Then the factorization property will be lost.

Future low Ta experiments and/or numerical simulations for various a will show how well these ideas to understand the existence and value of a_{opt}, being near or equal to a_{bis}, are correct or deserve modification. Of course, there will be some deviations due to the coherent structures in the flow at lower Ta, due to the influence of the number of rolls, etc. Similar as in RB the Nu-scaling shows discontinuities, the TC scaling exponent of Nu_ω shows all these structures for not sufficiently large Ta, see e.g. Fig. 3 of Lewis & Swinney [14] in which one sees how strongly the exponent α depends on Re up to 10^4 (Ta about up to 10^8).

4.4 Local LDA angular velocity radial profiles

We now wonder on whether the distinguishing property of the flow at a_{opt} — maximal angular velocity transport — is also reflected in other flow characteristics. We therefore performed LDA measurements of the angular velocity profiles in the bulk close to mid-height, $z/L = 0.44$, at various $-0.3 \leq a \leq 2.0$, see table 4.2 for a list of all measurements, Fig. 4.8 for the mean profiles $\langle\omega(r,t)\rangle_t$ at fixed height z, and Fig. 4.9 for the rescaled profiles $(\langle\omega(r,t)\rangle_t - \omega_o)/(\omega_i - \omega_o)$, also at fixed height z. With our present LDA technique, we can only resolve the velocity in the radial range $0.04 \leq \tilde{r} \leq 0.98$; there is no proper resolution in the inner and outer boundary layers. Because the flow close to the inner boundary region requires substantially more time to be probed with LDA, due to disturbing reflections of the measurement volume on the reflecting inner cylinder wall necessitating the use of more stringent Doppler burst criteria, we limit ourselves to the range $0.2 \leq \tilde{r} \leq 0.98$.

From Fig. 4.8 it is seen that for nearly all co- and counter-rotating cases $-0.3 \leq a \leq 2.0$ the slope of $\langle\omega(\tilde{r},t)\rangle_t$ is negative. Only around $a = 0.40$ we find a zero mean angular velocity gradient in the bulk. This case is within our a resolution the same as a_{opt}. The normalized angular velocity gradient as function of a is shown in Fig. 4.10a. Indeed, it has a pronounced maximum and zero mean angular velocity gradient very close to $a = a_{opt}$, the position of optimal angular velocity transfer. We note that in strongly turbulent RB flow the temperature also has a (practically) zero mean gradient in the bulk, see e.g. the recent review by Ahlers *et al.* [19].

A transition of the flow structure at $a = a_{opt}$ can also be confirmed in Fig. 4.9a, in which we have rescaled the mean angular velocity at fixed height as

$$\langle\tilde{\omega}(\tilde{r})\rangle_t = (\langle\omega(\tilde{r})\rangle_t - \omega_o)/(\omega_i - \omega_o). \tag{4.10}$$

We observe that up to $a = a_{opt}$ the curves for $\langle\tilde{\omega}(\tilde{r})\rangle_t$ for all a go through the mid-gap point $(\tilde{r} = 1/2, \langle\tilde{\omega}(1/2)\rangle_t \approx 0.35)$, implying the mid-gap value $\langle\omega(1/2)\rangle_t \approx 0.35\omega_i + 0.65\omega_o$ for the time averaged angular velocity. However, for $a > a_{opt}$, i.e. stronger counter-rotation, the angular velocity at mid-gap becomes larger, as seen in Fig. 4.9b. This transition resembles a continuous phase transition.

Figure 4.10b shows the relative contributions of the molecular and the turbulent transport to the total angular velocity flux J^ω (4.5), i.e. for both the diffusive and the advective term. The latter always dominates by far with values beyond 99%, but at $a = a_{opt}$ the advective term contributes 100% to the angular velocity flux and the diffusive term nothing, corresponding to the zero mean angular velocity gradient in the bulk at that $a = a_{opt}$. This special situation perfectly resembles RB turbulence for which, due to the absence of a mean temperature gradient in the bulk, the whole heat transport is conveyed by the convective term. In the (here unresolved) kinetic boundary layers the contributions just reverse: The convective term strongly decreases if $\tilde{r}$ approaches the cylinder walls at 0 or 1 since $u_r \to 0$ ($u_z \to 0$ in RB), while the

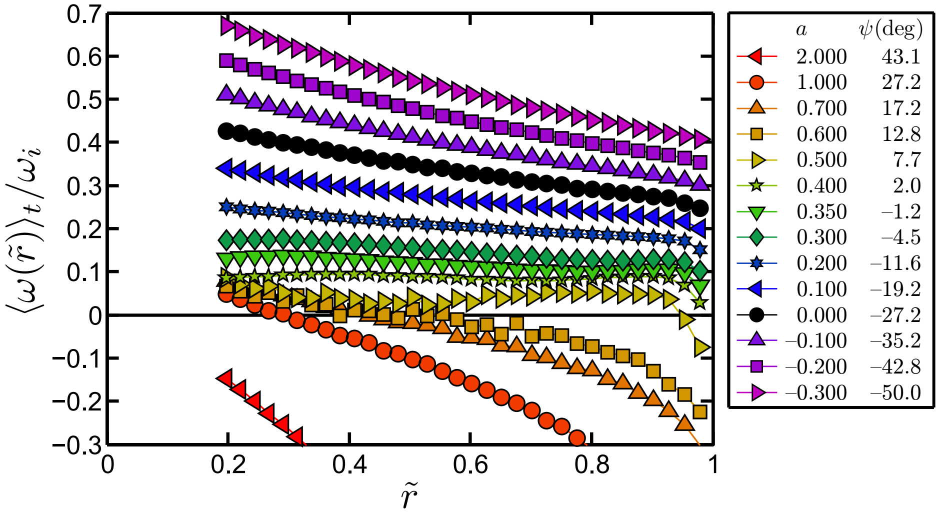

Figure 4.8: Radial profiles of the time-averaged angular velocity $\langle \omega(\tilde{r}) \rangle_t$ at fixed height $z/L = 0.44$, normalized by the inner cylinder angular velocity ω_i, for various cases of fixed a, as indicated by the blue filled circles in Fig. 4.4. All profiles are acquired at fixed angular rotation rates of the cylinders in such a way that $Re_i - Re_o = 1.0 \times 10^6$ is maintained. Instead of measuring at mid-height $z/L = 0.50$ we measure at $z/L = 0.44$, because this axial position encounters less visual obstructions located on the clear acrylic outer cylinder. To improve visual appearance the plotted range does not fully cover the profile corresponding to $a = 2.00$. The profiles of a = 0.50, 0.60, and 0.70 appear less smooth due to a fluctuating neutral line combined with slightly insufficient measuring time, i.e. convergence problems.

diffusive term (heat flux in RB) takes over at the same rate, as the total flux J^ω is an $\tilde{r}$-independent constant.

From the measurements presented in Fig. 4.8 we can extract the neutral line $\tilde{r}_n$, defined by $\langle \omega(\tilde{r}_n, t) \rangle_t = 0$ at fixed height $z/L = 0.44$ for the turbulent case. The results are shown in Fig. 4.11. Note that while for $a \leq 0$ (co-rotation) there obviously is no neutral line at which $\langle \omega \rangle_t = 0$, for $0 < a$ a neutral line exists at some position $\tilde{r}_n > 0$. As long as it still is within the outer kinematic BL, we cannot resolve it. This turns out to be the case for $0 < a < a_{opt}$. But for $a_{opt} < a$ the neutral line can be observed within the bulk and is well resolved with our measurements. So again we see two regimes: For $0 < a < a_{opt}$ in the laminar case the stabilizing outer cylinder rotation shifts the neutral line inwards, but due to the now *free boundary* between the stable outer cylinder r-range and the unstable range between the neutral line and the inner cylinder, the flow structures extend beyond $\tilde{r}_n$. Thus also in the turbulent flow case the unstable range flow extends to the close vicinity of the outer cylinder. The increased shear and the strong turbulence activity originating from the inner cylinder rotation are too strong and prevent that the neutral line is shifted off

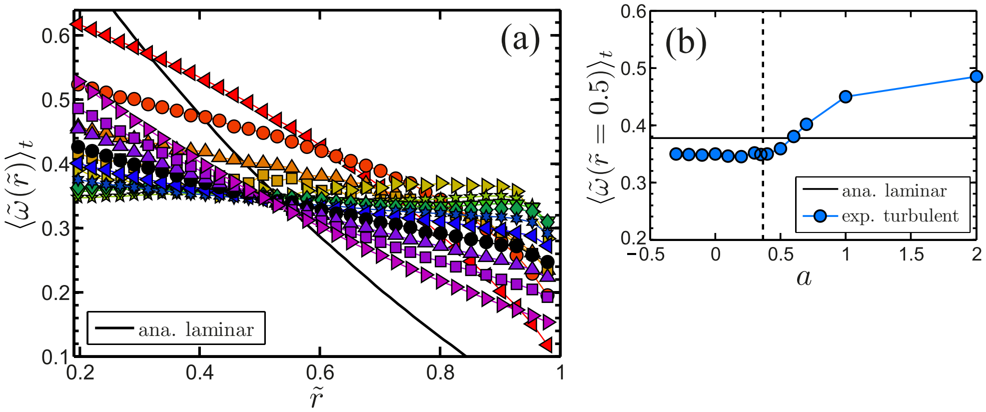

Figure 4.9: (a) Rescaled angular velocity profiles $\langle\tilde{\omega}(\tilde{r})\rangle_t = (\langle\omega(\tilde{r})\rangle_t - \omega_o)/(\omega_i - \omega_o)$ for various a. For $a \leq a_{opt} = 0.368$ all of these curves cross the point $(\tilde{r} = 1/2, \langle\tilde{\omega}\rangle_t = 0.35)$. For $a > a_{opt} = 0.368$ this is no longer the case. The transition of the quantity $\langle\tilde{\omega}(\tilde{r} = 1/2)\rangle_t$ if a increases from $a < a_{opt}$ to $a > a_{opt}$ is shown in (b). The dashed vertical line indicates $a_{bis} = 0.368 = a_{opt}$. The solid black lines in (a) and (b) show the $\tilde{\omega}(\tilde{r})$ values for the laminar solution (4.6).

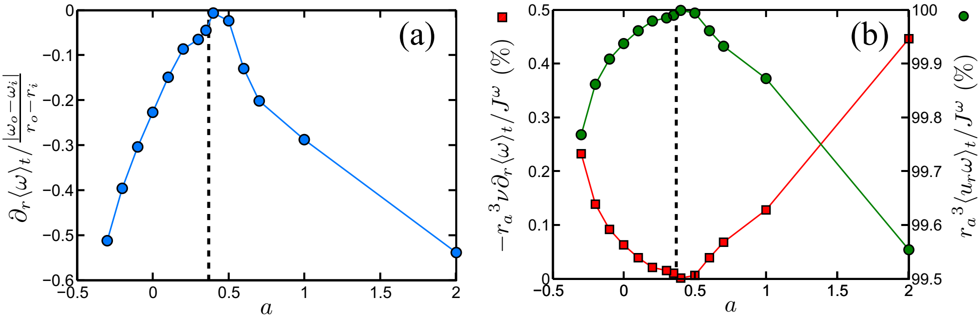

Figure 4.10: (a) Radial gradient $\partial_r\langle\omega\rangle_t$ of the angular velocity profile in the bulk of the flow, non-dimensionalized with the mean ω-slope $|\omega_o - \omega_i|/(r_o - r_i)$. The values are obtained from Fig. 4.8 by fitting a cubic smoothing spline to the profiles in order to increase the accuracy of the gradient amplitude estimate. Note that the radial gradients are *negative* throughout, and approach zero when close to $a = a_{opt}$. (The connecting lines are guides for the eyes.) (b) Resulting ratio of the viscous angular velocity transport term $-r_a^3\nu\partial_r\langle\omega\rangle_{A,t}$ to the total transport J^ω (red squares and left axis) and ratio of the advective angular velocity transport term $r_a^3\langle u_r\omega\rangle_{A,t}$ to the total transport J^ω (green circles and right axis) for the various a. These ratios correspond to the second and first term of equation (4.5), respectively.

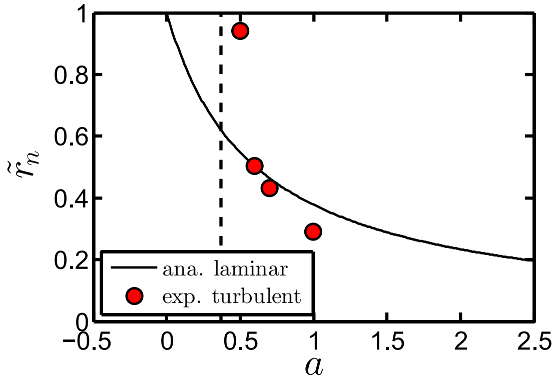

Figure 4.11: The measured radial position $\tilde{r}_n = (r_n - r_i)/(r_o - r_i)$ of the neutral line defined by $\langle \omega(\tilde{r}_n) \rangle_t = 0$ at fixed height $z/L = 0.44$ as function of a. The straight vertical line corresponds to $a_{opt} = 0.368$, below which the neutral line is within the outer BL and cannot be resolved by our LDA technique. The solid line corresponds to the neutral line in the laminar case calculated analytically with Eq. (4.6). Note that for significant counter-rotation $a = 1$ and for this particular height, the neutral line in the turbulent case lies farther inside, nearer to the inner cylinder, than in the laminar flow case.

the outer kinematic BL. As described in Esser & Grossmann [46], this is the very mechanism which shifts the minimum of the viscous instability curve to the left of the $\omega_o = 0$ axis. Therefore, the observed behavior of the neutral line position as a function of a is another confirmation of above idea that a_{opt} coincides with the angle bisector a_{bis} of the instability range in parameter space. The small Re_o and the large Re_o behaviors perfectly merge. For $a > a_{opt}$ the stabilizing effect from the outer cylinder rotation is strong enough, the width of the stabilized range is broad enough, so that a neutral line $\tilde{r}_n$ can be detected in the bulk of the TC flow.

Consequently one would expect that for much weaker turbulence $Ta \ll 10^{11}$ the capacity of the turbulence around the inner cylinder to push the neutral line outwards would decrease, leading to a smaller a_{opt} for these smaller Taylor numbers. Numerical simulations by H. Brauckmann and B. Eckhardt in Marburg (Ta up to 1×10^9) and independently ongoing DNS by R. Ostillo, R.J.A.M. Stevens *et al.* in Twente (presently Ta up to 1×10^7) seem to confirm this view.

For much weaker turbulence one would also expect a more pronounced height-dependence of the neutral line, which will be pushed outwards where the Taylor-rolls are going outwards and inwards where they are going inwards. Based on our height-dependence studies of section 4.2, we expect that this height dependence will be much weaker or even fully washed out in the strongly turbulent regime $Ta > 10^{11}$ in which we operate the TC apparatus. However, in Fig. 4.11 we observe that the neutral line in the turbulent case lies more inside than in the laminar case, and this result is difficult to rationalize apart from assuming some axial-dependence of the neutral line location, i.e. more outwards locations of the neutral line at larger and smaller height. In future work we will study the axial dependence of the neutral line in the turbulent and counter-rotating case in more detail.

While in this section we have only focused on the time-mean values of the angular velocity, in the following section we will give more details on the probability density functions (PDF) in the two different regimes below and above a_{opt} and thus on the different dynamics of the flow in these regimes: Another confirmation of the physical importance of the optimum line or angle bisector.

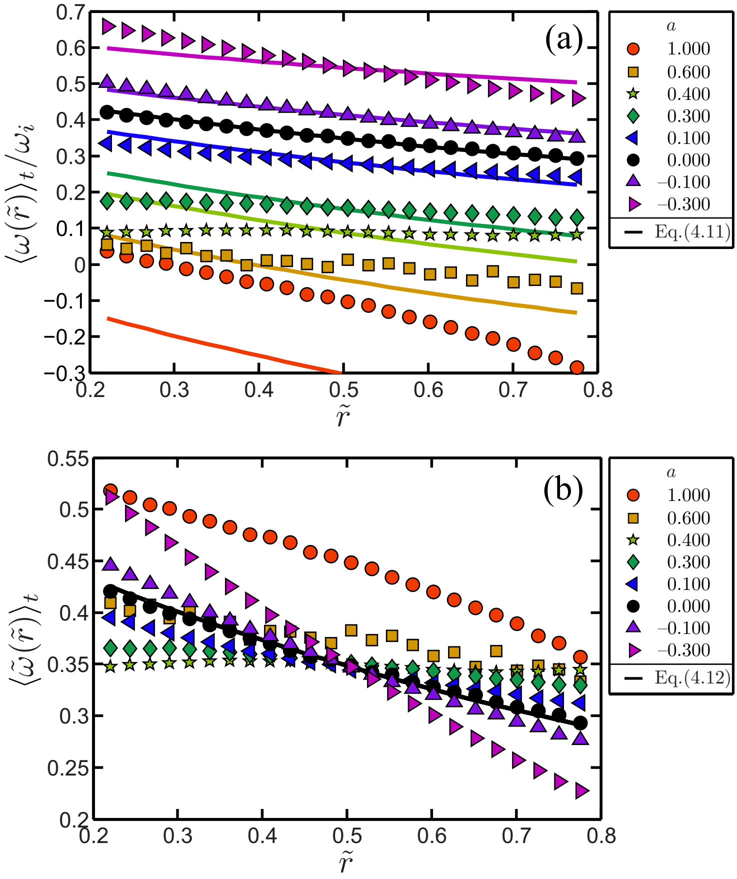

Figure 4.12: The symbols indicate the experimental data as already presented in Fig. 4.8 and Fig. 4.9a. To improve visual appearance only a selection on the a-cases is shown. The thick solid lines are given by Eq. (4.11) for $\eta = 0.716$. (a) angular velocity $\langle\omega(\tilde{r})\rangle_t$ versus normalized gap distance $\tilde{r}$ for various a. (b) rescaled angular velocity $\langle\tilde{\omega}(\tilde{r})\rangle_t = (\langle\omega(\tilde{r})\rangle_t - \omega_o)/(\omega_i - \omega_o)$ versus $\tilde{r}$ for various a. The profiles as given by Eq. (4.12) fall on top of each other for all a.

From considerations of bounds on solutions to the Navier-Stokes equation, Busse [53] derived an expression for the angular velocity in the limit of infinite Reynolds number. Translating his formulas to the notation used in the present thesis, reads

$$\omega = \frac{\omega_i - \omega_o}{r^2}\left[\frac{r_i^2}{4(1-\eta^2)}\right] + \omega_i\left[\frac{\eta^2 - 2\eta^4}{2-2\eta^4}\right] + \omega_o\left[\frac{2-\eta^2}{2-2\eta^4}\right]. \tag{4.11}$$

Excellent agreement is found for the case $a = 0.00$, however for a farther away from zero there is more discrepancy between the experimental data and the upper-bound theory by Busse [53], as shown in Fig. 4.12a. When we rescale the angular velocity profiles to $\tilde{\omega}$, according to Eq. (4.10), the profiles as given by the upper-bound theory [53] fall on top of each other for all a,

$$\tilde{\omega} = \frac{r_i^2}{4\left(r_o^4 - r_i^4\right)}\left[\frac{r_o^2\left(r_i^2 + r_o^2\right)}{r^2} + 2r_o^2 - 4r_i^2\right] \tag{4.12}$$

In contrast to the collapsing upper-bound profiles, the experimental data in Fig. 4.12b show a different trend. One would expect good agreement between the case of $a = a_{opt}$ and the upper-bound profiles, however we observe only a good match for the case of $a = 0.00$, which may be due to the complexity of the flow structure.

4.5 Turbulent flow organization in the TC gap

Time series of the angular velocity at $\tilde{r} = 0.60$ below the optimum amplitude at $a = 0.35 < a_{opt} = 0.368$ (co-rotation dominates) and above the optimum at $a = 0.60 > a_{opt} = 0.368$ (counter-rotation dominates) are shown in Fig. 4.13a and 4.13b, respectively. While in the former case we always have $\omega(t) > 0$ and a Gaussian distribution — see Fig. 4.14a — in the latter case we find a bimodal distribution with one mode fluctuating around a positive angular velocity and one mode fluctuating around a negative angular velocity. This bimodal distribution of $\omega(t)$ is confirmed in various PDFs shown in Fig. 4.14. We interpret this intermittent behavior of the time series as an indication of turbulent bursts originating from the turbulent region in the vicinity of the inner cylinder and penetrating into the stabilized region near the outer cylinder. We find such bimodal behavior for all $a > a_{opt}$, see Figs. 4.14d, e, f, g, h, and i, whereas for $a < a_{opt}$ we find a unimodal behavior, see Figs. 4.14a, b, and c. Apart from one case ($a = 0.50$) we do not find any long-time periodicity of the bursts in $\omega(t)$. In future work we will perform a full spectral analysis of long time series of $\omega(t)$ for various a and $\tilde{r}$.

Three-dimensional visualizations of the $\omega(t)$-PDF for all $0 < \tilde{r} < 1$ are provided in Fig. 4.15 for unimodal cases $a < a_{opt}$ and in Fig. 4.16 for bimodal cases $a > a_{opt}$. In the latter figure the switching of the system between positive and negative angular velocity becomes visible.

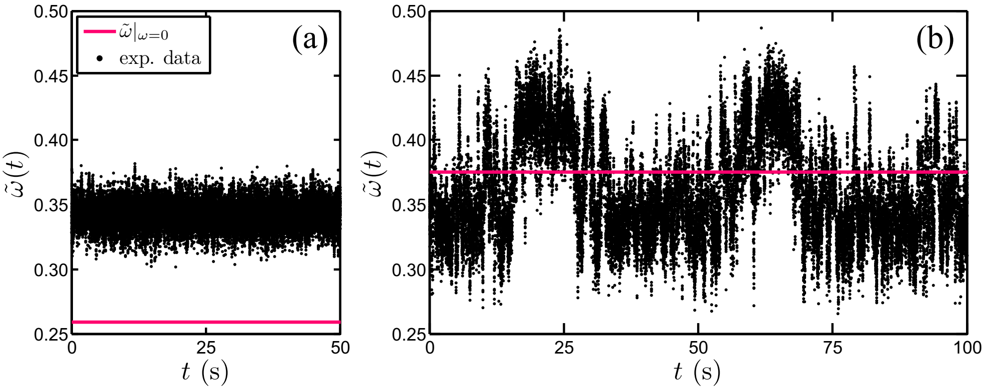

Figure 4.13: Time series of the dimensionless angular velocity $\tilde{\omega}(t)$ as defined in Eq. (4.10) but without t-averaging, acquired with LDA. (a) $a = 0.35$, co-rotation dominates, at $\tilde{r} = 0.60$ with an average data rate of 456 Hz. (b) $a = 0.60$, counter-rotation dominates, same $\tilde{r} = 0.60$ with an average data rate of 312 Hz. Figure (a) shows a unimodal velocity distribution whereas (b) reveals a bimodal distribution interpreted as caused by intermittent bursts out of the unstable inner regime with angular velocity between ω_i and $\omega = 0$, i.e. $(\omega_o - 0)/(\omega_o - \omega_i) < \tilde{\omega} < 1$ into the stable outer regime with angular velocity between $\omega = 0$ and ω_0, i.e. $0 < \tilde{\omega} < (\omega_o - 0)/(\omega_o - \omega_i)$. The solid pink line indicates the neutral line $\omega = 0$, corresponding to $\tilde{\omega} = \omega_o/(\omega_o - \omega_i) = a/(1+a)$, for the specific a.

Further details on the two observed individual modes such as their mean and their mixing coefficient are given in Figs. 4.17 (for $a = 0.60$) and 4.18 (for $a = 0.70$), both well beyond a_{opt}. In both cases one observes that the contribution from the large-ω-mode (red curve, $\omega > 0$, apart from positions close to the outer cylinder) is as expected highest at the inner cylinder and fades away when going outwards, whereas the small-ω-mode has the reverse trend. Note however that even at $\tilde{r} = 0.20$, e.g. relatively close to the inner cylinder, there are moments for which ω is negative, i.e. patches of stabilized liquids are advected inwards, just as patches of turbulent flow are advected outwards.

This mechanism resembles the angular velocity exchange mechanism suggested by Coughlin & Marcus [98] just beyond onset of turbulence. These authors suggest that for the counter-rotating case there is an outer region which is centrifugally stable, but subcritically unstable, thus vulnerable to distortions coming from the centrifugally unstable inner region. Inner and outer region are separated by the neutral line. For the low *Re* of Coughlin & Marcus [98] the inner region is not yet turbulent, but displays interpenetrating spirals, i.e. a chaotic flow with various spiral Taylor vortices. For our much larger Reynolds numbers the inner flow will be turbulent and the distortions propagating into the subcritically unstable outer regime will be turbulent bursts. These then will lead to intermittent instabilities in the outer regime. In future work these speculations must further be quantified.

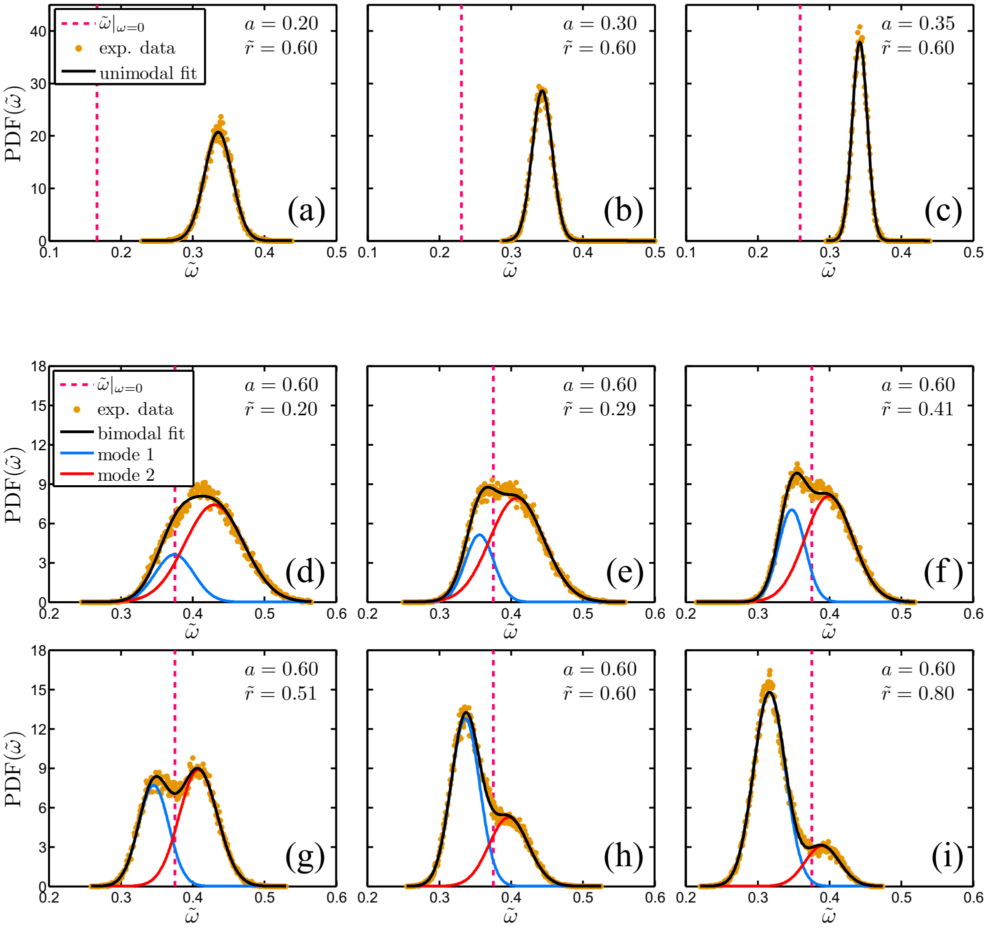

Figure 4.14: Probability density functions of the angular velocity $\tilde{\omega}(t)$ distributions for various cases of a and position $\tilde{r} = (r - r_i)/(r_o - r_i)$. (a) $a = 0.20$, $\tilde{r} = 0.60$, (b) $a = 0.30$, $\tilde{r} = 0.60$, and (c) $a = 0.35$, $\tilde{r} = 0.60$. The other panels all show $a = 0.60$ but at different non-dimensional gap distances $\tilde{r}$. (d) 0.20, (e) 0.29, (f) 0.41, (g) 0.51, (h) 0.60, and (i) 0.80. The gold circles indicate the measured distribution obtained by LDA. While for (a), (b), and (c) one Gaussian distribution (black solid curve) describes the data well, for (e) to (i) a superposition of two Gaussians is needed for a good fit (blue and red curves). We call the two Gaussians the two “modes” of the flow. The fitting algorithm gives the mean, the standard deviation, and the mixture coefficient of modes 1 and 2, which recombine to the black solid line, describing the measured distribution well. The dashed pink vertical line shows the neutral line $\omega = 0$, implying $\tilde{\omega} = \omega_o/(\omega_o - \omega_i) = a/(1 + a)$.

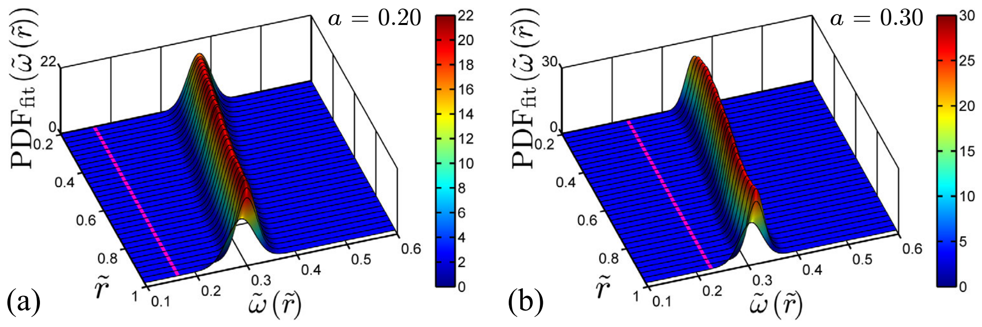

Figure 4.15: Three-dimensional visualization of the (normalized) angular velocity PDF with a contiuous scan of $\tilde{r}$ for two unimodal cases (a) $a = 0.20$ and (b) $a = 0.30$, both being smaller than $a_{opt} = 0.368$. The pink line corresponds to the neutral line $\omega = 0$, i.e. $\tilde{\omega} = \omega_o/(\omega_o - \omega_i) = a/(1+a)$.

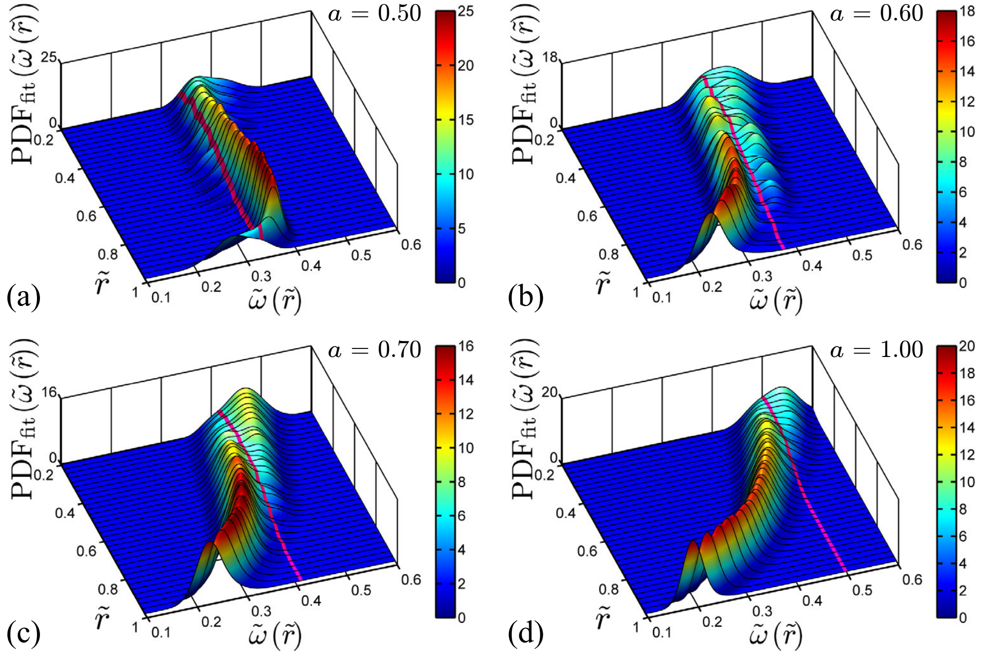

Figure 4.16: Same as in Fig. 4.15, but now for the bimodal cases $a > a_{opt} = 0.368$. (a) $a = 0.50$, (b) $a = 0.60$, (c) $a = 0.70$, and (d) $a = 1.00$. The bimodal character with one mode being left of the neutral line $\omega = 0$ and the other mode being right of the neutral line becomes particularly clear for (b) and (c).

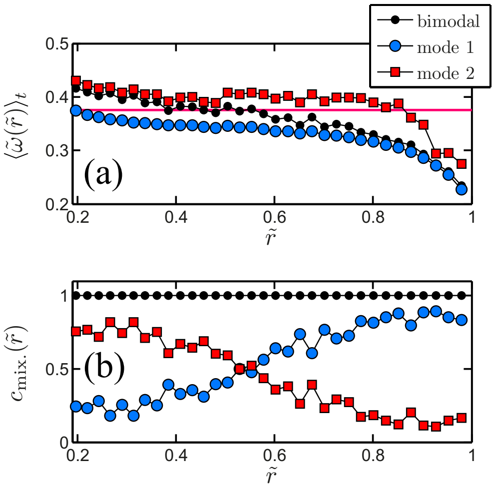

Figure 4.17: (a) The time-averaged, normalized angular velocity $\langle\tilde{\omega}(\tilde{r},t)\rangle_t$ (black symbols) and of the two individual modes (blue and red) for $a = 0.60$. (b) The mixing coefficient, showing the relative weight of the respective mode.

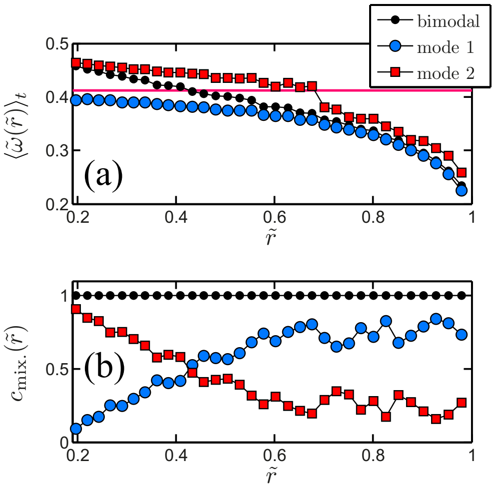

Figure 4.18: Same as in Fig. 4.17, but now for $a = 0.70$.

4.6 Boundary layers

Our LDA measurements also offer the opportunity to estimate the thickness of the boundary layers for the various control parameters a. Figure 4.19b shows the measured time-means $\langle\omega(\tilde{r})\rangle_t$ in the bulk as functions of $\tilde{r}$ in the interval $0.2 < \tilde{r} < 0.8$ for the (Ta, a) control parameter combinations of Fig. 4.4. As mentioned above, the BLs presently cannot be resolved with LDA measurements. However, nonetheless we can estimate the BL thicknesses, as on the one hand the angular velocity values at $\tilde{r} = 0$ (inner wall) and $\tilde{r} = 1$ (outer wall) are known, namely ω_i and ω_o, respectively, and on the other hand from our global measurements of the torque we know the ω-slopes, i.e. the gradients $\partial_r\langle\omega\rangle_{A,t}$ at the walls, namely from equation (4.5): At the inner wall $\tilde{r} = 0$ and the outer one $\tilde{r} = 1$ only the second, viscous term of the transport current contributes to J^ω and thus to Nu_ω. Therefore from the measured global Nu_ω we can derive the mean gradients of the ω-profile at the walls. Here, possible axial dependencies are neglected, which is justified at these high Ta, see Huisman *et al.* [95]. Figures 4.19a and c show how the linear extrapolations of the measured azimuthal velocity $u_\phi(r) = \langle\omega(r)\rangle \cdot r$ profiles in the bulk cross the extrapolations from the respective walls, resulting in kinetic boundary layer thicknesses λ_o^ω and λ_i^ω at the inner and outer wall, respectively.

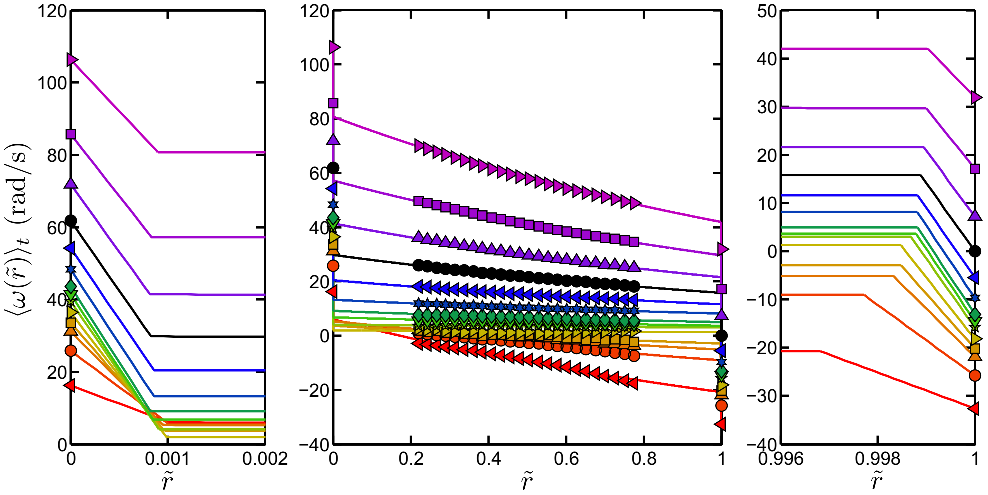

Figure 4.19: Time-averaged angular velocity $\langle \omega(\tilde{r}) \rangle_t$ for the various (Ta, a) of Fig. 4.4, see that figure for the color-code. The bulk values in (b) are obtained from our LDA measurements and are linearly extrapolated in azimuthal velocity $u_\phi = \omega r$ -space to the inner (a) and outer (c) cylinders, whose angular velocity is ω_i and ω_o, respectively. Since also the angular velocity gradients at the walls are known from the global Nu_ω measurements via Eq. (4.5), one can estimate the thicknesses λ_i^ω and λ_o^ω of the inner and outer kinematic BLs, i.e. the BL widths of the azimuthal motion.

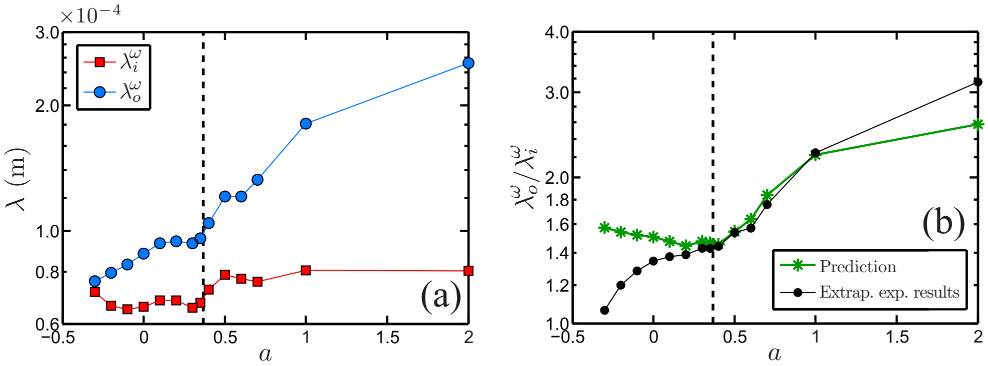

Figure 4.20: (a) Inner and outer viscous BL thicknesses λ_i^ω and λ_o^ω, respectively, as derived with the procedure sketched in the caption of Fig. 4.19. Note that Ta is not constant for the data points shown in this figure; the connecting lines are guides for the eyes. The respective Ta values are indicated in Fig. 4.4. – (b) Ratio $\lambda_o^\omega / \lambda_i^\omega$ for the extrapolated experimental results shown in (a) (solid black dots) and for the prediction given by Eq. (4.13) (green stars).

These thicknesses are shown in Fig. 4.20a. As expected, the outer boundary layer is much thicker than the inner one. This is an immediate consequence of equation (4.5), which leads to the relation $r_i^3 \partial_r \langle \omega(r_i) \rangle = r_o^3 \partial_r \langle \omega(r_o) \rangle$ for the slopes. The inner cylinder angular velocity profile slope thus is $\partial_r \langle \omega(r_i) \rangle = \eta^{-3} \partial_r \langle \omega(r_o) \rangle$. Thus for $\eta = 0.716$ the inner cylinder ω-profile slope is 2.724 times steeper as the outer cylinder one, leading to the correspondingly thinner BL at the inner cylinder. As Fig. 4.20a shows, the inner cylinder BL thickness hardly shows any a-dependence, while the outer cylinder BL width increases considerably with increasing degree of counter-rotation, viz. increasing a. Note that along the curves of Fig. 4.20a the Taylor number Ta is not constant. Therefore, in Fig. 4.20b we also show the ratio $\lambda_o^\omega / \lambda_i^\omega$ versus a, i.e. with increasing counter-rotation. In this figure we have also plotted the prediction for this thickness-ratio obtained from the EGL theory,

$$\frac{\lambda_o^\omega}{\lambda_i^\omega} = \eta^{-3} \frac{|\omega_o - \bar{\omega}|}{|\omega_i - \bar{\omega}|}. \tag{4.13}$$

According to the EGL theory $\bar{\omega}$ is the mean bulk angular velocity, here taken as the measured angular velocity averaged over the bulk ranging from $0.2 < \tilde{r} < 0.8$, i.e. $\bar{\omega} = \langle \bar{\omega}_{\text{center}} \rangle_t$. The EGL prediction nicely agrees with the measured data for $0.2 \lesssim a \lesssim 1$. For smaller control parameters $a \lesssim 0.2$, i.e., in the regime of co-rotation or very weak counter-rotation there is some disagreement. This might reflect the short-comings of our present extrapolation method to determine the BL thicknesses; in fact, given the crudeness of the method we consider the good agreement in the range $0.2 \leq a \leq 1$ more remarkable than the worse agreement in the other a-ranges. But it could also be another indication of the fundamental difference of the flow space below or above a_{opt}: as shown above there is mono-modal turbulence in the fully unstable gap for $a < a_{opt}$, in contrast to bi-modal flow in an only partly unstable (inner part) and partly stable (outer part) gap. Also for $a < a_{opt}$ as well as far above the optimum $a \gg a_{opt}$ the ω-profile has no longer zero slope in the bulk. The differences between both curves in Fig. 4.20b might well reflect this.

To understand the disagreement we study a different representation of $\bar{\omega}$, as shown in Fig. 4.21. We define a new $\langle \bar{\omega}_{\text{extrap}} \rangle_t$ by assuming Eq. (4.13) to hold for all a and by filling in the boundary layer ratio as found by the extrapolation method. There is good agreement between $\langle \bar{\omega}_{\text{center}} \rangle_t$ and $\langle \bar{\omega}_{\text{extrap}} \rangle_t$ in the range $0.2 \leq a \leq 1$ and the agreement is getting worse for other a-ranges, similar to the result in Fig. 4.20b. This might be explained by the larger angular velocity gradient in this a-range as shown in Fig. 4.10a. If the boundary layer thickness ratio as proposed by the EGL theory always holds, what then should the corresponding radial location $\tilde{r}|_{\langle \omega(\tilde{r}) \rangle_t = \langle \bar{\omega}_{\text{extrap}} \rangle_t}$ be to match $\bar{\omega}$. Figure 4.21b shows the corresponding radial location at which the measured angular velocity satisfies Eq. (4.13) as a function of a. Clearly it is different from $\tilde{r} = 0.5$ and the radial position strongly depends on a. This has to do with the non-Oberbeck-Boussinesq (NOB) effect of TC flow, which is analogous

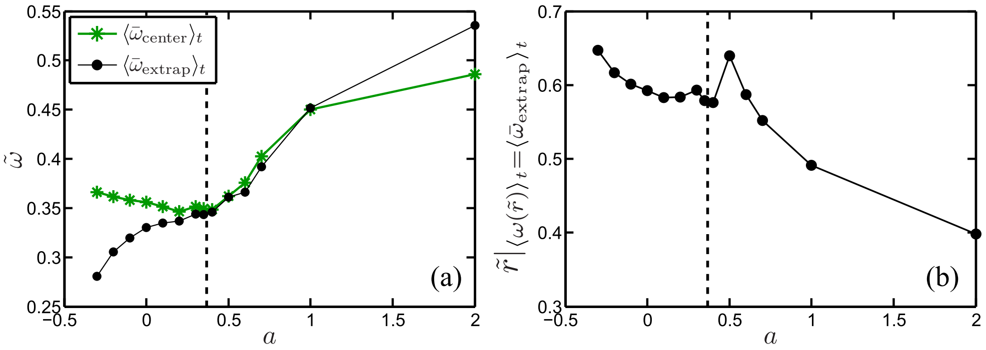

Figure 4.21: (a) The rescaled angular velocity versus a. The green stars indicate the measured rescaled angular velocity averaged over the bulk ranging from $0.2 < \tilde{r} < 0.8$. The black circles indicate the rescaled angular velocity extrapolation based on Eq. (4.13) by assuming this relation holds for all a. (b) The radial location at which the measured angular velocity satisfies Eq. (4.13) as a function of a.

to NOB-RB flow, see e.g. Ahlers *et al.* [99, 100], Sugiyama *et al.* [101]. Since TC flow is strongly NOB, the radial location of zero angular velocity gradient is shifted, similar to the bulk temperature shift in NOB-RB. Figure 4.21b quantifies this shift as function of a.

4.7 Summary, discussion, and outlook

In conclusion, we have experimentally explored strongly turbulent TC flow with $Ta > 10^{11}$ in the co- and counter-rotating regimes. We find that in this large Taylor number Ta regime and well off the instability lines the dimensionless angular velocity transport flux within experimental precision can be written as $Nu_\omega(Ta,a) = f(a)\cdot Ta^{\gamma(a)}$ with either $\gamma = 0.39 \pm 0.03$ universally for all a or with a slightly decreasing $\gamma(a)$ when decreasing the counter-rotation below the optimum $a = a_{opt}$. This is the effective scaling exponent of the ultimate regime of TC turbulence predicted by Grossmann & Lohse [26] for RB flow and transferred to TC by the close correspondence between RB and TC according to the EGL theory. When starting off counter-rotation, i.e. when increasing a beyond zero, the angular velocity transport current does not reduce but instead is first further enhanced, due to the enhanced shear, before finally, beyond $a = a_{opt} = 0.368$, the stabilizing effect of the counter-rotation leads to a reduction of the angular velocity transport flux Nu_ω. For optimal counter-rotation $\omega_o = -0.368\omega_i$ the angular velocity transport is maximal; the value of $a_{opt} = 0.368$ is assigned to our present radius ratio $\eta = 0.716$. At this very a-value the mean angular velocity profile was shown to have zero gradient in the bulk for the present large Ta. Despite already significant counter-rotation for $0 < a < a_{opt}$ there is no neutral line outside the outer

BL; furthermore the probability distribution function of the angular velocity has only one mode. For larger a, beyond $a > a_{opt}$, a neutral line can be detected in the bulk and the PDF here becomes bimodal, reflecting intermittent burst of turbulent patches from the turbulent inner r-regime towards the stabilized outer r-regime. We also presented first attempts to estimate the BL thicknesses at the inner and outer cylinder, and in agreement with the theoretical expectation the latter one is much thicker. — We offered a hypothesis which gives a unifying view and consistent understanding of all these various findings.

Clearly, the present study is only the start of a long experimental program to further explore turbulent TC flow. Much more work still must be done. In particular, we mention the following open issues:

- For strong counter-rotation, i.e. large a, the axial dependence must be studied in much more detail. This holds in particular for the location of the neutral line. We expect that for large $a \gg a_{opt}$, the flow will be so much stabilized that an axial dependence of the location of the neutral line shows up again, in spite of the large Ta numbers. It is then more appropriate to speak of a neutral *surface*.
- Modern PIV techniques should enable us to directly resolve the inner and outer BLs.
- With the help of PIV studies we also hope to visualize BL instabilities and thus better understand the dynamics of the flow, in particular in the strongly counter-rotating case. The key question is: How does the flow manage to transport angular velocity from the turbulent inner regime towards the outer cylinder – thereby crossing the stabilized outer regime?
- The studies must be repeated at lower Ta to better understand the transition from weakly turbulent TC towards the ultimate regime as apparently seen in the present work. In our present setup we can achieve such a regime with silicon oil instead of water.
- These studies should be complemented with direct numerical simulation of co- and counter-rotating TC flow. Just as happened in recent years in turbulent RB flow, cf. Stevens *et al.* [39, 102], also for turbulent TC flow we expect to narrow the gap between numerical simulation and experiment or even to close it for not too turbulent cases, allowing for one-to-one comparisons.
- Obviously, our studies must be extended to different η values, in order to check the hypothesis (4.8) and to see how this parameter affects the flow organization.

Clearly, many exciting discoveries and wonderful work with TC flow is ahead of us.

5

Angular momentum transport and turbulence in laboratory models of Keplerian flows* † ‡

We present angular momentum transport (torque) measurements in two recent experimental studies of the turbulent flow between independently rotating cylinders. In addition to these studies, we reanalyze prior torque measurements to expand the range of control parameters for the experimental Taylor-Couette flows. We find that the torque may be described as a product of functions that depend only on the Reynolds number, which describes the turbulent driving intensity, and the rotation number, which characterizes the effects of global rotation. For a given Reynolds number, the global angular momentum transport for Keplerian-like flow profiles is approximately 14% of the maximum achievable transport rate. We estimate that this level of transport would produce an accretion rate of $\dot{M}/\dot{M}_0 \sim 10^{-3}$ *in astrophysical disks. We argue that this level of transport from hydrodynamics alone could be significant.*

---

[*] Submitted to Astron. Astrophys. as: M.S. Paoletti, D.P.M. van Gils, B. Dubrulle, C. Sun, D. Lohse, and D.P. Lathrop, *Angular momentum transport and turbulence in laboratory models of Keplerian flows*.

[†] Experiments were performed on the TC facilities of the University of Maryland (UMD TC facility) and the University of Twente (T^{3}C facility).

[‡] This chapter uses a different notation for the geometric parameters and different non-dimensionalizations from the rest of this thesis as befits the astrophysical community.

5.1 Introduction

Astrophysical disks are ubiquitous in the universe, orbiting around a wide panel of massive objects, from black holes to stars. An essential ingredient of their dynamics is the radial transport of angular momentum that governs the rate of material falling onto the central object. Realistic models of this process are impeded by the complexity of the disk dynamics, including a wide variety of processes such as general relativistic effects, self-gravitation, radiation, dynamics of plasma magnetic fields and turbulence. In particular, the contribution from hydrodynamics to the angular momentum transport in such astrophysical flows is not yet understood.

A natural first-step in the construction of a robust model is to consider the minimal list of ingredients that can capture and reproduce the observed disk properties. Such a model has been proposed several decades ago by Shakura & Sunyaev [103] and Pringle [104], and was given the name α disks. In that model, the radial transport of angular momentum is parameterized by a turbulent viscosity coefficient, that needs to be prescribed, or measured. In the past, there have been a few attempts to measure this coefficient in numerical simulations (Dubrulle [105]).

An alternative promising option, as recognized by Zeldovich [106] and Richard & Zahn [107], is offered by focusing instead on laboratory experiments. Indeed, it may be shown (Hersant *et al.* [108]), that under simple, but well founded approximations, the equations governing an α disk are similar to the equation of motion of an incompressible rotating shear flow, with penetrable boundary conditions and cylindrical geometry. This kind of flow can be achieved in the Taylor-Couette flow (see Fig. 5.1), a fluid layer sheared between two independently rotating, coaxial cylinders.

This remark motivated several experimental studies of the transport properties in the Taylor-Couette flow, with contradicting conclusions. Depending upon the community, the strength of the turbulent transport is quantified in various ways. The most basic quantification (Wendt [5]) is the one through the torque T which is necessary to keep the inner cylinder rotating at a given velocity. The dimensionless version thereof is $G = T/(L_{mid}\rho\nu^2)$, where ρ is the fluid density, ν its kinematic viscosity and L_{mid} the effective length of the cylinders (Paoletti & Lathrop [18]). Eckhardt *et al.* [23] and van Gils *et al.* [88] used $Nu_\omega = G/G_{\mathrm{lam}}$, where G_{lam} is the laminar torque, to quantify the angular velocity flux from the inner to the outer cylinder, in order to highlight the analogy between Taylor-Couette and Rayleigh-Bénard flow (Dubrulle & Hersant [22], Eckhardt *et al.* [23, 82]). The engineering community prefers the drag-coefficient $c_f = G/Re^2$, where $Re = \frac{2}{1+\eta}|\eta Re_2 - Re_1|$ and $\eta = a/b$ is the radius ratio and $Re_{1/2}$ the Reynolds number of the inner/outer cylinder. In the astrophysics community, the same information is often expressed in terms of the β coefficient, defined by $\beta = 2G\eta^2/(\pi(1-\eta)^4 Re^2) = 2\eta^2 c_f/(\pi(1-\eta)^4)$, which can be interpreted as a dimensionless turbulent viscosity.

By reexamining previous data obtained by Wendt [5] and Taylor [6], Richard &

Zahn [107] showed that the β-parameter is on the order of $\beta_{RZ} \sim 10^{-5}$ for Keplerian disks. A more complete analysis, including results of new experiments on a classical Taylor-Couette flow from Richard [86], led to the same conclusion (Dubrulle *et al.* [75]). In contrast, an original experiment, built in Princeton (Ji *et al.* [109]) so as to minimize end effects, measured a β coefficient through radial Reynolds stresses and obtained a value smaller by more than an order of magnitude $\beta_P \sim 7 \times 10^{-7}$. Furthermore, the Princeton experiments could not distinguish the angular momentum transport in Keplerian flows from their measurements in solid-body rotation, where the cylinders rotate together thereby resulting in zero angular momentum transport.

In the present contribution, we report precise angular momentum transport (torque) measurements in two independent experiments performed at very large Reynolds number and compute the resulting β coefficient for different rotation profiles. To further study the scaling of angular momentum transport in rotating shear flows, we compare our measurements to those of Wendt [5], Taylor [6], Richard [86], and Dubrulle *et al.* [75]. We find a universal scaling of the torque for various rotation profiles that captures the effects of the various geometries used in the experiments summarized here.

5.2 Apparatus and experimental details

5.2.1 Apparatus: generalities

The experiments presented here all examine the transport of angular momentum (torque) in classical Taylor-Couette flow. Figure 5.1 shows a schematic representation of our experiments. The fluid is contained between concentric cylinders of radii $a < b$. The inner (outer) cylinder rotates at an angular velocity of Ω_1 (Ω_2). The overall height of the fluid contained between the axial boundaries is given by the length L. The geometry of a particular Taylor-Couette flow apparatus is often defined in dimensionless form by the radius ratio $\eta \equiv a/b$ and the aspect ratio $\Gamma \equiv L/(b-a)$.

The ideal Couette flow is infinite in axial extent. As such, several methods have been employed to handle the finite-size effects that are present in any laboratory experiment. The most common case has the axial boundaries rotate with one of the two cylinders. In other experiments, the axial boundaries are divided at the mid-gap and have the inner (outer) portion rotate with the inner (outer) cylinder. This split-ring approach has been further developed to allow for pairs of rings that can independently rotate with respect to the cylinders. Allowing the axial boundaries to independently rotate aids in the suppression of finite-size effects as detailed in Ji *et al.* [109], Schartman *et al.* [110], Burin *et al.* [111].

The data that we analyze and present stems from several different experiments, which are summarized in Table 5.1. The early experiments by Wendt [5] measured the torque required to drive the inner cylinder for three values of η. The system had

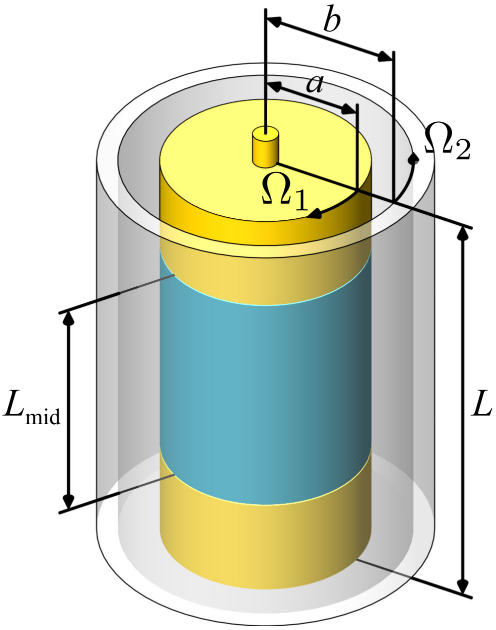

Figure 5.1: Taylor-Couette flow may be used to study angular momentum transport in rotating shear flows. The fluid is sheared between two independently rotating cylinders of radii $a < b$ that rotate at angular velocities Ω_1 and Ω_2 for the inner and outer cylinders, respectively. Although the total fluid height is given by L, some experiments only measure the contribution to the torque over a central section of length L_{mid} to minimize end effects, as in Lathrop *et al.* [10, 11], Lewis & Swinney [14], van den Berg *et al.* [15], Paoletti & Lathrop [18], van den Berg *et al.* [27, 61], van Gils *et al.* [88].

Table 5.1: A summary of the parameters used in the experiments discussed here. The geometry of the apparatus is given by the outer cylinder radius b, the radius ratio $\eta = a/b$ and the aspect ratio $\Gamma = L/(b-a)$. The range of turbulence intensities are governed by the inner and outer cylinder Reynolds numbers Re_1 and Re_2. The effects of rotation are parameterized by the rotation number R_Ω introduced by Dubrulle *et al.* [75].

Experiment	b (cm)	η	Γ	max(Re_1)	max(Re_2)	min(R_Ω)	max(R_Ω)
Wendt [5]	14.7	0.68	10.64	8.47×10^4	1.24×10^5	-0.71	0.47
Wendt [5]	14.7	0.85	22.93	4.95×10^4	5.83×10^4	-0.80	0.18
Wendt [5]	14.7	0.935	52.63	2.35×10^4	2.52×10^4	-0.42	0.11
Taylor [6]	8.11	0.79–0.973	50–384	0	1.08×10^5	0.03	0.27
Richard [86]	5.00	0.72	27.18	9.50×10^4	1.30×10^5	-1.43	-0.94
Richard [86]	5.00	0.72	27.18	9.50×10^4	1.30×10^5	0.38	0.58
Ji *et al.* [109]	20.3	0.35	2.1	1.20×10^6	4.50×10^5	-1.67	-1.08
Maryland	22.09	0.725	11.47	3.70×10^6	1.50×10^6	-2.04	1.46
Twente	27.9	0.716	11.68	2.00×10^6	1.40×10^6	-0.74	0.17

a free surface at the top, although we quote an effective aspect ratio defined using the axial length of the apparatus. The data from Taylor [6] determined the scaling of the torque for several values of η with the inner cylinder stationary ($\Omega_1 = 0$). Richard's experiments [75, 86] did not directly measure the torque. Instead, critical Reynolds numbers for various transitions were observed and the analysis presented by Dubrulle *et al.* [75] was used to estimate the corresponding torque. We do not present data from the experiments of Ji *et al.* [109], but rather use their reported measurements as a basis for comparison, as detailed in Section 5.4. The two most recent experiments by Paoletti & Lathrop [18] and van Gils *et al.* [88] are further described in the forthcoming sections.

5.2.2 Apparatus: the Maryland experiment

The experiments presented by Paoletti & Lathrop [18], henceforth referred to as the Maryland experiment, are conducted in the apparatus constructed by Lathrop *et al.* [10, 11], which was modified to allow the outer cylinder to rotate independently. The outer cylinder is an anodized aluminum cylinder with the same physical dimensions as in Lathrop *et al.* [10, 11], Lewis & Swinney [14], specifically $b = 22.085$ cm and a working fluid height $L = 69.50$ cm. The inner cylinder is stainless steel with a radius $a = 16.000$ cm yielding a radius ratio $\eta = 0.7245$ and an aspect ratio $\Gamma = 11.47$. The inner cylinder is rotated up to $\Omega_1/2\pi = 20\ \mathrm{s}^{-1}$ while the outer cylinder may be rotated in either direction up to $|\Omega_2/2\pi| = 10\ \mathrm{s}^{-1}$. Both angular velocities are measured by shaft encoders and controlled to within 0.2% of the set value.

The axial boundaries in the Maryland experiment rotate with the outer cylinder. To reduce end effects in the torque measurements the inner cylinder is divided axially into three sections of length 15.69, 40.64 and 15.69 cm (see schematics in Lathrop *et al.* [10, 11]). Only the central section of length $L_{\mathrm{mid}} = 40.64$ cm (see Fig. 5.1) senses the torque of the fluid as described by Lathrop *et al.* [10, 11]. The regions 2.58 gap widths from each of the axial boundaries, where secondary circulation setup by finite boundaries is strongest, are avoided in the torque measurements.

The desired accuracy of our measurements requires that the temperature of the water be precisely controlled. In contrast to prior experiments (Lathrop *et al.* [10, 11], Lewis & Swinney [14], van den Berg *et al.* [15, 27, 61], van Gils *et al.* [88]) where the system was cooled at the axial boundaries, we control the temperature of the water by heating and cooling the outer cylinder. This allows the working fluid to be temperature-controlled along the entire axial length of the experiment, yielding a 6.5 fold increase in the temperature-controlled surface area. This is particularly important for Rayleigh-stable flows, where mixing is greatly reduced. In our experiments the temperature is 50 ± 0.02°C yielding a kinematic fluid viscosity of $\nu = 5.5 \times 10^{-3}\ \mathrm{cm}^2/\mathrm{s}$, except for $Re > 2 \times 10^6$ where $T = 90\ ^\circ\mathrm{C}$ and $\nu = 3.2 \times 10^{-3}\ \mathrm{cm}^2/\mathrm{s}$.

5.2.3 Apparatus: the Twente experiment

The Twente turbulent Taylor-Couette (called T^{3}C) facility, here referred to as the Twente experiment, is described in great detail by van Gils *et al.* [112]. In short, the working fluid height is $L = 92.7$ cm, has an inner radius of $a = 20.0$ cm and an outer radius of $b = 27.94$ cm. The maximum inner and outer angular velocities are $\Omega_1/2\pi = 20$ Hz and $|\Omega_2/2\pi| = 10$ Hz, respectively. The system is fully temperature controlled through cooling of the upper and lower end plates, which co-rotate with the outer cylinder. The system is operated with water at a temperature of 20 °C, resulting in a kinematic viscosity of $\nu = 1.04 \times 10^{-2}$ cm^2/s. The torque is measured over the middle part of the inner cylinder of height $L_{\mathrm{mid}} = 53.6$ cm to minimize the influence of the end-plates (similar to Lathrop *et al.* [10, 11]). The torque is measured by a load cell imbedded inside the middle section of the inner cylinder in both the Twente and Maryland experiments, in contrast to measuring the torque on the drive shaft that would be affected by mechanical seals in the end plates or by velocimetry measurements, as in the Princeton experiments (Ji *et al.* [109], Schartman *et al.* [110], Burin *et al.* [111], Schartman *et al.* [113]).

5.2.4 Control parameters

The analysis of our results is simplified by a proper choice of the control parameters. As in Dubrulle *et al.* [75], we use the following three dimensionless control parameters, which fully describe the geometry and specify the state of the dynamical Taylor-Couette system:

$$Re = \frac{2}{1+\eta}|\eta Re_2 - Re_1|, \tag{5.1}$$

$$R_\Omega = (1-\eta)\frac{Re_1 + Re_2}{\eta Re_2 - Re_1}, \tag{5.2}$$

$$R_C = \frac{1-\eta}{\eta^{1/2}}, \tag{5.3}$$

where $Re_1 = a\Omega_1 d/\nu$ and $Re_2 = b\Omega_2 d/\nu$ are the Reynolds number of the inner and outer cylinder and $d = (b-a)$ is the gap width.

The above control parameters have been introduced so that their definitions apply to rotating shear flows in general and not strictly only to the Taylor-Couette geometry. It is very easy in this formulation to relate the Taylor-Couette flow to the shearing sheet (plane Couette flow with rotation), by considering the limit $R_C \to 0$. The linear stability properties of the fluid can also be neatly recast using these control parameters. In the inviscid limit ($Re \to \infty$), and for axisymmetric disturbances, the linear stability properties of the flow are governed by the Rayleigh criterion, namely that

Table 5.2: A summary of the Taylor-Couette control parameters related to some astrophysical disks, as computed by Hersant *et al.* [108]. Here, b is the disk's outer radius, and $\dot{M}$ the accretion rate.

Central object	b (a.u.)	η	Γ	$\max(Re_1)$	$\max(Re_2)$	R_Ω	$\dot{M}/\dot{M}_0$
TTauri	1000	0	0.94	10^{12}	10^{14}	-1.33	$10^{-5}-10^{-2}$
FuOri	5	0	0.94	10^{13}	10^{15}	-1.33	0.1-1

the fluid is stable if the Rayleigh discriminant is everywhere positive:

$$\frac{\Omega}{r}\partial_r L(r) > 0, \tag{5.4}$$

where $L(r) = r^2\Omega(r)$ is the specific angular momentum. Applying this criterion to the laminar profile leads to

$$(R_\Omega + 1)(R_\Omega + 1 - ab/r^2) > 0. \tag{5.5}$$

Since ab/r^2 varies between $1/\eta$ and η, one obtains that in the inviscid limit, the flow is unstable against infinitesimal axisymmetric disturbances when $R_\Omega^{\infty -} < R_\Omega < R_\Omega^{\infty +}$, where $R_\Omega^{\infty -} = -1$, respectively $R_\Omega^{\infty +} = 1/\eta - 1$, are the marginal stability thresholds in the inviscid limit (superscript ∞) in the cyclonic case ($R_\Omega > 0$, subscript $+$), and anticyclonic case ($R_\Omega < 0$, subscript $-$). This means that, in the anticyclonic case, any flow such that $R_\Omega < -1$ is linearly stable against axisymmetric disturbances. However, it may be non-linearly stable or unstable against non-axisymmetric disturbances, as found in the experiments described here.

In the present paper, we determine the intensity of the momentum transport by measuring the torque required to drive the inner cylinder for a given set of parameters (Re, R_Ω). Measurements described here suggest that at large enough Reynolds number, the nondimensional torque $G = T/(\rho\nu^2 L_{\mathrm{mid}})$, where T is the torque, ρ the fluid density, ν the kinematic viscosity and L_{mid} is defined in Fig. 5.1, varies approximately as $G \sim Re^\alpha$ with $1.75 < \alpha(Re) < 1.85$, even for Rayleigh-stable flows. We note that these exponents are less than a simple dimensional argument would give: Such an argument would say that in a fully turbulent regime the transport properties could not depend on the molecular viscosity, which would imply that the quantity $c_f \sim G/Re^2$ is Reynolds number independent. The deviations from $G \sim Re^2$ mean that the viscosity is always relevant for the transport, due to its dominance in the boundary layers. Only when the boundary layers are sufficiently disturbed by introducing wall roughness does one obtain $G \sim Re^2$, as we have shown in our previous work (van den Berg *et al.* [15]).

5.2.5 Astrophysically relevant quantity

In the astrophysical context, one often considers asymptotic angular velocity profiles of the form $\Omega(r) \sim r^{-q}$ where q characterizes the flow. In that case $q = -\partial \ln \Omega / \partial \ln r = -2/R_\Omega$, which relates astrophysical profiles in the control parameters space of Taylor-Couette flows. For Keplerian flow, $q = 3/2$ resulting in $R_\Omega = -4/3$, which is an example of a linearly stable, anticyclonic flow. While Keplerian profiles cannot be precisely achieved by Taylor-Couette flows, states with $R_\Omega < -1$ are all linearly stable, anticyclonic flows that may be used to approximate astrophysical settings. We will refer to cases with $R_\Omega < -1$ as quasi-Keplerian, as in Ji *et al.* [109].

Astrophysical disks are very wide with $a \ll b$. Therefore, their geometrical global value of $R_C \to \infty$. In a *local* description of disks, one often considers the shearing sheet approximation, in which $\eta \to 1$, so that $R_C \to 0$, as in plane-Couette flow. Here, we focus on global properties and consider only the limit $\eta = 0$ applicable to disks in the discussion. As a result of their astronomical size, the Reynolds numbers associated with accretion disks are very large. To give a few specific examples, parameters for typical TTauri and FuOri stars have been computed by Hersant *et al.* [108] and are given in Table 5.2.

In disks, angular momentum transport intensity is quantified through the accretion rate $\dot{M}$. In fact, as was shown by Dubrulle *et al.* [75], Hersant *et al.* [108], that this rate is directly related to the turbulent viscosity and the dimensionless torque through:

$$\frac{G}{Re^2} = \frac{\pi}{2R_C^4}\beta = \frac{\dot{M}}{\dot{M}_0}, \tag{5.6}$$

where β is a turbulent viscosity parameter such that $\nu_t = \beta S r^2$, with S a velocity shear, and $\dot{M}_0$ is an effective accretion rate given by the mean surface density $\bar{\Sigma}$, the disk inner radius r_* and the mean disk height $\bar{H}$ through

$$\dot{M}_0 = \bar{\Sigma} r_* \bar{r} \bar{\Omega} \left(\frac{\bar{H}}{\bar{r}}\right)^4. \tag{5.7}$$

As such, measurements of G/Re^2 in laboratory experiments may be used to estimate the hydrodynamical contribution to angular momentum transport in accretion disks.

5.3 Results

We study the scaling of the dimensionless torque G over a range of Reynolds numbers for various constant rotation numbers (see Fig. 5.2), spanning a wide variety of flow states, from anticyclonic flows to cyclonic flows. Corresponding torque measurements from the Twente experiment are shown as red squares in Fig. 5.3 while the data from Maryland are represented by black circles.

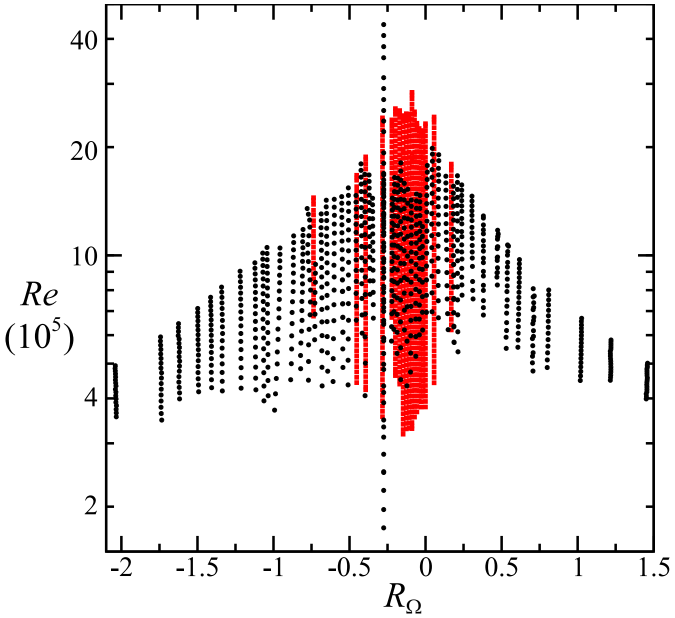

Figure 5.2: Our experiments span a large range of the Reynolds number Re, which controls the turbulence intensity, and the rotation number R_Ω, introduced by Dubrulle *et al.* [75], which compares shear to overall rotation. The rotation number can be used to distinguish between Rayleigh-stable flows ($R_\Omega \leq -1$ or $R_\Omega \leq (1-\eta)/\eta$) and those that are linearly unstable ($-1 < R_\Omega < (1-\eta)/\eta$). The data are taken from separate experiments by van Gils *et al.* [88] (red squares) and Paoletti & Lathrop [18] (black circles).

5.3.1 Existence of turbulence

In laminar flow, angular momentum is transported only by molecular viscosity, so that the dimensionless torque G is proportional to Re, with the prefactor depending upon R_Ω. In Fig. 5.3, we show the expected laminar angular momentum transport (blue line) for the range of Re explored in this study for the case $\Omega_2 = 0$. As can be seen all the torque measurements considered differ from the theoretical expectation for laminar flow in two ways: (*i*) they increase faster than Re and (*ii*) they are much higher than the theoretical laminar value. This is an indication that the fluid is turbulent, with enhanced angular momentum transport in all the cases reported here. Note that these cases encompass several situations with $R_\Omega < -1$ (anticyclonic flow) and $R_\Omega > 0.4$ (cyclonic flow).

In particular, (approximate) Keplerian flows at $R_\Omega = -4/3$ are turbulent at $Re \sim 10^5$ in our experiments. This is in agreement with direct, visual observations of Richard [86], performed at somewhat lower Reynolds number. We argue that this indicates that quasi-Keplerian flows can efficiently transport angular momentum in spite of their linear stability. However, the nature of this nonlinear instability remains unclear. We suggest that systematically perturbing quasi-Keplerian flow states at lower values of *Re* while measuring the torque, as in the experiments by Taylor [6], could aid in the description of this likely nonlinear instability.

5.3.2 Enhancement of momentum transport

We now try to quantify the enhancement of angular momentum transport with respect to its laminar value, as a function of both *Re* and R_Ω. As in Paoletti & Lathrop [18], van Gils *et al.* [88], the torque at a given *Re* may be either increased or reduced depending upon R_Ω; the Reynolds number alone is insufficient to describe the transport.

Variation with R_Ω

Paoletti & Lathrop [18] observed that variation of the torque at a given *Re* shows a pronounced maximum as a function of R_Ω. An analogous dependence of the amplitude of an effective power-law scaling was also observed by van Gils *et al.* [88]. To determine the effects of global rotation, we normalize G for each *Re* by $G(Re, R_\Omega = 0)$ (Dubrulle *et al.* [75]), which we denote as G_0. The dependence of G/G_0 on R_Ω is shown in Fig. 5.5 with the data from Maryland shown as black circles and Twente in red squares.

The agreement between the Twente and Maryland measurements is an important check, but not surprising given that the experiments have very similar geometries, measurement techniques and control parameters (see Table 5.1). Therefore, it remains unclear if the scaling of the normalized torque with R_Ω is universal or if it depends upon other parameters, such as the radius ratio η. While the Twente experiment is capable of examining other values of η in future measurements, we may compare our results to previous experiments by Wendt [5], Taylor [6] and Richard [86], which were analyzed by Dubrulle *et al.* [75]. The parameters of these past experiments are also summarized in Table 5.1. The measurements of Wendt (triangles), Taylor (orange diamonds) and Richard (magenta squares) are also shown in Fig. 5.4(a).

As can be seen in Fig. 5.4, the dependence of the normalized torque G/G_0 on R_Ω for various radius ratios in the range $0.68 \le \eta \le 0.973$ collapse well. The data appear to follow distinct approximate scalings given by

$$f(R_\Omega) = \begin{cases} 0.18 \pm 0.06 & : R_\Omega \le -1 \\ 1.79R_\Omega + 0.05e^{-4.35R_\Omega} + 1.59 & : -1 < R_\Omega \le -0.10 \\ -7.35R_\Omega + 1.49e^{2.28R_\Omega} - 0.51 & : -0.10 < R_\Omega < 0.32 \\ -0.13R_\Omega + 0.26 & : R_\Omega \ge 0.32 \end{cases} \tag{5.8}$$

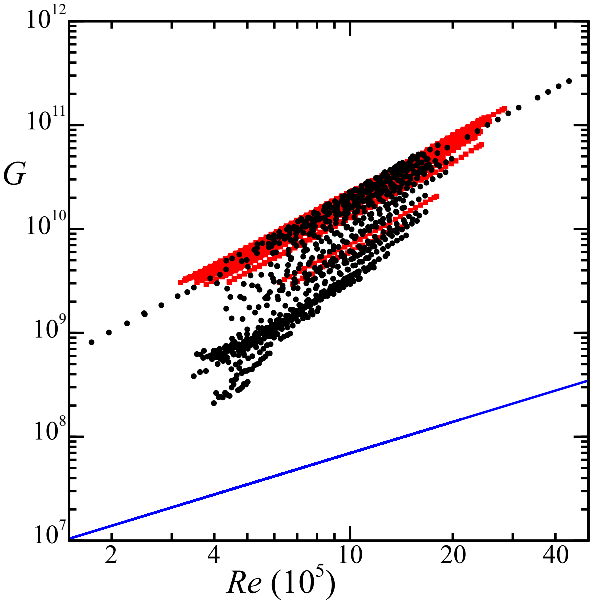

Figure 5.3: The scaling of the dimensionless torque G with the Reynolds number Re is independent of the rotation number R_Ω, however the amplitude varies as in Paoletti & Lathrop [18], van Gils *et al.* [88]. The measurements by Paoletti & Lathrop [18] are in black circles while the data from van Gils *et al.* [88] are shown by red squares. The thick blue line indicates the theoretical value for purely laminar flow, where angular momentum is transported only by molecular viscosity.

Given the rather different span of Re in each experiment and the varying measurement techniques, it is not surprising that a few outliers remain. For example, the values of G/G_0 from Richard's experiments [86] (magenta squares) were computed using theoretical predictions regarding the correlation between the torque and critical numbers for stability, as described in Dubrulle *et al.* [75]. The data from Wendt [5], Taylor [6], Paoletti & Lathrop [18] and van Gils *et al.* [88] are direct measurements of the torque, albeit with different apparati and measurement techniques.

Variation with Reynolds number

The fits given in Eq. (5.8) may be used to compensate the torque to account for the effects of global rotation. Figure 5.5 shows the dimensionless torque G compensated by the fit $f(R_\Omega)$ given in Eq. (5.8) as a function of Re. The data from Twente are shown as red squares while those of Maryland are given by black circles. In both cases, the data agree well with the best fit given by Lewis & Swinney [14] for the case $\Omega_2 = 0$ (blue line). This indicates that the amplitude of the torque is affected by global

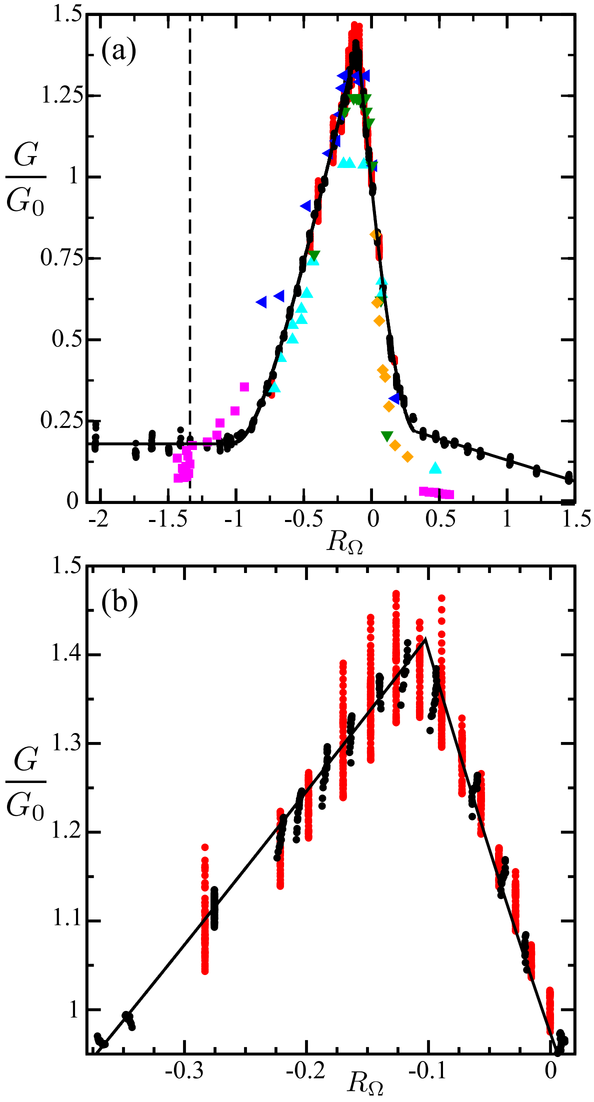

Figure 5.4: (a) The dimensionless torque G normalized by $G_0 \equiv G(Re, R_\Omega = 0)$ for different values of the radius ratio η nicely collapses when plotted as function of R_Ω. This normalization is different from Fig. 16 in Dubrulle *et al.* [75] where G is normalized by $G_\infty \equiv G(Re, \Omega_2 = 0)$. The data from Wendt [5] are shown as cyan ($\eta = 0.68$), blue ($\eta = 0.85$) and green ($\eta = 0.935$) triangles. Additional radius ratios are examined using the data from Taylor [6], shown as orange diamonds, Richard [75, 86], given by magenta squares, Paoletti & Lathrop [18] indicated by black circles and van Gils *et al.* [88] by red circles. The solid lines are fits given by Eq. (5.8) with smoothened transitions between the 4 regimes. Keplerian flow states are indicated by the dashed line at $R_\Omega = -4/3$. In (b) we focus on the peak of the curve shown in (a), but only present the data from Twente (van Gils *et al.* [88]) (red) and Maryland (Paoletti & Lathrop [18]) (black). The solid line is the fit (5.8).

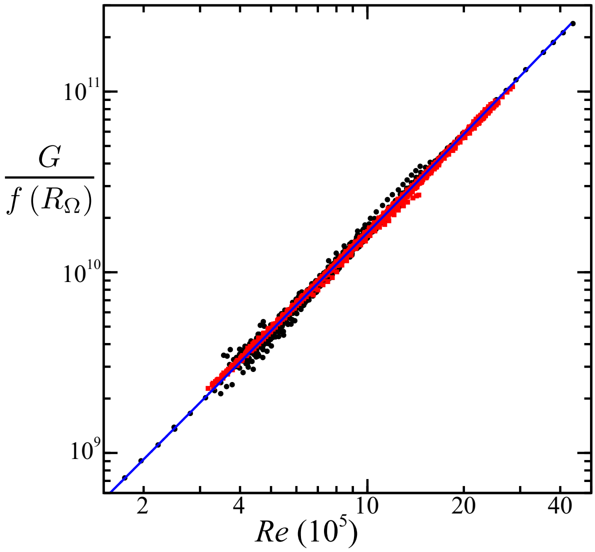

Figure 5.5: The dimensionless torque G may be compensated by the fit $f(R_\Omega)$ given by Eq. (5.8). The data from both Paoletti & Lathrop [18] (black circles) and van Gils *et al.* [88] (red squares) agree with the best fit from Lewis & Swinney [14] for the case where the outer cylinder was stationary (blue line).

rotation, as measured by G/G_0, while the scaling with Re seems to be independent of R_Ω in the investigated regime. Therefore the torque may be approximately factorized and written as

$$G = f(R_\Omega)g(Re), \tag{5.9}$$

where $f(R_\Omega)$ is measured in Fig. 5.4 and fit by Eq. (5.8) and our measurements of $g(Re)$, shown in Fig. 5.5, agree with previous measurements, and may be fit by effective power-laws or logarithmically varying functions such as the Prandtl-von Kármán form (Lathrop *et al.* [10, 11], Lewis & Swinney [14]).

Comments

In addition to the observed data collapse, other interesting features arise in the normalized torque scaling with R_Ω. The data from Taylor's experiments [6] were obtained with a stationary inner cylinder ($\Omega_1 = 0$), and the flow is therefore Rayleigh-stable. However, the data from Wendt [5], Maryland [18] and Twente [88] over the same range of the rotation number, namely $0 < R_\Omega < 0.27$, are obtained with counter-rotating cylinders. This configuration is linearly unstable, yet the measured values of G/G_0 agree between all four experiments. We argue, as in Taylor [6], that the flow states in Taylor's experiments could not have been laminar and must have undergone a subcritical transition to turbulence.

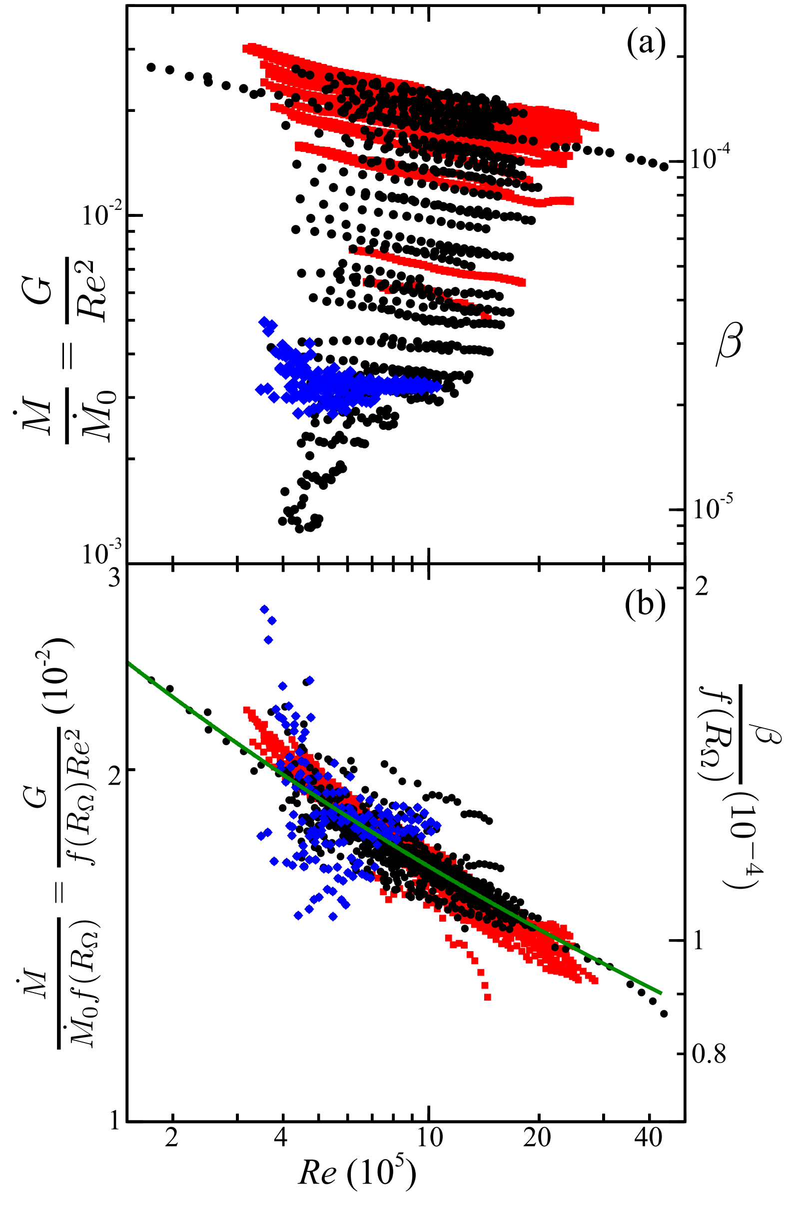

Figure 5.6: The scaling of (a) G/Re^2, which is proportional to the accretion rate $\dot{M}$ and viscosity parameter β, decays slowly with Re while having an amplitude that varies with the rotation number R_Ω (see Fig. 5.4). (b) The effects of global rotation can be accounted for by compensating G/Re^2 by the fits $f(R_\Omega)$ given in Eq. (5.8). The measurements from Twente are shown as red squares. The Maryland data are given by black circles, except for quasi-Keplerian flows ($R_\Omega \leq -1$), which are indicated by blue diamonds. The green continuous line is the theoretical fit given in Eq. (5.10) normalized by $f(R_\Omega = -0.2755)$, which corresponds to $\Omega_2 = 0$.

Paoletti & Lathrop [18] observed that the torque scaling varied linearly with R_Ω in four regions of the parameter space corresponding to: region I: $R_\Omega \leq -1$, region II: $-1 < R_\Omega \leq -0.10$, region III: $-0.10 < R_\Omega < 0.38$ and region IV: $0.38 < R_\Omega$, where we have reordered the region numbers to correspond to increasing R_Ω. Figure 5.4 shows that all of the data described here follow the region I–region II and region II–region III crossovers. The crossover between regions I and II corresponds to the Rayleigh stability criterion for all values of η. The crossover between regions II and III occurs at the observed maximum in the normalized torque G/G_0 as a function of R_Ω. While this maximum occurs for all of the Wendt [5], Maryland [18] and Twente [88] datasets, there is no general theoretical prediction for the exact location of this maximum yet.

The last crossover observed by Paoletti and Lathrop, between regions III and IV, corresponded to $\Omega_1 = 0$ with $\Omega_1 > 0$ and $\Omega_2 < 0$ in region III (counter-rotation) to $\Omega_1 > 0$ and $\Omega_2 > 0$ in region IV (co-rotation). It is unclear whether this crossover is set by $R_\Omega = 0.38$ or whether it always occurs at $R_\Omega(\Omega_1 = 0)$. The data from Taylor [6] has $\Omega_1 = 0$ but given the values of η used in those experiments $R_\Omega < 0.38$. The Richard data for $R_\Omega > 0.38$ fall below the observations by Maryland, although the scaling with R_Ω is similar. It is unclear if this disparity is a result of the analysis used to deduce the torques from Richard's measurements or the difference in the control parameters from the Maryland experiment (see Table 5.1). It would be fruitful to have independent, direct measurements of the torque in region IV to compare against those of Maryland at different radius ratios to better understand this final crossover.

The Richard and Maryland data both indicate that the observed torque for quasi-Keplerian flows states ($R_\Omega \leq -1$) is approximately 14% of the maximum observed torque for a given Reynolds number. This is in contrast to the results of Ji *et al.* [109], who deduced that such flow states are "essentially steady" and unable to transport angular momentum hydrodynamically. In addition to the different geometries between the experiments of Ji *et al.* [109] and those of Richard and Maryland (see Table 5.1), the measurement techniques and finite-size effects were different between the experiments. This contrast is further discussed in Section 5.4. Clearly, additional independent measurements of the angular momentum flux for quasi-Keplerian flows could aid this debate, as recently discussed by Balbus [114].

Astrophysical implications

As described in Section 5.2.5, the scaling of the torque with Reynolds number may be used to determine either the turbulent viscosity parameter β or the accretion rate $\dot{M}$ through Eq. (5.6). Our measurements of G/Re^2, which is proportional to both β and $\dot{M}$, are shown in Fig. 5.6(a). The measurements from Twente are shown as red squares while those of Maryland are given by black circles. The data indicated by blue diamonds are quasi-Keplerian flow states ($R_\Omega \leq -1$) from the Maryland experiment. The quantity G/Re^2 decreases slowly with Re (only logarithmically, see Grossmann & Lohse [26], Dubrulle *et al.* [75], Hersant *et al.* [108]) as expected since $G \propto Re^{\alpha}$ with $1.8 < \alpha(Re) \leq 2.0$ for $10^5 < Re < \infty$ (Lathrop *et al.* [10, 11], Lewis & Swinney [14]). The amplitude of G/Re^2 for a given Re is determined by R_{Ω}. The effects of global rotation may be accounted for by compensating the measurements of G/Re^2 by $f(R_{\Omega})$ (see. Eq. (5.8)), as shown in Fig. 5.6(b). As discussed by Dubrulle & Hersant [22] and Hersant *et al.* [108], the scaling may be fit by a logarithmically decaying function, such as:

$$\frac{G}{Re^2} = K_7 \frac{\eta^2}{(1-\eta)^{3/2}} \frac{1}{\ln[\eta^2(1-\eta)Re^2/K_8]^{3/2}}, \tag{5.10}$$

with the values chosen to be $K_7 = 0.4664$ and $K_8 = 10^4$ to describe the best fit for the torque scaling provided by Lewis & Swinney [14] for the case $\Omega_2 = 0$. An alternative logarithmic dependence between G/Re^2 and Re has been suggested by Grossmann & Lohse [26] (for the analogous case of ultimate Rayleigh-Bénard flow), and it equally well fits the data.

The expected accretion rate, measured by $G/Re^2 = 3.3 \times 10^{-3}$, for quasi-Keplerian flows (blue diamonds in Fig. 5.6) is approximately 14% of the maximum accretion rate, which occurs for $R_{\Omega} = -0.10$. This corresponds to a value of $\beta_{Md} = 2 \times 10^{-5}$ or $\dot{M}/\dot{M}_0 = 3.3 \times 10^{-3}$ at $Re = 7 \times 10^5$. Extrapolating towards astrophysical Reynolds numbers by using the formula of Hersant *et al.* [108], we get a value of $\dot{M}/\dot{M}_0 = 10^{-3}$ that is consist with values observed in disks around TTauri stars.

5.4 Discussion

The measured accretion rate for all of our quasi-Keplerian flows ($R_{\Omega} \leq -1$) is approximately 14% of the maximum accretion rate, which occurs at $R_{\Omega} = -0.10$, resulting in $\beta_{\mathrm{Md}} = 2 \times 10^{-5}$. This is close to the value computed by Richard and Zahn $\beta_{\mathrm{RZ}} = 10^{-5}$ and to the value of Dubrulle *et al.* [75] $\beta_{\mathrm{D}} = 8 \times 10^{-6}$. This is somewhat surprising given that quasi-Keplerian flow profiles are linearly stable while the maximum accretion rate occurs when the cylinders counter-rotate, which produces destabilizing shear that dominates the dynamics. This result is in stark contrast to the results presented by Ji *et al.* [109] and Schartman *et al.* [113], where β_{P} was measured to be an order of magnitude smaller, specifically $\beta_{\mathrm{P}} = 7 \times 10^{-7}$. Thus, they concluded that hydrodynamics alone cannot efficiently transport angular momentum in quasi-Keplerian flows.

Schartman *et al.* [113] state that these incompatible results are caused by differing interpretations of finite-size effects, namely Ekman circulation produced by the axial boundaries. In the Princeton experiments (Ji *et al.* [109], Schartman *et al.* [110], Burin *et al.* [111], Schartman *et al.* [113]) the aspect ratio is small ($\Gamma \approx 2$) and therefore finite-size effects would likely dominate. To minimize Ekman circulation, their axial boundaries are split into pairs of rings that can independently rotate with respect to the cylinders. This method has been shown to reduce the effects of Ekman circulation in the bulk of the fluid (Schartman *et al.* [110]). Furthermore, when Ekman circulation is not minimized their measured values of β for quasi-Keplerian flows are approximately half of the typical values presented here. Thus, Schartman *et al.* [113] argue that our larger values of β are the result of Ekman circulation that is present in other experiments, but is minimized in their apparatus.

We claim, on the other hand, that our measured torques cannot be solely attributed to finite-size effects. The main premise of our argument is that the normalized torques G/G_0 agree quite well for all of the different experimental data detailed here, even though the apparatus geometry, measurement techniques and control parameters vary greatly. Given this widespread disparity in geometry, rotation rates and range of Reynolds numbers, one would expect that the effects of Ekman circulation would differ and result in systematic discrepancies between the experiments. We do not observe such discrepancies and we further detail our arguments along these lines below.

The torques in the Maryland and Twente experiments are measured over only 56% of the axial length of the flow centered at the mid-height of the apparatus. This design has been intentionally implemented such that the torque measurements are unaffected by flows within 2.58 radial gap widths of either axial boundary where Ekman circulation is strongest. Wendt's experiments [5] had a free upper surface, which is therefore devoid of Ekman circulation. Even though Taylor's measurements [6] were affected by Ekman circulation for $\Gamma > 100$, his measurements of the torque for Rayleigh-stable flows that are expected to be most affected by Ekman circulation agree with our measurements of counter-rotating flows for the same value of R_Ω, where Ekman circulation is dwarfed by the dominant shear.

One of course wonders on whether this Ekman circulation caused by the co-rotating upper and lower plates affect the flow patterns. For laminar flow e.g. for purely outer cylinder rotation this clearly is the case (Coles & van Atta [74], Hollerbach & Fournier [89]). However, we argue that the strong turbulence destroys such an axial dependence of the flow field. To check this assumption, we have measured the full turbulent velocity profile with Laser Doppler Anemometry (LDA) (van Gils *et al.* [115]). The result is shown in Fig. 5.7. Evidently, over the length of the central section of the inner cylinder where we measure the torque there is no visible z-dependence of the mean velocity; the plate boundary layers only produce an axial dependence far above the domain of the central section of the inner cylinder.

Ji *et al.* [109] stated that their measured velocity fluctuations and values of β were much higher for more viscous fluids, even though the flow profiles were the same. They interpreted this observation to imply that the residual finite-size effects

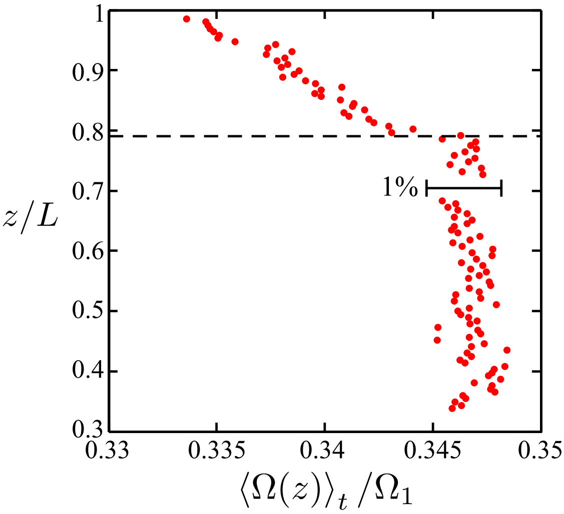

Figure 5.7: Finite-size effects may be characterized by axial profiles of the angular velocity Ω measured at the mid-gap ($r = (a+b)/2$) in the Twente experiment. In this example, the cylinder Reynolds numbers are $Re_1 = 1.0 \times 10^6$ and $Re_2 = 0$ (outer cylinder stationary). The global torque measurements are taken for $0.22 < z/L < 0.78$ with the top boundary of these measurements indicated by the dashed line at $z/L = 0.78$. The resolution of the laser-doppler anemometry prohibits measurements of the angular velocity in the boundary layer near $z/L = 1$ where $\Omega = \Omega_2 = 0$, in this case.

penetrate deeper into the bulk of the fluid at lower *Re*, even though Ekman circulation was claimed to have been minimized in both sets of measurements thereby resulting in similar (nearly ideal-Couette) flow profiles. The values of *Re* for the experiments presented here span two orders of magnitude while the values in viscosity vary by a factor of 34, yet no such systematic effects on the measured torques have been observed. Furthermore, given the small aspect ratio of the Princeton experiments one would expect Ekman circulation to produce significantly higher values of β when the axial boundaries co-rotate with the outer cylinder, as in the experiments presented here. However, even in this case their measured values are a factor of two smaller than those presented here and in Paoletti & Lathrop [18].

The normalized torque G/G_0 is approximately constant for each value of R_Ω characterized by the present experiments. This indicates that the amplitude of the torque varies with R_Ω, however the scaling with *Re* is unchanged (see Fig. 5.5). Paoletti & Lathrop [18] observed that their torque scaling for Rayleigh-stable and unstable flows agreed with the Prandtl–von Kármán description of Lathrop *et al.* [10] and Lewis & Swinney [14]. The Twente data, initially presented in van Gils *et al.* [88], was well-described by the theoretical predictions of Eckhardt *et al.* [23] for all rotation numbers explored. If Ekman circulation significantly contributed to the torque for Rayleigh-stable flows, as argued by Schartman *et al.* [113], then one would expect systematic disparities between these theoretical descriptions and the measured torques. As shown in Fig. 5.5, though, the torque scaling agrees well with the observations of Lewis & Swinney [14] for the case $\Omega_2 = 0$ *for all values of* R_Ω.

The Princeton experiments (Ji *et al.* [109], Schartman *et al.* [110], Burin *et al.* [111], Schartman *et al.* [113]) measure *local velocity correlations to determine the global angular momentum flux*, whereas the Maryland and Twente experiments directly measure the global angular momentum flux using precision calibrated force-arm measurements. The distinction between the measured quantities has made direct comparisons of the experiments difficult. To bridge this gap, Burin *et al.* [111] recently used their local velocity measurements to determine the corresponding torque G. To compare to previous studies with $\Omega_2 = 0$ (Lathrop *et al.* [10, 11], Lewis & Swinney [14]) Burin *et al.* [111] fit the scaling of $c_f^{-1/2}$ to $\log_{10}(Re * c_f)$, where $c_f \equiv G/Re^2$, and determined a slope of 1.40 ± 0.16. The authors claim that this value agrees with the measured value of 1.52 reported by Lathrop *et al.* [10, 11] and 1.56 measured by Lewis & Swinney [14]. However, the appropriate Prandtl–von Kármán scaling predicts the following relationship (Lathrop *et al.* [10, 11], Lewis & Swinney [14])

$$\frac{1}{\sqrt{c_f}} = N \log_{10}(Re\sqrt{c_f}) + M, \tag{5.11}$$

in contrast to the scaling shown in Fig. 5 of Burin *et al.* [111]. Furthermore, the fit parameters N and M are predicted to depend upon the radius ratio in the following way

$$N = [(1-\eta^2)\ln 10]/(\eta\kappa\sqrt{2\pi}) \tag{5.12}$$

$$M = \frac{N}{\ln 10}\left[\ln\left\{\left(\frac{1-\eta}{1+\eta}\right)\frac{1}{y_0^+\sqrt{2\pi}}\right\} + \kappa y_0^+\right], \tag{5.13}$$

where $\kappa = 0.40$ is the von Kármán constant and $y_0^+ = 5$. The radius ratio $\eta = 0.35$ in the Princeton experiments, therefore the Prandtl–von Kármán skin friction law predicts $N = 5.76$ and $M = -3.15$. These values do not agree with our analysis of the data in Burin *et al.* [111] where $N \approx 2$ and $M \approx -0.4$. In fact, the measured values of G determined by the local velocity fluctuations are on average five times larger than those predicted by the Prandtl–von Kármán skin friction law that has been verified using direct torque measurements (Lathrop *et al.* [10, 11], Lewis & Swinney [14], Paoletti & Lathrop [18]). Therefore, we argue that the local velocity fluctuation measurements used in the Princeton experiments (Ji *et al.* [109], Schartman *et al.* [110], Burin *et al.* [111], Schartman *et al.* [113]) face severe experimental challenges. In fact, Huisman *et al.* [95] showed that the local angular momentum transport undergoes fluctuations that are two orders of magnitude larger than the mean value.

However, once the local angular momentum transport is averaged long enough and over a large enough region, Huisman *et al.* [95] achieved perfect agreement between the *local* and the *global* measurements.

Clearly the contrasting conclusions of the Princeton experiments (Ji *et al.* [109], Schartman *et al.* [110], Burin *et al.* [111], Schartman *et al.* [113]) and those presented here warrant further experimental and theoretical investigation, as suggested by Balbus [114]. It appears that measurements of the local velocity fluctuations may not accurately determine the global angular momentum transport, as attempted by Burin *et al.* [111]. On the other hand, the effects of the axial boundaries on the global torque measurements presented here have not yet been characterized in detail. The Twente experiments [95] provide both local velocities as well as the global torque, which thereby presents future opportunities to clarify these distinctions. Vice versa, direct global torque measurements in a split axial-ring apparatus, such as the Princeton device, would also be scientifically useful.

5.5 Conclusions

The measurements that we present here indicate that the dimensionless torque G may be described as a product of functions that separately depend upon the Reynolds number Re and the rotation number R_Ω. The rotation number R_Ω introduced by Dubrulle *et al.* [75] collapses all of the experimental data presented here for various radius ratios, aspect ratios and Reynolds numbers (see Table 5.1). The effects of global rotation, measured by G/G_0, where $G_0 \equiv G(Re, R_\Omega = 0)$, are shown to be well-described by the function $f(R_\Omega)$ given in Eq. (5.8) for the entire range of R_Ω explored in the present studies.

The most astrophysically relevant result is the scaling of G/Re^2, which is proportional to both the turbulent viscosity parameter β and the accretion rate $\dot{M}$. We observe that the expected accretion rate for quasi-Keplerian flows ($R_\Omega \leq -1$) is approximately 14% of the maximum attainable rate for a given Reynolds number. We therefore get a dimensionless angular transport parameter $\beta_{\mathrm{Md}} = 2 \times 10^{-5}$, in agreement with Richard and Zahn but more than an order of magnitude larger than the Princeton experiments. Such angular momentum transport is able to produce dimensionless accretion rates on the order of $\dot{M}/\dot{M}_0 \sim 10^{-3}$, which are compatible with observations in disks around TTauri stars (Hersant *et al.* [108]). We have argued that our results are not easily attributed to finite-size effects, such as Ekman circulation. As such, we conclude that hydrodynamics may be able to transport angular momentum at astrophysical rates in spite of the linear stability provided by the radially-increasing angular momentum profile. This level of transport must result from turbulent means, thereby implying that quasi-Keplerian flows can be nonlinearly unstable to finite amplitude disturbances.

— PART III —

Bubbly Taylor-Couette flow

6

Bubbly turbulent drag reduction is a boundary layer effect [*] [†]

In turbulent Taylor-Couette flow, the injection of bubbles reduces the overall drag. On the other hand, rough walls enhance the overall drag. In this work, we inject bubbles into turbulent Taylor-Couette flow with rough walls (with a Reynolds number up to 4×10^5*), finding an enhancement of the dimensionless drag as compared to the case without bubbles. The dimensional drag is unchanged. As in the rough-wall case no smooth boundary layers can develop, the results demonstrate that bubbly drag reduction is a pure boundary layer effect.*

---

[*] Based on: T.H. van den Berg, D.P.M. van Gils, D.P. Lathrop, and D. Lohse, *Bubbly turbulent drag reduction is a boundary layer effect*, Phys. Rev. Lett. **98**, 084501 (2007).

[†] These experiments were performed on the TC facility of the University of Maryland (UMD).

6.1 Introduction

Turbulent drag reduction can be achieved by polymers [116–120], by bubbles [27, 55, 59, 120–125], or by a combination of both [126]. The phenomenon has huge potential for applications in the naval transport sector [58]. Even a small reduction of a few percent on the fuel consumption of ships means a considerable annual saving. One drag reduction method is to reduce the skin friction through microbubble injection at the ships hull. Using this, a research team in Japan has found drag reduction on an experimental ship, the Seiun-Maru, of up to 5% [57]. An U.S. research team achieved reductions of $5\% - 15\%$ with a catamaran supplied with a microbubble drag reduction system [127]. A generally accepted explanation of the effect is lacking. Several theories are competing: Based on numerical simulations, Ferrante and Elghobashi [128] argue that the microbubbles in a spatially developing turbulent boundary layer push the developing streamwise vortices away from the wall, leading to less dissipation in the boundary layer. Numerical simulations by Lu, Fernandez, and Tryggvason [28] show that deformable bubbles lead to a significant reduction of the drag by the suppression of streamwise vorticity. Van den Berg *et al.* [27] show that both mechanisms contribute, though the deformability of the bubbles seems to be of main importance, leading to stronger drag reduction. Lo, L'vov, and Procaccia [129] conclude that bubble volume oscillations and, thus, the compressibility of the bubble-water mixture play an important role for the drag reduction.

In this chapter, we investigate the effect of the wall roughness on bubbly drag reduction: first, because for practical applications rough walls are more realistic than smooth ones; second, in order to get more insight into the mechanism of bubbly drag reduction; and, in particular, to probe whether boundary layer (BL) effects play a role. Rough walls drastically modify the dynamics in the laminar BLs and trigger the development of turbulent BLs. Indeed, by roughening the walls in a single-phase flow Taylor-Couette setup, the overall drag could be increased by a factor of 50 [15, 130]. Moreover, the drag scales more steeply with the Reynolds number as compared to the smooth-wall case [15, 130], in coherence with what one would expect when transferring the ideas of the unifying scaling theory for thermal convection [49–52] to the Taylor-Couette case [81].

The effect of bubbles on the drag within a turbulent water tunnel with rough walls has been examined in Ref. [131]. In these experiments, the drag force was directly measured with a drag balance, as a function of the downstream position and of the (injected) gas flow rate. In spite of the wall roughness, the addition of bubbles reduced the drag, similarly as the addition of polymers reduced the drag in such water tunnel experiments [131, 132]. In these experiments [131, 132], wavy structures or grits were attached to the surfaces of the walls. In the rough-wall case, the drag reduction effect of the polymers was even stronger than in the smooth-wall case, presumably because of the higher absolute drag for the rough-wall case [132]. In contrast, Cadot, Bonn, and Douady [133] did not find any polymeric drag reduction for *inertially forced* (with baffles) turbulence. They concluded that the polymeric drag reduction effect observed in the smooth-wall case is related solely to a diminution of the dissipation in the viscous boundary layer where most of the energy is dissipated. This is consistent with the present theoretical understanding of polymeric drag reduction; see, e.g., Refs. [119, 134] and references therein.

6.2 Experimental method

To measure the potential drag reduction effect of bubbles in turbulence in a system with rough walls, we again choose the Taylor-Couette geometry, just as we did in Ref. [15] for the effect of rough walls only and in Ref. [27] for the effect of bubbles only. The advantage of the Taylor-Couette system is that it is *closed*, which makes it possible to deduce the overall dissipation rate ε from the well-controlled energy input rate determined by the torque. Moreover, statistically stationary states are easy to achieve. Thus, by measuring the torque on the inner cylinder (rotating with fixed angular velocity ω_i), the total energy dissipation rate of the flow can be deduced, which in turn is a measure of the drag:

$$\varepsilon = \frac{\tau\omega_i}{\pi\rho L({r_o}^2 - {r_i}^2)} = \frac{2\nu^2 G\omega_i}{{r_o}^2 - {r_i}^2}. \tag{6.1}$$

Here τ is the torque, $G = \tau/2\pi\rho\nu^2 L$ is its nondimensionalized form[‡], ρ is the density of the liquid, and ν is the kinematic viscosity. The height of the cylinder is L, and the inner and outer radii are r_i and r_o, respectively. The drag coefficient c_ε follows from nondimensionalization:

$$c_\varepsilon = \frac{\varepsilon(r_o - r_i)}{{\omega_i}^3 {r_i}^3} = \frac{\tau}{\pi\rho L{\omega_i}^2 {r_i}^3 (r_o + r_i)}. \tag{6.2}$$

The Taylor-Couette setup used for these experiments is described in detail in Refs. [11, 14, 15, 27]. Here we only briefly summarize its specifications and refer to the mentioned papers for more information. The setup has an inner cylinder with radius $r_i = 16$ cm and an outer cylinder with radius $r_o = 22$ cm; the liquid-containing gap is thus 6 cm. The outer cylinder is stationary; the inner one can rotate to frequencies up to 16 Hz, resulting in a maximum $\mathrm{Re} \approx 10^6$ for the single-phase water case. The total length is $L = 69.5$ cm, resulting in an aspect ratio of $\Gamma = L/(r_o - r_i) = 11.6$. To minimize the effects of the top and bottom boundaries, the inner cylinder consists of three parts, with a measuring section in the middle. The length of this section is

---

[‡] This definition of G differs by a factor of 2π with the published version to conform to Eckhardt, Grossmann & Lohse [23] as is the case throughout this thesis apart from chapter 5. It has no further consequences to the text or the graphs as originally published [61].

40 cm. It is attached to the inner shaft by low friction bearings. The actual torque on this part is measured by means of a load cell and strain gauges, which are measured by means of a lock-in amplifier. The top and bottom sections of the fluid volume serve as heat sinks in order to maintain a constant temperature of the working liquid. In this way, we were able to keep the temperature constant within a tenth of a degree. Therefore, we assume the dynamic viscosity and the density to remain constant. In the experiments with rough walls, the roughening was achieved by attaching 16 square Perspex rods (thickness 3 mm) equally spaced in azimuthal angle on the inner and outer cylinders, as in Refs. [15, 130]. Note that in the rough-wall case the Taylor-Reynolds number is considerably larger than in the smooth-wall case, due to the enhanced forcing [15, 130, 133].

The air bubbles are injected into the turbulent flow through eight needles located at the bottom of the outer cylinder. The void fraction α was estimated by measuring the excess volume pushed out of the system because of the added gas as in Ref. [27]. The bubble size is dictated by the strength of the shear and is typically in the range of $2-0.5$ mm [135]. The boundary layer inner length scale is significantly smaller, $y_0 = \nu/u_* \approx 3\mu$m, with $u_* = \sqrt{\tau_w/\rho}$ and the shear stress τ_w being estimated as [11, 14] $\tau_w = \tau/2\pi r_i{}^2 L$.

Because of centrifugal forces, the air bubbles tend to accumulate near the inner cylinder, which eventually would lead to a decoupling of the working liquid from the inner cylinder. However, when limiting the void fractions to values of up to 8%, the decoupling can be prevented.

When injecting bubbles into the flow, the kinematic viscosity and density are changed. It is $\rho = \rho_0(1-\alpha)$, and the kinematic viscosity for a bubbly liquid is assumed to obey [136]

$$\nu = \nu_0(1+\frac{5}{2}\alpha), \tag{6.3}$$

where $\nu_0 = \nu(\alpha = 0)$. Another reason to limit ourselves to low overall gas fractions of up to 8% is that relation (6.3) becomes more and more questionable for larger gas fractions (see, e.g., Ref. [137]) — but note that the *local* gas concentration can be higher than 8% due to bubble accumulation in the vortices. The flow Reynolds number is defined with the viscosity of the bubbly liquid:

$$\mathrm{Re} = \frac{\omega_i r_i (r_o - r_i)}{\nu} = \frac{\omega_i r_i (r_o - r_i)}{\nu_0(1+\frac{5}{2}\alpha)}. \tag{6.4}$$

Altogether, we had four different experimental settings: smooth walls with single-phase liquid, smooth walls with two-phase liquid, rough walls with single-phase liquid, and rough walls with two-phase liquid. The Reynolds number range spans $1\times10^5 < \mathrm{Re} < 4\times10^5$, which is limited by the maximum available torque of the motor.

The experimental procedure was as follows: We first measured the dimensionless drag without bubble injection as a function of the Reynolds number, $c_\varepsilon(\alpha = 0, \mathrm{Re})$. The resulting data are fitted by a spline or in the smooth-wall case by a crossover function [27, 138], leading to two curves $c_\varepsilon^{\mathrm{fit}}(\alpha = 0, \mathrm{Re})$, namely, one for the smooth-wall case [shown in the inset in Fig. 6.1(a)] and one for the rough-wall case. We then kept the rotation rate of the inner cylinder constant and slowly increased the void fraction while continuously measuring both α and the torque.

In order to keep the measured torque inside the accuracy range of the TC facility and in order to achieve the same Reynolds number range across the smooth-walls and rough-walls case, different liquids are used. In the smooth-walls case the employed liquid is a 36/64 glycerine/water mixture at 27° C with $\rho_0 = 1102$ kg/m^3 and $\nu_0 = 2.53 \times 10^{-6}$. In the rough-walls case the employed liquid is water at 22° C with $\rho_0 = 998$ kg/m^3 and $\nu_0 = 9.57 \times 10^{-7}$ m^2/s.

6.3 Results

In Fig. 6.1(a), we show the compensated drag coefficient $c_\varepsilon(\alpha, \mathrm{Re})/c_\varepsilon^{\mathrm{fit}}(0, \mathrm{Re})$ vs the Reynolds number for increasing void fractions α for the smooth-wall case. Once α exceeds a threshold of about 2% volume concentration, a strong drag reduction of up to 25% can be observed, as compared to the single-phase case.

For the rough-wall case, the behavior is very different, as can be seen from Fig. 6.1(b). In contrast to the smooth-wall case, the drag coefficient increases with increasing void fraction α, even up to 16% for the 8% void fraction case. We conclude that the wall roughness prevents bubbly drag reduction. Apparently, drag reduction by bubbles is a boundary layer effect, just as polymeric drag reduction [133]: In the rough-wall case, the structure of the viscous BLs and, thus, the energy injection mechanism into the system seem to be so strongly modified that the mechanism for bubbly drag reduction can no longer be active.

We point the reader to some interpretation ambiguities on what drag reduction means. In Fig. 6.2, we present the data for the rough- and smooth-wall cases in their *dimensional* form. For the smooth-wall case [Fig. 6.2(a)], with increasing void fraction a reduction in the required torque for constant rotation rate is observed, just as expected. However, in the rough-wall case [Fig. 6.2(b)], the dimensional torque does not seem to depend on the (increasing) void fraction. This means that only when compensating for the change in density and viscosity can the rough-wall results be interpreted as drag increase through bubble injection. The smooth-wall case is free of this interpretation ambiguity: Both the dimensional and the dimensionless drag decrease with increasing void fraction α.

In order to compare our results with theoretical approaches [129], it would be of prime interest to know the bubble concentration profile, both in the smooth- and in

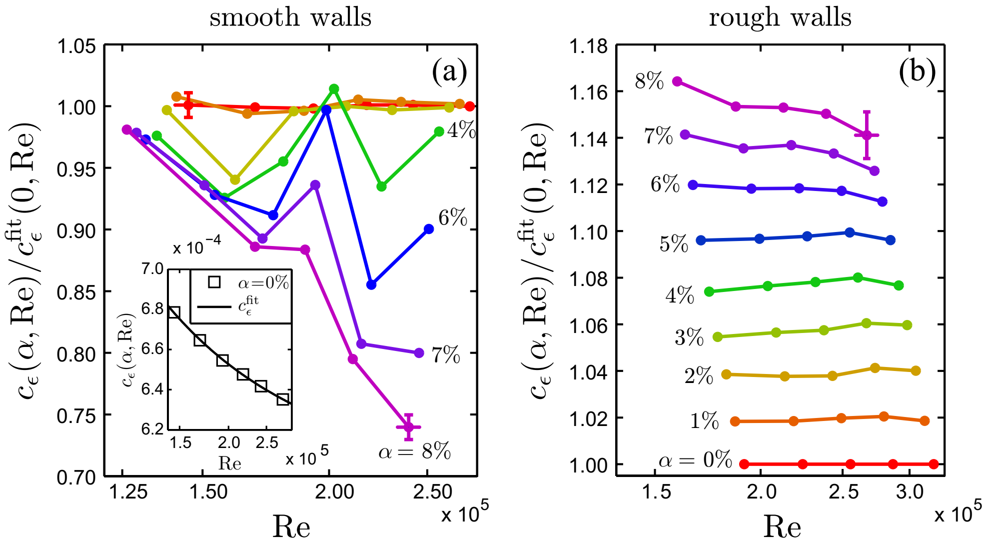

Figure 6.1: Compensated drag coefficient $c_\varepsilon(\alpha,\mathrm{Re})/c_\varepsilon^{\mathrm{fit}}(0,\mathrm{Re})$ vs the Reynolds number for increasing void fractions α for (a) the smooth-wall case and (b) the rough-wall case. While (a) in the smooth-wall case, the drag decreases up to 25%, (b) in the rough-wall case, the bubble injection leads to a drag enhancement.

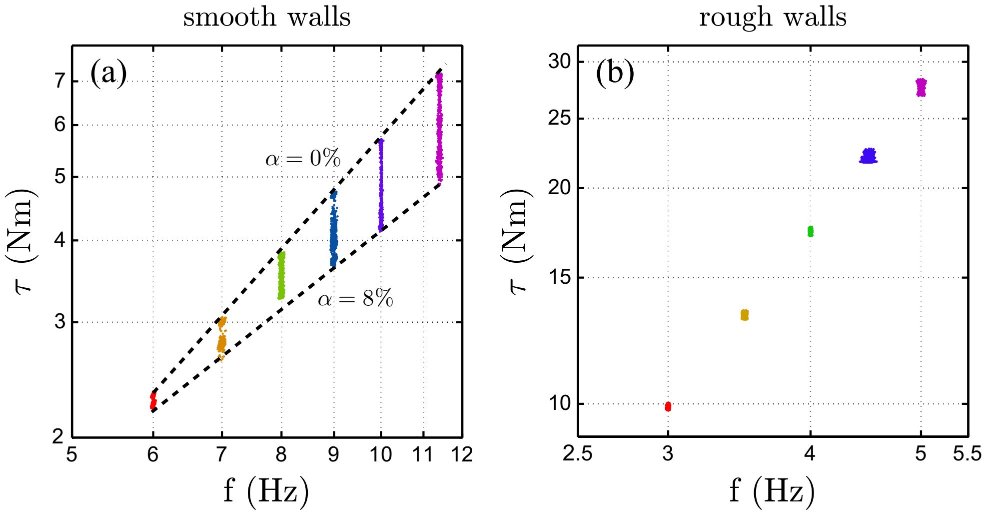

Figure 6.2: Torque (in Nm) versus the rotation rate (in hertz) of the inner cylinder for increasing void fractions: (a) smooth-wall case and (b) rough-wall case. In (a), a decrease of dimensional torque with increasing void fraction α can be seen. In (b), the dimensional torque seems to be independent of the void fraction.

the rough-wall cases. For low Re, such measurements have been done, revealing a strong Re dependence of the radial bubble distribution [139]. Corresponding measurements in the large Re case are presented in chapter 7.

6.4 Conclusion

In conclusion, we have measured the drag for bubbly turbulence in a Taylor-Couette system for smooth and rough walls. For the smooth-wall case, a strong reduction in drag coefficient was found, in agreement with our earlier experimental results [27] and in agreement with theory [129]. For the rough-wall case, we found an enhancement of the dimensionless drag coefficient with increasing void fraction, whereas the dimensional torque did not change. Independent of these interpretation ambiguities, the general conclusion is quite clear: There is no drag reduction for Taylor-Couette turbulence with rough walls — at least not in the (Taylor-)Reynolds number regime accessible in our experimentswhereas a strong drag reduction is observed for the smooth-wall case. Bubbly drag reduction is, hence, a boundary layer effect.

Through our results, one can understand why growth of barnacles or other organic material at the ship hull or its corrosion drastically degrade the drag reduction effect of injected bubbles: The roughness caused by the organic material or by the corrosion destroys the smooth BL and, therefore, the mechanism leading to bubbly drag reduction.

7

Bubble deformability is crucial for strong drag reduction in turbulent Taylor-Couette flow [*]

Bubbly turbulent Taylor-Couette (TC) flow at Reynolds numbers of Re $= 5.1 \times 10^5$, 1.0×10^6 *and* 2.0×10^6 *is globally and locally studied in the case of a stationary outer cylinder and a mean bubble diameter around 1 mm. We measure the drag reduction (DR) based on the global dimensional torque as a function of the global gas volume fraction* (α_{global}) *over the range 0% up to 4%. We observe a moderate DR up to 7% for* $Re = 5.1 \times 10^5$. *Significantly stronger DR is achieved for Re* $= 1.0 \times 10^6$ *and* 2.0×10^6 *with, remarkably, more than 40% of DR for* $\alpha_{global} = 4\%$ *at* $Re = 2.0 \times 10^6$.

To shed light on the two apparently different regimes of moderate *DR and* strong *DR we investigate the statistics of the local liquid flow velocity and the local gas concentration for the two different cases;* $Re = 5.1 \times 10^5$ *at* $\alpha_{global} = 3 \pm 0.5\%$ *in the moderate DR regime and* $Re = 1.0 \times 10^6$ *at* $\alpha_{global} = 3 \pm 0.5\%$ *in the strong DR regime.*

In both cases the bubbles mostly accumulate close to the inner cylinder, as can be quantified by a 'centripetal Froude number' comparing the velocity fluctuations to the centripetal force. Surprisingly, the maximum local gas concentration near the inner cylinder for $Re = 1.0 \times 10^6$ *is* ≈ 2.6 *times lower than that for* $Re = 5.1 \times 10^5$,

---

[*] To be submitted to J. Fluid Mech. as: D.P.M. van Gils, D. Narezo Guzman, C. Sun, and D. Lohse, *Bubble deformability is crucial for strong drag reduction in turbulent TC flow*.

in spite of the stronger DR. A higher local gas concentration near the inner wall does not guarantee a larger DR: However, for both cases the local centripetal Froude number can account for the difference in the local gas concentration maxima.

By quantifying a local bubble Weber number (We) scanned along one third of the TC gap close to the inner cylinder wall, we observe that the crossover of $We \sim 1$ *roughly occurs at the crossover from the moderate to the strong DR regime. In the strong DR regime at* $Re = 1.0 \times 10^6$ *we find* $We > 2$ *reaching a value of 8 when approaching the inner wall, indicating that the bubbles increasingly deform when approaching the inner wall. In the moderate DR regime at* $Re = 5.1 \times 10^5$ *the local We is around or less than 1, indicating nearly spherical bubbles even though the mean bubble diameter is larger (1.3 mm) as compared to the* $Re = 1.0 \times 10^6$ *case (0.9 mm). Hence, we conclude that bubble deformability is the relevant mechanism behind the observed strong drag reduction. These local results match the conclusion on the global results as found by van den Berg* et al. *[27].*

7.1 Introduction

Theoretical, numerical and experimental studies on drag reduction of a solid body moving in a turbulent flow have been performed in the last three decades. Drag reduction can be achieved by using surfactants (Saeki *et al.* [140], Drappier *et al.* [141]), polymers (Virk [116], Berman [117], Benzi *et al.* [118], Bonn *et al.* [142], White & Mungal [143], Procaccia *et al.* [144]) and bubbles (van den Berg *et al.* [27], Ceccio [54], Madavan *et al.* [55], Takahashi *et al.* [56], van den Berg *et al.* [61], Murai *et al.* [62], Madavan *et al.* [123], Sanders *et al.* [125], Deutsch *et al.* [126], Murai *et al.* [139], Kato *et al.* [145], Clark III & Deutsch [146], Latorre [147], Sugiyama *et al.* [148], Elbing *et al.* [149], Gutierrez-Torres *et al.* [150], Jacob *et al.* [151]). The proper implementation and understanding of drag reduction through bubbles is specially relevant for naval applications, since it can lead to significant reduction of the fuel consumed by ships without adding substances into water. Despite all effort done to understand the fundamental mechanisms behind this effect, a solid understanding of the drag reduction mechanisms occurring in bubbly flows is still missing. Several mechanisms have been proposed as relevant, namely bubble splitting (Meng & Uhlman [152]) that may lead to changes in the flow, bubble compressibility (Lo *et al.* [129]) or deformability (van den Berg *et al.* [27], Lu *et al.* [28]) and effective compressibility of the flow (Ferrante & Elghobashi [128]). It has been found that the mechanism responsible for the reduction of drag depends on the Reynolds number Re of the flow and on the bubble size (Merkle & Deutsch [153], Moriguchi & Kato [154], Shen *et al.* [155]).

The conventional systems for studying bubbly DR are channel flows (Kodama *et al.* [58]), flat plates (Merkle & Deutsch [59], Latorre *et al.* [60], Sanders *et al.*

[125]), and cavity flows (see the review article by Ceccio [54]). A general explanation of the physical mechanism behind drag reduction is complicated since the flow in each type of the aforementioned systems can exhibit either spatial dependence like developing boundary layers, or temporal dependence like air film build-up and bubble shedding. This and other factors make it difficult to collapse all bubbly drag reduction data from different setups, see for example the review by Ceccio [54] on experimental work on bubbly drag reduction measured on plates and on the boundary of channel flows. More recently experiments on Taylor-Couette flow have been conducted overcoming this problem since statistically steady states are easy to achieve (van den Berg *et al.* [27, 61], Murai *et al.* [139], Sugiyama *et al.* [148], Djeridi *et al.* [156]). The Taylor-Couette system has the advantage of having a well defined energy balance (Eckhardt, Grossmann & Lohse [23]), which has a perfect analogy with the Rayleigh-Bénard system (Ahlers *et al.* [19]). In addition, Taylor-Couette flow enables the possibility of measuring global torque and gas volume fraction with good accuracy. Taking these various aspects into account, Taylor-Couette flow is ideal for studying the drag that a surface experiences when moving in a bubbly flow.

Bubbly Taylor-Couette flow has been experimentally studied (Murai *et al.* [139]) and theoretically modeled (Sugiyama *et al.* [148]) for low Re numbers ($< 10^4$). The mechanism responsible for the drag reduction in this regime is that the injected bubbles destroy the coherent flow structures, which leads to drag reduction. The efficacy of this particular mechanism gets lost for high Reynolds numbers when typical fluid fluctuations are larger and coherent structures are unsteady.

In high-Reynolds number regimes, the experimental work by van den Berg *et al.* [27] on Taylor-Couette flow employing bubbles on one hand and buoyant non-deformable particles on the other, has proven the existence of two different drag reduction regimes within Re ranging between 7×10^4 and 10^6. The division between the two regimes roughly occurs at a Weber number We ~ 1. The Weber number compares the strength of the liquid velocity fluctuations around the bubble surface to the surface tension. In the regime for Re $\lesssim 6 \times 10^5$ and We < 1 the bubbles remain close to spherical. In this regime the drag reduction is moderate, found to be around 5%. The mechanism of effective compressibility of the mixture, suggested in the numerical work by Ferrante & Elghobashi [128] explains the drag reduction obtained in this regime. In the regime for larger Re we have We > 1 and the drag reduction is significant, reaching up to around 20%. In this regime effective compressibility becomes less dominant and the relevant mechanism is related to the deformability of the bubbles (which are much larger than the Kolmogorov length scale η). In support of this view, van den Berg *et al.* [27] find that using non-deformable buoyant particles of the same size lead to little drag reduction. This interpretation has also been suggested in the numerical work by Lu, Fernandez & Tryggvason [28]. From their simulations these authors conclude that the deformable bubbles close to the wall push high vorticity regions far away from the wall, reducing the drag. Therefore, the physical mechanism consists on the bubble alignment between the bulk and the boundary layer, blocking the momentum transfer.

In a later work on the same TC setup van den Berg *et al.* [61] compare the bubbly drag reduction for smooth versus rough walls with Re ranging between 1×10^5 and 4×10^5. Their results support the claim that bubbly drag reduction is a boundary layer effect, as bubbly drag reduction totally vanishes for the rough-wall case.

Significant bubbly drag reduction with smooth walls has been measured by van den Berg *et al.* [27] in a narrow Re regime from 6×10^5 to 1×10^6. Given above interpretation on bubble deformability it is expected that a system capable of larger Reynolds numbers should lead to more DR. This assumption needs to be validated. Furthermore, previous drag reduction measurements were based on the global torque, leaving many issues of the mechanism responsible for this effect unknown: How do bubbles modify the liquid flow? How do they distribute themselves inside the gap? What is the local Weber number of the bubbles? To gain more insight, local information on the flow and bubbles is required.

In the present work we explore the Re parameter space with pure inner cylinder rotation up to $\mathrm{Re} = 2.0 \times 10^6$ and we measure the drag reduction as function of the global gas volume fraction. For $\mathrm{Re} = 5.1 \times 10^5$ and 1.0×10^6, we investigate the *local* modifications to the azimuthal velocity of the fluid due to the bubbles, we quantify the local spatial confinement of the bubbles, and we present their local Weber number. We chose these two Re numbers because the smaller one corresponds to the moderate drag reduction regime and the higher one to the strong drag reduction regime.

The outline of the paper is as follows. The experimental setup and global measurement techniques are introduced in Sec. 7.2, the local measurement techniques in Sec. 7.3. The results on the global parameters are presented in Sec. 7.4, and the local parameters in Sec. 7.5. Finally conclusions are drawn in Sec. 7.6 followed by a discussion and outlook in Sec. 7.7.

7.2 Experimental setup and global measurement techniques

7.2.1 Experimental setup

The experiments are performed in the Twente Turbulent Taylor-Couette (T^3C) facility. We refer to section 2.2 for a detailed description of the system. We refer to Fig. 2.2 for a schematic view of the setup and to table 7.1 for the values of the geometric parameters. The inner cylinder of the T^3C is divided into three separate sections, and the height of the midsection of the inner cylinder (IC_{mid}) is $L_{mid} = 0.536$ m, 58% of the full cylinder height $L = 0.927$ m. The inner cylinder has a radius of $r_i = 20.00$ cm and the outer cylinder of $r_o = 27.94$ cm, and the maximal inner and outer angular velocities are $\omega_i/2\pi = 20$ Hz and $\omega_o/2\pi = \pm 10$ Hz, respectively. The system is fully

Table 7.1: Geometric parameters of the present Taylor-Couette system (T^3C). The aspect ratio is given by $\Gamma \equiv L/(r_o - r_i)$ and the radius ratio by $\eta \equiv r_i/r_o$.

$r_i[m]$	$r_o[m]$	L [m]	L_{mid} [m]	Γ	η	V_{gap} [m^3]
0.2000	0.2794	0.927	0.536	11.68	0.716	0.111

temperature controlled through cooling of the upper and lower plate. In the present work we only rotate the inner cylinder and keep the outer cylinder stationary, and we use decalcified water as the working fluid and filtered instrument air for the bubble injection.

The Reynolds number Re for pure IC rotation flow is given by

$$Re = U_i(r_o - r_i)/\nu \tag{7.1}$$

where $U_i = \omega_i r_i$ is the azimuthal velocity of the inner cylinder, ω_i is the angular velocity and ν is the kinematic viscosity of the liquid.

7.2.2 Torque measurement

As shown in Fig. 2.2 the inner cylinder (IC) of the T^3C is divided into three separate sections, top, mid and bottom, each designed to measure the torque by acquiring load-cell deformation. Each section is basically a hollow cylinder suspended onto the IC's drive axle by two low-friction ball bearings. A metal arm goes from the drive axle to the inner wall of each IC section. It consists of two parts and these are bridged by a load cell, see Fig. 2.7. The load, equivalently, torque measurements are performed only on the middle section of the IC of length L_{mid} in order to minimize the end plate effects.

7.2.3 Bubble injection and global gas volume fraction measurement

In the bottom plate eight equally distributed bubble injectors are built in. Each consists of a capillary housed inside a plug ending flush with the wall facing the flow. The injected bubble size depends only on the shear stress in the flow (Risso & Fabre [135]) for the Re range examined here. In all our measurements we employed the same capillaries of diameter 1 mm. The gas injection rate is regulated by two mass flow controllers, resulting in 216 liters per minute at the maximum injection rate.

When air injection is activated, the excess of liquid and air needs to go out of the tank to avoid pressure build up. Water and air escape through four exits (to which we refer to as overflow channels) connecting the inner volume to the outside. The overflow channels are located on the top plate, close to the IC. Hoses are attached to them and lead to a bucket where the escaping water is collected. A balance registers the weight of the hanging bucket containing the ejected water (see Fig. 7.1).

We set the weight of the bucket for single phase flow as the weight zero-offset. Once the air injection is activated and the two-phase flow achieves stability, i.e., the continuous measurement of the bucket's weight is practically constant over time, the air volume contained inside V_{gap} can be calculated. Considering the continuously acquired temperature of the flow, the density of the water at each moment is known and thus the gas volume in the tank. The global gas volume fraction α_{global} is given by the gas volume in the gap as percentage of V_{gap}.

The small distance between the IC sections introduce an increasing error over time in the global gas volume fraction estimation. The centripetal force pushes the bubbles through the small separations and into the cavities between the sections. Part of the water that initially was inside is pushed eventually into the flow and contributes to the fluid collected in the bucket, thus overestimating the actual global gas volume fraction. We conduct experiments to quantify a maximal error of 0.5% for the global gas concentration of 3%, and the error is smaller for the small gas concentrations.

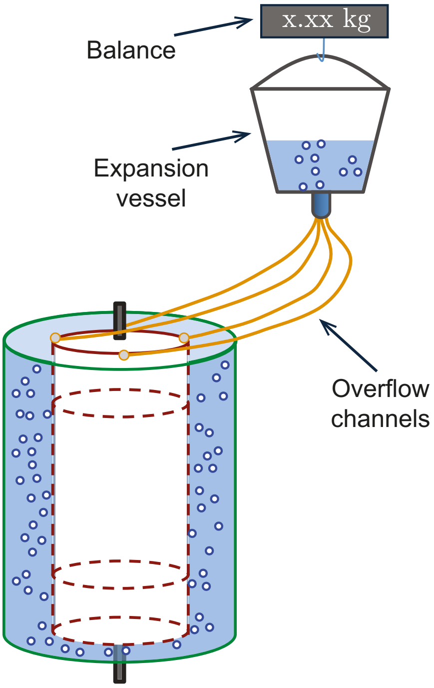

Figure 7.1: Schematic view of the setup showing the overflow channels through which excess water and air exit. The ejected water is collected in the bucket. The balance is continuously weighing it, which provides α_{global}.

7.3 Local measurement techniques

7.3.1 Gas concentration measurement - Optical fiber

The optical fiber probe technique has been widely used in bubbly flows (Martinez Mercado *et al.* [68], van den Berg *et al.* [69], Guet *et al.* [70], Xue *et al.* [71], Mudde & Saito [157], Xue *et al.* [158], Luther *et al.* [159], Wu *et al.* [160]). For measuring the local gas fraction inside the flow, a custom made optical glass fiber probe (0.37 NA Hard Polymer Clad Multimode Fiber, Thorlabs Inc., diameter of 200μm) is used. The optical probe is a local phase detection device. Light emitted by a LED is sent through one end of the optical fiber. When the light reaches the other end of the fiber ("tip") part of the light is reflected. The reflection coefficient depends on the refractive index of the phase in which the fiber tip is submerged. For a detailed description of the working principle we refer to Cartellier & Achard [161].

In our case the internally reflected light at the (in-house made spherical dome shaped) probe's tip, see Fig. 7.2a, is collected by a photodiode and is electronically amplified (4pp Electronics, Kramer Laboratories). In all our experiments an acquisition card (National Instruments 6221) samples the fiber signal with 16 bit resolution at a sampling frequency of 120 kHz. The optical probe sticks through a sensor-hole of the outer cylinder with the fiber tip placed inside the TC gap, parallel to the azimuth axis. It is mounted on a manual traversing system with a total radial traveling distance of 27 ± 0.02 mm along the gap, which is around one third of the gap between the cylinders. Fig. 7.2b shows a top view of the gap and the optical probe, made possible due to transparent windows on the end plates of the T^3C.

The accuracy of this technique has been studied in water-air flows by Julia *et al.* [162] with bubbles of diameter 2.8-5.2 mm and velocities 0.22-0.28 m/s (one order of magnitude smaller than in our experiments). The residence time is the time the fiber tip is immersed in one bubble and we refer to it as T_{bubble}. Julia *et al.* [162] report a small underestimation of T_{bubble}, which – according to these authors – is caused by the local deformation of the bubble due to probe-induced liquid pressure over the bubble or due to being hit by the probe in itself. The bubble can possibly also be decelerated or deviated from its path by an upstream high-pressure region induced by the probe's presence. In our experiments the bubble velocities are one order of magnitude larger than in Julia *et al.* [162], and hence they have a larger added mass. Therefore it is less probable that a bubble is decelerated or deviated from its trajectory by the probe's presence.

In Fig. 7.3a a typical voltage signal as acquired in this work is shown. We see many voltage peaks with different heights and widths, each indicating bubble-probe interactions. In Fig. 7.3b a closer look of the voltage signal is shown. What is typically reported in literature is that a signal plateau is reached when the fiber tip has enough time to dewet completely inside the interacting bubble. In our case the

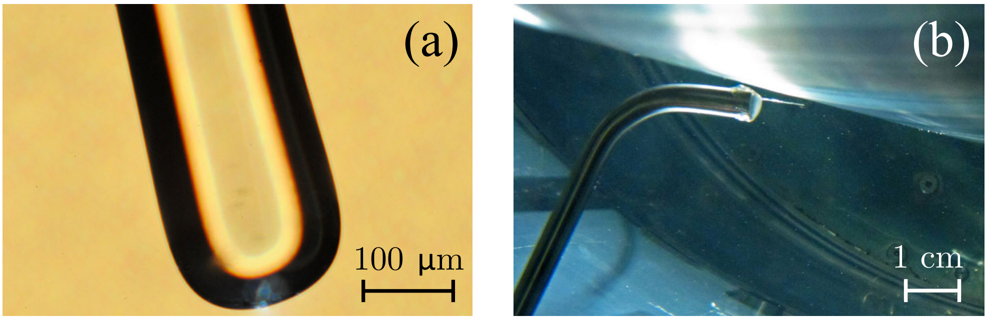

Figure 7.2: (a) Microscopic photograph of the fiber tip. (b) T^3C gap - top view: mounted optical fiber probe to measure the local gas volume fraction close to the IC wall.

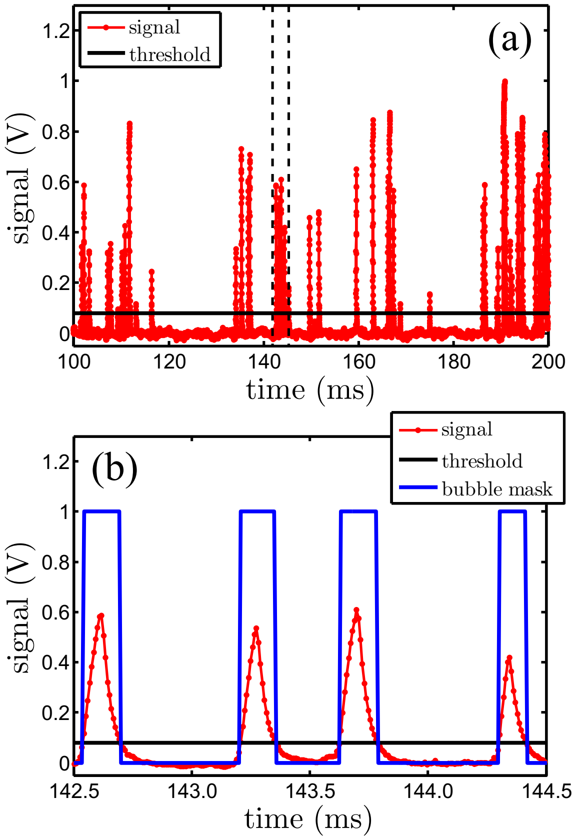

Figure 7.3: (a) Typical voltage signal at $\mathrm{Re} = 1.0 \times 10^6$, $\alpha_{global} = 3\%$. Each peak above the threshold corresponds to the tip immersed in a bubble. (b) Enlarged view of the signal between the dashed lines in (a) showing four typical bubble-probe interactions. The width of the bubble's mask is taken as its residence time T_{bubble}.

bubbles have velocities greater than 2 m/s, leading to smaller signal amplitudes and wedge-shaped signals because the complete dewetting process of the tip does not occur before the tip encounters the water again, as explained by Julia *et al.* [162]. As the edges of the bubble are still clearly detected, the acquired bubble-probe interaction time is not affected by the non-complete dewetting of the tip.

We create a binary bubble mask as indicated by the blue line in Fig. 7.3b by setting a voltage threshold, chosen to be 0.08 V throughout this work, on the detrended voltage signal. The statistics we obtain out of this masking does not depend on the selection of the threshold due to the steep rise and fall times of the bubble-probe interactions. Its value is chosen in order to filter noise out of the signal. Every time the voltage signal rises above and consecutively drops below this threshold, a bubble is counted. The residence time of one bubble T_{bubble} is now given by the corresponding width of the bubble mask. The widths of the peaks depend on the bubble size, the bubble velocity, and also on the point the probe's tip pierces the bubble.

7.3.2 Azimuthal liquid velocity measurement - LDA

Laser Doppler anemometry (LDA) is used to study the fluid's azimuthal velocity component of the two-phase flow. We make use of a LDA system from Dantec Dynamics, consisting of a back-scatter probe head (85 mm probe 60X81) with a beam expander (55X21) of 1.98 expansion and an achromatic front lens of 500 mm focal distance. This results in a measurement volume of dimensions width x height x depth = 0.07 mm x 0.07 mm x 0.3 mm. The probe head is mounted on a custom-built computer controlled traversing system, rigidly attached to the T^{3}C frame. The LDA system further consists of two photomultipliers (57X18) and a burst spectrum analyzer (BSA F80). The seeding particles we use are round and have a density of 1.03 g/cm^3 and a mean diameter of 5 μm (Polyamid seeding particles, PSP-50 Dantec Dynamics).

When applying LDA to our setup the two laser beams in the horizontal plane refract in a non-linear way due to the curved surface of the OC. Therefore the angle between them, θ, depends on the radial position of the focal point when located inside the gap between the cylinders. To correct for the curvature effect, not taken into account in the Dantec software, the measured speed is multiplied by the factor

$$C_\theta = \frac{n_{air}\sin(\theta_{air}/2)}{n_{water}\sin(\theta_{water}/2)} \tag{7.2}$$

where n_{air} and n_{water} are the refractive indices of air and water. θ_{air} and θ_{water} are the angles between beams when found in air or water. We refer to the work of Huisman [72] for a more detailed explanation of the LDA method used in our Taylor-Couette setup.

7.4 Global drag reduction measurements

7.4.1 Measurement procedure

We perform measurements on the global torque τ on the middle section of the inner cylinder (IC_{mid}) as function of the global gas volume fraction α_{global}, with the IC rotating at a fixed rate. We carry out experiments at $\mathrm{Re} = 5.1 \times 10^5$, 1.0×10^6 and 2.0×10^6, corresponding to inner cylinder rotation frequencies of $\omega_i/2\pi = 5.0$, 10, and 20 Hz, respectively. We start each experiment with single phase flow and once temperature stability at $21 \pm 0.1^\circ$ C is achieved, the acquisition of the torque is initiated and the injection of air follows. We start with a small injection rate ~ 1 l/min. Initially nearly all the air bubbles become trapped in the strong turbulent fluctuations of the TC flow with little air escaping into the expansion vessel and hence the global gas volume fraction gradually increases. Eventually the flow becomes saturated with bubbles and a dynamic equilibrium settles in between the volume of air entering and leaving the flow, making α_{global} stable. From now on we increase the injection rate gradually over time forcing more air into the flow until we reach $\alpha_{global} \approx 4\%$. This ramp on α_{global} takes between 25 and 160 minutes depending on the investigated Reynolds number. Higher Reynolds number flow accumulates bubbles faster and hence α_{global} increases more rapidly.

7.4.2 Results

In Fig. 7.4 the dimensional torque data normalized by the torque of the single phase flow $T(0)$ are plotted as function of α_{global}. The general trend of each experiment, carried out at a fixed rotation rate, shows a decrease in dimensional torque for increasing global gas volume fraction α_{global}. Furthermore, the larger the Re number, the more effective is the reduction of the drag. It is remarkable that there is a major DR of 40% at $\mathrm{Re} = 2.0 \times 10^6$ with $\alpha_{global} = 4 \pm 0.5\%$ only, which was not attainable by previous measurements in turbulent Taylor-Couette flows.

In the figure unpublished data from van den Berg *et al.* [61] have been included, carried out on the University of Maryland TC facility, or UMD TC for short. Their data, taken at $\mathrm{Re} = 7.9 \times 10^5$, lies well between the present data of $\mathrm{Re} = 5.1 \times 10^5$ and 1.0×10^6. Thus good agreement for bubbly drag reduction has been found between the present measurements and those by van den Berg *et al.* [61]. Also note the very good repeatability as demonstrated by duplicating measurement series taken at Re $= 5.1 \times 10^5$ and 1.0×10^6.

One could argue that the reduction of torque can be explained by just a change of effective density and viscosity of the liquid due to bubble injection. We show in Appendix 7.8, by introducing a non-dimensional representation of the torque compensating for this density and viscosity dependance on the gas volume fraction, that

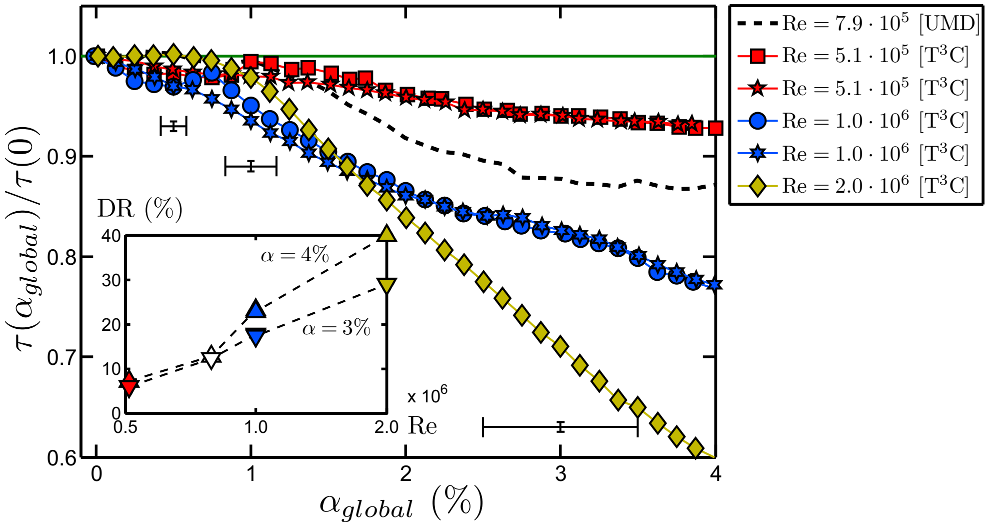

Figure 7.4: Normalized dimensional torque τ as function of α_{global}. Closed symbols are data sets from the present experiments for various fixed Re numbers. The horizontal bars indicate the error of the gas concentration for the present measurements. Data are included from van den Berg *et al.* [61] carried out on the University of Maryland (UMD) TC setup (dashed line). Inset: drag reduction defined as the dimensional torque reduction ratio $\mathrm{DR} = 1 - \tau(\alpha_{global})/\tau(0)$ for various Re numbers at constant α_{global} = 3% and 4%. Colored symbols are the present results, and the open black symbols are results of van den Berg *et al.* [61].

this dependance can not account for the DR as observed in the strong DR regime by at least a factor of 2 in the $\mathrm{Re} = 5.1 \times 10^5$ case and a factor of 4 in the 1.0×10^6 case. The bubbles must modify the flow actively in addition to simply changing the fluid properties.

A straightforward way to define the drag reduction is $\mathrm{DR} = 1 - \tau(\alpha_{global})/\tau(0)$, where $\tau(\alpha_{global})$ and $\tau(0)$ are the dimensional torque values of the two-phase and single-phase case, respectively. Using this drag reduction definition, the net, practical effect on the torque is quantified. The inset of the figure shows this DR percentage for the data points at constant $\alpha_{global} = 3\%$ and 4%, as function of Re. van den Berg *et al.* [27] find a pronounced drag reduction for $\mathrm{Re} \gtrsim 6 \times 10^5$, and weak drag reduction for Re less than this. The present measurements show a similar result: strong drag reduction for $\mathrm{Re} = 1.0 \times 10^6$ and 2.0×10^6, and moderate drag reduction for $\mathrm{Re} = 5.1 \times 10^5$. The DR is about 6% at $\mathrm{Re} = 5.1 \times 10^5$ for $\alpha_{global} = 3 \pm 0.5\%$, and the DR at $\mathrm{Re} = 1.0 \times 10^6$ is about 18% for the same gas concentration. We will focus on these two cases for the local measurements, the smaller one ($\mathrm{Re} = 5.1 \times 10^5$) corresponding to the moderate DR regime and the larger one ($\mathrm{Re} = 1.0 \times 10^6$) falling into the strong DR regime.

7.5 Local measurements

Based on the global DR results we select two cases, one falling into the moderate DR regime and one into the strong DR regime, of which we will study the local flow profiles and bubble concentrations inside the TC flow. The two cases we study are Re $= 5.1 \times 10^5$, corresponding to the moderate DR regime, and Re $= 1.0 \times 10^6$, falling into the strong DR regime, both at a global gas volume fraction of $\alpha_{global} = 3 \pm 0.5\%$. To provide the reader with a qualitative sense of how such flows look like, we present high-speed image snapshots of the two examined Re-cases in Fig. 7.5.

We will present profiles on the local azimuthal liquid velocity and the local gas concentration, both scanned in the radial direction at middle height of the TC cell. Profiles at two other axial positions for the Re $= 1.0 \times 10^6$ case were also taken, which we present separately in Appendix 7.9.

7.5.1 Measurement procedure

The global gas volume fraction is maintained at a constant $\alpha_{global} = 3.0 \pm 0.5\%$ for both cases of constant Re $= 5.1 \times 10^5$ and 1.0×10^6, corresponding to IC rotation rates of 5.0 and 10 Hz, respectively. The temperature of the liquid is maintained at 21 ± 0.5°C.

The local gas concentration profiles are scanned with the optical fiber probe which is logged by an acquisition card (National Instruments PCI-6221) with 16 bit resolution at a sampling frequency of 120 kHz during 300 s for each radial position. The measurement time of 300 s is chosen to ensure statistical convergence. The first radial position is as far from the IC wall as the traversing system allows, which is ≈ 27 mm from the IC wall and roughly one-third into the gap towards the OC. In around 20 evenly radially distributed steps we scan up to the last radial position, which is as close as the probe's tip can safely be to the IC wall, i.e. down to 0.03 mm. The profile of Re $= 1.0 \times 10^6$ is measured twice to demonstrate repeatability.

The local azimuthal liquid velocity profiles are scanned by particle image velocimetry (PIV) in the pure single-phase case (details to be published elsewhere) and by laser Doppler anemometry (LDA) in the two-phase case. Both techniques provide the full radial profiles apart from the near-wall boundary layers which presently we cannot resolve. The profiles acquired with LDA consist of around 40 equally distributed radial positions. The number of detected Doppler burst for each radial position ranges from 6×10^3 to 50×10^3 for Re $= 5.1 \times 10^5$, and from 28×10^3 to 50×10^3 for Re $= 1.0 \times 10^6$. The inner radial positions are increasingly harder to probe with LDA due to the visual shielding of the bubbles. Hence we achieve an average data acquisition rate of ≈ 20 Hz close to the IC, going up to > 500 Hz when entering the bulk flow region.

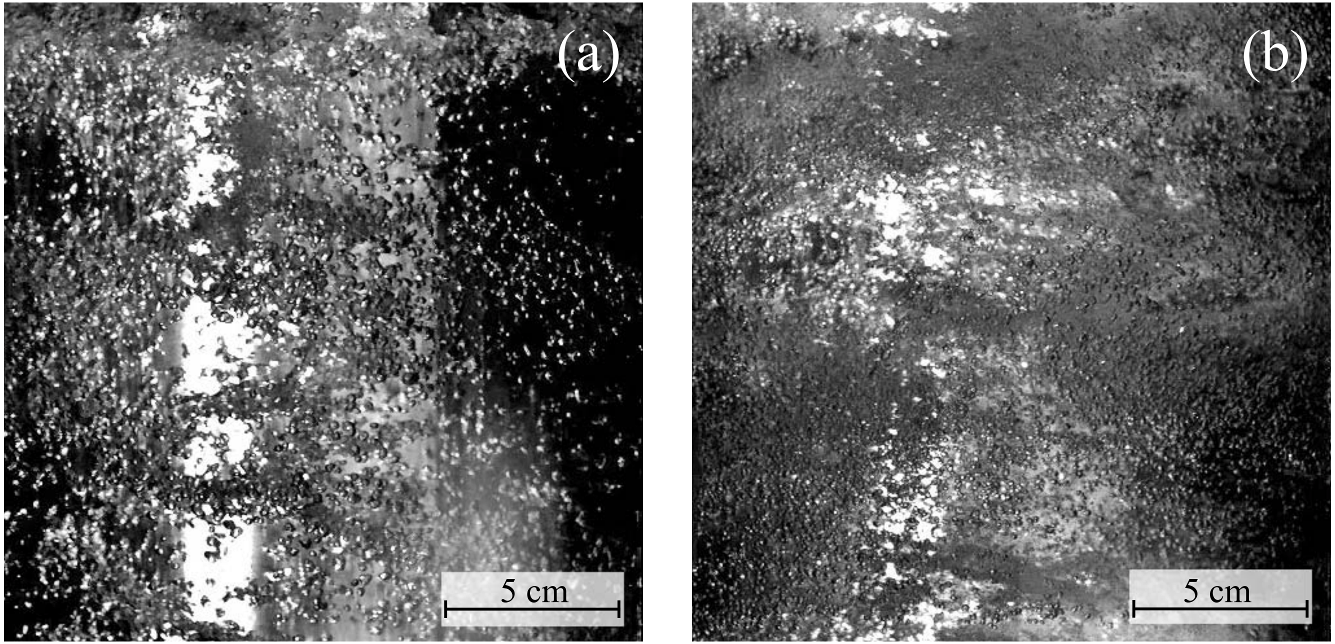

Figure 7.5: High-speed images of the bubbly turbulent flow taken through the transparent OC of the T^{3}C facility for the two locally examined DR regimes at $\alpha_{global} = 3 \pm 0.5\%$. (a) Re $= 5.1 \times 10^5$, (b) Re $= 1.0 \times 10^6$.

7.5.2 Results

Azimuthal liquid velocity profiles

Firstly, we study how the liquid velocity is modified by the injected bubbles in the two different Re-cases by comparing the single-phase case to the two-phase case. We measure the time-averaged local azimuthal velocity $\langle U_\theta(r)\rangle_t$ and the standard deviation of the local azimuthal velocity fluctuations $u'_\theta(r)$. Throughout the rest of the paper we will work with the non-dimensional gap distance $\tilde{r} \equiv (r - r_i)/(r_o - r_i)$, with 0 indicating the IC wall and 1 indicating the OC wall. The results are displayed in Fig. 7.6 with (a) the mean velocity normalized by the IC wall velocity, which is $U_i = 6.28$ m/s for Re $= 5.1 \times 10^5$ and $U_i = 12.6$ m/s for Re $= 1.0 \times 10^6$, and (b) the standard deviation of the normalized velocity fluctuations. The solid lines are the single-phase cases as measured by PIV and the colored symbols are data on the two-phase cases obtained by LDA. LDA measurements were also performed on the single-phase cases and they are found to be in good agreement (within 0.6%) of the PIV data, but they are left out of the plot as PIV has superior spatial resolution.

The rescaled mean velocity profiles in Fig. 7.6a fall on top of each other in the single-phase flow case for both Reynolds numbers. The bubbles clearly destroy this similarity. Since we do not have enough spatial resolution to resolve the boundary layers, we will focus on the bulk regime taken as $0.2 < \tilde{r} < 0.8$. The mean azimuthal velocity profiles for both the single and two-phase cases follow roughly the same shape in the bulk. The reduction of the bulk azimuthal velocity due to the bubble injection is $\approx 4\%$ at Re $= 5.1 \times 10^5$ and $\approx 12\%$ at Re $= 1.0 \times 10^6$. This is not unexpected as this velocity reduction should reflect the torque reduction ratio on the IC wall.

As shown in Fig. 7.6b, the standard deviation of the normalized velocity fluctuations are nearly identical in the single-phase flow case for both Reynolds numbers. For the bubbly flow we observe an increase in u'_θ as compared to that of the single-phase flow at radial locations $\tilde{r} \lesssim 0.3$, i.e. close to the IC. For the higher Re-case this increment is stronger. The next step is too determine whether the local increase in the velocity fluctuations can be linked to the spatial distribution of the bubbles.

Local bubble size

Out of the fiber probe data we compute the histogram of the bubble residence time T_{bubble} at each radial position. Figure 7.7 shows typical probability density functions (pdf's) for three non-dimensional gap distances $\tilde{r}$ at Re $= 1.0 \times 10^6$. As can be appreciated, the mode of the pdf's (defined here as the average of the bubble residence time corresponding to normalized probabilities higher than 0.85) is displaced to the right the more distant the fiber tip is located from the IC. This is to be expected since the azimuthal flow velocity drops with increasing radius. By multiplying the mean

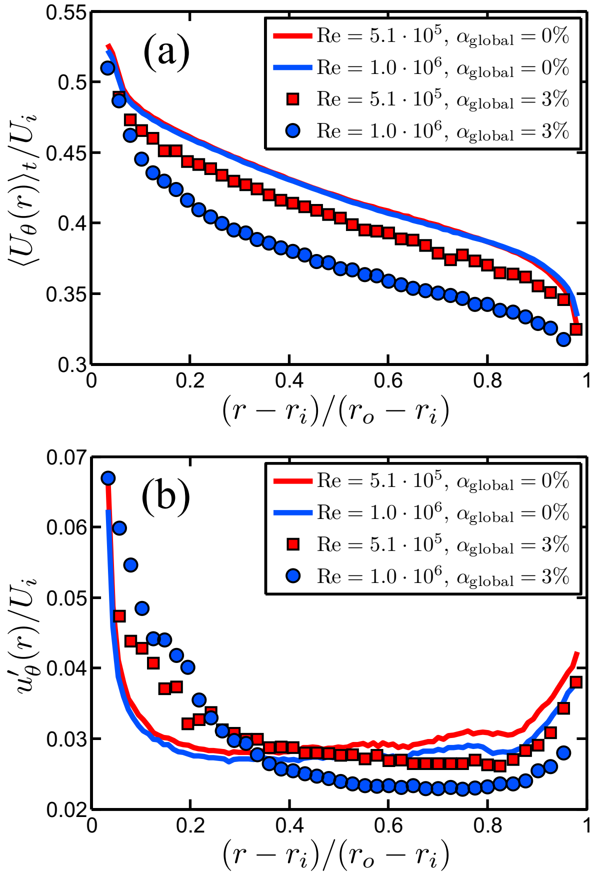

Figure 7.6: The radial profiles of (a) the azimuthal liquid mean velocity normalized by the velocity of the inner wall U_i and (b) the standard deviation of the normalized velocity fluctuations, both at middle height of the TC cell. The solid lines are obtained by PIV and the colored symbols are obtained by LDA.

azimuthal liquid velocity of the bubbly flow from Fig. 7.6a with the pdf's mode of the bubble residence time for each radial position, the mean (horizontal) bubble diameter as function of the gap distance $\langle D_{bubble}(r) \rangle_t$ is computed.

Figure 7.8a presents these calculated local mean bubble diameters and we report an overall larger mean bubble diameter of 1.3 mm for the $\mathrm{Re} = 5.1 \times 10^5$ case as compared to 0.9 mm for the $\mathrm{Re} = 1.0 \times 10^6$ case due to the stronger shear in the latter. The size of the bubbles weakly depend on the radial position. We also use high-speed image recordings to measure the bubble size optically at one radial position (focusing at a distance $\tilde{r} \approx 0.3$) for each Reynolds number. Out of the high-speed imaging we report for $\mathrm{Re} = 5.1 \times 10^5$ an average diameter of 1.8 mm with a standard deviation of

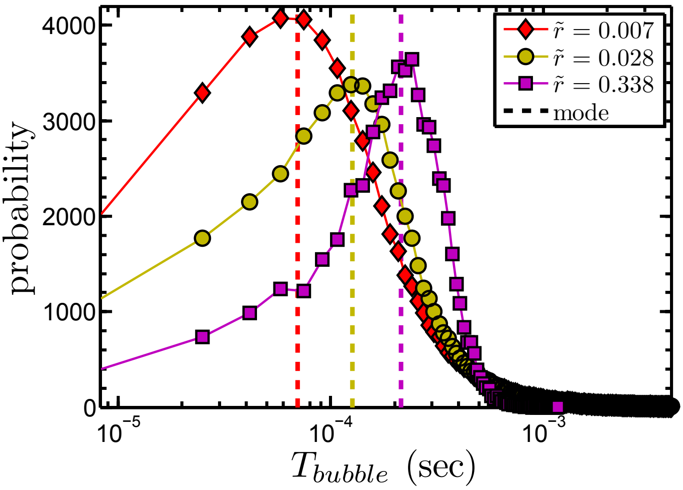

Figure 7.7: Probability density functions of the bubble residence time acquired by the optical fiber probe for Re $= 1.0 \times 10^6$ at three non-dimensional gap distances $\tilde{r} = (r - r_i)/(r_o - r_i)$. The mode of the pdf increases with increasing $\tilde{r}$.

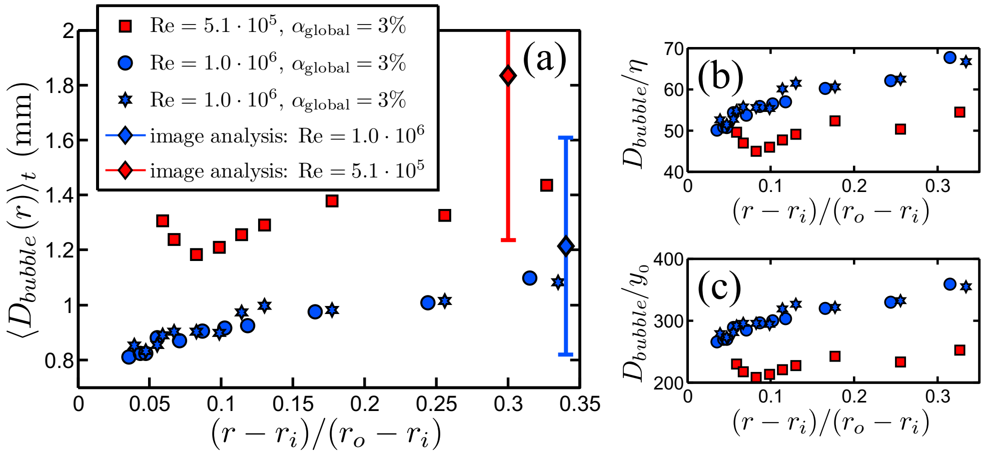

Figure 7.8: (a) Calculated local mean bubble diameter obtained from the optical fiber signals and the LDA velocity profiles. The diamonds with the error bars are the results from image analysis. (b) Mean bubble diameter expressed in the Kolmogorov length scale η and (c) expressed in the wall unit y_0.

0.6 mm, taken over 234 in-focus bubbles. For $\mathrm{Re} = 1.0 \times 10^6$ the average diameter is 1.2 mm with a standard deviation of 0.4 mm, taken over 144 focused bubbles. The high-speed imaging results are plotted as the diamond symbols with the vertical error bars indicating the standard deviation. It confirms the order of magnitude of the estimated bubble diameter from the optical fiber signals. The imaging results also show that the bubbles in the lower Re-case are less homogeneous in size as its standard deviation is higher than that for the higher Re-case.

We now compare in Figs. 7.8b and 7.8c the local mean bubble diameter to the Kolmogorov length scale η and the wall unit y_0, both calculated out of the globally measured torque of the single-phase flow at the corresponding Re-numbers, see Lathrop *et al.* [10], Eckhardt *et al.* [23] for the definitions. In the radial region of $0.05 < \tilde{r} < 0.35$ the bubble diameter in the moderate DR case is around 50 η or 230 y_0, and in the strong DR case it is around 60 η or 300 y_0, similar to what has been reported by van den Berg *et al.* [27].

Gas concentration profiles

We calculate the time-averaged local gas volume fraction as a function of the radial position out of the bubble mask obtained from the fiber probe data (see Sec. 7.3.1) by summing over all bubble residence times and dividing this by the total measurement time, i.e.

$$\langle \alpha(r) \rangle_t = \frac{\sum_{i=1}^{N_{bubbles}} T_{bubble,i}}{T_{total}}, \tag{7.3}$$

with $N_{bubbles}$ the total number of detected bubbles. The resulting radial profiles on the gas concentration are shown as percentages in Fig. 7.9a. We stress the good quality of repeatability as made apparent by the two independently measured and nonetheless collapsing profiles at $\mathrm{Re} = 1.0 \times 10^6$.

Fig. 7.9a clearly shows that the bubbles tend to accumulate close to the IC boundary regime for both Reynolds numbers. This phenomena is not surprising as in centrifugally driven flow there is in average a favorable pressure gradient, pushing the bubbles towards the center of rotation, here with an acceleration $a_{cent}(r) = U_\theta^2/r$ equal to $\sim 3g$ for $\mathrm{Re} = 5.1 \times 10^5$, and $\sim 9g$ for $\mathrm{Re} = 1.0 \times 10^6$. For this estimate we took the measured azimuthal liquid velocity at the center of the TC gap.

Next, we discuss the radial distance from the IC wall $r_{\alpha_{\max}}$ at which the gas concentration is maximum, $\alpha_{\max} \equiv \max\{\langle \alpha(r) \rangle_t\}$. For $\mathrm{Re} = 5.1 \times 10^5$ this distance is $r_{\alpha_{\max}} \approx 1.2$ mm, equivalent to $\tilde{r} \approx 0.016$. For the higher Re-case it is located at $r_{\alpha_{\max}} \approx 0.6$ mm, equivalent to $\tilde{r} \approx 0.008$. The value of $r_{\alpha_{\max}}$ for each Reynolds number is close to the respective mean bubble diameter as presented in Fig. 7.8a. However, from our measurements we cannot conclude that the $r_{\alpha_{\max}}$ we measure is the correct radial distance at which the true maximum gas volume fraction occurs

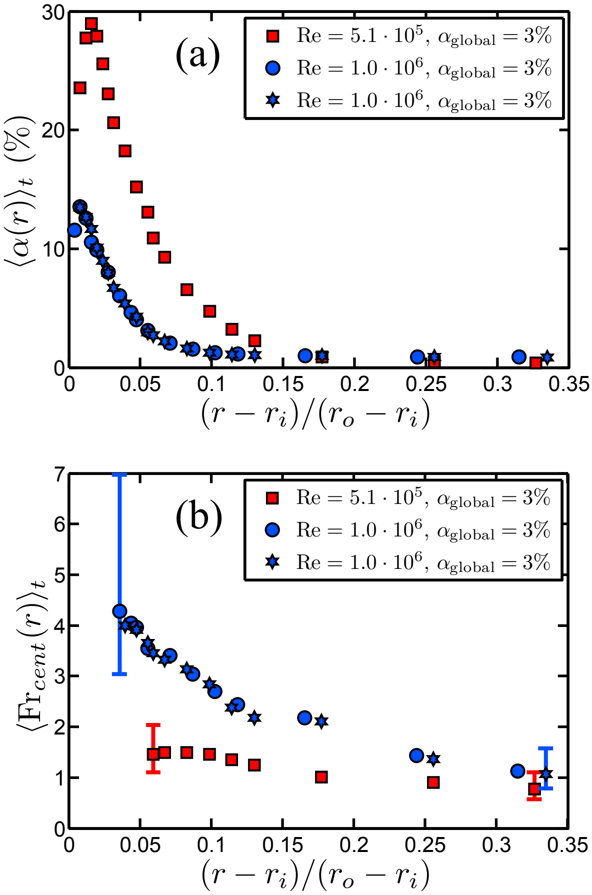

Figure 7.9: Radial profiles at mid-height of the two examined DR regimes: moderate DR at $\mathrm{Re} = 5.1 \times 10^5$ and strong DR at $\mathrm{Re} = 1.0 \times 10^6$, both at a global gas volume fraction $\alpha_{global} = 3 \pm 0.5\%$, (a) local gas concentration and (b) local centripetal Froude number.

along the gap. It could be the case that the (intrusive) fiber probe, when located very near the IC wall, pushes the bubbles away from the tip due to an induced up-flow high pressure region and hence underestimates $\langle \alpha(r) \rangle_t$. Further experiments are required to measure this aspect in detail.

Finally, we compare the amplitude of the maximum local gas concentration for these two Reynolds numbers. For $\mathrm{Re} = 1.0 \times 10^6$ we find $\alpha_{\max} \approx 13\%$, whereas for $\mathrm{Re} = 5.1 \times 10^5$ it arrives to about 30%, which is 2.3 times higher. To understand this difference we now evaluate the local Froude number.

If the flow were fully laminar then *all* the bubbles would be pushed against the IC wall due to the radial pressure gradient associated with the centrifugally driven flow. With the addition of sufficiently strong turbulent liquid velocity fluctuations the bubbles will experience pressure fluctuations, leading the bubbles to be pulled away from the wall into the bulk of the flow. We estimate the relative importance of the pressure fluctuations' induced acceleration acting on the bubbles $a_{press\ fluct}$ as compared to the centripetal acceleration $a_{cent}(r)$ by introducing a 'centripetal Froude number',

$$\mathrm{Fr}_{cent}(r) = \frac{a_{press\ fluct}}{a_{cent}(r)} = \frac{u'^2/D_{bubble}}{U_\theta^2/r}, \tag{7.4}$$

with u' the standard deviation of the liquid velocity fluctuations, U_θ the mean azimuthal liquid velocity, D_{bubble} the bubble diameter and r the radial position to be considered.

For u' we take the azimuthal liquid velocity fluctuations $u'_\theta(r)$ of the two-phase LDA data, see Fig. 7.6. Taking only the azimuthal component for u' is sound as Burin *et al.* [111] and Huisman [72] report the same order of magnitude for the three cylindrical components of the liquid velocity fluctuations inside turbulent single-phase TC flow as measured by multi-component LDA. We assume that this similarity can also be applied to the two two-phase flow cases. For D_{bubble} we take the time-averaged radial profile $\langle D_{bubble}(r)\rangle_t$ as shown in Fig. 7.8. Because we use the local time-averaged profiles of each of these quantities, we can calculate the local time-averaged Froude number $\langle \mathrm{Fr}_{cent}(r)\rangle_t$ which is presented in Fig. 7.9b. For both Re-cases we find $\mathrm{Fr}_{cent} \gtrapprox 1$ and hence the turbulent fluctuations are strong enough to pull the bubbles against the centripetal force towards the bulk region of the flow away from the inner wall, which explains the spatial broadening around the gas concentration maxima of Fig. 7.9a.

Now we evaluate the local Fr_{cent}-number at the radial position $r_{\alpha_{\max}}$ to understand the different $\alpha_{\max}$ for each Re-case. The closest we can get is $\tilde{r} \approx 0.06$ for which we find $\mathrm{Fr}_{cent} \sim 1.5$ for $\mathrm{Re} = 5.1 \times 10^5$ and $\mathrm{Fr}_{cent} \sim 3.5$ for $\mathrm{Re} = 1.0 \times 10^6$. The lower Re-case has a lower Fr_{cent}-number by a factor of 2.3, indicating that the *effective* centripetal force on the bubbles is higher and hence, the bubble accumulation is stronger near the IC wall at the expense of a lower concentration in the bulk, as observed. The Fr_{cent}-number ratio matches the maximum gas concentration ratio between both Re-cases.

What is remarkable is the following: one would expect that the DR efficiency is correlated to the bubble concentration near the inner wall, and that a higher local gas volume fraction should give a larger DR. However, the present measurements show an opposite trend: the local gas concentration near the inner wall is higher in the moderate DR regime than that in strong DR regime. This clearly suggests that the higher local gas concentration near the inner wall does not guarantee a larger DR. What then is the dominant effect for the strong DR at the high Reynolds numbers? To answer this question we will follow van den Berg *et al.* [27] and now look into bubble deformability and thus the local Weber number.

Local Weber number

Following van den Berg *et al.* [27], we define the bubble Weber number as

$$\mathrm{We} = \frac{\rho u'^2 D_{bubble}}{\sigma}, \tag{7.5}$$

with u' the standard deviation of the velocity fluctuations and σ the surface tension of the bubble-liquid interface. Relation (7.5) is identical[†] to what it used in van den Berg *et al.* [27].

For u' we take the azimuthal liquid velocity fluctuations $u'_\theta(r)$ of the two-phase LDA data, see Fig. 7.6b, following the same reasoning as used for the Fr_{cent}-number estimation in section 7.5.2. For D_{bubble} we use the local time-averaged bubble diameter $\langle D_{bubble}(r)\rangle_t$ of the optical fiber probe data, see Fig. 7.8a. Substituting the values $\rho = 998$ kg/m^3 and $\sigma = 0.0727$ N/m, corresponding to water at 21°C, provides us now with the local time-averaged Weber number of the bubbles inside the TC gap, scanned over 1/3 of the radius close to the IC at middle height of the TC cell. We present these $\langle \mathrm{We}(r)\rangle_t$ profiles for the two examined DR regimes in Fig. 7.10.

The vertical error bars show the Weber number variation due to the uncertainty in the velocity fluctuations and the bubble size at those $\tilde{r}$. For $\mathrm{Re} = 1.0 \times 10^6$ we see $\mathrm{We} > 2$ and that the bubbles increasingly deform when approaching the IC wall, where the liquid velocity fluctuations are stronger, finally leading to $\mathrm{We} \sim 8$ closest to the inner wall. The bubble Weber number for $\mathrm{Re} = 5.1 \times 10^5$ remains lower and it remains nearly constant with a value around 1. This implies that the bubbles remain nearly spherical although they are larger (1.3 mm) than those for the higher Re-case (0.9 mm), because in the former the velocity fluctuations are not strong enough to deform the bubbles. At $\mathrm{Re} = 5.1 \times 10^5$, with nearly spherical bubbles, the global DR is around 6% whereas the DR is about 18% for the case of $\mathrm{Re} = 1.0 \times 10^6$ with bubbles of higher deformability. The results thus clearly demonstrate that the bubble deformability is crucial for the observed strong DR, which is consistent with the findings by van den Berg *et al.* [27] and van den Berg *et al.* [61], based on their global torque measurements, and by Lu, Fernandez & Tryggvason [28], based on their numerical calculations. Here we provide a solid evidence on the crucial role of the bubble deformability for strong DR in bubbly turbulent TC flow.

[†] Few typographical errors appear in van den Berg *et al.* [27]: the Weber number definition lists the radius of the bubble R_b while it should read the bubble diameter D_{bubble}. This concerns Eq. 4 and the Weber number definition three lines above it. Also the abstract should read '$R = 0.5$ mm' as the value of the used bubble radius, and in the conclusion the statement '$R_b = 42\eta = 300y_0$' should read '$R_b = 21\eta = 150y_0$'. The rest of the values, including the right-hand side of Eq. 4, and the graphs they present are correct.

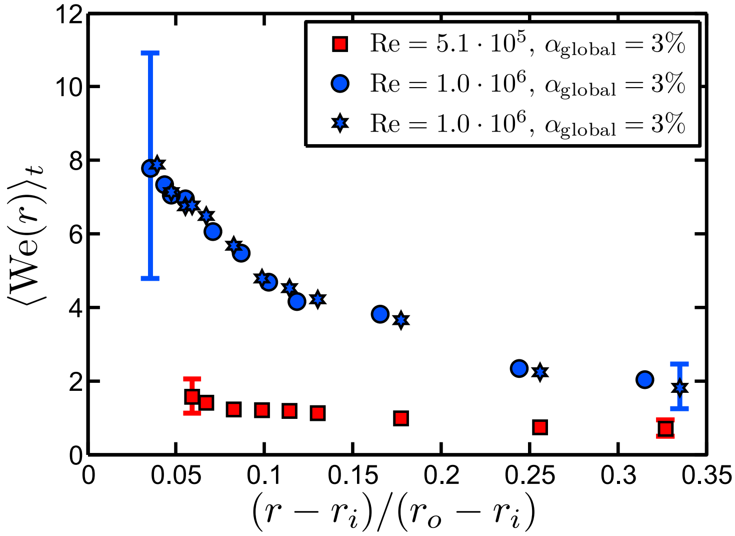

Figure 7.10: Local Weber number profiles at of the two examined drag reduction regimes: moderate DR at Re $= 5.1 \times 10^5$ and strong DR at Re $= 1.0 \times 10^6$.

7.6 Conclusion

We have shown that the net DR, based on global dimensional torque measurements in bubbly turbulent TC flow with pure inner rotation up to Re $= 2.0 \times 10^6$, increases with increasing global gas volume fraction $\alpha_{global} \leq 4\%$ and that the efficiency of the DR increases for increasing Reynolds numbers. We find a net DR of remarkably 40% obtained at $\alpha_{global} = 4 \pm 0.5\%$ for Re $= 2.0 \times 10^6$, which was not attainable by previous TC setups. The present measurements at Re $= 5.1 \times 10^5$ and 1.0×10^6 show good agreement with previous measurements from van den Berg *et al.* [61]. We observe a moderate DR for Re $= 5.1 \times 10^5$ up to 7%, and a strong DR for Re $= 1.0 \times 10^6$ and 2.0×10^6 up to 23% and 40%, respectively.

We chose two Re-numbers that each fall into a different DR regime and study the flow locally at fixed $\alpha_{global} = 3 \pm 0.5\%$. The smaller one, Re $= 5.1 \times 10^5$, represents the moderate DR regime at DR = 6% and the larger one, Re $= 1.0 \times 10^6$, represents the strong DR regime at DR = 18%.

We investigated the azimuthal liquid velocity in the single and two-phase flow for each Re. The amplitude of the mean azimuthal velocity in the bulk ($0.2 < \tilde{r} < 0.8$) for the bubbly flow decreases ≈ 4% at Re $= 5.1 \times 10^5$, and ≈ 12% at Re $= 1.0 \times 10^6$ as compared to that of the single-phase case. These reduction ratios match the global torque reduction ratios. Furthermore, we measured increased liquid velocity fluctuations close to the IC in both two-phase cases as compared to their equivalent single-phase case. This increase was linked to the spatial distribution of the bubbles.

The local gas concentration measurements show that the bubbles tend to accumulate close to the IC boundary regime for both Re-numbers. This can be explained by the centrifugally driven flow pushing the bubbles towards the IC wall with an acceleration of around 3 to 9 g. The velocity fluctuations are strong enough to pull the bubbles towards the bulk of the flow again, as expressed by the centripetal Froude number $\mathrm{Fr}_{cent} \gtrapprox 1$. The radial distance from the IC wall at which we find the maximum local gas concentration is close to the respective bubble diameter. Surprisingly, the maximum local gas concentration at $\mathrm{Re} = 5.1 \times 10^5$, i.e. in the moderate DR regime, is much higher than that at $\mathrm{Re} = 1.0 \times 10^6$, i.e. in the strong DR regime. While we find a match between the local $\mathrm{Fr}_{cent}(r)$ and the maximum gas concentration near the inner wall explaining this huge concentration difference, this finding clearly suggests that the higher local gas concentration near the inner wall does not guarantee a larger drag reduction.

By directly measuring the local Weber number $\mathrm{We}(r)$ of the bubbles, we conclude that the larger liquid velocity fluctuations deform the smaller bubbles of $D_{bubble} \approx 0.9$ mm in the strong DR regime at $\mathrm{Re} = 1.0 \times 10^6$ since $\mathrm{We} > 2$. The local Weber number increases with decreasing distance from the inner wall, reaching $\mathrm{We} \sim 8$ close to the inner wall. This suggests that the deformation of the bubbles is stronger near the IC wall, where a large amount of bubbles gather. In the moderate DR regime at $\mathrm{Re} = 5.1 \times 10^5$ the bubbles remain close to spherical because $\mathrm{We} \sim 1$ in the bulk and near the inner boundary, even though they are larger in size with $D_{bubble} \approx 1.3$ mm.

We conclude that increasing the gas volume fraction has a positive influence on the azimuthal liquid velocity decrease, which is responsible for the observed drag reduction. What is really crucial for strong DR is that bubbles deform ($\mathrm{We} > 1$) close to the boundary layer regime of the IC wall, leading to a large azimuthal velocity decrease and thus a strong DR. These local results match the conclusion on the global torque results as found by van den Berg *et al.* [27] and van den Berg *et al.* [61], and on the numerical results by Lu, Fernandez & Tryggvason [28].

7.7 Discussion & outlook

7.7.1 Taylor-Couette flow

Both the two-phase cases at $\mathrm{Re} = 5.1 \times 10^5$ and $\mathrm{Re} = 1.0 \times 10^6$ show a pronounced increase in the liquid azimuthal velocity fluctuations $u'_\theta(\tilde{r})$ close to the inner cylinder wall at $\tilde{r} \lesssim 0.3$ when compared to the corresponding single-phase cases, see Fig. 7.6b. As both the Fr_{cent}- and We-number rely heavily on $u'_\theta(\tilde{r})$, it is important to know the cause of this increase. The local $u'_\theta(\tilde{r})$ increase is clearly linked to the bubble distribution as the local gas concentration rises significantly for both Re-cases in the radial region $\tilde{r} \lesssim 0.1$, although it does not extend to $\tilde{r} \lesssim 0.3$, see Fig. 7.9a. To support the increase of $u'_\theta(\tilde{r})$ in the region $0.1 < \tilde{r} < 0.3$ we reason that — either the inner region of high gas concentration causes turbulent bubble laden structures to be shed (incidentally as no periodicity has been found in the bubble signal time series at any of the examined radial locations) into the region $0.1 < \tilde{r} < 0.3$ — or $u'_\theta(\tilde{r})$ as induced from the inner region of high gas concentration is 'diffused' outwards into $0.1 < \tilde{r} < 0.3$. What causes the induction of higher $u'_\theta(\tilde{r})$ due to the presence of bubbles in the first place, is however still not discussed.

The difficulty is that we enter a coupled problem: bubbles are drawn into a radial distribution as dictated by $\mathrm{Fr}_{cent}(\tilde{r})$ and at the same time the magnitude of $\mathrm{Fr}_{cent}(\tilde{r})$ is determined by the velocity fluctuations induced by the presence of bubbles. And likewise the effect of bubble deformability could also influence the velocity fluctuations' strength. The effect of bubble deformability can be taken out of the discussion by injecting *rigid* neutrally buoyant particles into the flow, instead of using bubbles, similar to what was used in experiments by van den Berg *et al.* [27] to investigate bubbly TC flow on a global level. One could also further study above problem by changing the Fr_{cent}- and We-number independently of each other. This can be achieved by changing the liquid density ρ as it enters the We-definition but not the Fr_{cent}-definition. Note that changing the surface tension σ will not results in independently changing Fr_{cent} from We as a different surface tension results in a different mean bubble diameter, which enters both the Fr_{cent} and We definition again.

In this present work the bubble diameter is linked to the driving control parameter Re, because the shear strength of the flow dominates the bubble size. One can achieve a different coupling between the Reynolds number and the bubble size by adding a low concentration of surfactant into the bubble carrier liquid. Even small concentrations of surfactant are known to significantly increase the effective surface tension of the liquid/bubble interface as it results in changing the bubble surface boundary condition from a slip to a no-slip condition, see e.g. the review article by Takagi & Matsumoto [163]. Different low concentrations of different surfactants can result in a variety of mean bubble sizes and deformability, and hence different We. Of course, the huge shear strength of our flows will still play a role. Surfactants also prevent bubble coalescence and lead to a more monodisperse bubble size distribution, both aiding the simplicity of the flow. We assume that adding small amounts of surfactants will not change the turbulent flow properties, which should be tested experimentally. The bubble deformability and the connection to the global torque DR can be further studied in bubbly turbulent TC flow.

So far we have examined bubbly turbulent TC flow by only rotating the inner cylinder and keeping the outer cylinder at rest. The flow profile inside the TC gap becomes completely different once outer cylinder rotation is activated, which is elaborated on in chapter 4. In the co-rotation regime the flow will become less turbulent and is hence not the first choice to examine. In the case of counter-rotation the flow will experience more shear and a ‘neutral line’, i.e. the radial position where the mean angular velocity is zero, will exist inside the TC gap, thereby changing the overall radial pressure gradient induced by the centrifugal force. This could have a pronounced effect on the bubble distribution, possibly allowing indirect control of the radial position of maximum gas concentration $r_{\alpha_{\max}}$ from the boundary layer region towards the bulk region. The effect of changing the bubble distribution profile on the global torque should be examined further.

7.7.2 Wall-bounded flows

Other flow geometries that are widely used to study air-induced DR are channel and flat-plate flows, see the review article by Ceccio [54]. The air phase can be injected as bubbles, like as in the current work, or an air sheet or cavity can be generated along the top plate of the channel, or likewise underneath the flat plate. Gravity will hence act in favor of pushing the air towards the underside of the top surface. Given the mean flow velocity U and appropriate length scale d — in the case of bubbly flow d can be set to the mean bubble diameter, for air sheets or air cavities d can be chosen as the maximum sheet length or cavity length, respectively — one can define a Froude number as $\mathrm{Fr} = U/\sqrt{gd}$, comparing the buoyancy effect to the mean flow velocity. This Froude number definition bears great resemblance to the centripetal Froude number of two-phase TC flow, see Eq. (7.4). Whereas for channel/plate flow geometry gravity acts in favor of pushing the air towards the underside of the (top) plate, likewise for TC flow the centripetal force pushes air towards the inner cylinder wall. Both Froude-number definitions decrease as indication of stronger favorable air accumulation along the wall.

Now how do all the different wall-bounded flow geometries (TC flow/channel flow/flat plate flow) relate to each other in the single-phase case? When we assume fully developed turbulent single-phase flow then, of course, all these wall-bounded flows have compatible boundary layer structures. The channel and plate flows are most conveniently described in a rectangular coordinate system, whereas centrifugally driven TC flow is best described in cylindrical coordinates. This is reflected in the mathematical description of the boundary layers, and we refer to section VII of Lathrop *et al.* [10] for the modeling of the boundary layers in turbulent TC flow in cylindrical coordinates. At constant driving strength and in combination with a constantly maintained fluid temperature, turbulent TC flow results in a statistically stationary flow state. To be specific: No mean velocity gradient exists in the streamwise (azimuthal) direction and the boundary layer thicknesses of the inner and outer cylinder walls remain constant. This can be in contrast to the channel and flat-plate geometries where measurements could take place in *developing* boundary layers along the streamwise direction. If one would like to compare the bubbly DR results of channel/flat plate flows with developing boundary layers against TC flow, then one should simulate a developing boundary layer in the TC flow. This can be achieved by repeated statistically stationary TC experiments over which the driving strength, i.e. the inner and outer Reynolds number, is increased leading to different boundary layer thicknesses. By means of post-processing these repeated experiments can then be integrated along the Re-axis to simulate a developing boundary layer.

7.7.3 Application towards ships

One of the complications towards practical application of bubble induced skin-friction DR on ships is keeping the bubbles in the boundary layer regime of the hull, not only at the bubble injection point but also downstream of it. An alternative approach to air induced DR is the creation of air cavities underneath the flat bottom of a ship, trapping the pockets of air. Air cavities can also be created and studied in bubbly TC flow by attaching annular strips at several axial locations onto the otherwise smooth inner cylinder surface, in combination with air injection through the inner cylinder wall. As similar to what is stated in section 7.7.2: The role of gravity in the applied ship-case is now resembled by the centripetal force in TC flow, pushing air into the annular cavities. We expect to observe major slip of the inner cylinder as a decoupling between the wall and bulk fluid will be created by the air sheet captured in the cavities.

7.8 Appendix A: Non-dimensional torque reduction ratio

When injecting bubbles into a liquid, for small gas concentrations the effective kinematic viscosity and density of the two-phase fluid can be respectively approximated as follows:

$$\rho_{\alpha_{global}} = \rho(1-\alpha_{global}), \tag{7.6}$$

$$\nu_{\alpha_{global}} = \nu(1+\frac{5}{2}\alpha_{global}), \tag{7.7}$$

where α_{global} is the global gas volume fraction, and ρ and ν are the density and viscosity of the liquid at $\alpha_{global} = 0$. The "Einstein" equation (7.7) (Einstein [136]) is a first order approximation only and assumes the dispersed phase to be non-self-interacting and to be of the same density as the carrier phase. Though the applicability becomes questionable at the bubbly turbulent flows with up to 8% gas concentration, we will use (7.7) throughout this work.

To estimate the magnitude of the torque reduction, purely caused by the change of fluid properties when injecting bubbles into the flow, we define a non-dimensional

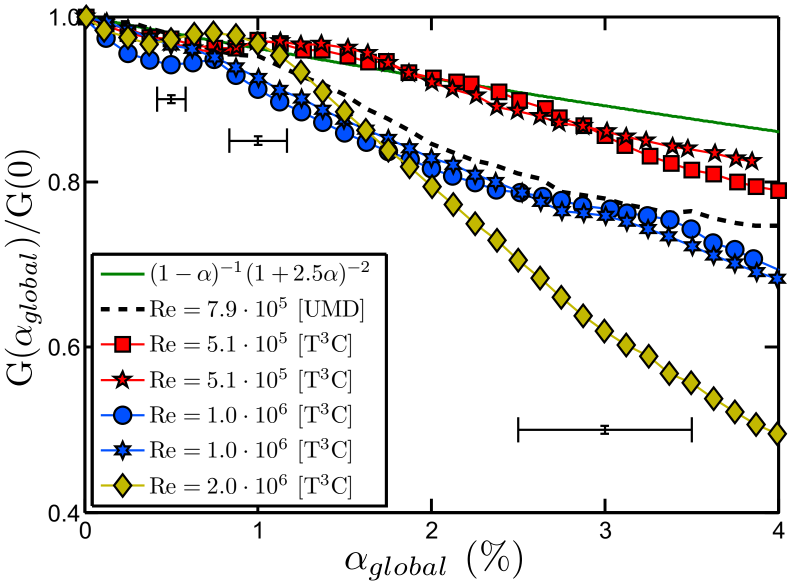

Figure 7.11: Normalized non-dimensional torque G as function of α_{global}. This figure shows an alternative representation of the data in Fig. 7.4. The thick green line shows the analytical dependence of α_{global} on the density and viscosity terms of the normalized non-dimensional torque.

torque based on the two-phase viscosity and density as:

$$G(\alpha_{global}) = \frac{\tau}{2\pi\rho_{\alpha_{global}} \nu^2_{\alpha_{global}} L_{mid}} = \frac{\tau}{2\pi\rho(1-\alpha_{global})\nu^2(1+\frac{5}{2}\alpha_{global})^2 L_{mid}}, \quad (7.8)$$

with τ as the measured torque on the middle section of the IC. We focus on the effect of bubbles on the torque and neglect the change of the Reynolds number.

The experimental results on the non-dimensional torque reduction are plotted in Fig. 7.11, comparable to the dimensional torque presented in Fig. 7.4. The reason for the shift in the UMD data can be contributed to a different fluid temperature of 24 °C. The solid green curve represents the analytical dependence of α_{global} on the density and viscosity terms of the normalized non-dimensional torque. Therefore, the difference between the solid green curve and each of the measured curves tells us the contribution to the DR that is not solely caused by a change of fluid properties. This difference is close to zero for all curves when α_{global} lies between 0 and 1%. In the case of Re $= 5.1\times10^5$ the difference remains very small even up to $\alpha_{global} \approx 2.5\%$, but it increases significantly when $\alpha_{global} > 1\%$ for Re $= 1.0\times10^6$ and 2.0×10^6. Hence, the bubbles in the strong DR regime must modify the flow actively in addition to simply changing the fluid properties.

7.9 Appendix B: Axial dependence at $\mathrm{Re} = 1.0 \times 10^6$

We also investigate the axial dependence of the flow at $\mathrm{Re} = 1.0 \times 10^6$ with $\alpha_{global} = 3 \pm 0.5\%$. The outer cylinder provides three locations through which the optical probe can be inserted. These are located at $z_{mid} = L/2$, $z_{bot} = z_{mid} - 15$ cm and $z_{top} = z_{mid} + 15$ cm, see Fig. 7.12. We will first focus on the mean azimuthal liquid velocity profiles $\langle U_\theta(r) \rangle_t$ at these locations, which are presented in Fig. 7.13.

For the single-phase case we find no axial dependence over the examined range as the mean velocity profiles are identical to within 0.7%. Hence we represent the single-phase case as the single blue solid line. When we inject bubbles into the flow we observe a weak axial dependence on the mean azimuthal velocity, see the colored symbols. The relative amplitude difference in the bulk of the flow for the z_{top} and z_{bot} profiles is $\pm 4\%$ when compared to the z_{mid} profile. Can this be linked to the bubble distribution?

So next we examine the corresponding gas concentration profiles, see Fig. 7.14. We note an increase in the maximal value of the local gas concentration $\langle \alpha(r) \rangle_t$ for increasing height. Between z_{top} and z_{mid} and between z_{mid} and z_{bot} there is a factor ≈ 2.7 difference. These increments in gas volume fraction can be due to two factors: more bubbles or bigger bubbles.

Hence we calculate, in the same manner as described in Sec. 7.5.2, the local bubble diameter individually for each axial position, see the inset of Fig. 7.14. No axial dependence on the bubble size is found. When we consecutively calculate the bubble detection rate for each axial position, we indeed find a match to the maximum gas volume fractions.

The reason for this strong axial gradient on the gas volume fraction becomes apparent when exploring the following force balance. Let g denote the standard gravity: we find that the bubbles experience a centripetal acceleration U_θ^2/r of $\sim 9g$ in the bulk of the flow as compared to the $1g$ of axial upward acceleration due to buoyancy. These factors are not well enough apart to neglect the influence of gravity on the gas distribution.

We conclude that the local gas concentration strongly depends on the axial position, however, the liquid velocity profiles change only weakly. This suggests that the azimuthal velocity reduction is not sensitive to the local gas concentration along the axial direction.

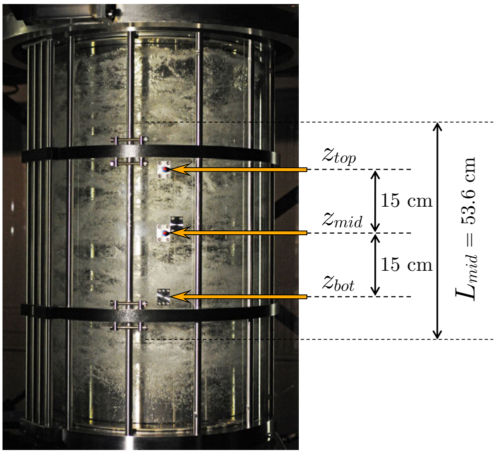

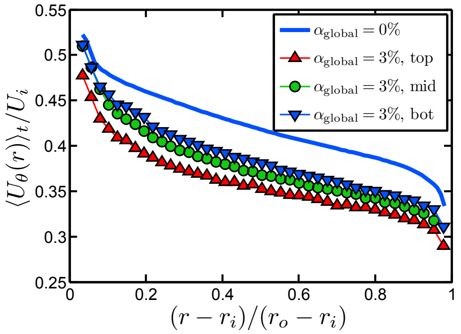

Figure 7.12: Snapshot of the T^{3}C setup at Re $= 1.0 \times 10^6$ and α_{global} = 3%. The axial measurement locations are tagged.

Figure 7.13: The radial profiles of the liquid azimuthal mean velocity normalized by the IC wall velocity U_i at different axial locations.

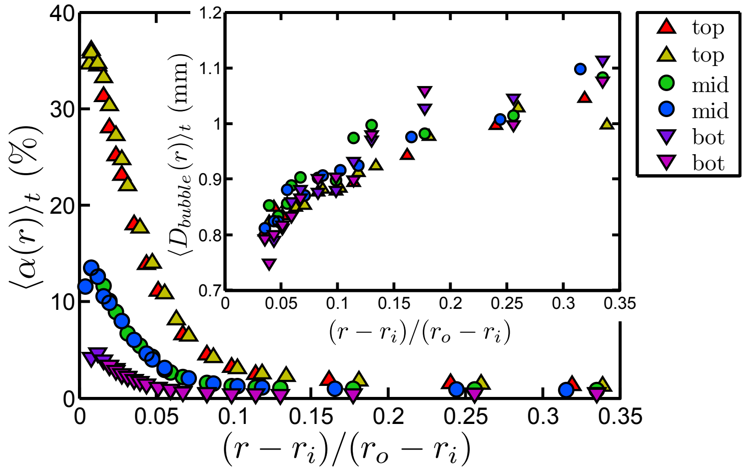

Figure 7.14: Local gas concentration profiles at three axial positions in the flow at Re $= 1.0 \times 10^6$ and α_{global} = 3%. Inset: corresponding local mean bubble diameter. Two independent measurements are performed at each height to show the measurement repeatability.

— PART IV —

Conclusions

8

Conclusions and Outlook

In this thesis we studied various aspects of highly turbulent Taylor-Couette (TC) flow using a combination of experimental and theoretical techniques. In PART I we introduced the new turbulent TC facility of our Physics of Fluids group, called the T^3C for short. In PART II we focused on single-phase TC flow between independently rotating cylinders, and in particular on the associated angular velocity transport. And in PART III we added an extra dimension to TC flow by injecting air bubbles into turbulent TC flow and studying the bubbles' effects on the flow and the relation to skin-friction drag reduction. The most important conclusions for each part of this thesis are summarized below by answering the questions that were formulated in the introduction. When appropriate an outlook on future research is given at the end of each section.

8.1 Part I — Experimental setup

The Twente turbulent Taylor-Couette facility

In chapter 2 we presented in detail the features of this new TC facility and we demonstrated the accuracy of the main control and response parameters, such as rotation rate stability within 0.01% of the setpoint (Fig. 2.4), temperature control within 0.1K (Fig. 2.6) and torque sensing (Fig. 2.9). Laser Doppler anemometry (LDA) measurements can be successfully performed on this facility as we demonstrated perfect agreement between the solid-body rotation flow profile as measured by LDA and the theoretically expected profile (Fig. 2.10).

8.2 Part II — Single-phase TC flow

Torque scaling in turbulent Taylor-Couette flow with co- and counter-rotating cylinders

- Does a universal scaling law between Nu_ω and Ta exist, i.e. is γ constant in $Nu_\omega = \text{prefactor}(a) \times Ta^\gamma$ over the investigated range?
- If so, what is the amplitude of the prefactor as function of a?
- And at what a does maximum transport of angular velocity occur?

Indeed, in the investigated high Reynolds-number regime we found a universal scaling of $Nu_\omega \propto Ta^{0.38}$ when scanning the (Re_i, Re_o) parameter space along the diagonals of fixed $a \equiv -\omega_o/\omega_i$ between $-0.4 < a < 2$. It is remarkable that the effective scaling exponent $\gamma \approx 0.38$ exactly resembles the analogous effective scaling exponent in $Nu \propto Ra^{0.38}$ in RB convection in the ultimate regime of thermal convection [24, 25], reflecting the analogy between TC and RB flow also in the strongly turbulent regime. Figure 3.5 shows the amplitude of the prefactor as function of a, obtained by averaging $Nu_\omega/Ta^{0.38}$ over the investigated Ta-range per a-case as shown in Fig. 3.4b. The maximum transport occurred at $a_{opt} \approx 0.4$, indicating that slight counter-rotation improves the transport of angular velocity from the inner to the outer cylinder wall.

Optimal Taylor-Couette turbulence

By extending the angular velocity transport measurements of the previous chapter with a higher resolution in a, we found that the experimental data are well captured by the common power law ansatz $Nu_\omega(Ta,a) = f(a) \cdot Ta^\gamma$, with $\gamma = 0.39 \pm 0.03$ as can be seen in Fig. 4.5. The a-dependence on the amplitude of the angular velocity transport is given by $f(a) = Nu_\omega(Ta,a)/Ta^{0.39}$, as shown in Fig. 4.6, and we observed maximum transport at $a_{opt} = 0.368$.

- Does the prediction $Nu_\omega \sim Ta^{1/2} \times$ log-corrections match the observations?

Yes, as can be seen in Fig. 4.5a the prediction is practically indistinguishable from the observed effective scaling law $Nu_\omega \propto Ta^{0.39}$ when the log-corrections $\mathscr{L}$ are taken as $\mathscr{L}(Re_w(Ta))$ with the wind Reynolds number $Re_w = 0.0424 \times Ta^{1/2}$ as experimentally found by Huisman *et al.* [95]. This result again strengthens the analogy between the RB and the TC system as the prediction originates from the RB system as $Nu \propto Ra^{1/2} \times$ log-corrections given by Grossmann & Lohse [26].

- Can we give an interpretation of the maximum in $f(a)$?
- How does this maximum depend on the radius ratio η?

The mutual importance of 1) the shear enhancement of the flow and 2) the stabilizing effect on the flow, due to outer cylinder rotation is reflected in the a-dependence of $f(a)$. When starting off counter-rotation, i.e. when increasing a beyond zero, the angular velocity transport does not reduce but instead is first further enhanced, due to the enhanced shear, before finally, beyond $a = a_{opt} = 0.368$, the stabilizing effect of the counter-rotation leads to a reduction of the angular velocity transport Nu_ω.

We expect maximal transport for all points in the (Re_i, Re_o) parameter space, which are equally distant from both the right branch (1^{st} quadrant of Fig. 4.3, co-rotation) of the instability border and its left branch (2^{nd} quadrant of Fig. 4.3, counter-rotation). In inviscid approximation these two branches are the Rayleigh lines given by the relations $a = -\eta^2$ and $a = \infty$, respectively. The line of equal distance from both is the angle bisector of the instability range, which we denote by $a_{bis}(\eta)$ and is given by Eq. (4.8) and plotted in Fig. 4.7b. For $\eta = 0.716$ this gives $a_{bis} = 0.368$ which is identical to the value of $a_{opt} = 0.368$ within our experimental resolution. It needs to be tested whether $a_{bis}(\eta)$ also predicts optimal transport for *all* η.

- What is the connection between the transport Nu_ω and the mean $\langle\omega(r)\rangle_t$ profiles?

From Fig. 4.8 it is seen that the slope of $\langle\omega(r)\rangle_t$ in the bulk is negative for all measured cases of $-0.30 \leq a \leq 2.00$ except for $a = 0.40$ in which the slope equals zero. The case of $a = 0.40$ is, within our LDA a-resolution, the same as a_{opt}. We note that in strongly turbulent RB flow the temperature also has a (practically) zero mean gradient in the bulk, see e.g. Ahlers *et al.* [19]. The rescaled mean angular velocity $\langle\tilde{\omega}(\tilde{r})\rangle_t = (\langle\omega(\tilde{r})\rangle_t - \omega_o)/(\omega_i - \omega_o)$, plotted in Fig. 4.9a, shows a 'phase' transition around a_{opt} for the mid-gap value $\langle\tilde{\omega}(1/2)\rangle_t$ as shown in Fig. 4.9b: The mid-gap mean angular velocity consists of the relative contributions of the cylinder walls as $\approx 0.35\omega_i + 0.65\omega_o$ for weak counter-rotation $a < a_{opt}$ and the relative contribution of the inner cylinder starts to increase for stronger counter-rotation $a > a_{opt}$.

- What are the relative contributions of the convective and viscous parts of the angular velocity flux J^ω per individual case of a?

For all investigated a-cases the convective contribution dominates the viscous contribution by far with values beyond 99%, see Fig. 4.10. At $a = a_{opt}$ the convective contribution even reaches 100% as the gradient $\partial_r\langle\omega\rangle_t$ becomes zero. This special situation perfectly resembles RB turbulence for which, due to the absence of a mean temperature gradient in the bulk, the whole heat transport is conveyed by the convective term.

- What is the radial position of zero angular velocity, i.e. $\langle\omega(r)\rangle_t = 0$ or the so called 'neutral line', in the counter-rotation cases $a > 0$?

Figure 4.11 shows the measured radial position of the neutral line $\tilde{r}_n$ for the examined turbulent profiles as compared to $\tilde{r}_n$ corresponding to the equivalent laminar profiles. Again we see two regimes: For $0 < a < a_{opt}$ in the laminar case the stabilizing outer cylinder rotation shifts the neutral line inwards, but due to the now (i.e. in the turbulent case) *free boundary* between the stable outer cylinder r-range and the unstable range between the neutral line and the inner cylinder, the flow structures extend beyond the laminar $\tilde{r}_n$. The increased shear and the strong turbulence activity originating from the inner cylinder rotation are too strong and push the neutral line towards the outer kinematic boundary layer. For $a > a_{opt}$ the stabilizing effect from the outer cylinder rotation is strong enough so that a neutral line $\tilde{r}_n$ can be detected in the bulk of the TC flow.

- How does the turbulent flow organization change for different a?

For the cases $a > a_{opt}$, for which we observed a neutral line in the bulk of the flow, we found a bimodal probability distribution of the instantaneous angular velocity around $\tilde{r}_n$, as compared to the otherwise unimodal distribution of the angular velocity in the bulk for $a < a_{opt}$, see Figs. 4.13 to 4.18. We interpret this intermittent behavior as an indication of turbulent bursts originating from the turbulent region in the vicinity of the inner cylinder and penetrating into the stabilized region near the outer cylinder.

- Does the prediction by Eckhardt, Grossmann & Lohse [23] on the boundary layer ratio fall in line with our approximations?

The a-cases near $a_{opt} = 0.368$, namely $0.2 \leq a \leq 1.0$, showed good agreement, whereas the outlying a-cases showed some disagreement, as can be seen in Fig. 4.20b. Given the crude boundary layer approximation of extrapolating the experimental results as depicted in Fig. 4.19, is it remarkable that we found some good agreement.

Outlook
We point the reader to the open issues as listed on page 72.

Angular momentum transport and turbulence in laboratory models of Keplerian flows

The T^{3}C and UMD TC facility were used to scan the (Re, R_Ω) parameter space as shown in Fig. 5.2, with the total Reynolds number Re as given by Eq. (5.1), and R_Ω as the rotation number comparing shear to overall rotation (Dubrulle *et al.* [75]) given by Eq. (5.2). To clarify: The (Re, R_Ω) space can be projected onto (Ta, a) space, but the former is preferred by the astrophysical community. Both facilities measured the torques associated to flows of constant R_Ω. The cases of $R_\Omega \leq -1$, equivalent to $a \leq -0.512$ for the used T^{3}C radius ratio of $\eta = 0.716$, indicate quasi-Keplerian flow, similar to Ji *et al.* [109].

- Do quasi-Keplerian TC flows exhibit turbulent viscous dissipation?

Figure 5.3 shows the measured non-dimensional torque G against Re. All the examined flows, including the quasi-Keplerian flow, reveal a higher torque than the theoretical value for purely laminar flow. This is an indication that the fluid is turbulent and that the angular momentum transport is enhanced by turbulent viscous dissipation.

- What is the amplitude of the non-dimensional momentum transport inside the TC apparatuses, in specific for quasi-Keplerian profiles?

The non-dimensional angular momentum transport amplitude is presented in Fig. 5.4 as the ratio of G over $G_0 \equiv G(Re, R_\Omega = 0)$. This renormalization scheme allows for the nice collapse of data obtained from different TC facilities of different radius ratios η. The data shows maximal transport at $R_\Omega = -0.10$. For quasi-Keplerian flows $R_\Omega \leq -1$ the transport amplitude is still $\approx 14\%$ of this maximum, indicating that angular momentum is transferred hydrodynamically.

- Does the accretion rate $\dot{M}$ deduced from the TC experiments match the observed accretion rates as found in astrophysical disks?

We used the procedure as outlined in section 5.3.2 to deduce the normalized accretion rate $\dot{M}/\dot{M}_o$ from the global torque measurements. It was found that $\dot{M}/\dot{M}_o = 10^{-3}$, consistent with values observed in disks around TTauri stars [108], see Table 5.2.

- Can TC flow correctly simulate the astrophysical disk flows, taking into account finite-size effects?

Ideally, TC flow should be envisioned as flow in between two infinitely long cylinders. In practice one has a restriction on the length of the cylinders, leading to finite-size effects such as Ekman circulation. The normalized torques G/G_0 as presented in Fig. 5.4 originate from a wide variety of TC apparatuses. If the effects of Ekman circulation on the torque were to play an important role, than one would expect systematic discrepancies between the different data sources. As all the normalized torques agree quite well over the different apparatuses, we claim that our measured torques cannot be solely attributed to finite-size effects. Furthermore, the T^{3}C and UMD TC facility only acquire the torque acting on the mid-section of the inner cylinder. The flow at mid-gap along this section has been shown to not exhibit an axial dependence on the azimuthal velocity as presented in Fig. 5.7, which otherwise could be taken as an indication of significant finite-size effects.

Outlook

The effects of the axial boundaries on the global torque measurements have only been characterized for inner cylinder rotation and not for co- or counter-rotation.

Additional local velocity measurements in the co- and counter-rotating regime are helpful in this case. Furthermore, additional independent torque measurements in the quasi-Keplerian regime should be provided. This regime can be accessed by the T^{3}C facility with the use of viscous oil as the employed liquid, thereby increasing the torque towards our torque sensitivity range.

8.3 Part III — Bubbly TC flow

Bubbly turbulent drag reduction is a boundary layer effect

- Does the injection of large bubbles still lead to DR when the TC walls are step-like roughened hence preventing a smooth turbulent boundary layer to develop?

When injecting bubbles up to a gas volume fraction of $\alpha = 8\%$ in TC flow at $Re \approx 2.5 \times 10^5$ we observed a DR of up 28% in the case of smooth walls, whereas for step-like roughened walls we did *not* observe DR, see Fig. 6.2 for the dimensional torque reduction. In the rough-walls case the structure of the viscous BLs and, thus, the energy injection mechanism into the system seem to be so strongly modified that the mechanism for bubbly DR can no longer be active. Hence, bubbly turbulent DR is a BL effect.

Bubble deformability is crucial for strong drag reduction in turbulent Taylor-Couette flow

We observed DR when injecting bubbles with diameters ~ 1 mm up to global gas volume fractions of $\alpha_{global} = 4\%$ into turbulent TC flow at Re between 10^5 and 2×10^6, with a remarkable maximal observed DR of 40% at $\alpha_{global} = 4\%$ for $\mathrm{Re} = 2 \times 10^6$.

- Do we observe the same DR behavior as found by van den Berg *et al.* [27]?
- Does the trend of increasing DR with increasing *Re* continue in our experiments?

The DR results based on the global dimensional torque under influence of bubble injection can be found in Fig. 7.4. Indeed, we observed the same behavior as found by van den Berg *et al.* [27] on the UMD TC setup as compared to the current work on the T^{3}C setup. The trend of increasing DR with increasing *Re* was found to continue for $\alpha_{global} \gtrsim 1\%$ up to the maximum explored value of $\alpha_{global} = 4\%$. The two cases we used to study the local properties of the flow, i.e. $Re = 5.1 \times 10^5$ in the moderate DR regime and $Re = 1.0 \times 10^6$ in the strong DR regime, both at $\alpha_{global} = 3 \pm 0.5\%$, resulted in a DR of 6% and 18%, respectively.

- How do the bubbles in the two two-phase flow cases change the liquid azimuthal flow profile with respect to the single-phase case?
- What is the local gas concentration profile across the TC gap for the two cases?
- Does the amplitude of the gas concentration profiles match the Fr_{cent} profiles?

As shown in Fig. 7.6a the mean azimuthal velocity in the bulk of the flow at mid-height of the TC gap diminished by $\approx 4\%$ and $\approx 12\%$ under influence of bubble injection at $\alpha_{global} = 3\%$ for the cases of $Re = 5.1 \times 10^5$ and $Re = 1.0 \times 10^6$, respectively, when compared to their equivalent single-phase flow velocity profile. This is not unexpected as this velocity reduction should reflect the torque reduction ratio on the IC wall. The standard deviation on the azimuthal velocity fluctuations, presented in Fig. 7.6b, showed significantly increased amplitudes close to the IC at $\tilde{r} \lesssim 0.3$ for both cases. This matches the observed radial region of preferred bubble accumulation $\tilde{r} \lesssim 0.1$, as can be seen in Fig. 7.9a. Remarkably, the maximum gas concentration $\alpha_{\max}$, which for both cases is roughly located within one bubble diameter from the IC wall with $\alpha_{\max} \approx 30\%$ for $Re = 5.1 \times 10^5$ and $\alpha_{\max} \approx 13\%$ for $Re = 1.0 \times 10^6$, is 2.3 times higher for the moderate DR case than for the strong DR case. We explained this difference in $\alpha_{\max}$ for both cases satisfactorily by introducing the local centripetal Froude number, presented in Fig. 7.9b. Moreover, apparently: a higher local gas concentration near the wall does not necessarily result in stronger DR. A different mechanism must hence be active.

- Do the measured local Weber number profiles match the assumption that bubble deformability is the dominant mechanism behind strong DR in turbulent TC flow?

The local Weber number profiles can be found in Fig. 7.10. Indeed, the bubbles in the strong DR case deformed more ($We > 2$, with $We \sim 8$ when approaching the IC wall) than in the moderate DR regime ($We \sim 1$ throughout the scanned gap) although the mean reported bubble diameter is smaller in the former case ($D_{bubble} \approx 0.9$ mm) as compared to the latter ($D_{bubble} \approx 1.3$ mm), see Fig. 7.8. It is the liquid velocity fluctuations strength that dictates the Weber number amplitude. So, we found confirmation to above question and we conclude that bubble deformability is crucial for strong DR in turbulent TC flow.

Outlook

As detailed in section 7.7 it would be worthwhile to add surfactants to the bubbly flow in order to alter the mean bubble diameter and bubble deformability dependence on the Reynolds number. Furthermore, the coupling between the velocity fluctuations and the preferred bubble distribution as expressed by Fr_{cent}, and the coupling between the velocity fluctuations and the bubble deformability We, should be examined in more detail; one could study this problem by changing the density of the liquid. Lastly: Air cavities could be investigated in turbulent TC flow and it could be compared against flat-plate/channel cavity flows. Air cavities in TC flow can be achieved by attaching annular strips around the inner cylinder at fixed axial locations in combination with gas injection into these cavities out of the inner cylinder itself.

References

References

[1] TAYLOR, G. I., *Stability of a viscous liquid contained between two rotating cylinders*. Philos. Trans. R. Soc. London, Ser. A **223**, 289 (1923).

[2] DIPRIMA, R. C. & SWINNEY, H. L., *Instabilities and transition in flow between concentric rotating cylinders*. Hydrodynamic Instabilities and the Transition to Turbulence (ed. H. L. Swinney & J. P. Gollub), Springer, New York pp. 139–180 (1981).

[3] ANDERECK, C. D., LIU, S. S. & SWINNEY, H. L., *Flow regimes in a circular Couette system with independently rotating cylinders*. J. Fluid Mech. **164**, 155 (1986).

[4] DOMINGUEZ-LERMA, M. A., CANNELL, D. S. & AHLERS, G., *Eckhaus Boundary and Wavenumber Selection in Rotating Couette-Taylor Flow*. Phys. Rev. A **34**, 4956 (1986).

[5] WENDT, F., *Turbulente Strömungen zwischen zwei rotierenden konaxialen Zylindern*. Arch. Appl. Mech. **4**, 577–595 (1933).

[6] TAYLOR, G. I., *Fluid friction between rotating cylinders*. Proc. R. Soc. London A **157**, 546–564 (1936).

[7] SMITH, G. P. & TOWNSEND, A. A., *Turbulent Couette flow between concentric cylinders at large Taylor numbers*. J. Fluid Mech. **123**, 187–217 (1982).

[8] TOWNSEND, A. A., *Axisymmetric Couette flow at large Taylor numbers*. J. Fluid Mech. **144**, 329 (1984).

[9] TONG, P., GOLDBURG, W. I., HUANG, J. S. & WITTEN, T. A., *Anisotropy in turbulent drag reduction*. Phys. Rev. Lett. **65**, 2780–2783 (1990).

[10] LATHROP, D. P., FINEBERG, J. & SWINNEY, H. L., *Transition to shear-driven turbulence in Couette-Taylor flow*. Phys. Rev. A **46**, 6390–6405 (1992).

[11] LATHROP, D. P., FINEBERG, J. & SWINNEY, H. L., *Turbulent flow between concentric rotating cylinders at large Reynolds numbers.* Phys. Rev. Lett. **68**, 1515–1518 (1992).

[12] LATHROP, D. P., *Turbulent Drag and Transport in High Reynolds number Couette-Taylor Flow*. PhD thesis, University of Texas at Austin (1992).

[13] LEWIS, G. S., *Velocity fluctuations, wall shear stress and the transition in torque scaling at Re = 13000 in Turbulent Couette-Taylor flow*. PhD thesis, University of Texas at Austin (1996).

[14] LEWIS, G. S. & SWINNEY, H. L., *Velocity structure functions, scaling, and transitions in high-Reynolds-number Couette-Taylor flow.* Phys. Rev. E **59**, 5457–5467 (1999).

[15] VAN DEN BERG, T. H., DOERING, C., LOHSE, D. & LATHROP, D. P., *Smooth and rough boundaries in turbulent Taylor-Couette flow.* Phys. Rev. E **68**, 36307 (2003).

[16] RAVELET, F., DELFOS, R. & WESTERWEEL, J., *Influence of global rotation and Reynolds number on the large-scale features of a turbulent Taylor-Couette flow.* Phys. Fluids **22**, 055103 (2010).

[17] BORRERO-ECHEVERRY, D., SCHATZ, M. F. & TAGG, R., *Transient turbulence in Taylor-Couette flow.* Phys. Rev. E **81**, 25301 (2010).

[18] PAOLETTI, M. S. & LATHROP, D. P., *Angular momentum transport in turbulent flow between independently rotating cylinders.* Phys. Rev. Lett. **106**, 024501 (2011).

[19] AHLERS, G., GROSSMANN, S. & LOHSE, D., *Heat transfer and large scale dynamics in turbulent Rayleigh-Bénard convection.* Rev. Mod. Phys. **81**, 503 (2009).

[20] LOHSE, D. & XIA, K. Q., *Small-scale properties of turbulent Rayleigh-Bénard convection.* Annu. Rev. Fluid Mech. **42**, 335–364 (2010).

[21] BRADSHAW, P., *The analogy between streamline curvature and buoyancy in turbulent shear flow.* J. Fluid Mech. **36**, 177–191 (1969).

[22] DUBRULLE, B. & HERSANT, F., *Momentum transport and torque scaling in Taylor-Couette flow from an analogy with turbulent convection.* Eur. Phys. J. B **26**, 379–386 (2002).

[23] ECKHARDT, B., GROSSMANN, S. & LOHSE, D., *Torque scaling in turbulent Taylor-Couette flow between independently rotating cylinders.* J. Fluid Mech. **581**, 221–250 (2007).

[24] CHAVANNE, X., CHILLA, F., CASTAING, B., HEBRAL, B., CHABAUD, B. & CHAUSSY, J., *Observation of the ultimate regime in Rayleigh-Bénard convection.* Phys. Rev. Lett. **79**, 3648–3651 (1997).

[25] CHAVANNE, X., CHILLA, F., CHABAUD, B., CASTAING, B. & HEBRAL, B., *Turbulent Rayleigh-Bénard convection in gaseous and liquid He.* Phys. Fluids **13**, 1300–1320 (2001).

[26] GROSSMANN, S. & LOHSE, D., *Multiple scaling in the ultimate regime of thermal convection.* Phys. Fluids **23**, 45108 (2011).

[27] VAN DEN BERG, T. H., LUTHER, S., LATHROP, D. P. & LOHSE, D., *Drag reduction in bubbly Taylor-Couette turbulence.* Phys. Rev. Lett. **94**, 044501 (2005).

[28] LU, J., FERNANDEZ, A. & TRYGGVASON, G., *The effect of bubbles on the wall drag in a turbulent channel flow.* Phys. Fluids **17**, 95102 (2005).

[29] CROSS, M. C. & HOHENBERG, P. C., *Pattern formation outside of equilibrium.* Rev. Mod. Phys. **65**, 851 (1993).

[30] BODENSCHATZ, E., PESCH, W. & AHLERS, G., *Recent developments in Rayleigh-Bénard convection.* Annu. Rev. Fluid Mech. **32**, 709–778 (2000).

[31] CASTAING, B., GUNARATNE, G., HESLOT, F., KADANOFF, L., LIBCHABER, A., THOMAE, S., WU, X. Z., ZALESKI, S. & ZANETTI, G., *Scaling of hard thermal turbulence in Rayleigh-Bénard convection.* J. Fluid Mech. **204**, 1–30 (1989).

[32] GEBHARDT, T. & GROSSMANN, S., *The Taylor-Couette eigenvalue problem with independently rotating cylinders.* Z. Phys. B Condens. Matter **90**, 475–490 (1993).

[33] GLAZIER, J. A., SEGAWA, T., NAERT, A. & SANO, M., *Evidence against ultrahard thermal turbulence at very high Rayleigh numbers.* Nature **398**, 307–310 (1999).

[34] NIEMELA, J., SKRBEK, L., SREENIVASAN, K. R. & DONNELLY, R., *Turbulent convection at very high Rayleigh numbers.* Nature **404**, 837–840 (2000).

[35] BROWN, E., FUNFSCHILLING, D., NIKOLAENKO, A. & AHLERS, G., *Heat transport by turbulent Rayleigh-Bénard convection: Effect of finite top- and bottom conductivity.* Phys. Fluids **17**, 075108 (2005).

[36] SUN, C., REN, L.-Y., SONG, H. & XIA, K.-Q., *Heat transport by turbulent Rayleigh-Bénard convection in 1 m diameter cylindrical cells of widely varying aspect ratio.* J. Fluid Mech. **542**, 165–174 (2005).

[37] DU PUITS, R., RESAGK, C., TILGNER, A., BUSSE, F. H. & THESS, A., *Structure of thermal boundary layers in turbulent Rayleigh-Bénard convection.* J. Fluid Mech. **572**, 231–254 (2007).

[38] AHLERS, G., BODENSCHATZ, E., FUNFSCHILLING, D. & HOGG, J., *Turbulent RayleighBénard convection for a Prandtl number of 0.67.* J. Fluid Mech. **641**, 157 (2009).

[39] STEVENS, R. J. A. M., VERZICCO, R. & LOHSE, D., *Radial boundary layer structure and Nusselt number in Rayleigh-Benard convection.* J. Fluid Mech. **643**, 495–507 (2010).

[40] *See the Focus issue of New Journal of Physics on New Perspectives in High-Rayleigh-Number Turbulent Convection (ed. J. Schumacher & E. Bodenschatz), January* (2011).

[41] COLES, D., *Transition in circular Couette flow.* J. Fluid Mech. **21**, 385–425 (1965).

[42] PFISTER, G. & REHBERG, I., *Space dependent order parameter in circular Couette flow transitions.* Phys. Lett. **83**, 19–22 (1981).

[43] MULLIN, T., CLIFFE, K. A. & PFISTER, G., *Unusual time-dependent phenomena in Taylor-Couette flow at moderately low Reynolds-numbers.* Phys. Rev. Lett. **58**, 2212–2215 (1987).

[44] PFISTER, G., SCHMIDT, H., CLIFFE, K. A. & MULLIN, T., *Bifurcation phenomena in Taylor-Couette flow in a very short annulus.* J. Fluid Mech. **191**, 1–18 (1988).

[45] BUCHEL, P., LUECKE, M., ROTH, D. & SCHMITZ, R., *Pattern selection in the absolutely unstable regime as a nonlinear eigenvalue problem: Taylor vortices in axial flow.* Phys. Rev. E **53**, 4764–4777 (1996).

[46] ESSER, A. & GROSSMANN, S., *Analytic expression for Taylor-Couette stability boundary.* Phys. Fluids **8**, 1814–1819 (1996).

[47] DONG, S., *Direct numerical simulation of turbulent Taylor-Couette flow.* J. Fluid Mech. **587**, 373–393 (2007).

[48] DONG, S., *Turbulent flow between counter-rotating concentric cylinders: a direct numerical simulation study.* J. Fluid Mech. **615**, 371 (2008).

[49] GROSSMANN, S. & LOHSE, D., *Scaling in thermal convection: a unifying theory.* J. Fluid. Mech. **407**, 27–56 (2000).

[50] GROSSMANN, S. & LOHSE, D., *Thermal convection for large Prandtl number.* Phys. Rev. Lett. **86**, 3316–3319 (2001).

[51] GROSSMANN, S. & LOHSE, D., *Prandtl and Rayleigh number dependence of the Reynolds number in turbulent thermal convection.* Phys. Rev. E **66**, 16305 (2002).

[52] GROSSMANN, S. & LOHSE, D., *Fluctuations in turbulent Rayleigh-Bénard convection: The role of plumes.* Phys. Fluids **16**, 4462–4472 (2004).

[53] BUSSE, F. H., *The bounding theory of turbulence and its physical significance in the case of turbulent Couette flow.* Statistical models and turbulence, the Springer Lecture Notes in Physics **12**, 103 (1972).

[54] CECCIO, S. L., *Friction drag reduction of external flows with bubble and gas injection.* Annu. Rev. Fluid Mech. **42**, 183 (2010).

[55] MADAVAN, N. K., DEUTSCH, S. & MERKLE, C. L., *Reduction of turbulent skin friction by microbubbles.* Phys. Fluids **27**, 356–363 (1984).

[56] TAKAHASHI, T., KAKUGAWA, A., MAKINO, M., YANAGIHARA, T. & KODAMA, Y., *A brief report on microbubble experiments using 50-m long flat plate ship*. 74th General meeting of SRI (2000).

[57] KODAMA, Y., KAKUGAWA, A., NAGAYA, S. & KAWAMURA, T., *Drag Reduction of Ships by Microbubbles*. Report of 24th US-Japan Joint Meeting, Marine Facilities Panel of the U.S.-Japan Cooperative Program in Natural Resources (2001).

[58] KODAMA, Y., KAKUGAWA, A., TAKAHASHI, T. & KAWASHIMA, H., *Experimental studies on microbubbles and their applicability to ships for skin friction reduction.* Int. J. Heat Fluid Flow **21**, 582–588 (2000).

[59] MERKLE, C. & DEUTSCH, S., *Microbubble drag reduction*. Frontiers in Experimental Fluid Mechanics – Lecture notes in Engineering, Vol. 46, edited by M. Gad-el-Hak, Springer, Berlin p. 291 (1989).

[60] LATORRE, R., MILLER, A. & PHILIPS, R., *Micro-Bubble Resistance Reduction on a model SES catamaran.* Ocean Eng. **30**, 2297 (2003).

[61] VAN DEN BERG, T. H., VAN GILS, D. P. M., LATHROP, D. P. & LOHSE, D., *Bubbly turbulent drag reduction is a boundary layer effect.* Phys. Rev. Lett. **98**, 084501 (2007).

[62] MURAI, Y., OIWA, H. & TAKEDA, Y., *Frictional drag reduction in bubbly Couette-Taylor flow.* Phys. Fluids **20**, 034101 (2008).

[63] ISO 10816-1:1995, *Part 1: General guidelines: Mechanical vibration – Evaluation of machine vibration by measurements on non-rotating parts*. International Organization for Standardization, Geneva, Switzerland (1995).

[64] SUN, C., MULLIN, T., VAN WIJNGAARDEN, L. & LOHSE, D., *Drag and lift forces on a counter-rotating cylinder in rotating flow.* J. Fluid Mech. **664**, 150–173 (2010).

[65] ZENIT, R., KOCH, D. L. & SANGANI, A. S., *Measurements of the average properties of a suspension of bubbles rising in a vertical channel.* J. Fluid Mech. **429**, 307–342 (2001).

[66] LUTHER, S., RENSEN, J., VAN DEN BERG, T. H. & LOHSE, D., *Data analysis for hot-film anemometry in turbulent bubbly flow.* Exp. Therm. Fluid Sci. **29**, 821–826 (2005).

[67] VAN DEN BERG, T. H., *The effect of bubbles on developed turbulence*. PhD thesis, University of Twente (2006).

[68] MARTINEZ MERCADO, J., CHEHATA GOMEZ, D., VAN GILS, D. P. M., SUN, C. & LOHSE, D., *On bubble clustering and energy spectra in pseudo-turbulence.* J. Fluid Mech. **650**, 287–306 (2010).

[69] VAN DEN BERG, T. H., WORMGOOR, W. D., LUTHER, S. & LOHSE, D., *Phase Sensitive Constant Temperature Anemometry.* Macromol. Mater. Eng. **296**, 230–237 (2011).

[70] GUET, S., FORTUNATI, R. V., MUDDE, R. F. & OOMS, G., *Bubble velocity and size measurement with a four-point optical fiber probe.* Part. Part. Syst. Charact. **20**, 219–230 (2003).

[71] XUE, J., AL-DAHHAN, M., DUDUKOVIC, M. P. & MUDDE, R. F., *Four-point optical probe for measurement of bubble dynamics: Validation of the technique.* Flow Meas. and Instrum. **19**, 293–300 (2008).

[72] HUISMAN, S. G., *Local velocity measurements in Twente Turbulent Taylor-Couette*. Master's thesis, University of Twente (2011).

[73] LANDAU, L. D. & LIFSHITZ, E. M., *Fluid Mechanics*. Oxford: Pergamon Press (1987).

[74] COLES, D. & VAN ATTA, C., *Measured distortion of a laminar circular Couette flow by end effects.* J. Fluid Mech. **25**, 513 (1966).

[75] DUBRULLE, B., DAUCHOT, O., DAVIAUD, F., LONGARETTI, P.-Y., RICHARD, D. & ZAHN, J.-P., *Stability and turbulent transport in Taylor-Couette flow from analysis of experimental data.* Phys. Fluids **17**, 095103 (2005).

[76] LOHSE, D., *Particles go with the flow.* Physics **1**, 18 (2008).

[77] TOSCHI, F. & BODENSCHATZ, E., *Lagrangian Properties of Particles in Turbulence.* Annu. Rev. Fluid Mech. **41**, 375–404 (2009).

[78] LANCE, M. & BATAILLE, J., *Turbulence in the liquid phase of a uniform bubbly air-water flow.* J. Fluid Mech. **222**, 95–118 (1991).

[79] RENSEN, J. M., LUTHER, S. & LOHSE, D., *The effect of bubbles on developed turbulence.* J. Fluid Mech. **538**, 153–187 (2005).

[80] CALZAVARINI, E., KERSCHER, M., LOHSE, D. & TOSCHI, F., *Dimensionality and morphology of particle and bubble clusters in turbulent flow.* J. Fluid Mech. **607**, 13–24 (2008).

[81] ECKHARDT, B., GROSSMANN, S. & LOHSE, D., *Scaling of global momentum transport in Taylor-Couette and pipe flow.* Eur. Phys. J. B **18**, 541–544 (2000).

[82] ECKHARDT, B., GROSSMANN, S. & LOHSE, D., *Fluxes and energy dissipation in thermal convection and shear flows.* Europhys. Lett. **78**, 24001 (2007).

[83] PIRRO, D. & QUADRIO, M., *Direct numerical simulation of turbulent Taylor-Couette flow.* Eur. J. Mech. B-Fluids **27**, 552–566 (2008).

[84] BILSON, M. & BREMHORST, K., *Direct numerical simulation of turbulent Taylor-Couette flow.* J. Fluid Mech. **579**, 227–270 (2007).

[85] MULLIN, T., PFISTER, G. & LORENZEN, A., *New observations on hysteresis effects in Taylor-Couette flow.* Phys. Fluids **25**, 1134–1136 (1982).

[86] RICHARD, D., *Instabilités Hydrodynamiques dans les Ecoulements en Rotation Différentielle*. PhD thesis, Université Paris VII (2001).

[87] VAN HOUT, R. & KATZ, J., *Measurements of mean flow and turbulence characteristics in high-Reynolds number counter-rotating Taylor-Couette flow.* Phys. Fluids **23**, 105102 (2011).

[88] VAN GILS, D. P. M., HUISMAN, S. G., BRUGGERT, G.-W., SUN, C. & LOHSE, D., *Torque scaling in turbulent Taylor-Couette flow with co- and counterrotating cylinders.* Phys. Rev. Lett. **106**, 024502 (2011).

[89] HOLLERBACH, R. & FOURNIER, A., *End-effects in rapidly rotating cylindrical Taylor-Couette flow*. In *MHD Couette flows: experiments and models* (ed. R Rosner, G Rudiger & A Bonanno), *AIP conference proceedings*, vol. 733, pp. 114–121. INAF; Catania Univ; Banca Roma, American Institute of Physics (2004).

[90] TAGG, R., *The Couette-Taylor problem*. Nonlinear Science Today **4**, 1 (1994).

[91] GREENSPAN, H. P., *The theory of rotating fluids*. USA: Breukelen Press (1990).

[92] DOMINGUEZ-LERMA, M. A., AHLERS, G. & CANNELL, D. S., *Marginal stability curve and linear growth rate for rotating Couette-Taylor flow and Rayleigh-Bénard convection.* Phys. Fluids **27**, 856 (1984).

[93] AHLERS, G., FUNFSCHILLING, D. & BODENSCHATZ, E., *Addendum to Transitions in heat transport by turbulent convecion at Rayleigh numbers up to 10^15.* New J. Phys. **13**, 49401 (2011).

[94] HE, X., FUNFSCHILLING, D., NOBACH, H., BODENSCHATZ, E. & AHLERS, G., *Transition to the ultimate state of turbulent Rayleigh-Bénard convection*. Submitted to Phys. Rev. Lett.

[95] HUISMAN, S. G., VAN GILS, D. P. M., GROSSMANN, S., SUN, C. & LOHSE, D., *Ultimate Taylor-Couette turbulence*. Phys. Rev. Lett. (in print), http://arxiv.org/abs/1111.0063.

[96] GROSSMANN, S., *The onset of shear flow turbulence.* Rev. Mod. Phys. **72**, 603–618 (2000).

[97] DUTCHER, C. & MULLER, S., *Explicit analytic formulas for Newtonian Taylor-Couette primary instabilities.* Phys. Rev. E **75**, 047301 (2007).

[98] COUGHLIN, K. & MARCUS, P. S., *Turbulent bursts in Couette-Taylor flow.* Phys. Rev. Lett. **77**, 2214–2217 (1996).

[99] AHLERS, G., BROWN, E., FONTENELE ARAUJO, F., FUNFSCHILLING, D., GROSSMANN, S. & LOHSE, D., *Non-Oberbeck-Boussinesq effects in strongly turbulent Rayleigh-Bénard convection.* J. Fluid Mech. **569**, 409–445 (2006).

[100] AHLERS, G., FONTENELE ARAUJO, F., FUNFSCHILLING, D., GROSSMANN, S. & LOHSE, D., *Non-Oberbeck-Boussinesq effects in gaseous Rayleigh-Bénard convection.* Phys. Rev. Lett. **98**, 54501 (2007).

[101] SUGIYAMA, K., CALZAVARINI, E., GROSSMANN, S. & LOHSE, D., *Flow organization in non-Oberbeck-Boussinesq Rayleigh-Bénard convection in water.* J. Fluid Mech. **637**, 105–135 (2009).

[102] STEVENS, R. J. A. M., LOHSE, D. & VERZICCO, R., *Prandtl and Rayleigh number dependence of heat transport in high Rayleigh number thermal convection*. Submitted to J. Fluid Mech. http://arxiv.org/abs/1102.2307.

[103] SHAKURA, N. I. & SUNYAEV, R. A., *Black holes in binary systems. Observational appearance*. Astron. Astrophys. **24**, 337–355 (1973).

[104] PRINGLE, J. E., *Accretion discs in astrophysics.* Annu. Rev. Astron. Astrophys. **19**, 137–162 (1981).

[105] DUBRULLE, B., *A turbulent closure model for thin accretion disks*. Astron. Astrophys. **266**, 592–604 (1992).

[106] ZELDOVICH, Y. B., *On the friction of fluids between rotating cylinders.* R. Soc. London Proc. A **374**, 299–312 (1981).

[107] RICHARD, D. & ZAHN, J. P., *Turbulence in differentially rotating flows. What can be learned from the Couette-Taylor experiment*. Astron. Astrophys. **347**, 734–738 (1999).

[108] HERSANT, F., DUBRULLE, B. & HURÉ, J.-M., *Turbulence in circumstellar disks.* Astron. Astrophys. **429**, 531–542 (2005).

[109] JI, H., BURIN, M., SCHARTMAN, E. & GOODMAN, J., *Hydrodynamic turbulence cannot transport angular momentum effectively in astrophysical disks.* Nature **444**, 343–346 (2006).

[110] SCHARTMAN, E., JI, H. & BURIN, M. J., *Development of a Couette-Taylor flow device with active minimization of secondary circulation.* Rev. Sci. Instrum. **80**, 024501 (2009).

[111] Burin, M. J., Schartman, E. & Ji, H., *Local measurements of turbulent angular momentum transport in circular Couette flow.* Exp. Fluids **48**, 763–769 (2010).

[112] van Gils, D. P. M., Bruggert, G.-W., Lathrop, D. P., Sun, C. & Lohse, D., *The Twente turbulent Taylor-Couette (T3C) facility: strongly turbulent (multi-phase) flow between independently rotating cylinders.* Rev. Sci. Instrum. **82**, 25105 (2011).

[113] Schartman, E., Ji, H., Burin, M. J. & Goodman, J., *Stability of quasi-Keplerian shear flow in a laboratory experiment*. ArXiv e-prints (2011). http://arxiv.org/abs/1102.3725

[114] Balbus, S. A., *Fluid dynamics: A turbulent matter.* Nature **470**, 475–476 (2011).

[115] van Gils, D. P. M., Huisman, S. G., Grossmann, S., Sun, C. & Lohse, D., *Optimal Taylor-Couette turbulence*. Submitted to J. Fluid Mech.

[116] Virk, P. S., *Drag reduction fundamentals.* AIChE J. **21**, 625–656 (1975).

[117] Berman, N. S., *Drag reduction by polymers.* Annu. Rev. Fluid Dyn. **10**, 47–64 (1978).

[118] Benzi, R., Ching, E. S. C., Horesh, N. & Procaccia, I., *Theory of concentration dependence in drag reduction by polymers and of the maximum drag reduction asymptote.* Phys. Rev. Lett. **92**, 78302 (2004).

[119] L'vov, V. S., Pomyalov, A., Procaccia, I. & Tiberkevich, V., *Drag reduction by polymers in wall bounded turbulence.* Phys. Rev. Lett. **92**, 244503 (2004).

[120] Pal, S., Deutsch, S. & Merkle, C. L., *A comparison of shear-stress fluctuation statistics between microbubble modified and polymer modified turbulent boundary-layers.* Phys. Fluids A **1**, 1360–1362 (1989).

[121] Xu, J., Maxey, M. R. & Karniadakis, G. E., *Numerical simulation of turbulent drag reduction using micro-bubbles.* J. Fluid Mech. **468**, 271–281 (2002).

[122] Sugiyama, K., Kawamura, T., Takagi, S. & Matsumoto, Y., *The Reynolds Number Effect on the Microbubble Drag Reduction*. In *Proceedings of the 5th Symposium on Smart Control of Turbulence*, pp. 31–43. University of Tokyo, Tokyo (2004).

[123] MADAVAN, N. K., DEUTSCH, S. & MERKLE, C. L., *Measurements of local skin frictions in a microbubble-modified turbulent boundary layer.* J. Fluid Mech. **156**, 237–256 (1985).

[124] L'VOV, V. S., POMYALOV, A., PROCACCIA, I. & TIBERKEVICH, V., *Drag reduction by microbubbles in turbulent flows: the limit of minute bubbles.* Phys. Rev. Lett. **94**, 174502 (2005).

[125] SANDERS, W. C., WINKEL, E. S., DOWLING, D. R., PERLIN, M. & CECCIO, S. L., *Bubble friction drag reduction in a high-Reynolds-number flat-plate turbulent boundary layer.* J. Fluid Mech. **552**, 353–380 (2006).

[126] DEUTSCH, S., FONTAINE, A. A., MOENY, M. J. & PETRIE, H., *Combined polymer and microbubble drag reduction on a large flat plate.* J. Fluid Mech. **556**, 309–327 (2006).

[127] LATORRE, R., MILLER, A. & PHILIPS, R., *Micro-bubble resistance reduction for high speed craft*. Trans. Soc. Nav. Arch. Mar. Eng. **110**, 259 (2002).

[128] FERRANTE, A. & ELGHOBASHI, S., *On the physical mechanisms of drag reduction in a spatially-developing turbulent boundary layer laden with microbubbles.* J. Fluid Mech. **503**, 345 (2004).

[129] LO, T. S., L'VOV, V. S. & PROCACCIA, I., *Drag reduction by compressible bubbles.* Phys. Rev. E **73**, 36308 (2006).

[130] CADOT, O., COUDER, Y., DAERR, A., DOUADY, S. & TSINOBER, A., *Energy injection in closed turbulent flows: Stirring through boundary layers versus inertial stirring.* Phys. Rev. E **56**, 427–433 (1997).

[131] DEUTSCH, S., MOENY, M., FONTAINE, A. A. & PETRIE, H., *Microbubble drag reduction in rough walled turbulent boundary layers with comparison against polymer drag reduction.* Exp. in Fluids **37**, 731–744 (2004).

[132] VLACHOGIANNIS, M. & HANRATTY, T. J., *Influence of wavy structured surfaces and polymer aggregation on drag reduction.* Exp. Fluids **36**, 685–700 (2004).

[133] CADOT, O., BONN, D. & DOUADY, S., *Turbulent drag reduction in a closed flow system: Boundary layer versus bulk effects.* Phys. Fluids **10**, 426 (1998).

[134] BENZI, R., ANGELIS, E. D., L'VOV, V. S., PROCACCIA, I. & TIBERKEVICH, V., *Maximum drag reduction asymptotes and the cross-over to the Newtonian plug.* J. Fluid Mech. **551**, 185–195 (2006).

[135] RISSO, F. & FABRE, J., *Oscillations and breakup of a bubble immersed in a turbulent field*. J. Fluid Mech. **372**, 323–355 (1998).

[136] EINSTEIN, A., *A new determination of molecular dimensions*. Ann. Phys. (Leipz.) **19**, 289–306 (1906).

[137] ACRIVOS, A., *Bingham award lecture - 1994. Shear-induced particle diffusion in concentrated suspensions on noncolloidal particles*. J. Rheol. **39**, 813–826 (1995).

[138] LOHSE, D., *Crossover from high to low Reynolds number turbulence*. Phys. Rev. Lett. **73**, 3223–3226 (1994).

[139] MURAI, Y., OIWA, H. & TAKEDA, Y., *Bubble behavior in a vertical Taylor-Couette flow*. J. Phys.: Conf. Ser. **14**, 143–156 (2005).

[140] SAEKI, T., DE GUZMAN, M. R., MORISHIMA, H., USUI, H. & NISHIMURA, T., *A flow visualization study of the mechanism of turbulent drag reduction by surfactants*. Nihon Reoroji Gakkaishi **20**, 35–40 (2000).

[141] DRAPPIER, J., DIVOUX, T., AMAROUCHENE, Y., BERTRAND, F., RODTS, S., CADOT, O., MEUNIER, J. & BONN, D., *Turbulent drag reduction by surfactants*. Europhys. Lett. **74**, 362 (2006).

[142] BONN, D., AMAROUCHÈNE, Y., WAGNER, C., DOUADY, S. & CADOT, O., *Turbulent drag reduction by polymers*. J. Phys. Condens. Matter **17**, S1195 (2005).

[143] WHITE, C. M. & MUNGAL, M. G., *Mechanics and prediction of turbulent drag reduction with polymer additives*. Annu. Rev. Fluid Mech. **40**, 235–256 (2008).

[144] PROCACCIA, I., LVOV, V. S. & BENZI, R., *Colloquium: Theory of drag reduction by polymers in wall-bounded turbulence*. Rev. Mod. Phys. **80**, 225–247 (2008).

[145] KATO, H., MIURA, K., YAMAGUCHI, H. & MIYANAGA, M., *Experimental study on microbubble ejection method for frictional drag reduction*. J. Mar. Sci. Technol. **3**, 122–129 (1998).

[146] CLARK III, H. & DEUTSCH, S., *Microbubble skin friction on an axisymmetric body under the influence of applied axial pressure gradients*. Phys. Fluids **A3**, 2948–2954 (1991).

[147] LATORRE, R., *Ship hull drag reduction using bottom air injection.* Ocean Eng. **24**, 161–175 (1997).

[148] SUGIYAMA, K., CALZAVARINI, E. & LOHSE, D., *Microbubble drag reduction in Taylor-Couette flow in the wavy vortex regime.* J. Fluid Mech. **608**, 21–41 (2008).

[149] ELBING, B. R., WINKEL, E. S., LAY, K. A., CECCIO, S. L., DOWLING, D. R. & PERLIN, M., *Bubble-induced skin-friction drag reduction and the abrupt transition to air-layer drag reduction.* J. Fluid Mech. **612**, 1–36 (2008).

[150] GUTIERREZ-TORRES, C. C., HASSAN, Y. A. & JIMENEZ-BERNAL, J. A., *Turbulence structure modification and drag reduction by microbubble injections in a boundary layer channel flow.* J. Fluids Eng. **130**, 111–304 (2008).

[151] JACOB, B., OLIVIERI, A., MIOZZI, M., CAMPANA, E. F. & PIVA, R., *Drag reduction by microbubbles in a turbulent boundary layer.* Phys. Fluids **22**, 115104 (2010).

[152] MENG, J. C. S. & UHLMAN, J. S., *Microbubble formation and splitting in a turbulent boundary layer for turbulence reduction.* In *Proceedings of the International Symposium on Seawater Drag Reduction* (ed. US Office of Naval Research Arlington), pp. 341–355. Newport, Rhode Island (1998).

[153] MERKLE, C. L. & DEUTSCH, S., *Microbubble drag reduction in liquid turbulent boundary layers.* Appl. Mech. Rev. **45**, 103–127 (1992).

[154] MORIGUCHI, Y. & KATO, H., *Influence of microbubble diameter and distribution on frictional resistance reduction.* J. Mar. Sci. Technol. **7**, 79–85 (2002).

[155] SHEN, X., CECCIO, S. & PERLIN, M., *Influence of bubble size on microbubble drag reduction.* Exp. Fluids **41**, 415–424 (2006).

[156] DJERIDI, H., GABILLET, C. & BILLARD, J. Y., *Two-phase Couette-Taylor flow: Arrangement of the dispersed phase and effects on the flow structures.* Phys. Fluids **16**, 128–139 (2004).

[157] MUDDE, R. F. & SAITO, T., *Hydrodynamical similarities between bubble column and bubbly pipe flow.* J. Fluid Mech. **437**, 203–228 (2001).

[158] XUE, J., AL-DAHHAN, M., DUDOKOVIC, M. P. & MUDDE, R. F., *Bubble dynamics measurements using four-point optical probe.* Can. J. Chem. Eng. **81**, 375–381 (2003).

[159] LUTHER, S., RENSEN, J. M. & GUET, S., *Bubble aspect ratio and velocity measurement using a four-point fiber-optical probe.* Exp. Fluids **36**, 326–333 (2004).

[160] WU, C., SUDDARD, K. & AL-DAHHAN, M. H., *Bubble dynamics investigation in a slurry bubble column.* AIChE Journal **54**, 1203–1212 (2008).

[161] CARTELLIER, A. & ACHARD, J. L., *Local phase detection probes in fluid/fluid two-phase flows.* Rev. Sci. Instrum. **62**, 279–303 (1991).

[162] JULIA, J. E., HARTEVELD, W. K., MUDDE, R. F. & DEN AKKER, H. E. A. V., *On the accuracy of the void fraction measurements using optical probes in bubbly flows.* Rev. Sci. Instrum. **76**, 35103 (2005).

[163] TAKAGI, S. & MATSUMOTO, Y., *Surfactant effects on bubble motion and bubbly flows.* Annu. Rev. Fluid Mech. **43**, 615–636 (2011).

Summary

Science is served by experiments over which one has full control of the system and driving parameters and which allow for unambiguous observations of the response parameters. For the field of fluid mechanics the Taylor-Couette (TC) flow geometry facilitates the design of such well controlled experiments. TC flow *in essence* is described by a fluid confined between two concentric cylinders and thereby set into motion by the rotation of the inner and/or outer cylinder. Under the proper experimental conditions, this closed flow geometry ensures a beautiful relation between the large-scale power input into the flow and the small-scale fluid's energy dissipation rate manifesting itself as a torque on the cylinder walls.

The research issues addressed in this mostly experimental thesis, concern highly turbulent TC flow ($Re > 10^5 \Leftrightarrow Ta > 10^{11}$) — at a fundamental level to aid our understanding of (TC) turbulence and to interpret towards astrophysical disks — and at a practical level as applications can be found in skin-friction drag reduction towards ships. In PART I we introduce the new TC facility of our Physics of Fluids group, called the Twente turbulent Taylor-Couette (T^3C) facility. In PART II we focus on highly turbulent single-phase TC flow; we use the scaling of the torque as thread and we provide *local* angular velocity measurements. In PART III we study the effect of bubbles on highly turbulent TC flow, focusing not only on the global drag reduction, but also on the *local* bubble distribution and angular velocity profiles.

In chapter 2 of PART I we present the T^3C facility in great detail. It features *inter alia* two independently rotating cylinders capable of rotation rates of 10's of revolutions per second, precise temperature and rotation rate control, torque sensors, bubble injection and gas volume fraction control, and it features transparent outer cylinders of different radii providing full optical access to the internal flow. We demonstrate the system's accuracy and we provide benchmarks on initial torque measurements and local angular velocity profiles as measured by laser Doppler anemometry.

In chapter 3 of PART II we measure the global torque to investigate the dimensionless transport flux of the angular velocity as function of the driving control parameters. We show that the driving parameters are ideally expressed by the Taylor number and the ratio of the outer cylinder angular velocity to the inner cylinder angular velocity, hence revealing universal scaling of power 0.38 for constant driving ratios. The observed effective scaling exponent is an indication that the TC gap is completely occupied by two fully turbulent kinematic boundary layers and a turbulent bulk, analogous to scaling as observed in kinematically fully turbulent Rayleigh-Bénard convection cells. We find maximum transport for slight counter-rotation, namely when the outer cylinder counter-rotates at ≈ 0.4 times the angular velocity of the inner cylinder. This value is determined for the current radius ratio at the explored high Taylor number regime.

In chapter 4 of PART II we go in detail into the flow examined in the previous chapter, extending it with local angular velocity information and increasing our resolution in the driving ratios. We find optimum angular velocity transport at slight counter-rotation, now at the more precise driving ratio of 0.368. This ratio coincides with the bisector of the (Re_i, Re_o)-instability range. Apparently, there is a competition between the effects on the flow induced by outer cylinder counter-rotation: Shear enhancement and thus turbulence amplification at slight counter-rotation, and flow stabilization and thus turbulence degeneration for stronger counter-rotation. We provide radial profiles on the angular velocity by laser Doppler anemometry. We find that the flow at optimal transport is characterized by zero slope of the angular velocity associated with fully convective transport. We also focus on the neutral line, defined as the radial position of zero angular velocity, and we find that only for strong counter-rotation, i.e. rotating the outer cylinder faster than the maximum transport case, the neutral line is shifted out of the outer cylinder boundary layer towards the inner cylinder. The flow around the neutral line in the bulk is characterized by bi-modal velocity distributions, interpreted as turbulent burst arising from the unstable inner cylinder region and crossing the neutral line into the stable outer cylinder region, opposite to the otherwise mono-modal velocity distributions.

In chapter 5 of PART II the main topic is whether the accretion of matter in astrophysical disks can be attributed to turbulent viscous dissipation; a highly debated issue. We study the Keplerian profiles associated to these disks with the use of TC apparatuses, and we measure the angular momentum transport based on global torque measurements. We argue that these quasi-Keplerian profiles can reflect the physics found in astrophysical disks, taking into account finite size effects of experimental TC flow. We measure enhanced angular momentum transport above the theoretically expected laminar transport. Hence, we conclude that quasi-Keplerian profiles exhibit turbulent viscous dissipation. The momentum transport can be transformed into an accretion rate, which is found to be in line with accretion rates as found for disks around TTauri stars [108].

In chapter 6 of PART III we measure the drag on the inner cylinder wall while bubbles of 1 mm in diameter are injected into turbulent TC flow. We find drag reduction (DR) due to bubble injection in the case of smooth cylinder walls, whereas for step-like roughened cylinder walls we find no DR. As in the rough-wall case no smooth boundary layers can develop, the results demonstrate that bubbly DR is a pure boundary layer effect.

Finally, in chapter 7 of PART III, we study DR in highly turbulent TC flow under influence of bubble injection of 1 mm in diameter, focussing on global and *local* parameters. The global DR, based on the measured torque, reaches up to 40% when injecting bubbles up to just 4% gas volume fraction. Two different regimes are apparent in the global DR results: One regime with moderate DR and the other regime with strong DR. This was already observed in global experiments by van den Berg *et al.* [27] who attributed the crossover into the strong DR regime to the bubble deformability mechanism becoming significantly active, in line with the numerical simulations by Lu, Fernandez & Tryggvason [28]. Here we provide local results on the angular velocity modifications and bubble distribution profiles inside the TC gap for the two different regimes. We find that the bubbles are highly concentrated in the inner cylinder boundary regime for both DR regimes. We confirm that the bubbles in the moderate DR regime stay nearly spherical and that they deform in the strong DR regime. We end the chapter with a discussion on how these findings can be projected onto other wall-bounded flows.

Samenvatting

Wetenschap heeft baat bij experimenten, waarbij men volledige controle heeft over de systeem- en aansturingsparameters en waarbij men de reactieparameters eenduidig kan observeren. In het vakgebied van de stromingsleer wordt het ontwerp van dergelijke gecontroleerde experimenten, vergemakkelijkt door de geometrie van Taylor-Couette (TC) stroming. TC stroming kan *in essentie* omschreven worden als een vloeistof opgesloten tussen twee concentrische cylinders en daarmee in gang gebracht door de binnenste en/of buitenste cilinder te roteren. Onder de juiste experimentele omstandigheden zorgt deze gesloten stroming voor een elegante relatie tussen het grootschalige toegevoerde vermogen en het kleinschalige vloeistofdissipatiefvermogen, dat zich manifesteert als een koppel op de cilinderwanden.

De vraagstellingen in dit, voornamelijk experimenteel, proefschrift hebben betrekking op hoog turbulente TC stroming ($Re > 10^5 \Leftrightarrow Ta > 10^{11}$) — op een fundamenteel niveau om ons begrip van (TC) turbulentie te ondersteunen en om het toe te passen op astrofysische schijven — en op een praktisch niveau aangezien toepassingen denkbaar zijn ter vermindering van de huidwrijvingsweerstand van schepen. In DEEL I introduceren we de nieuwe TC faciliteit van onze Physics of Fluids onderzoeksgroep, genaamd de Twente turbulente Taylor-Couette (T^{3}C) faciliteit. In DEEL II richten we ons op hoog turbulente enkelfasige TC stroming; de schaling van het koppel dient als rode draad en we presenteren *lokale* hoeksnelheidsmetingen. In DEEL III bestuderen we het effect van luchtbellen geïnjecteerd in hoog turbulente TC stroming, waarbij we ons niet enkel richten op de globale weerstandsvermindering, maar ook op de *lokale* bellenconcentratie- en hoeksnelheidsprofielen.

In hoofdstuk 2 van DEEL I detaileren we de T^{3}C faciliteit. Het beschikt, onder meer, over twee onafhankelijk van elkaar draaiende cilinders waarvan de rotatiesnelheden tientallen omwentelingen per seconde bereiken, exacte temperatuurs- en rotatiesnelheidscontrole, koppelsensoren, belleninjectie en gas-volume-fractie controle, en het beschikt over transparante buitencilinders van verschillende radii, waarmee men optische toegangelijkheid verkrijgt tot het inwendige van de stroming. We demonstreren de nauwkeurigheid van het systeem en we presenteren ijkpunten van de eerste koppelmetingen en lokale hoeksnelheidsprofielen, verkregen door laser-Doppler-snelheidsmetingen.

In hoofdstuk 3 van DEEL II meten we het globale koppel om de dimensieloze transport flux van de hoeksnelheid te onderzoeken als functie van de aansturingsparameters. We laten zien dat de aansturingsparameters idealiter uitgedrukt worden door het Taylor-getal en de verhouding van de buitenste cilinder hoeksnelheid op de binnenste cilinder hoeksnelheid, en zodoende een universele schaling onthullen van de macht 0.38, zolang een constante hoeksnelheidsverhouding wordt gebruikt. De waargenomen effectieve schalingsexponent is een aanwijzing dat de TC spleet volledig bezet wordt door twee volledig turbulente kinematische grenslagen en een turbulente bulk, analoog aan de schaling zoals waargenomen in kinematisch volledig turbulente Rayleigh-Bénard convectiecellen. We vinden maximaal transport van de hoeksnelheid voor lichte contra-rotatie, namelijk wanneer de buitenste cilinder ca. 0.4 keer de hoeksnelheid van de binnenste cilinder heeft. Deze waarde is verkregen voor de huidige radius-ratio bij het verkende hoge Taylor-getal regime.

In hoofdstuk 4 van DEEL II gaan we gedetaileerd in op de stroming zoals onderzocht in het vorige hoofdstuk, door het uit te breiden met lokale hoeksnelheidsinformatie en door de resolutie in de hoeksnelheidsverhoudingen te vergroten. We vinden een optimaal transport van de hoeksnelheid voor lichte contra-rotatie, nu bij de meer nauwkeurige verhouding van 0.368. Deze verhouding komt overeen met de bissectrice van de (Re_i, Re_o)-instabiliteitsruimte. Blijkbaar is er een concurrentie tussen de effecten op de stroming veroorzaakt door buitencilinder contra-rotatie: versterking van de afschuifspanning en dus een toename van turbulentie bij lichte contra-rotatie, en stabilisering van de stroming en dus afname van turbulentie bij sterkere contra-rotatie. We tonen radiale profielen van de hoeksnelheid verkregen door laser-Doppler-snelheidsmetingen. We vinden dat de stroming bij optimaal transport wordt gekenmerkt door een vlakke helling van het hoeksnelheidsprofiel, typerend voor volledig convectief transport. We richten ons ook op de neutrale lijn, gedefinieerd als de radiale positie van hoeksnelheid nul, en we vinden dat alleen voor sterke contra-rotatie, d.w.z. wanneer de buitencilinder harder draait dan de verhouding die geldt voor maximaal transport, de neutrale lijn uit de buitencilinder grenslaag komt en verschuift richting de binnencilinder. De stroming rond de neutrale lijn wordt gekenmerkt door bi-modale snelheidsdistributies, geïnterpreteerd als turbulente uitbarstingen die vanuit de onstabiele binnencilinder regio de neutrale lijn oversteken naar de stabiele buitencilinder regio, in tegenstelling tot de anders mono-modale snelheidsdistributies.

In hoofdstuk 5 van DEEL II stellen we de hoofdvraag of de accretie van materie in astrofysische schijven, toegeschreven kan worden aan turbulent visceuze dissipatie; een zeer controversieel onderwerp. We bestuderen de Kepleriaanse profielen die toebehoren aan deze schijven door gebruik te maken van TC apparaten, en we meten het hoekmomenttransport aan de hand van globale koppelmetingen. We stellen dat deze quasi-Kepleriaanse profielen de fysica nabootsen, zoals aangetroffen kan worden in astrofysische schijven, en we nemen hierbij het effect van de eindige grootte van experimentele TC stroming in ogenschouw. We meten een verhoogd hoekmomenttransport ten opzichte van het theoretisch verwachte laminair transport. Hieruit concluderen we dat quasi-Kepleriaanse profielen turbulente visceuze dissipatie vertonen. Het hoekmomenttransport kan omgezet worden in een accretiesterkte die in overeenstemming is met de aangetroffen accretiesterktes in TTauri sterren [108].

In hoofdstuk 6 van DEEL III meten we de stromingsweerstand op de binnencilinder, terwijl belletjes van 1 mm in diameter geïnjecteerd worden in turbulente TC stroming. We vinden vermindering van de weerstand, ten gevolge van belleninjectie, in het geval van gladde cilinderwanden, terwijl we voor stapachtig geruwde cilinderwanden geen vermindering vinden. Omdat er zich geen glad-verlopende grenslagen kunnen ontwikkelen in het geval van geruwde wanden, tonen de resultaten dat weerstandvermindering onder invloed van belleninjectie een grenslaag-effect is.

Tenslotte bestuderen we in hoofdstuk 7 van DEEL III de weerstandsvermindering in hoog turbulente TC stroming onder invloed van belleninjectie van 1 mm in diameter, gericht op globale en *lokale* parameters. De globale weerstandsvermindering, gebaseerd op het gemeten koppel, reikt tot wel 40% bij slechts een gas-volumefractie van 4%. Twee verschillende regimes zijn duidelijk zichtbaar in de globale weerstandsvermindering: het ene regime met een gematigde weerstandvermindering en het andere regime met een forse weerstandsvermindering. Dit werd al waargenomen in de globale experimenten door van den Berg *et al.* [27], die de transitie naar het forse weerstandsvermindering-regime toeschreven aan het significant actief worden van het bellenvervormbaardheids-effect, in lijn met de numerieke simulaties van Lu, Fernandez & Tryggvason [28]. We presenteren hier nu lokale resultaten aangaande de hoeksnelheidswijzigingen en bellendistributieprofielen in de TC spleet voor de twee verschillende regimes. We vinden dat de bellen zich, voor beide regimes, sterk concentreren in het binnencilinder gebied. We bevestigen dat de bellen in het gematigde weerstandsvermindering-regime nagenoeg bolvormig blijven, maar dat ze vervormen in het forse weerstandsvermindering-regime. Het hoofdstuk sluit af met een discussie over het toepassen van de gevonden resultaten op andere wand-begrensde stromingen.

Scientific output

PUBLICATIONS IN PEER-REVIEWED JOURNALS

1. T.H. VAN DEN BERG, D.P.M. VAN GILS, D.P. LATHROP & D. LOHSE,
   Bubbly turbulent drag reduction is a boundary layer effect,
   Phys. Rev. Lett. **98**, 084501 (2007).
   See chapter 6 of this thesis.

   - Highlighted by "Bubbels zinloos bij ruwe scheepsromp", De Volkskrant, February 2nd 2007.
     http://www.volkskrant.nl/vk/nl/2672/Wetenschap-Gezondheid/article/detail/838869/2007/02/21/Bubbels-zinloos-bij-ruwe-scheepsromp.dhtml

2. J. MARTINEZ MERCADO, D. CHEHATA GOMEZ, D.P.M. VAN GILS, C. SUN & D. LOHSE,
   On bubble clustering and energy spectra in pseudo-turbulence,
   J. Fluid Mech. **650**, 287–306 (2010).

3. D.P.M. VAN GILS, G.-W. BRUGGERT, D.P. LATHROP, C. SUN & D. LOHSE,
   The Twente turbulent Taylor-Couette (T^3C) facility: strongly turbulent (multiphase) flow between independently rotating cylinders,
   Rev. Sci. Instrum. **82**, 025105 (2011).
   See chapter 2 of this thesis.

4. D.P.M. VAN GILS, S.G. HUISMAN, G.-W. BRUGGERT, C. SUN & D. LOHSE,
   Torque scaling in turbulent Taylor-Couette flow with co- and counterrotating cylinders,
   Phys. Rev. Lett. **106**, 024502 (2011).
   See chapter 3 of this thesis.

   - Selected as an "Editor's suggestion".
   - Highlighted by "Exploring the extremes of turbulence", A.G. Smart, Physics Today **64**, 18–20 (2011).
   - Highlighted by "Fluid Dynamics: A turbulent Matter", Steven A. Balbus, Nature **470**, 475–476 (2011).

- Highlighted by “Heat and twist of turbulent flows”, D. van Heijnsbergen, Physics: Spotlighting Exceptional Research. http://physics.aps.org/synopsis-for/10.1103/PhysRevLett.106.024502

5. D.P.M. VAN GILS, S.G. HUISMAN, S. GROSSMANN, C. SUN & D. LOHSE,
   Optimal Taylor-Couette turbulence,
   submitted to J. Fluid Mech.
   See chapter 4 of this thesis.

6. S. PAOLETTI, D.P.M. VAN GILS, B. DUBRULLE, C. SUN, D. LOHSE & D.P. LATHROP,
   Angular momentum transport and turbulence in laboratory models of Keplerian flows,
   submitted to Astron. Astrophys.
   See chapter 5 of this thesis.

7. D.P.M. VAN GILS, D. NAREZO GUZMAN, C. SUN & D. LOHSE,
   Bubble deformability is crucial for strong drag reduction in turbulent TC flow,
   submitted to J. Fluid Mech.
   See chapter 7 of this thesis.

8. S.G. HUISMAN, D.P.M. VAN GILS & C. SUN,
   Applying Laser Doppler Anemometry inside a Taylor-Couette geometry — Using a ray-tracer to correct for curvature effects,
   submitted to EJM-B/Fluids.

9. S.G. HUISMAN, D.P.M. VAN GILS, S. GROSSMANN, C. SUN & D. LOHSE,
   Ultimate Taylor-Couette turbulence.
   Phys. Rev. Lett. (in print), http://arxiv.org/abs/1111.0063.

CONTRIBUTED TALKS

1. 61st Annual DFD Meeting, San Antonio, Texas (USA), *Bubbly turbulent drag reduction is a boundary layer effect,* November 23–25, 2008.

2. 1st Fermat-Impact Meeting, L’Institut de Mécanique des Fluides de Toulouse, Toulouse (France), *Bubbly drag reduction in turbulent Taylor-Couette flow,* December 17–19, 2008.

3. 62nd Annual DFD Meeting, Minneapolis, Minnesota (USA), *Twente turbulent Taylor-Couette,* November 22–24, 2009.

4. 63rd Annual DFD Meeting, Long Beach, Florida (USA), *Torque scaling in turbulent Taylor-Couette flow with co- and counterrotating cylinders,* November 21–23, 2010.

5. J.M. Burgersdag, Delft University of Technology, Delft (The Netherlands), *Torque scaling in turbulent Taylor-Couette flow with co- and counterrotating cylinders,* January 1, 2011.
6. Mini-symposium on bubbly flow in Twente, University of Twente, Enschede (The Netherlands), *Bubble deformability is crucial for strong drag reduction in bubbly turbulent Taylor-Couette flow,* July 15, 2011.
7. 17th International Couette-Taylor Workshop, University of Leeds, Leeds (UK), *Drag reduction, bubble distribution and velocity profiles in bubbly turbulent Taylor-Couette flow,* July 25–27, 2011.
   Awarded the best student presentation price
8. 13th European Turbulence Conference, University of Warsaw, Warsaw (Poland), *Drag reduction, bubble distribution and velocity profiles in bubbly turbulent Taylor-Couette flow,* September 12–15, 2011.

STUDENT MENTORING

1. Sander G. Huisman, *Local velocity measurements in Twente turbulent Taylor-Couette*, Master Thesis, November 8, 2010.
2. Daniela Narezo Guzman, *Bubble deformability is crucial for strong drag reduction in bubbly turbulent Taylor-Couette flow*, Master Thesis, May 11, 2011.
3. Erik Dietrich, *Beer flow dynamics*, external Master Thesis at Heineken, October 31, 2011.
4. Tim J.G. Jannink, *Optimal Taylor-Couette turbulence at different radius ratios*, Master Thesis, ongoing.

TEACHING EXPERIENCE

1. Teaching assistant for the 2nd year Bachelor course “Physics of Fluids Practical” of the study Applied Physics in Twente, 2009–2010.
2. Teaching assistant for the 1st year Bachelor’s final project “P-project” of the study Applied Physics in Twente, 2010.

Acknowledgements

The research described in this thesis was primarily carried out at the Physics of Fluids group of the Faculty of Science and Technology of the University of Twente. This research is supported by the Dutch Technology Foundation STW, which is part of the Netherlands Organisation for Scientific Research (NWO) and partly funded by the Ministry of Economic Affairs, Agriculture and Innovation (project number 07781). I gratefully acknowledge their support.

∼ · ∼ · ∼ · ∼ · ∼ · ∼ · ∼ · ∼ · ∼ · ∼ · ∼ · ∼

Science heavily leans on the continuation of previous research and on the cooperation between fellow scientists, and is therefore never a single man's or woman's feat. Many people contributed to the work in this thesis and I express my gratitude towards everyone that supported it. Some people I would like to thank in particular.

∼ · ∼ · ∼ · ∼ · ∼ · ∼ · ∼ · ∼ · ∼ · ∼ · ∼ · ∼

First of all, I thank my promotor prof. Detlef Lohse for the opportunities he offered me. He gave me the freedom to explore the engineering side of building up a new TC facility, additional to experimental research. Thanks for your great job in leading a successful group of which I am proud to have been part of. I greatly value the scientific discussions we had, providing me each time with physical interpretations behind new data. Making presentations is a skill I learned from you. My thanks also go to my daily supervisor and assistant-promotor dr. Chao Sun. Your enthusiasm and energy are always uplifting and your guidance is pleasant and good. I will remember the great dinners at your place (your wife makes the best dumplings). Thanks, Detlef and Chao, for teaching me how to do science.

Much insight and physical interpretation to this work were also provided by the professors Siegfried Grossmann, Guenter Ahlers, Bruno Eckhardt and Gerd Pfister. I thank them sincerely for their valuable input. My gratitude also goes towards the professors Leen van Wijngaarden, Roberto Verzicco, Theo van der Meer, Tom van Terwisga and Jerry Westerweel for taking place in my PhD committee.

In light of the STW programme on ship-drag reduction by air lubrication, I thank all the project members for their effort and their helpful discussions and feedback: From the Delft University prof. Tom van Terwisga (always kindly leading the programme), dr. René Delfos, prof. Jerry Westerweel, ir. Oleksandr Zverkhovskyi and ir.

Marc Harleman, from MARIN dr. Evert-Jan Foeth, from DST in Duisburg dr. Cornell Thill, from Bluewater dr. Clemens van der Nat, from STW dr. Corine Meuleman and from Spaarnwater Eelco van Rietbergen who also participated in the very first T^{3}C measurements and whose help was appreciated on the torque calibration and balancing.

I also owe a debt of gratitude towards prof. Dan Lathrop of the University of Maryland (UMD). It was in his group that I got my first taste of experimental TC flow by letting me perform my internship on the UMD TC facility. Also the design of the T^{3}C facility started on the fundamental design plans of the UMD TC facility. Without prof. Lathrop, dr. Matthew Paoletti from UMD and prof. Bérengère Dubrulle from the French CNRS center, this thesis would lack chapter 5. I am thankful to them for letting me incorporate our joint-publication as part of my thesis.

Another one who should not go unmentioned is dr. Ramon van den Berg, former PhD candidate of our Physics of Fluids group and now working for Heineken. He supervised me during my internship and partly during my masters. I had a great time together with him in Maryland and he kindly helped me a lot with all the foreign housing and visa paperwork. I thank him for his work on the publication as featured in chapter 6. He was the first PhD student to help draw up the T^{3}C device and to calculate its design parameters.

The T^{3}C facility could not have been realized without the technical expertise of the following people. Our group's technician Gert-Wim Bruggert deserves much credit for the overall design. His well-thought-out and detailed 3D-design plans have made the T^{3}C setup easy to work with and a charm to diss- and reassemble. You can only guess at the wonderful support tools that are invented by this man to aid in adjusting the TC setup to meet specific needs. There is also TCO to thank, the technical service group of the University of Twente. In specific: Sip Jan Boorsma for mechanical design, Geert Mentink for electrical design, Rindert Nauta for system automation, and Henk Waayer for electrical installation. This service group is a valuable asset to the university as they provide a clear link between scientific demands and technological realizations. Sandra Bekman and Jan Schepers are acknowledged for their support during machining and initial assembly at VDL-ETG in Almelo. For the background and technical support on the optical fiber probe technique, I thank prof. Rob Mudde and technician Jaap van Raamt of Delft University.

Three other invaluable cornerstones of our group also deserve my gratitude. Our nice secretary Joanita without whom many paperwork would go amiss, technician Martin Bos for his always fast service with a smile, and our administrator Bas Benschop for maintaining the computer park and having always nice stories to share.

I now come to the colleagues in our group. The daily T^{3}C team consists of several people with whom I shared a good time. Besides Chao Sun, I thank Sander Huisman, who started as master student under my supervision in the lab and who has been my roommate for the last year, for his sharp mind, master student Tim Jannink for his hard work on TC measurements, and once visiting PhD student Agathe Chouippe for her high-speed imaging of bubbly flows. I also owe thanks to my other (former) roommates, for warning me not to become deaf by the volume of my earphones and for their pleasant company: Richard Stevens, Rodolfo Ostilla Monico, Julian Martinez Mercado and Marine Guemas. I shared a great time with all the people in the group, simply too many to list. Thanks for creating a nice and inspiring atmosphere. In particular I thank Ivo Peters for helping me with organizing the children's experiments day, Sander Huisman, Koen Winkels and Vivek Nagendra Prakash for their support during open-house-day demonstrations, and Hanneke Gelderblom for kindly succeeding me as Burgerscentrum group representative and also for helping me out during open house days.

A special place is reserved for Daniela Narezo Guzman. As my former master student, she did all of the local bubble-profile measurements of chapter 7 with relentless effort. She made my days in the lab shine when working together, and this was mutual. It was therefore unavoidable that our paths in life existed next to each other. I am looking forward to visiting you in Santa Barbara or Mexico and I wish you all the luck and happiness from the bottom of my heart. *Espero que nuestros caminos se crucen otra vez.*

I would not have come so far without my loving parents and close family. I will address them in Dutch. *Pa en ma, bedankt voor jullie onvoorwaardelijke liefde en steun. Ik denk graag dat mijn affiniteit voor mechanica en sleutelen te danken is aan jou, pa, en de werkplaats, waar ik als kleine jongen altijd graag naar de autoschadegevallen keek en waar je me veel technieken hebt geleerd. Ik bedank ook m'n zus en haar man, waar ik altijd welkom ben. Sandra en René; het geeft me veel vreugde om oom te zijn van twee sterke jongens.*

Dennis van Gils
November 10th, 2011

About the author

Dennis Paulus Maria van Gils was born on May 2$^{\text{nd}}$ in Noord-Brabant, the Netherlands, where he lived in a village called Steenbergen. Dennis graduated from high school "Het Mollerlyceum" in Bergen op Zoom in 1999, where he also earned his B-diploma on playing the piano at the local music school. Several months later he moved to Enschede to study Applied Physics at the University of Twente. He participated in various sports and musical activities and he was chairman of a physics symposium committee in 2001. In 2002 he decided that it would be a good time for a sabbatical, so he became full-time board member for a year of the study association for applied physics "Arago" as commissary of external relations, while also filling a student representative post for the department Applied Physics of "KIVI NIRIA", and programming database applications for the department of Communication Sciences as a side-job. After a study tour through the south of Europe at end of 2003, he realized that it was becoming about time to finish his studies and so he choose the fluid mechanics track at the Physics of Fluids group.

In 2005 Dennis did his external internship at the University of Maryland (USA) in the group of prof. Dan Lathrop on the topic of 'Drag reduction in bubbly rough-walled Taylor-Couette flow', leading to a joint-publication. He continued his Master project in the Physics of Fluids group on experimental techniques in turbulent flows, working on the Twente water tunnel and helping design the Twente turbulent Taylor-Couette. In December 2007 Dennis earned his Master's degree, after which he immediately continued in the Physics of Fluids group as PhD candidate in January 2008. He was teaching assistant for the 2$^{\text{nd}}$-year's practical on fluid physics in 2009 and 2010, and from 2008 up to 2010 he was the group's representative of the J.M. Burgerscentrum, the Dutch research school for fluid mechanics. He could often be found during the university's open-house days, giving demonstrations on fluid mechanics to visitors, and in 2009 he organized, with the help of his colleagues, a physics and chemistry experiments day for primary school children.

Dennis likes to communicate science to a broad audience. His spare time is filled with music, dance, swimming and programming. He has had +12 years of lessons in ballroom and latin dancing and he is currently learning to play the drums.